FULL-FIELD MODELING OF CRACK TIP SHIELDING PHENOMENA

YANWEI LU

PhD

2011

Copyright Statement

FULL-FIELD MODELLING OF CRACK TIP SHIELDING PHENOMENA

by

YANWEI LU

A thesis submitted to the University of Plymouth

in partial fulfilment for the degree of

DOCTOR OF PHILOSOPHY

Schools of Marine Science and Engineering/Computing and Mathematics
Faculty of Science and Technology

August 2011

Abstract

The application of fracture mechanics to engineering design has provided significant advances in understanding of the causes and mechanisms of failure and crack growth. Despite this, there are still some aspects that remain incompletely understood, such as the crack closure/crack shielding effect. The presence of crack closure/shielding acts to reduce $\Delta \boldsymbol{K}$. The mechanisms of crack closure/shielding are complicated, and have not been fully understood. This work focuses on the plasticity-induced crack tip shielding mechanism and presents a novel approach to characterise the elastic stress fields under the influence of the plastic enclave surrounding the crack tip. The model is successfully applied to determine the four stress parameters experimentally using full-field photoelastic stress analysis on polycarbonate CT specimens, following studies of the effect of the crack tip position and the valid data collection zone giving the best fit between the model predictions and the experimental data. The predicted values from the model demonstrate good data repeatability, and exhibit sensible trends as a function of crack length and load ratio that are interpretable in terms of physically meaningful changes to the plastic enclave. In addition, the model is proven to describe the stress field around a crack more accurately than classic Williams' stress solution. The model is also extended to AL 2024-T3 specimens using a full-field displacement measurement technique, digital image correlation. Using the Sobel edge detection method to identify the crack tip from the displacement fields with a rectangular shaped data collection zone employed in the current study, reasonable trends were again demonstrated in the experimental results as a function of crack length.

Contents

List of Figures

List of Tables

Nomenclature

a	Crack length, mm
z	Complex coordinate in the physical plane, $z = x + iy$
A, B, C, D, E	Coefficients.
σ_x, σ_y	Stresses in x and y direction, MPa
σ_{xy}	Shear stress, MPa
K_I	Mode I stress intensity factor, MPa √m
K_{II}	Mode II stress intensity factor, MPa √m
K_S	Shear stress intensity factor, MPa √m
K_R	Retardation stress intensity factor, MPa √m
K_{max}	Maximum stress intensity factor, MPa √m
K_{min}	Minimum stress intensity factor, MPa √m
K_{op}	Crack opening stress intensity factor, MPa √m
K_{cl}	Stress intensity factor at closure, MPa √m
ΔK_{eff}	Effective stress intensity factor range, MPa √m
N	Fringe order
h	Thickness of the specimens, mm
f	Material fringe constant (7MPa.mm/fringe , Polycarbonate)
C_f	Stress-optic coefficient for photoelastic materials
σ_1, σ_2	Principal stresses, MPa
σ_{ys}	Yield stress, MPa
Φ	Airy stress function
φ χ	Analytical functions in Muskhelishvili's approach

$\phi(z)$,$\psi(z)$	Muskhelishvili's complex potentials
r , θ	Notations for polar coordinates
r_p	Plastic radius around the crack tip
α	Irwin's constraint parameter
P	Applied load, N
E	Young's Modulus, MPa
v	Poisson's ratio.
μ	Shear modulus, MPa
χ	Function of Poisson's ratio
u_x, u_y	Horizontal and vertical displacements
$\mathcal{G}$	Energy release rate
Re	Real part in complex
Im	Imaginary part
σ_r, σ_θ	Stresses in r and θ direction, MPa
$\sigma_{r\theta}$	Shear stress in polar coordinates, MPa

Acknowledgements

I would like to start these acknowledgements by thanking my supervisors, Neil James, Colin Christopher and Eann Patterson, for their time and dedication, continuing support and guidance, and friendly supervision throughout my time here at the University of Plymouth.

I would also like to thank Philip Siegmann, Chiara Colombo, Ying Du and Amol Patki for sharing their knowledge and advice with me. I would also like to thank Terry Richards for all his help in the lab as well as other staff in the Structural Integrity Laboratory.

I would also like to extend these acknowledgements to all the staff members of the school of Computing and Mathematics for all the help they provided during my study. Thanks are also given to my colleagues: Golnaz Shahtahmassebi, Poonam Sharma, Christopher Harvey, Muhannad Al-Saadony, Waleed Aziz, Israa Tawfik, Merfat Raddadi, Nicola Iji, Amina Al-Hajri and Alan Wright for making my time here so nice.

Last, I would like to thank my beloved parents, Shanqian and Suyun, and my brother and sisters for their encouragement and support.

Author's Declaration

At no time during the registration for the degree of Doctor of Philosophy has the author been registered for any other University award without prior agreement of the Graduate Committee.

This study was financed with the aid of a studentship from the Faculty of Science and Technology at the University of Plymouth and carried out in collaboration with the Structural Integrity Laboratory at the University of Plymouth and the Composite Vehicle Research Centre at Michigan State University.

Relevant scientific seminars and conferences were attended at which work was presented; external institutions were visited for consultation purposes and several papers were prepared for publication.

Publications:

M. N. James, Yanwei Lu, C. J. Christopher and E. A. Patterson. A multiparameter fracture mechanics approach to plasticity-induced crack tip shielding. Proceedings of the Workshop on Problems of Fracture in Engineering Materials, Italian Fracture Group, Forni di Sopra, Italy, 7-9 January 2010, pp3-10.

M. N. James, Yanwei Lu, C.J. Christopher, E.A. Patterson. Full-field modelling of crack tip shielding via the 'plastic inclusion' concept. Proceedings of the 2nd International Conference on Advances in Product Development and Reliability (PDR2010), Shenyang, China, 28–30 July 2010. Advanced Materials Research, Vols. 118-120 (2010), pp1-9.

M. N. James, C. J. Christopher, Yanwei Lu, K. F. Tee and E. A. Patterson. Crack tip shielding from a plastic 'inclusion'. Proceedings of the 6th International Conference on Materials Structure and Micromechanics of Fracture, Brno, Czech Republic, 28-30 June 2010. Key Engineering Materials Vol. 465 (2011) pp 1-8.

M. N. James, C.J. Christopher, Yanwei Lu, E.A. Patterson. The plastic 'inclusion' as a bridge between local crack plasticity and global elastic field. Proceedings of the 1st International Conference on Characterization of Crack Tip Stress Fields, Forni di Sopra, Udine, Italy, 7-9 March 2011, pp178-184.

M. N. James, C.J. Christopher, Yanwei Lu, E.A. Patterson. The plastic 'inclusion' as a meso-scale bridge between local crack tip mechanisms and the global elastic field, submitted to the International Journal of Fatigue.

Presentation and Conferences Attended:

SEM Annual Conference and Exposition on Experimental and Applied Mechanics Society for Experimental Mechanics, Albuquerque, New Mexico, USA, 1-4, June, 2009.

Oral presentation in the School of Computing and Mathematics, University of Plymouth, Mathematics Seminars, 2010.

Word count of main body of thesis: 54,644

Signed.....Yanwei Lu.....

Date.....30.09.2011.....

Chapter 1 Introduction

1.1Motivation and aims of the research

Fatigue cracks have been one of the main sources of in-service structural failures. Current design of engineering structures demands an increasingly precise knowledge of the damage occurring in the materials during service. Since the first attempts to mathematically model fracture in the mid-twentieth century, there has been impressive progress in this field. The application of fracture mechanics to engineering design has provided further understanding into the causes and mechanisms of failure and crack growth. Despite this, there are still some aspects that remain incompletely understood, with such a case being the crack closure/crack tip shielding effect. The presence of crack closure acts to reduce the applied range of stress intensity, ΔK, to a lower effective value, ΔK_{eff}, and this leads to a break-down in the similitude effect. Similitude implies that two crack of different sizes subject to loads giving rise to the same stress and strain fields, experience the same ΔK value and hence show the same fatigue crack growth rate. Crack closure is one of a number of crack-tip shielding mechanisms, so-called because they shield the crack tip from the full applied stress intensity range. The first identified shielding mechanism was plasticity-induced crack closure [1-34], and other shielding mechanisms have subsequently been identified, such as roughness-induced crack closure [6, 8, 9, 17, 20, 21, 35-42], oxide-induced crack closure [13, 43-

45], viscous fluid-induced crack closure [46], phase transformation-induced crack closure [46-50]. The mechanisms of crack closure are complicated, and have not been fully understood, at least in the sense of being able to make accurate predictions of closure magnitudes and effects. This lack of understanding arises principally from the difficulties associated in quantifying the phenomenon and measuring its effect on the crack driving force. There is also a terminology issue, in that a view has been emerging over the last few years that shielding occurs not only from plasticity-induced crack wake contact effects (the origin of the term closure), but from compatibility effects at the elastic-plastic interface. Hence the term 'shielding' provides a more complete description of the influences that does the word 'closure'.

The aim of this thesis is hence to study plasticity-induced crack tip shielding, i.e. to determine how crack flank and tip plasticity influence the applied elastic stress field, how to quantify this effect and calculate the actual effective stress intensity factors. The ultimate intention is to be better able to make predictions of plasticity-induced shielding, its effect on fatigue crack growth rates and consequently for the prediction on the crack growth rate and life prediction. The methodology used in this work will combine two full-field experimental techniques, photoelasticity and digital image correlation, with a novel mathematical model and analysis [51, 52].

1.2 Description of the contents

This thesis focuses on experimental work using photoelastic stress analysis and digital image correlation (DIC) techniques to assess the accuracy of a new four parameter mathematical model through investigation of its output parameters as

a function of different crack lengths and different loading conditions. Regarding these objectives, this thesis is organized into seven chapters:

Chapter 2 presents a literature survey of the most commonly used mathematical models characterising the stress fields or the displacement field ahead of the crack tip. Following this, the phenomenon of fatigue crack closure is described, and the mechanism of crack shielding induced by plastic deformation in the fatigue crack enclave is reviewed. Finally this chapter introduces the two full-field stress fields and displacement fields measurement techniques used in this work, photoelastic stress analysis and digital image correlation.

Chapter 3 reviews a number of the different methods for measuring and estimating the crack closure effect. It starts with a brief introduction of numerical/analytical evaluation models. Next, reviews on experimental techniques for measuring the fatigue crack closure effect are presented. In particular, the chapter focuses on the limitations, ambiguities, and uncertainties in the experimental techniques and on the controversies existing in the explanation of the concept of crack closure.

Chapter 4 introduces the new four-parameter mathematical model characterising the elastic stress fields surrounding a crack tip contained in a plastic enclave, and then extends it to describe the displacement fields surrounding the crack tip, hence making possible the application of the model to metallic specimens by using the digital image correlation technique. The model is employed in the current study to calculate the four parameters from the experimental data, i.e. three new definitions of stress intensity factor and T-stress. A detailed description of the specimen configuration is then given. In the third part of this chapter, the apparatus and methods adopted in the

experimental photoelastic stress analysis and digital image correlation are described.

Chapter 5 describes the complete process of analysing experimental photoelastic data for real fatigue cracks in polycarbonate compact tension (CT) specimens. Initially, the chapter presents the crack growth data obtained from representative polycarbonate CT specimens. Subsequently, an account of the work done to validate the optimum data collection region for the model in order to obtain the best quality fit and hence solution for the four stress parameters. The chapter then discusses the way to locate the coordinates of the crack tip more accurately. Finally, the results for the four stress parameters inferred from experimental photoelastic data by the mathematical model are presented for polycarbonate CT specimens.

Chapter 6, in a similar way, describes the complete process for analysing experimental data obtained using the DIC technique for real fatigue cracks in aluminium alloy CT specimens. Initially, the chapter presents an evaluation procedure for extracting displacement information from experimentally acquired raw DIC data on the aluminium CT specimens. Subsequently, it reports the crack growth data observed on representative aluminium alloy CT specimens. Next, this chapter describes the method for fitting the model to the experimental displacement data. This chapter then discusses the method of identifying the coordinates of the crack tip, and studies how to define and collect valid data to obtain the best quality fit. Finally, the results for the four stress parameters inferred from experimental DIC data are reported for aluminium CT specimens.

Chapter 7 draws the main conclusions of this thesis, and gives some recommendations for future work.

Chapter 2 Theory

2.1 Introduction

The intent in this chapter is to review some of the fundamental, concepts and theories of crack tip stress fields, fracture mechanics and fatigue that will be employed in subsequent chapters of this thesis.

The chapter starts with a brief description of some basic concepts in the theory of plane elasticity. Subsequently, the most commonly used forms of stress fields and displacement fields around a crack tip are introduced. After that, the phenomenon of fatigue crack closure will be described. In particular, the plasticity-induced crack shielding mechanism is reviewed.

At the end of this chapter, the two full-field stress and displacement measurement techniques used in this work, photoelastic stress analysis and digital image correlation, are introduced.

2.2 Mathematical description of a crack tip

2.2.1 Plane elasticity

The theory of plane elasticity gives the governing equations which are simplifications of general relationships in elasticity [53]. The equations are subject to the following restrictions:

- Two-dimensional stress state (i.e. plane stress or plane strain)
- Homogeneous, isotropic material
- Quasistatic, isothermal deformation
- Body forces are absent from the problem. (In problems where body forces are present, a solution can first be obtained in the absence of body forces, and then modified by superimposing the body forces.)

Imposing these restrictions simplifies crack problems, and permits closed-form solutions in many cases.

The equilibrium equations for rectangular Cartesian coordinates can be written as:

$$\frac{\partial \sigma_x}{\partial x} + \frac{\partial \sigma_{xy}}{\partial y} = 0$$

$$\frac{\partial \sigma_{xy}}{\partial x} + \frac{\partial \sigma_y}{\partial y} = 0 \qquad (2.1)$$

and the compatibility equation:

$$\nabla^2(\sigma_x + \sigma_y) = 0 \qquad (2.2)$$

where,

$$\nabla^2 = \frac{\partial^2}{\partial x^2} + \frac{\partial^2}{\partial y^2}$$

According to the theory of plane elasticity, for a two-dimensional continuous elastic medium, there exists a function $\Phi(x, y)$ from which the stresses can be derived:

$$\sigma_x = \frac{\partial^2 \Phi}{\partial y^2}, \qquad \sigma_y = \frac{\partial^2 \Phi}{\partial x^2}, \quad \sigma_{xy} = -\frac{\partial^2 \Phi}{\partial x \, \partial y} \tag{2.3}$$

Φ is the so-called Airy stress function which was first introduced by Airy in 1862 [54].

The stress sum, according to equation (2.3), can be written as:

$$\sigma_x + \sigma_y = \nabla^2 \Phi \tag{2.4}$$

Substituting equation (2.3) into equation (2.2), the compatibility equation can be written as:

$$\frac{\partial^4 \Phi}{\partial x^4} + 2\frac{\partial^4 \Phi}{\partial x^2 y^2} + \frac{\partial^4 \Phi}{\partial y^4} = 0 \tag{2.5}$$

or

$$\nabla^2 \nabla^2 \Phi = 0 \tag{2.6}$$

Equation (2.5) and (2.6) is called the Biharmonic equation and its solutions are called Biharmonic functions.

2.2.2 Crack tip stress fields

The stress field around a crack tip can be described by a set of linear elastic field equations [55]. The following sections discuss the most commonly used forms of stress field equations, including the Westergaard stress field equation, the Williams stress field equation, and the Muskhelishvili complex representation of the stress field. (More detailed information can be found in the book [53])

2.2.2.1 The Westergaard stress field

Westergaard [56] introduced a complex stress function $Z(z)$ to analyze stresses in crack bodies for a certain class of problems, where $z = x + iy$ and $i = \sqrt{-1}$. The relationship between Westergaard stress function and the Airy stress function is given as follows [53]:

$$\Phi = Re \iint Z + yIm \int Z \tag{2.7}$$

Where Re and Im denote the real and imaginary parts of the function respectively, and $\int$ represents integration with respect to z.

Substituting equation (2.7) into equation (2.3), gives

$$\sigma_x = ReZ - yImZ'$$

$$\sigma_y = ReZ + yImZ' \tag{2.8}$$

$$\sigma_{xy} = -yReZ'$$

When $y = 0$, the imaginary parts of σ_x and σ_y, and the shear stress σ_{xy} vanish which indicates that the crack plane is a principal plane. Therefore, the stresses are symmetric about the crack plane, i.e. $\theta = 0$ and equation (2.8) implies Mode I loading [53].

Considering a through crack in an infinite plate subject to biaxial remote tension, if the origin of the coordinate system is defined at one of the tips of the crack, the Westergaard stress function is given as follows

$$Z(z) = \frac{K_I}{\sqrt{2\pi z}}, \quad K_I = \sigma\sqrt{\pi a} \tag{2.9}$$

where σ is the remote stress and a is the half crack length, as defined in Figure 2.1 [53].

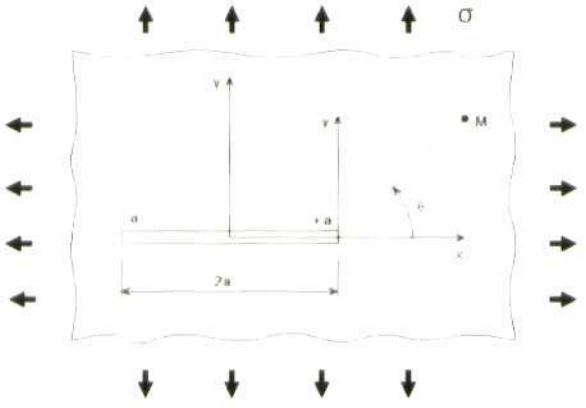

Figure 2.1 Through-thickness crack in an infinite plate loaded in biaxial tension [53].

Substituting equation (2.9) into equation (2.8), stress fields can be expressed as:

$$\sigma_x = \frac{K_I}{\sqrt{2\pi r}} cos\left(\frac{\theta}{2}\right)\left[1 - sin\left(\frac{\theta}{2}\right) sin\left(\frac{3\theta}{2}\right)\right] \tag{2.10a}$$

$$\sigma_y = \frac{K_I}{\sqrt{2\pi r}} cos\left(\frac{\theta}{2}\right)\left[1 + sin\left(\frac{\theta}{2}\right) sin\left(\frac{3\theta}{2}\right)\right] \tag{2.10b}$$

$$\sigma_{xy} = \frac{K_I}{\sqrt{2\pi r}} sin\left(\frac{\theta}{2}\right) cos\left(\frac{\theta}{2}\right) cos\left(\frac{3\theta}{2}\right) \tag{2.10c}$$

Westergaard approach could correctly describe the singular Mode I stresses in certain configurations but not sufficiently to be applied to all Mode I problems [53]. Irwin [55] found that the photoelastic fringe patterns observed by Wells and Post [57] on centre-cracked panels did not match the shear strain contours predicted by Westergaard's stress function. Moreover, Irwin showed that good agreement between theory and experiment could be achieved by subtracting a uniform horizontal (transverse) stress [53], which depends on the remote stress:

$$\sigma_x = ReZ - yImZ' - \sigma_{oxx} \tag{2.11}$$

The stress σ_y and σ_{xy}remain the same as equation (2.8). It was also revealed that a transverse compressive stress develops in a centre-cracked panel which

was loaded in uniaxial tension. Therefore, Irwin's modification to the Westergaard stress solution has a physical basis with respect to a centre-cracked panel [53]. In addition, Shi [58] provided a theoretical basis for the Irwin's modification.

2.2.2.2 Williams stress solution

Williams [59, 60] postulated the Airy stress function for analyzing stresses in a cracked body (Figure 2.2) as follows,

$$\Phi = r^{\lambda+1}\varphi(\theta^*,\lambda). \tag{2.12}$$

Substituting equation (2.12) into the biharmonic equation in plane polar coordinates, and solving it, Φ can be written as:

$$\Phi = r^{\lambda+1}\left[c_1 sin\left((\lambda+1)\theta^*\right) + c_2 cos\left((\lambda+1)\theta^*\right) + c_3 sin\left((\lambda-1)\theta^*\right) + c_4 cos\left((\lambda-1)\theta^*\right)\right] \tag{2.13}$$

where c_1, c_2, c_3, c_4 and λ are to be determined from the boundary conditions.

With applying the following expressions

$$\sigma_r = \frac{1}{r^2}\frac{\partial^2\Phi}{\partial\theta^2} + \frac{1}{r}\frac{\partial\Phi}{\partial r},$$

$$\sigma_\theta = \frac{\partial^2\Phi}{\partial r^2},$$

$$\sigma_{r\theta} = -\frac{1}{r}\frac{\partial^2\Phi}{\partial r\partial\theta} + \frac{1}{r^2}\frac{\partial\Phi}{\partial\theta},$$

the stresses in polar coordinates are given by:

$$\sigma_r = r^{\lambda-1}\left[\frac{\partial^2\varphi(\theta^*,\lambda)}{\partial\theta^{*2}} + (\lambda+1)\varphi(\theta^*,\lambda)\right] \tag{2.14 a}$$

$$\sigma_\theta = r^{\lambda-1}[\lambda(\lambda+1)\varphi(\theta^*,\lambda)] \tag{2.14 b}$$

$$\sigma_{r\theta} = r^{\lambda-1}\left[-\lambda\frac{\partial\varphi'(\theta^*,\lambda)}{\partial\theta^*}\right]. \tag{2.14 c}$$

By considering that the crack surfaces are traction free, i.e. $\sigma_\theta(0) = \sigma_\theta(2\pi) = \sigma_{r\theta}(0) = \sigma_{r\theta}(2\pi) = 0$, which leads to:

$$\varphi(0) = \varphi(2\pi) = \varphi'(0) = \varphi'(2\pi) = 0\ , \tag{2.15}$$

boundary conditions can only be satisfied when $\sin(2\pi\lambda) = 0$, thus $\lambda = \frac{n}{2}, n = 1,2,3,\ldots$. Therefore, there are an infinite number of λ values that satisfy the boundary conditions. The most general solution to a crack problem is a polynomial of the form

$$\Phi = \sum_{n=1}^{N}\left(r^{\frac{n}{2}+1}\varphi\left(\theta^*,\frac{n}{2}\right)\right), \tag{2.16}$$

where N is the order of the stress function polynomial.

Equation (2.15) also gives that

$$c_1 = -\frac{\mathrm{n}-2}{\mathrm{n}+2}c_3\ ,\ \ c_2 = -c_4$$

Thus, the stresses are given by

$$\sigma_r = \sum_{n=1}^{N} r^{\frac{n}{2}-1}\left\{c_3\left[\left(\frac{n}{2}-1\right)sin\left(\frac{n}{2}+1\right)\theta^* - \left(\frac{n}{2}-3\right)sin\left(\frac{n}{2}-1\right)\theta^*\right]\right.$$

$$\left. +c_4\left[\left(\frac{n}{2}+1\right)cos\left(\frac{n}{2}+1\right)\theta^* - \left(\frac{n}{2}-3\right)cos\left(\frac{n}{2}-1\right)\theta^*\right]\right\}\left(\frac{n}{2}\right) \tag{2.17a}$$

$$\sigma_\theta = \sum_{n=1}^{N} r^{\frac{n}{2}-1}\left\{c_3\left[sin\left(\frac{n}{2}-1\right)\theta^* - \left(\frac{n-2}{n+2}\right)sin\left(\frac{n}{2}+1\right)\theta^*\right]\right.$$

$$\left. +c_4\left[cos\left(\frac{n}{2}-1\right)\theta^* - cos\left(\frac{n}{2}+1\right)\theta^*\right]\right\}\left[\frac{n}{2}\left(\frac{n}{2}+1\right)\right] \tag{2.17b}$$

$$\sigma_{r\theta} = \sum_{n=1}^{N} r^{\frac{n}{2}-1}\left\{c_3\left[\left(\frac{n}{2}-1\right)cos\left(\frac{n}{2}-1\right)\theta^* - \left(\frac{n-2}{2}\right)cos\left(\frac{n}{2}+1\right)\theta^*\right]\right.$$

$$\left. +c_4\left[\left(1-\frac{n}{2}\right)sin\left(\frac{n}{2}-1\right)\theta^* + \left(\frac{n}{2}+1\right)sin\left(\frac{n}{2}+1\right)\theta^*\right]\right\}\left(-\frac{n}{2}\right), \qquad (2.17c)$$

and

$$\sigma_{ij} = \sum_{n=1}^{N}\left(r^{\frac{n}{2}-1}\Gamma_{ij}(\theta^*, n)\right) = \frac{\Gamma_{ij}\left(\theta^*, -\frac{1}{2}\right)}{\sqrt{r}} + \sum_{n=2}^{N}\left(r^{\frac{n}{2}-1}\Gamma_{ij}(\theta^*, n)\right). \qquad (2.18)$$

When $r \to 0$, the first term in equation (2.18) approaches infinity, while the higher order terms remain finite or approach zero. Thus, higher order terms are negligible close to the crack tip, and the stress exhibits a $1/\sqrt{r}$ singularity. Without assuming a specific configuration, it can be concluded that the inverse square-root singularity is universal for cracks in isotropic elastic body.

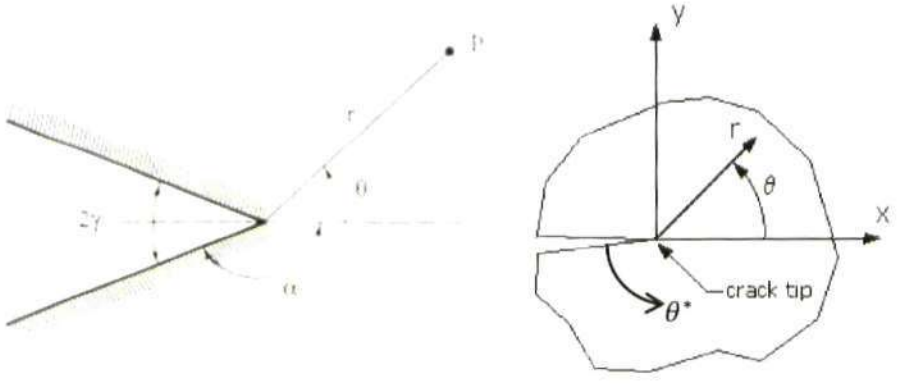

(a) (b)

Figure 2.2 (a) V-notch configuration; (b) a case of sharp crack.

Substituting $\theta^* = \theta$ into equation (2.16) and (2.17) yields

$$\Phi = r^{\frac{3}{2}}\left[s_1\left(-cos\frac{\theta}{2} - \frac{1}{3}cos\frac{3\theta}{2}\right) + t_1\left(-sin\frac{\theta}{2} - sin\frac{3\theta}{2}\right)\right] + s_2 r^2[1 - cos2\theta] + o\left(r^{\frac{5}{2}}\right)$$

$$\sigma_r = \frac{1}{4\sqrt{r}}\left\{s_1\left[-5cos\frac{\theta}{2} + cos\frac{3\theta}{2}\right] + t_1\left[-5sin\frac{\theta}{2} + 3sin\frac{3\theta}{2}\right]\right\} + 4s_2 cos^2\theta + o\left(r^{\frac{1}{2}}\right)$$

$$\sigma_\theta = \frac{1}{4\sqrt{r}}\left\{s_1\left[-3cos\frac{\theta}{2} - cos\frac{3\theta}{2}\right] + t_1\left[-3sin\frac{\theta}{2} - 3sin\frac{3\theta}{2}\right]\right\} + 4s_2 sin^2\theta + o\left(r^{\frac{1}{2}}\right)$$

$$\tau_{r\theta} = \frac{1}{4\sqrt{r}}\left\{s_1\left[-sin\frac{\theta}{2} - sin\frac{3\theta}{2}\right] + t_1\left[cos\frac{\theta}{2} + 3cos\frac{3\theta}{2}\right]\right\} - 2s_2 sin2\theta + o\left(r^{\frac{1}{2}}\right)$$

The stress function consists of symmetric components associated with cosine terms and a constant s_1 and antisymmetric components associated with sine terms and a constant t_1 with respect to $\theta = 0$ [53]. Symmetric loading and antisymmetric loading correspond to Mode I and Mode II respectively, see Figure 2.3, thus the constants s_1 and t_1 were replaced by the Mode I and Mode II stress intensity factors [53],

$$s_1 = -\frac{K_I}{\sqrt{2\pi}} \quad , \quad t_1 = \frac{K_{II}}{\sqrt{2\pi}}.$$

where K_I is the Mode I stress intensity factor; K_{II} is the Mode II stress intensity factor.

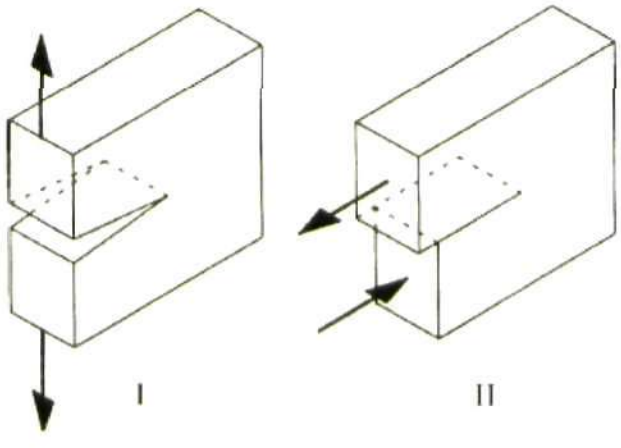

Figure 2.3 Crack loading modes: (left) I, normal; (right) II, sliding.

Thus, assuming that the high order terms are negligible, the crack tip stress field for Mode I (symmetric) loading is given by,

$$\sigma_r = \frac{K_I}{\sqrt{2\pi r}}\left[\frac{5}{4}cos\left(\frac{\theta}{2}\right) - \frac{1}{4}cos\left(\frac{3\theta}{2}\right)\right]$$

$$\sigma_\theta = \frac{K_I}{\sqrt{2\pi r}}\left[\frac{3}{4}cos\left(\frac{\theta}{2}\right) + \frac{1}{4}cos\left(\frac{3\theta}{2}\right)\right] \quad (2.19)$$

$$\sigma_{r\theta} = \frac{K_I}{\sqrt{2\pi r}}\left[\frac{1}{4}sin\left(\frac{\theta}{2}\right) + \frac{1}{4}sin\left(\frac{3\theta}{2}\right)\right].$$

Note that Westergaard's stress solution is equivalent to Williams' solution, except that the latter is expressed in terms of polar coordinates.

2.2.2.3 Muskhelishvili's complex representation of the stresses

The Airy stress function defined in the previous section is limited to bodies with smooth boundaries and represents a special case of the more general complex stress functions developed by Muskhelishvili [61]. Following Muskhelishvili's work on complex functions, stresses for the two-dimensional equations of elasticity may be defined in terms of two functions, the Airy stress function Φ (biharmonic function) and some other function Ψ. The functions Φ and Ψ are given in terms of two analytical functions $\varphi(z)$ and $\chi(z)$ of the complex variable $z = x + iy$. Therefore, the stress function takes the form:

$$\Phi = Re\{\bar{z}\varphi(z) + \chi(z)\}$$

And

$$\Psi = Im\{\bar{z}\varphi(z) + \chi(z)\} \quad (2.20)$$

Where Re and Im refer to the real and imaginary parts in complex notation respectively, and the bar over z denotes the conjugate.

Substituting equation (2.20) into equation (2.4), the stresses in terms of $\varphi(z)$ and $\chi(z)$ are given by

$$\sigma_x + \sigma_y = 2\left[\varphi'(z) + \overline{\varphi'(z)}\right] = 4Re\{\varphi'(z)\} = 4Re\{\phi(z)\} \quad (2.21)$$

where $\phi(z) = \varphi'(z)$, with the prime denoting differentiation with respect to z.

Doing further complex operations with the stress function described in equation (2.20) and using equation (2.3) to express the stress as a function of Φ, a second equation is obtained to fully describe the stress fields:

$$\sigma_y - \sigma_x + 2i\sigma_{xy} = 2[\bar{z}\varphi''(z) + \chi''(z)] = 2[\bar{z}\,\phi'(z) + \psi(z)] \tag{2.22}$$

where $\psi(z) = \chi''(z)$.

or

$$\sigma_x + i\sigma_{xy} = 2Re\{\varphi'(z)\} - z\overline{\varphi''(z)} - \overline{\chi''(z)} \tag{2.23}$$

$$\sigma_y - i\sigma_{xy} = 2Re\{\varphi'(z)\} + z\overline{\varphi''(z)} + \overline{\chi''(z)} \tag{2.24}$$

The functions $\phi(z)$ and $\psi(z)$, are known as Muskhelishvili's complex potentials.

2.2.3 Crack tip displacement fields

For plane strain conditions, the in-plane displacements are related to the Westergaard stress function as follows:

$$u_x = \frac{1}{2\mu}[(1-2v)Re\bar{Z} - yImZ]$$

$$u_y = \frac{1}{2\mu}[2(1-v)Im\bar{Z} - yReZ] \tag{2.25}$$

So, by inserting equation (2.7) into equation (2.24), displacements can be given by:

$$u_x = \frac{K_I}{2\mu}\sqrt{\frac{r}{2\pi}}cos\left(\frac{\theta}{2}\right)\left[\kappa - 1 + 2sin^2\left(\frac{\theta}{2}\right)\right]$$

$$u_y = \frac{K_I}{2\mu}\sqrt{\frac{r}{2\pi}}sin\left(\frac{\theta}{2}\right)\left[\kappa + 1 - 2cos^2\left(\frac{\theta}{2}\right)\right] \tag{2.26}$$

Where, v is Poisson's ratio:

$\kappa = 3 - 4v$ (plane strain), $\kappa = \frac{3-v}{1+v}$ (plane stress).

Note that Williams also derived relationships for radial and tangential displacements near the crack tip, but the Westergaard approach for deriving displacements is somewhat more compact.

Based on Muskhelishvili's complex potentials, the displacements are given by

$$2\mu(u_x + iu_y) = \kappa\varphi(z) - z\overline{\varphi'(z)} - \overline{\chi'(z)} \tag{2.27}$$

where $\mu = \frac{E}{2(1+v)}$.

2.2.4 Conclusions

In the first part of the present work, a new mathematical model of the crack tip stress fields built from Muskhelishvili's complex potential extension to Williams crack tip stress field will be employed to explicitly express the elastic stress field with consideration of localised plasticity existing in front of the crack tip and along the crack flanks. The phenomenon of crack tip shielding induced by plasticity will be discussed in Chapter 3 of this thesis. The new mathematical model of the crack tip stress fields will be introduced in Chapter 4 and used to study the influence of plastic deformation on the elastic field of the crack tip in combination with photoelasticity technology.

The second part of the thesis work will extend the new model of the crack tip stress fields to displacement fields, which characterise the full-field displacement in the elastic material surrounding the crack tip under the influence of local plasticity. This model, combined with digital image correlation technology, will be employed to study the plasticity-induced shielding phenomenon in metallic alloys (aluminium alloy in current experimental work).

2.3 Fundamentals of crack closure

2.3.1 Introduction

The concept of crack closure was first introduced by Elber in 1970 [62]. Based on experimental observation, Elber noted that fatigue cracks in a body could remain closed even when subjected to fully reversed tensile loads. According to Elber a fatigue crack subjected to a tension-tension cyclic load is completely open only at relatively high load levels, that is, at low load levels a fraction of the crack near the tip remains 'closed', i.e. the surfaces are in contact, throughout the lower part of the applied load cycle. Elber also argued that a zone of residual tensile deformation is left in the wake of a fatigue crack tip when it grows [63]. This phenomenon is known as plasticity-induced closure, and was the first closure mechanism to be described. It is common practice to identify either an opening point in the loading half-cycle, equivalent to an opening stress intensity factor, K_{op}, or a closing point in the unloading half-cycle, K_{cl}, and hence to calculate an effective range of stress intensity factor $\Delta K_{eff} = K_{max} - K_{op}$ or K_{cl}.

The phenomenon of fatigue crack closure means that surfaces of the fatigue crack can transmit load and therefore act as though the crack is 'closed', essentially shielding the crack tip from the full range of applied load even under fully reversed cyclic loading conditions [63]. Closure can appear not only at the crack tip but also along the wake of the fatigue crack. Crack closure can hence either occur via an 'unzipping' model or by discrete contact at particular points along the crack wake. Plasticity-induced closure is generally accepted as more likely to occur by an unzipping mechanism. Closure leads to premature contact

between crack flanks, and causes a reduction in the apparent crack driving force for fatigue crack advance.

Since the first closure mechanism was found, a significant research effort has been devoted to the study of plasticity-induced crack closure. However, details of the mechanisms of crack closure have remained controversial since the publication of Elber's work. In the 1970s and early 1980s it became evident that Elber's arguments represent only one possible mechanism associated with fatigue crack closure. Crack closure investigations also revealed that the fatigue crack growth rate was not only affected by the instantaneous value of imposed ΔK, but also the prior loading history, crack size and state of stresses. Therefore, crack closure may be promoted by a number of different mechanisms. Later, additional mechanisms of closure were identified, arising from microscopic roughness of the fatigue surfaces, stress- or strain-induced phase transformations at the crack tip, oxide layers or debris formed within a fatigue crack, or hydrodynamic effects associated with the presence of viscous fluids within a crack [63]. The identification of other mechanisms of closure has brought some new insight to this problem. Crack closure has been the topic of an increasing number of studies, and has been employed in explanations of a number of fatigue phenomena [64]. The most important crack closure mechanisms are illustrated schematically in Figure 2.4.

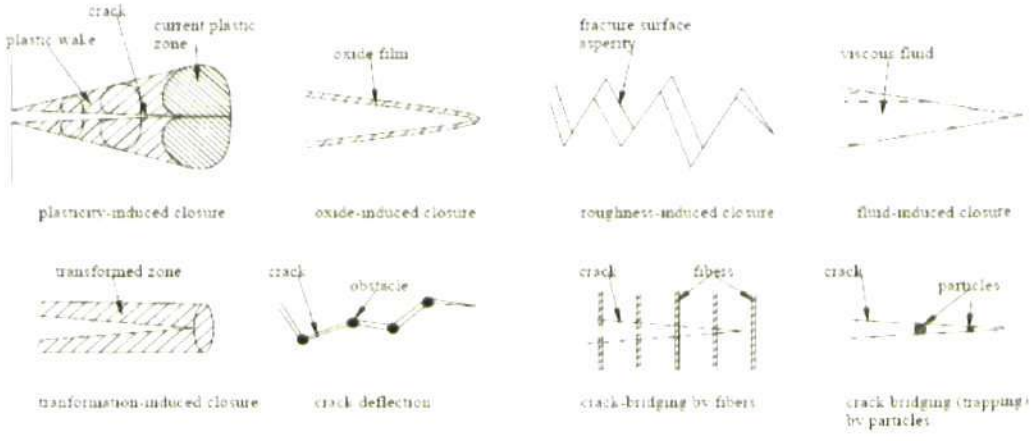

Figure 2.4 Crack closure mechanisms (reproduced from [63]).

The existence of fatigue crack closure complicates fatigue life prediction and because its causative mechanisms and the resulting magnitudes of closure are not fully understood [65], conservative assumptions are usually made in component and structural design, i.e. assuming that the growth rates will always be closure-free, equivalent to high values of stress ratio R.

Crack closure usually occurs under cyclic loading conditions, especially at low stress ratios when the crack-tip opening displacements are relatively small. Under such conditions, premature contact of the fracture surfaces may occur, closing the crack before the minimum stress intensity factor is reached [65]. Thereby, the fatigue crack growth is no longer determined by the nominal value of the stress intensity factor range. Instead, the crack growth rate (CGR) is determined by an effective stress intensity factor range ΔK_{eff} that accounts for the details of fracture surface contact in the wake of the advancing fatigue crack tip [63].

The effective stress intensity factor range is defined as:

$$\Delta K_{eff} = K_{max} - K_{op} \tag{2.28}$$

Where, K_{op} corresponds to the opening load P_{op}, as shown in Figure 2.5. In the crack closure model by Budiansky and Hutchinson [66], the crack opening load was found to be different from the crack closure load P_{cl}. The difference is, however, small. In general these two values are assumed to be equal, as CGR calculations are relatively insensitive to their difference.

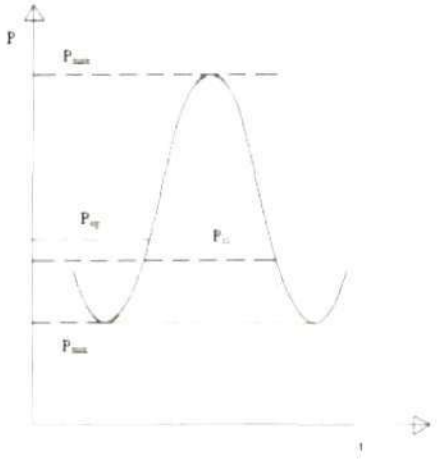

Figure 2.5 Crack opening and closure loads (reproduced from [63]).

2.3.2 Plasticity-induced crack closure

An ideal, perfectly sharp crack will close only under zero or compressive loads. In the real material, this no longer applies. The propagation of a fatigue crack gives rise to a wake of material that has been previously deformed plastically and to compatibility constraints at the elastic-plastic boundary. In Elber's work the development of a steady increasing plastic wake under constant amplitude cyclic tensile loads, arises from the increase in K_{max} and ΔK as the crack increases in length, as is shown in Figure 2.6.

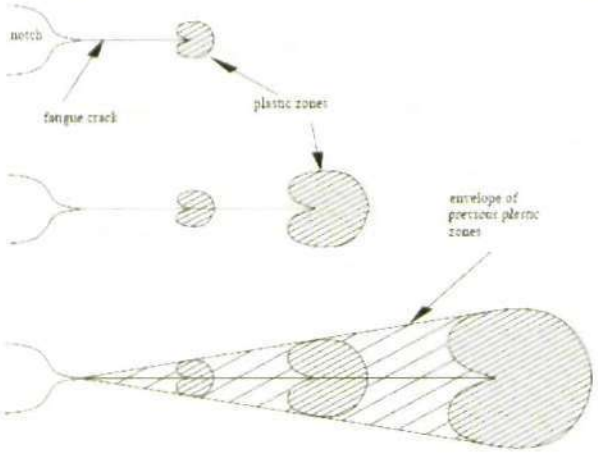

Figure 2.6 Development of a plastic wake (reproduced from [63]).

The fatigue crack advances through the existing plastic zone creating the second plastic zone but leaving the first plastic zone behind the crack tip. This process repeats as the fatigue crack grows. With the increase in ΔK and in the size of the plastic zone due to the crack advance, the permanently deformed material behind the crack tip forms an envelope of plastic zones in the wake of the crack front, as shown in Figure 2.6. The effect of the plastic zones/residual stretch between the crack flanks leads to closure of the crack, known as plasticity-induced crack closure, whilst compatibility and Poisson's ratio effects lead to other plasticity-induced shielding stresses which act on the applied elastic field, essentially acting as 'back stresses' which retard crack growth. The work described in this thesis is the only endeavour known to the author to take account of the effects of these latter stresses.

This phenomenon can be visualized by plotting of the applied far-field tensile stress σ against crack opening displacement δ during a fatigue cycle, as shown in Figure 2.7. This diagram shows the compliance of a specimen which is well known to be affected by plastic zones at notches or crack tips.

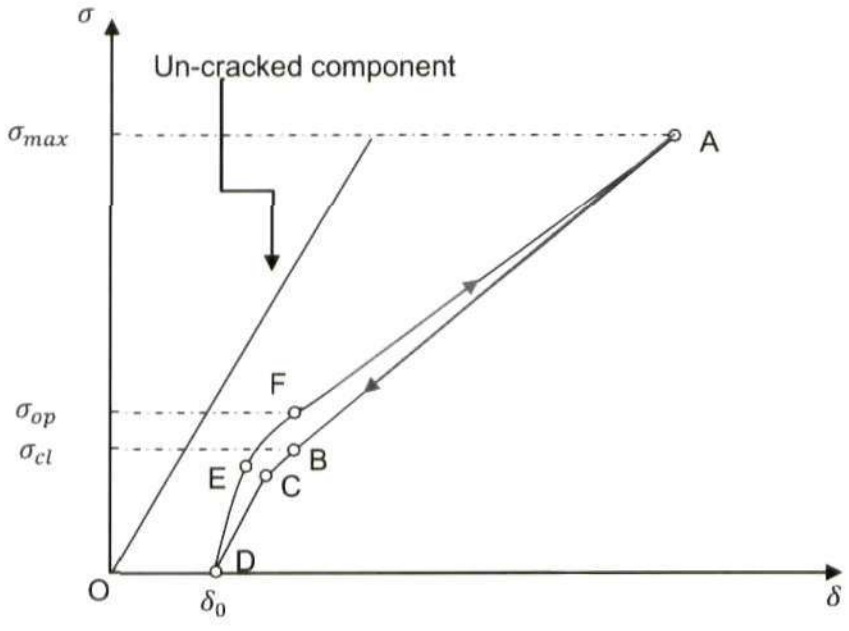

Figure 2.7 Schematic illustration of the relationship between externally applied stress vs. displacement given by strain gauges when crack closure exists in a fatigue crack.

Figure 2.7 indicates the following: In the unloading phase ($A \rightarrow B \rightarrow C \rightarrow D$)

(1) Between points A and B the crack remains open.

In this section, a linear behaviour is observed. The compliance curve exhibits a constant slope similar to the measured stiffness of an identical sheet with an ideal slot of the same length as the fatigue crack.

(2) Between points B and C the crack is in a state of partial closure.

In this phase, the stiffness increases, and the second derivative of the compliance curve $\mathrm{d}^2\sigma/\mathrm{d}\delta^2$ becomes negative and the only mechanisms that can induce this change are either contact of the crack faces or residual stress effects which act only during part of the load cycle. It is typically assumed that during unloading the first

contact between the crack flanks takes place at point B. Below point B the crack gradually closes and at point C it is completely closed.

(3) Between the points C and D the crack remains closed.

A linear behaviour is shown again in this stage. The slope of the line is equal to the stiffness of an identical plate without the fatigue crack.

Similarly, in the loading phase from $D \rightarrow E \rightarrow F \rightarrow A$, whilst applying a tensile load to a cracked specimen, the crack remains closed until the point E is reached. At this point the crack begins to 'peel' open gradually, and at the point F it is completely open. It can be seen from Figure 2.7 that the relation between σ and δ in the loading phase of the cycle is slightly different from that in the unloading phase. It indicates a difference between σ_{op} and σ_{cl}, as that between P_{op} and P_{cl}, indicated in Figure 2.5. In practice, the difference between σ_{op} and σ_{cl} is generally approximately $< 10\%$, and so generally these two values are taken to be equal.

2.4 Experimental techniques for crack stress analysis

There are several full-field experimental techniques which can be employed to measure stress or displacement fields and strain maps in a component. Among them, photoelastic stress analysis and thermoelastic stress analysis provide stress fields; moiré interferometry, electronic speckle pattern interferometry and digital image correlation provide displacement fields and strain contours. Theoretically, if the stress or displacement field around a crack tip is known, the characterising parameters, i.e. stress intensity factors can be derived directly from them. Each of these techniques has its own advantages and disadvantages [67, 68].

In this thesis, the phenomenon of crack closure and its shielding effect on the elastic stress field around the tip of fatigue cracks have been studied using photoelasticity and digital image correlation (DIC). They will be introduced and reviewed in more detail in the following two sections.

2.4.1 Photoelastic Stress Analysis

2.4.1.1 Introduction

Photoelasticity is one of the oldest methods for measuring and visualizing stresses and strains in structures. As the name implies, photoelasticity was developed to apply optical principles to solve engineering problems of elasticity. The method relies on the birefringence property exhibited by some transparent materials. Specially, the phenomenon of stress-induced birefringence is utilised to view the stress contour/interference fringes where the material becomes optically anisotropic/birefringent under the influence of external loading or residual birefringence.

The formation of photoelastic fringes was first observed by David Brewster in the early nineteenth century in glass and the relationship between fringes and stresses was deduced in the 1850s [69]. Although photoelasticity of glass has generated great interest, glass was far from an ideal material for practical applications [70]. The work by Coker and Filon [71] made great progress in this regard. Since then, more versatile materials have been utilised as a model. With this background, two-dimensional photoelasticity found widespread application in many industrial applications. Photoelasticity can also be applied in three dimensions. The potential of 3-D stress analysis was developed by Oppel [72] and Hetenyi [73] and to this day it remains as one of the very few

experimental methods for 3-D stress analysis. The theory and procedure are complex and time consuming in comparison with the two-dimensional method.

The instrument employed in 2-D photoelastic stress analysis is called a polariscope (or photoelastic interferometer). Two dimensional photoelasticity comes in two forms: transmission photoelasticity where the polarised light is transmitted through a translucent model and reflection photoelasticity where the polarised light is directed onto the photoelastic coating and viewed through an analyser after reflection off the metal surface.

The polariscope used in this work applies circular transmission polarization. The polariscope contains a light source, a polarizing filter known as the 'Polariser', and a second polarizing filter known as the 'Analyser' and two quarter-wave plates that are inserted between polariser and analyser, as shown in Figure 2.8. Quarter-wave plates are used to convert linearly polarised light to circularly polarised light through a retarding process [74], in which linearly polarised light incident from the polariser will be divided into two electric field components with equal amplitude but different indices of refraction when passing at 45° to the optic axis through the first quarter-wave plate, and one of the two components with a higher index of refraction will be retarded by 90° in phase by it.

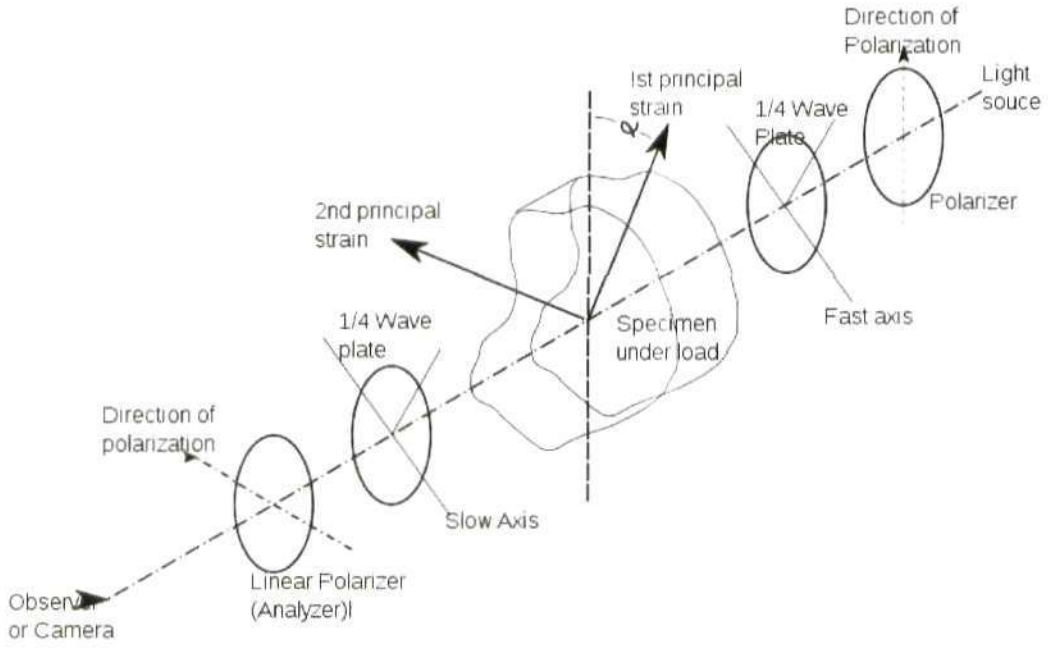

Figure 2.8 The illustration of a typical circular transmission polariscope (reproduced from [75]).

2.4.1.2 Stress-Optic Law

When polarised light passes through a stressed transparent material where they *become refractive or "birefringent", the light separates into two wave fronts* travelling at different velocities, each orientated parallel to a direction of principal stress σ_1 , σ_2 in the material, but perpendicular to each other (Figure 2.9).

Birefringence results in the stressed material having two different indices of refraction. In deformed glass and plastics, the index of refraction determined by the magnitude of the principal stresses and the orientation of a given light amplitude vector with respect to the principal stress axes [76, 77]. This gives rise to the Stress-Optic Law (Brewster Law).

$$n_1 - n_2 = C_f(\sigma_1 - \sigma_2) \tag{2.29}$$

where n_1, n_2 are indices of refraction; C_f is the stress-optical coefficient for photoelastic material; σ_1, σ_2 are the principal stresses.

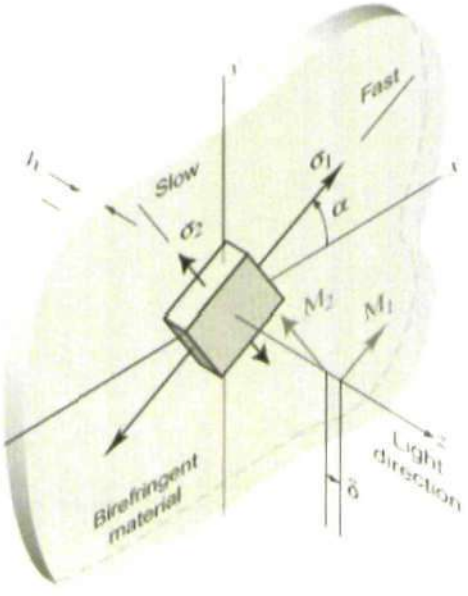

Figure 2.9 Birefringent effect (reproduced from [76]).

The phase difference between the two light vectors travelling through the material at different velocities (fast, slow) is known as retardation, commonly represented by δ. The retardation value divided by the material's thickness h is proportional to the difference between the two indices of refraction.

$$\frac{\delta}{h} = n_1 - n_2 \tag{2.30}$$

The components of the two light waves interfere with each other resulting in a characteristic colour spectrum when the light source is white light, or black/white spectrum under monochromatic light. Each integer multiple of the wavelength of light gives rise to a fringe N.

There are two different types of fringes can be observed in photoelasticity: isochromatic and isoclinic fringes, as shown in Figure 2.10. Isochromatic fringes are lines of constant principal stress difference $(\sigma_1 - \sigma_2)$. The difference

in principal stresses is related to the birefringence and hence the fringe order N through the Stress-Optic Law (Equation 2.29). For any two-dimensional photoelastic fringe pattern, the relationship between the difference of the principal stresses and fringe order N can be expressed in the form [78]:

$$\sigma_1 - \sigma_2 = \frac{Nf}{h} \tag{2.31}$$

where, f is the material fringe constant.

Isoclinic fringes occur whenever either direction of the principal stress in the *model coincides with the polarisation axis of the polariser.* Isoclinic fringes therefore provide information about the directions of the principal stresses in the model. When combined with the difference of the principal stress $(\sigma_1 - \sigma_2)$ from the photoelastic isochromatic fringe pattern, isoclinic fringes provide the necessary information for the complete solution of a two-dimensional stress problem [79].

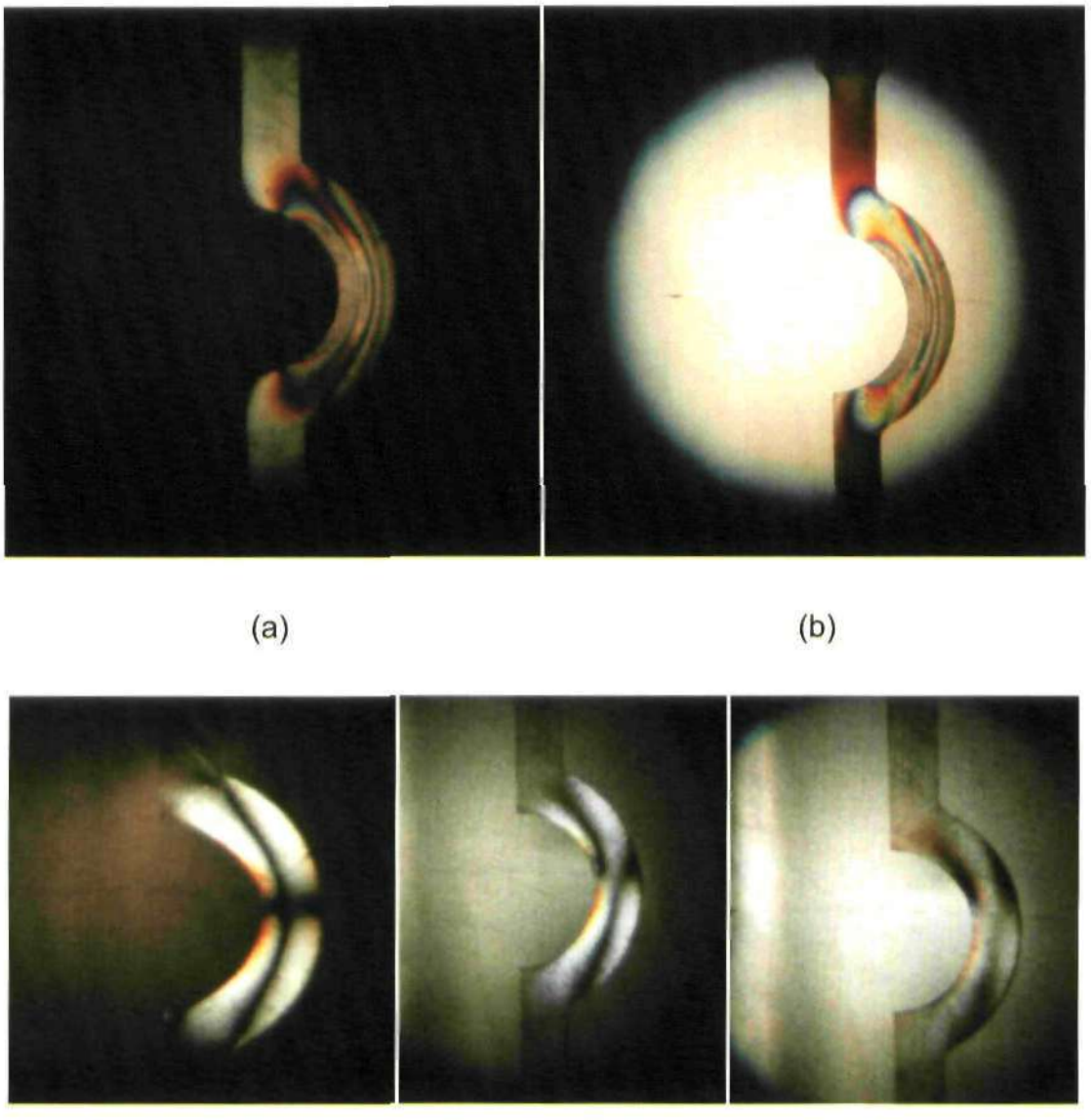

(a) (b)

(c) (d) (e)

Figure 2.10 Photoelastic response of a curved bar: (a) Dark field isochromatic fringes; (b) Light field isochromatic fringes; (c) Zero degree isoclinic; (d) 20 degree isoclinic; (e) 45 degree isoclinic. (After [80])

2.4.1.3 Photoelasticity stress analysis

Photoelasticity enables experimental stress analysis by extracting information from the fringe patterns that reveals the stress distribution over the extent of the model. There are two groups of interference fringe patterns: one set are the isochromatic fringes which indicate lines of constant principal stress difference (maximum shear stress). The other family are isoclinic fringes which are

employed to determine the orientation of the principal stress axes for a specimen.

Photoelastic studies of cracks have often concentrated on the determination of stress intensity factors (SIFs) for a specific geometry from the characteristic features of the fringe loop in the neighbourhood of the crack tip [81].

Irwin [55] was the first to suggest the use of photoelastic data to extract stress intensity factors through the discussion of a pioneering work by Wells and Post [57]. Subsequently, a number of algorithms were proposed for determining stress intensity factors from photoelastic data. In the earlier studies, algorithms for extracting stress intensity factors or stress fields from photoelastic fringe patterns mainly employed data from only one or two points [55, 82] or along the selected line $\theta = \frac{\pi}{2}$ [83] in the fringe map and did not fully utilise all the information available, as illustrated in Figure 2.11.

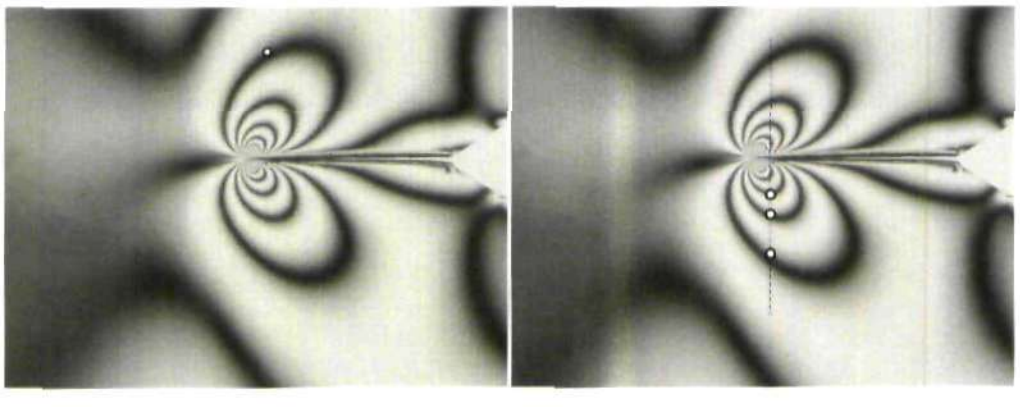

(a) (b)

Figure 2.11 Illustration showing the location of the collected data points for (a) single point measurement, (b) a few points along the selected line.

Irwin [55] proposed a classical approach to evaluating stress intensity factors. He suggested the measurement of the distance between the crack tip and the farthest point on a given fringe loop near to the crack tip in the isochromatic

fringe pattern, as well as the corresponding angle of inclination, for the determination of the two stress intensity factors. Bradley and Kobayashi [82] proposed a differencing procedure and made measurements on crack tip isochromatic patterns in an attempt to improve the evaluation of stress intensity factors and minimise the inconsistency in the results and measurement inaccuracies. Theocaris and Gdoutos [84] introduced a new evaluation process based on the comparison between the near and far stress field and then proposed a method [85] for evaluating stress intensity factors without using data from the region near to the crack tip. Smith et al suggested a collocation technique based on a Taylor series correction method to evaluate the stress intensity factors [86-88]. However, these point-measurement methods were found to be highly sensitive to inaccuracies when measuring the fringe order and the coordinates of the points employed.

In 1979, a new data collection methodology, the multi-point over-deterministic method (MPODM) [89], was developed and has greatly promoted the utility of photoelastic studies of cracks. It should be noted that in 1973 Berghaus [90] had already used the least-squares method for obtaining an over-determined photoelastic solution to stress distribution problems, by constructing a group of weighted equations to incorporate the various relations (the photoelastic effect, boundary conditions, and static-equilibrium conditions). The MPODM method involves fitting the theoretical stress field to a large number of points selected arbitrarily from the photoelastic fringe pattern. The resulting over-determined set of equations are solved through a surface fitting process employing Newton-Raphson iteration and least squares minimisation in order to calculate both the Mode I and Mode II SIF (i.e. K_I and K_{II}). This algorithm seems to give reliable stress intensity factors estimates with rapid convergence if good initial estimates

are made [91]. This method may be modified to account for possible inaccuracy in crack tip position. A solution was given to solve this problem by Sanford [81] by allowing the crack tip as an unknown in the solution. Since then, the MPODM has been the preferred method for the determination of stress intensity factors associated with the full-field photoelastic fringe patterns.

Recently, to account for non-uniform stress fields in real structures, Nurse and Patterson [92] employed Muskhelishvili's approach to describe the stress fields around the crack tip rather than the Westergaard equations used previously in Sanford's MPODM method. In their work, the two analytical functions in the Muskhelishvili's approach were given in a complex Fourier series form. The solution method used Newton-Raphson iteration as well as a least squares minimisation to solve the parameters. More recently, Pacey, et al [93] used Muskhelishvili's approach to model the stress fields around a fatigue crack tip and fitted this to full-field photoelastic data using a combination of genetic algorithms and the downhill simplex method.

2.4.2 Digital image correlation (DIC)

2.4.2.1 Introduction

Several methods can provide full-field information about displacement, such as moiré interferometry, electronic speckle pattern interferometry, and digital image correlation. Within this group, moiré interferometry and electronic speckle pattern interferometry can determine, based on the interferometry technique, the displacements of a surface with high resolution. However, there are strict requirements for system stability and very specific requisites when applying these techniques: moiré interferometry needs a grating to be bonded to the object with a flat surface; and electronic speckle pattern interferometry requires

being isolated from vibration and apparatus employed is expensive [94]. Digital image correlation, however, does not have such strict requirements. In this technique, preparation of the specimen is relatively simple as the speckle patterns are made by spray painting on the surface of the object, and the image correlation equipment itself is less expensive.

2.4.2.2 Principles

Digital image correlation is a non-contact optical method that employs tracking and image registration techniques for accurate 2D or 3D measurements of full-field displacement and strain during deformation of structures from digital images.

The image correlation equipment consists of a CCD camera in 2-D image correlation or two CCD cameras in 3-D image correlation, a computer, and an illumination system (naturally white light or artificial illumination). A typical set up for 2-D image correlation technique is shown in Figure 2.12.

After obtaining full-field information by recording deformation and motion of speckle patterns on a specimen surface before and after deformation of the body, the computer compares and matches the sequential images acquired at different states. During the matching process, the first image recorded before deformation is normally taken as a reference image, and the other images are compared with this reference. The matching is based on the mathematical correlation of the change in intensity characteristics of the sequentially recorded digital images. The correlation is based on the observation that if the intensities of one image correlate with those of a subsequent image of the same object, it is likely that both images are from the same region.

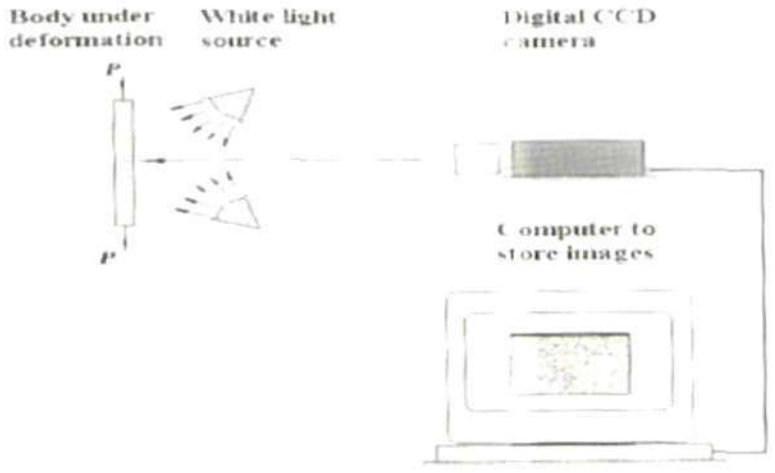

Figure 2.12 Typical schematic of experimental configuration for 2-D image correlation analysis (reproduced from [95]).

Theoretically, the intensity of light of each pixel in the reference image can be traced and the displacement vector can be determined. Practically, however, it is not possible to trace every single pixel in the images. It is shown that at least 3×3 pixels area is required for one recognizable feature [96]. Thereby, in order to extract the full-field displacement vector map, digital images are divided into smaller sub-images (also called facets, subsets or interrogation windows) and the correlation is performed for each of these sub-images. For each sub-image, the centre of it will represent the characteristic for the entire sub-image region, and one single data point of the result. After the digital images recorded after deformation are correlated with the reference one, the resulting map that contains the information on displacements of each sub-images for the entire image will be obtained.

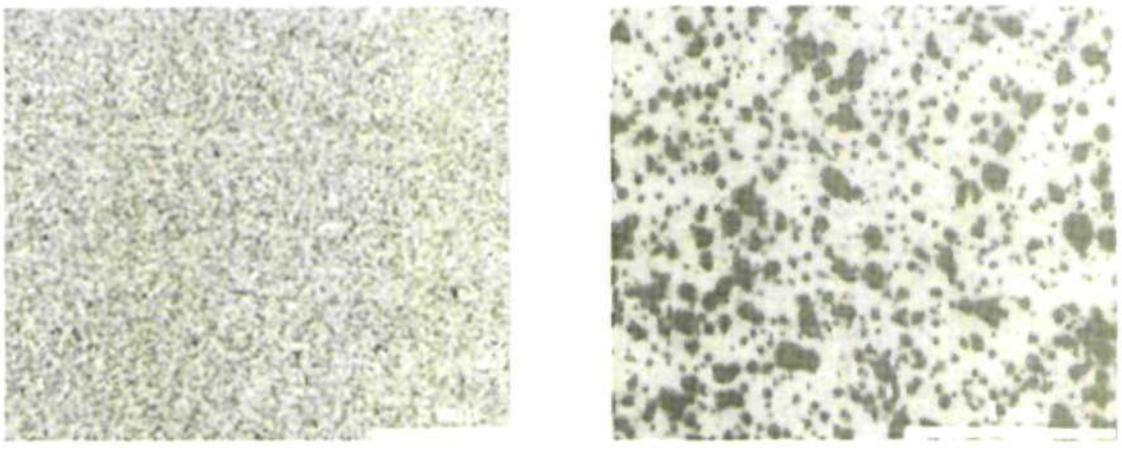

(a) Fine speckle pattern (b) Coarse speckle pattern

Figure 2.13 Typical speckle patterns on specimen surface with paint spraying: (a) fine speckle pattern, (b) coarse speckle pattern. (reproduced from [95])

Image correlation is efficient on objects with textured surface. To achieve a characteristic contrast pattern on a specimen surface which can then form a unique sub-image, such techniques as spraying, painting, randomly scratching and carving the specimen surface can be employed if the surface is featureless. No matter which technique used in creating speckles, speckles must, of course, fit the scale of observation. Thus, for the nano-scale, a smaller speckle pattern must be used than for the macro-scale. In practice, useful techniques include for small speckles, spraying with white paint and sprinkling with carbon particles; for moderate speckles, spraying with white paint and over spraying with the black paint [97, 98], or making a random network of scratches with silicon carbide paper of an appropriate grade; for large speckles, spraying with white paint and brushing with black paint. For very high resolution, fluorescent paint is used [95]. In some cases, at high magnification levels, the microstructure of the material provides a natural characteristic surface pattern and thus no artificial speckle pattern is required [96, 99] .

The size of the subsets should be small enough to provide the required spatial displacement resolution, but also must be large enough to contain a characteristic part of the pattern with sufficient contrast features to be uniquely recognizable within the whole image, otherwise poor correlation results could be obtained and sometimes no correlation will be possible. The minimum facet size is limited by the roughness of the speckle pattern on the object surface. Increasing the facet size causes smoothing of the result, but decreases the number of sub-images and hence the total number of data points in the result because of lower spatial resolution. Thus, an appropriate size of sub-image should be selected to reach a compromise between these conflicting requirements, which depends on the problem being tackled.

There are several algorithms to perform the subset comparison, one example is shown in Figure 2.14. In order to speed up the process, in some algorithms the images are first transformed into frequency domain using fast Fourier transform (FFT) [100]. Various improvements in correlation algorithms in the last decade have led to image correlation techniques maturing into a fast, stable and reliable full-field displacement and strain measurement tool.

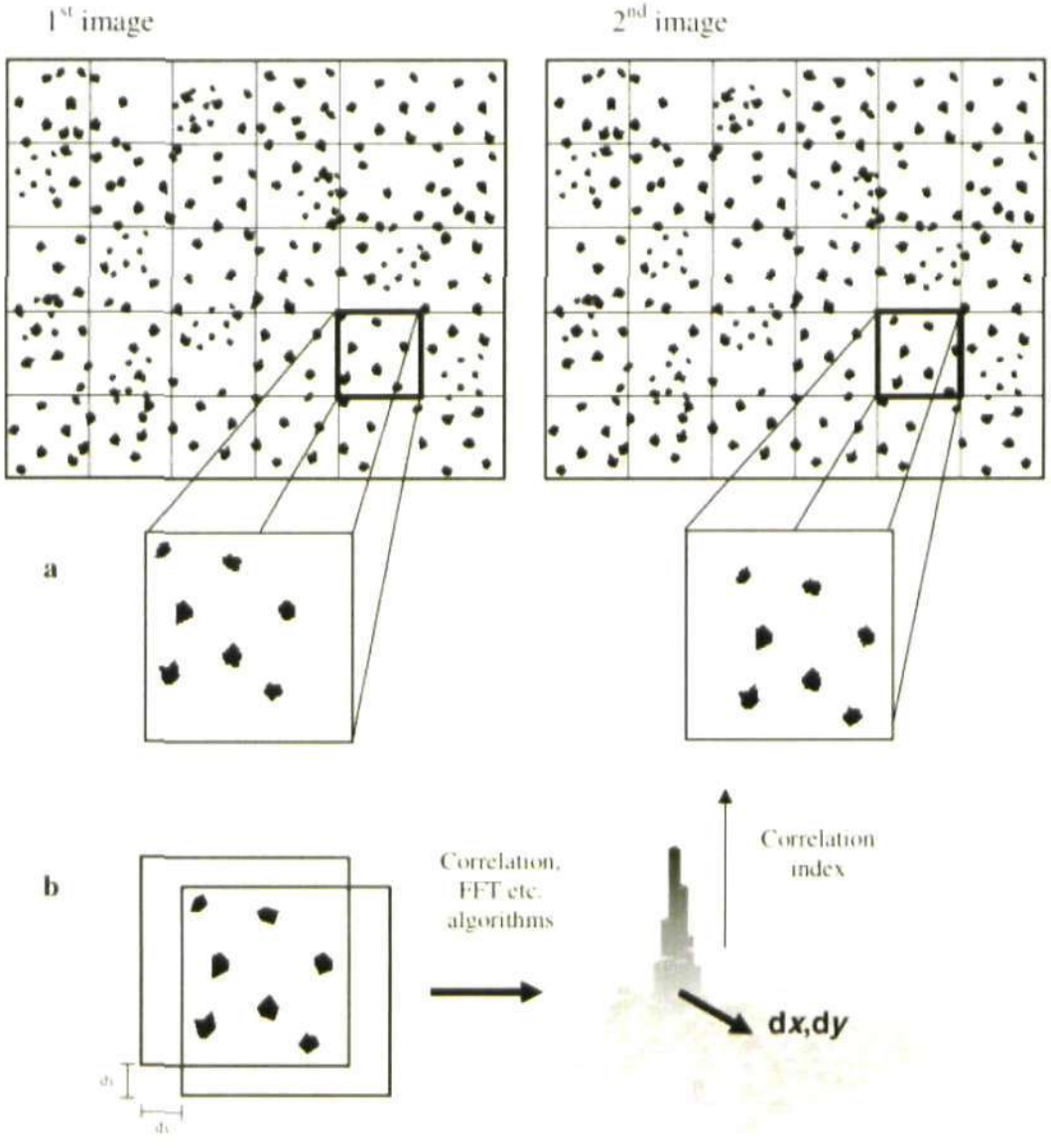

Figure 2.14 (a) Image correlation is a displacement mapping technique. To create a displacement map, the two images obtained at different strains are divided into smaller sub regions. (b) Pairs of sub regions are then compared computationally, using correlation or FFT algorithms. The displacement vector joins the centre of the sub region and the point of highest correlation. This operation is repeated for all sub region pairs to create a displacement map. (reproduced from [96])

In the current work, a Dantec system is employed, for more information please refer to [101]. The correlation algorithm of Dantec's DIC system [101, 102] is based on a pseudo-affine coordinate transformation from one image to another. Assume that a point $P(x,y)$ in the reference image is mapped into point $P^*(x^*,y^*)$ in another image of the same object after it subjected to some deformation with/without rigid body movement, the relation between $P(x,y)$ and $P^*(x^*,y^*)$ can be written as:

$$u(x,y) = x^* - x$$

$$v(x,y) = y^* - y \tag{2.30}$$

Where, $u(x,y), v(x,y)$ represent the horizontal and vertical displacement respectively.

In the correlation algorithm, a quality parameter, Residuum R is defined by:

$$R = \min_{a_0,\dots a_7, g_0, g_1} \sum_{x,y} \|G_T(x,y) - G(x,y)\| \tag{2.31}$$

Where,

$$G_T(x,y) = g_0 + g_1 G^*(x^*,y^*)$$

$$x^* = a_0 + a_1 x + a_2 y + a_3 xy$$

$$y^* = a_4 + a_5 x + a_6 y + a_7 xy$$

G^* grey value of light intensities of the deformed image

G grey value for the reference image, as shown in Figure 2.15

g_0 , g_1 illumination parameter

a_0, …, a_7 affine transformation coefficient, see Figure 2.16.

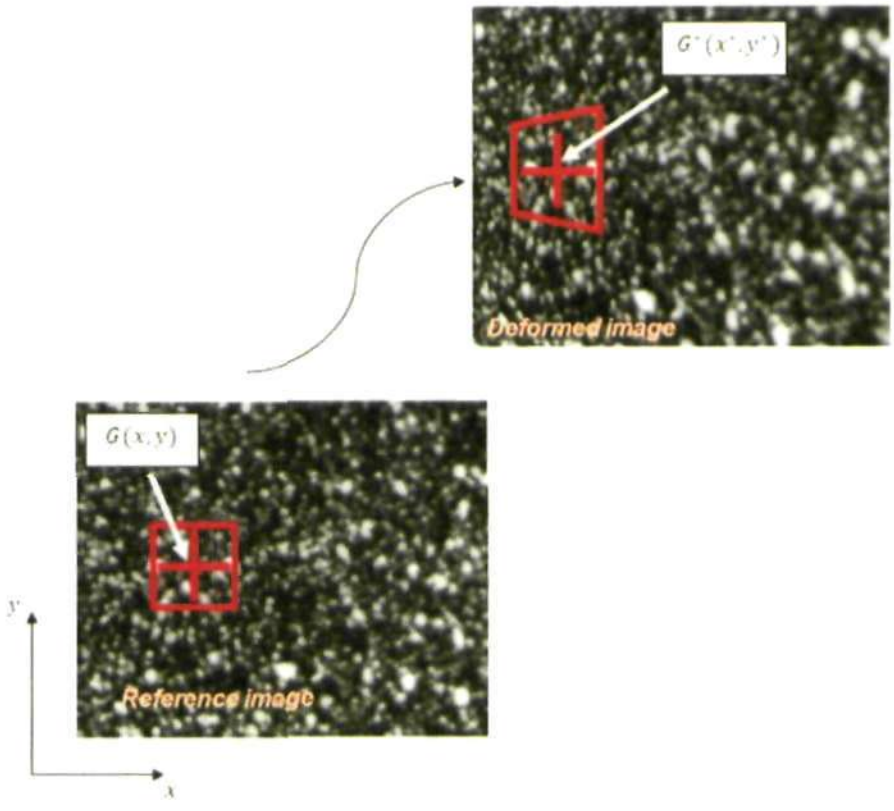

Figure 2.15 Mapping concept of Digital Image Correlation

The possible transformations consist of a combination of translation, stretch, shear and distortion.

Affine transformation:

Translation a_0, a_4

Stretching a_1, a_6

Shear a_2, a_5

Distortion a_3, a_7

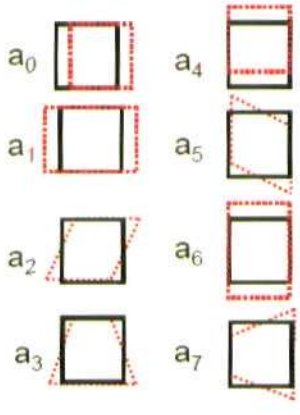

Figure 2.16 Affine transformation coefficients.

2.4.2.3 Review

One of the earliest papers to determine fracture parameters from displacement data is the work by Evans and Luxmoore [103] in 1974. Their work described how the displacement relative to crack was extracted from laser speckle patterns on single edge-crack tensile specimens made of Araldite CT 200. By plotting the displacement relative to crack against the root of radial distance from the crack tip, the Mode I stress intensity factor was determined. A subsequent development was to extend the methodology to image correlation techniques [97, 104-109]. The earliest work on applying image correlation techniques to determine the stress intensity factor from displacement fields was conducted by McNeill et al [105]. This procedure was applied to C-shaped and three-point bend Plexiglass specimens subjected to Mode I loading conditions, and displacement fields were obtained by digital image correlation. Then an error function was defined, and the stress intensity factor was determined by finding the minimum of the error function using the least squares method. It should be noted that in their study, the stress intensity factor was also taken as an unknown in the error function. However, relatively scattered results were obtained in calculating the pure mode I stress intensity factor. This might have occurred because only vertical displacement was used in evaluating the stress intensity factor, while horizontal displacement was ignored. Errors might also have been caused by employing less accurate image correlation algorithms in the early development of this technique. This can be observed in Figure 2.17 by comparing the vertical displacement field found using digital image correlation (a) and the theoretical solution (b) where a noticeable difference is observed particularly in the cracked area.

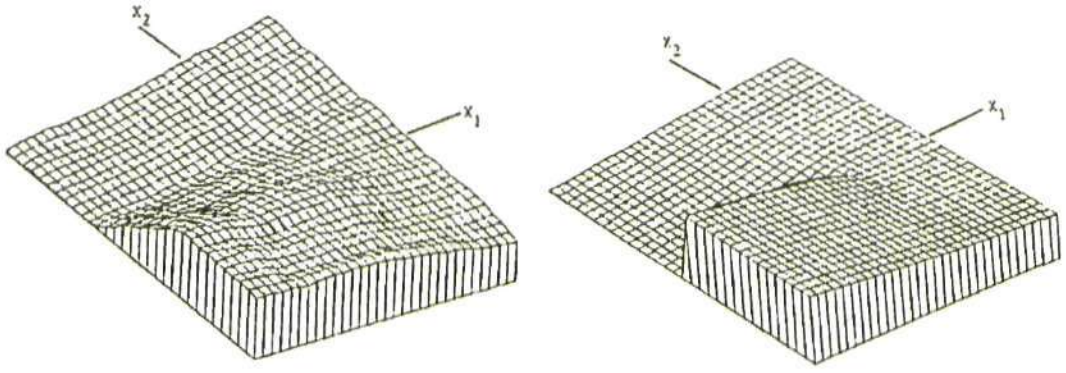

(a) (b)

Figure 2.17 (a) Experimental vertical displacement; (b) Theoretical vertical displacement. (reproduced from [105])

In particular, Sutton et al [97, 106] suggested a new technique based on Newton-Raphson methods to determine displacement fields by digital image correlation. This method reduced the calculation expense, and has been applied by many researchers since then to solve various fracture problems. Mixed-mode cracks were studied using image correlation by Durig et al [108]. This work also employed Williams solution, and took the stress intensity factor as an unknown in the error function, as in the work conducted by McNeill et al [105]. The results were compared with those obtained from photoelasticity, and satisfactory results were only found in the opening mode component stress intensity factor. Note that this study also did not use horizontal displacement for extracting Mode I stress intensity factor. In the previous study, the crack tip position was determined when the minimum of the error function was found by shifting an estimated crack tip location by some pixels. In Yoneyama et al. [110, 111], not only mixed-mode stress intensity factors and displacement components, but also crack tip location were taken as unknowns in the displacement field equation, and these parameters were determined simultaneously using nonlinear least squares based on the Newton–Raphson

method. Recently, Lopez-Crespo [94] applied digital image correlation to determine displacement fields and stress intensity factors based on the Muskhelishvili's complex function and not Williams's solution as used in the previous studies. They also employed the Sobel edge-finding routine to locate the crack tip. This methodology will be employed in this thesis and will be discussed in more detail later on.

In recent years, image correlation has grown into a fast, stable, and reliable 2-D and 3-D full-field displacement and strain measurement tool and has been applied to a wide variety of problems, such as extraction of stress intensity factors for mixed-mode crack problems [108, 112], measurement of crack tip opening displacement [113-116], strain measurement [117-121], crack growth studies [122], damage and fracture detection [123-127] in various materials and structures, real-time monitoring of cracks and force in structures [128], the crack closure effect from image correlation data [94, 129, 130], and measurement of velocity in flows [131].

Chapter 3 Literature review

3.1 Introduction

The phenomenon of premature crack closure during unloading, since its first observation by Elber in 1970 [62], has been one of the most intensively studied topics because of its potential influences on fatigue crack initiation, fatigue crack growth, crack growth retardation mechanisms, load interactions, environmental effects and other fatigue and fracture problems. However, crack closure and shielding effects remain poorly understood, and a wide spectrum of uncertain, controversial, anomalous, and contradictory results have been presented in the literature. This chapter reviews a number of different methods for measuring and estimating the crack closure effect. It starts with a brief introduction of numerical/analytical evaluation models. Next, it presents a review of experimental techniques for measuring the fatigue crack closure effect, which particularly focuses on the limitations, ambiguities, and uncertainties in the experimental techniques and the existing controversies in understanding of the concept of crack closure.

3.2 Analytical evaluation of crack closure

Since Elber first proposed the concept of plasticity-induced fatigue crack closure, many mathematical and analytical approaches based on different mechanical concepts have been developed to investigate the plasticity-induced crack closure problem over the last forty years. The most commonly used approaches are those based on the Dugdale strip-yield model [132], which assumes that plastic yielding would occur in a narrow strip lying along the extension of the crack line, that the material behaviour is elastic-perfectly plastic and that a state of plane stress exists. In 1978, Budiansky and Hutchinson [66] developed a theoretical approach by using Muskhelishvili's complex potential approach on a Dugdale strip-yield model. In this way, they derived crack opening loads and the size of residual stretches in the plastic wake as a function of externally applied load. According to their work, the residual stretch left behind the advancing fatigue crack is as high as 86% of the crack tip opening displacement at K_{max}. This work rationalised the effect of load ratio R on the fatigue crack closure process and also offered a theoretical justification for the use of ΔK_{eff} to characterise fatigue crack growth behaviour. The limitations of this approach are that only one mechanism of fatigue crack closure, i.e. plasticity-induced crack closure is taken into account, and it pertains to plane stress deformation only without any mechanisms of fatigue crack growth being invoked [63]. Apart from this comprehensive analytical approach by Budiansky and Hutchinson, there are many other approaches based on the strip-yield model suggested by other researchers, like Dill and Staff [133], Fuhring and Seeger [134], Codrington and Kotousov [135]. Dill and Saff [133] suggested a simple contact stress closure model in 1976. Codrington and Kotousov [135] developed a theoretical model based on the strip-yield

assumption to determine a normalised load ratio U as a function of three governing parameters, i.e. material properties, specimen thickness, load ratio. The normalised load ratio U was used to describe the extent of plasticity-induced crack closure as well as to determine the effective stress intensity factor range ΔK_{eff}. Good correlation was found with various experimental investigations in their study. In 1981, Newman [136] proposed an approach, in which the plastic region ahead of the crack tip and the residual plastic stretches left behind the crack tip were modelled as constant stress bar elements, which either stayed intact or were invalid at a particular applied stress level. In the study crack opening stresses were estimated as functions of externally applied load as well as crack length, and were then used to evaluate the effective stress intensity factor range ΔK_{eff} and the crack growth rates. In 1992 Provan and Majid [137, 138] proposed a rigid-insert crack closure model for the analysis and assessment of fatigue crack closure phenomena. The proposed model was designed to account for the nonlinear elastic behaviour of a fatigue crack and estimated the combined effect of residual plastic stretches, asperity mismatch, and corrosion debris on the closure behaviour of a fatigue crack by a hypothetical rigid insert located in an ideal crack wake.

Numerical simulations have become an important supplement to the analytical and experimental approaches for the study of fatigue crack closure. Such work mostly uses finite element methods [4, 16, 130, 139-141] or boundary element methods [142, 143]. Numerical modelling of crack closure has some advantages, such as accurate resolution of the displacements, stress and strain fields, efficient treatment of many different problems and insights into previously unknown features of the closure process, especially in the case of complex loadings and geometries [63]. However, there are limitations that restrict the

widespread application of numerical analysis methods, such as mesh refinement and convergence, crack surface contact, node release scheme and the computational requirements [135], whilst computational methods are based on continuum theory which does not involve microscopic and sub-microscopic features that control fracture behaviour in real materials.

3.3 Methods for experimental evaluation of crack closure

Since Elber [62] firstly observed the phenomenon of premature closure of the crack during the unloading part of a cycle, several experimental methods have been proposed to evaluate the crack closure effect in the past forty years.

These experimental methods for measuring crack closure can be divided into four main groups [144]:

- Direct observation of the crack closure at the crack tip.

  Such methods include optical microscopy, scanning electron microscopy, replica techniques, photography, optical and laser interferometry, surface strain, and caustics.
- Physical measurement methods, such as the potential drop technique, eddy current, ultrasonic, or acoustic emission.
- Indirect methods based on fatigue crack growth.

  These methods are based on the observation of the striation spacing on fatigue crack surfaces and crack growth rate observations during variable amplitude loading.
- Compliance-based methods.

  The methods include strain gauges, clip gauges, and laser extensometry.

Due to their simplicity and relatively low cost, compliance methods are the most widely used. These methods aim to determine a point below/above which the

crack is fully closed/open through identifying a virtual change of the crack length during crack closure by the measurement of compliance either at locations remote from the crack tip (global methods) or locations adjacent to the crack tip (local methods). However, the measured values of opening/closing load vary with the placement of the gauges, and there is some ambiguity in the interpretation of the results.

Some researchers have used combinations of the above methods to measure crack closure. One advantage of using combinations of methods is that they can provide a cross-check of measurements for the same experiment. In particular, in 1978, Jones et al [145] employed optical interferometry, an interferometry displacement gauge and a displacement gauge in three distinct regions of a CT specimen to obtain displacement-load profiles. In their study, the displacement-load behaviour was determined at discrete distances ahead of the crack tip with optical interferometry; the crack tip opening displacement at various distances behind the crack tip was measured with an interferometry displacement gauge; and a displacement gauge was used for the measurement of the displacements at the notch mouth. This study indicated that the location of the measurement devices has a significant effect on experimental results. In 1988, the work by Bowman et al [146] reached a similar conclusion that the location of the measurement devices was an important factor affecting the results. In their study, they used back-face strain gauges, front-face clip gauges and a laser extensometer for measuring closure loads, and found that the laser extensometer provided the most reliable results among the three techniques. Also in 1988, Hudak et al [147] reported that local closure measurements with a stereoimaging technique provided higher opening values compared to the far-field closure measurements conducted by Minakawa et al [148]. In 1997 Evans

and Spence [149] employed three different monitoring techniques: potential drop, strain gauges and replica monitoring techniques, to study crack closure. Good correlation among the three techniques was observed in this study.

In 1998 Huang et al [150] was able to measure crack closure by using a clip gauge, surface strain gauges and the potential drop technique. They also claimed that different placements of the strain or displacement gauges may result in different levels of crack closure. In addition, some researchers also showed that the resolution of the technique and the position in the crack wake, where a major contribution to crack closure occurs, are critical factors in obtaining accurate results rather than approximate estimations [151, 152]. Garz and James [151] employed a back-face strain gauge and a clip gauge for measuring crack closure, while James and Knott [152] used a back-face strain gauge together with an offset elastic displacement circuit to measure the crack closure effect. Gan and Weertman [153] and later Pippan [154] investigated this by studying the sensitivity of the near-crack tip strain gauge to different locations and orientations.

Adding to the uncertainty over measuring techniques, in 1986 Vecchio et al [155] found that closure is also dependent on the geometry of the specimen being tested. In 1991 by using a scanning electron microscope combined with stereoimaging techniques, Davidson [156] showed that the magnitudes of closure loads were dependent on the specimen geometry, while the stress intensity factor (ΔK) was not.

In recent years, photoelasticity, thermoelasticity and image correlation have also been implemented to study crack closure. In 1999 Sutton et al [157] used image correlation to evaluate crack closure. Crack closure loads were estimated from the crack tip opening displacement at a distance behind the

crack tip in a $0.5\ mm \times 0.5\ mm$ region. The work of Pacey et al [93] provided new insights into fatigue crack closure using photoelasticity combined with finite element methods and compliance measurements. They developed a mathematical model based on the Muskhelishvili stress potential function [61] to describe the stress fields around the tip of a fatigue crack experiencing crack closure, and aimed to evaluate the wake contact forces which were thought to affect the effective stress intensity factor range. The theoretical model was fitted to experimental photoelastic fringe patterns observed in polycarbonate compact tension specimens by a combination of a generic algorithm and the downhill simplex method. Mixed-mode stress intensity factors were estimated from the fitted theoretical stress field during two load cycles, as shown in Figure 3.1. The results clearly showed evidence of crack closure. Furthermore, they also reported that the crack closure experienced by the fatigue crack was likely to be experienced as a kind of 'back stress' applied to the total plastic enclave on the crack tip stress field, having observed from their results only a weak correlation between the contact force and the effective stress intensity factors. Diaz et al [158] were able to evaluate phenomena like the presence of residual stresses or crack closure by means of thermoelastic stress analysis. A direct measurement of the effective stress intensity factor of growing fatigue cracks was achieved directly from stress data ahead of the crack tip.

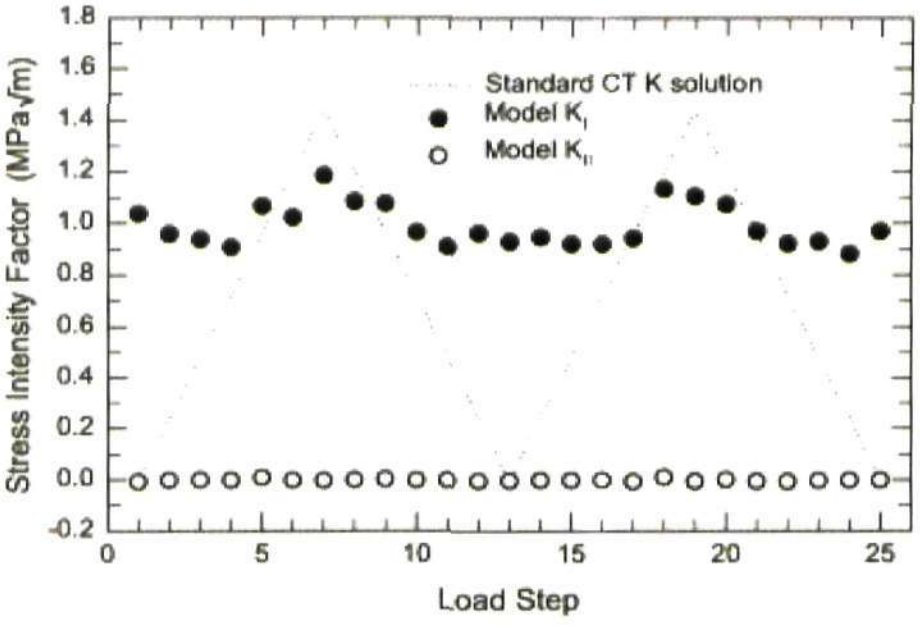

Figure 3.1 The stress intensity factors variation measured during the two load cycles, showing the measured mode I stress intensity factor as closed squares, the mode II stress intensity factor as closed triangles and the theoretical mode I stress intensity factor neglecting closure as the dashed line. (reproduced from [93])

The methods developed in Pacey et al [93] and Diaz et al [158] both allow for the extraction of crack wake contact force information, which cannot be obtained with compliance measurements, and avoid problems arising from the subjective interpretation of crack opening load and other difficulties associated with compliance measurements (installation time or gauge damage). In addition, Diaz et al [158] also used the effective stress intensity factors for fatigue crack life prediction. Lopez-Crespo [94] and Matos and Nowell [130] made similar studies of crack closure using digital image correlation instead of photoelasticity or thermoelasticity. Lopez-Crespo [94] followed the same approach as described in [93, 158], and evaluated the effective stress intensity factor from full-field displacement information provided by an image correlation method. Matos and Nowell [130] studied the effect of specimen thickness on

crack closure behaviour, and used three methods to assess crack closure, back-face strain gauges, crack-mouth clip gauges and digital image correlation. Their study also suggested that a back-face strain gauge is the most suitable technique for measuring effective crack closure for the purposes of predicting crack growth rate. A recent methodology for quantifying the crack closure effect is the work done by Christopher et al [51, 52]. To characterise the plasticity-induced crack closure effect on the elastic stress fields around the tip of a fatigue crack experiencing closure, they postulated a new mathematical model which contains four parameters to model the stress fields around the crack tip. The model was derived from the Muskhelishvili stress potential approach and contains two new parameters to include the shielding effect, i.e. a retardation intensity factor and an interfacial shear stress intensity factor, together with a modified Mode I stress intensity factor and the T-stress. With this model, they were able to study the shielding effect by using photoelasticity in polycarbonate compact tension specimens. The work in this thesis, follows the methodologies introduced in [51, 52] and [94], and studies the effect of plasticity-induced crack closure by two experimental techniques: photoelastic stress analysis and digital image correlation methods.

For compliance-based measurements, various procedures have been proposed to derive crack opening load P_{op} or crack closure load P_{cl} from load vs. displacement curves. The extraction of the point of transition, which characterises the closure, from compliance traces, is also a critical issue, as it is not easy to identify it with certainty in such plots.

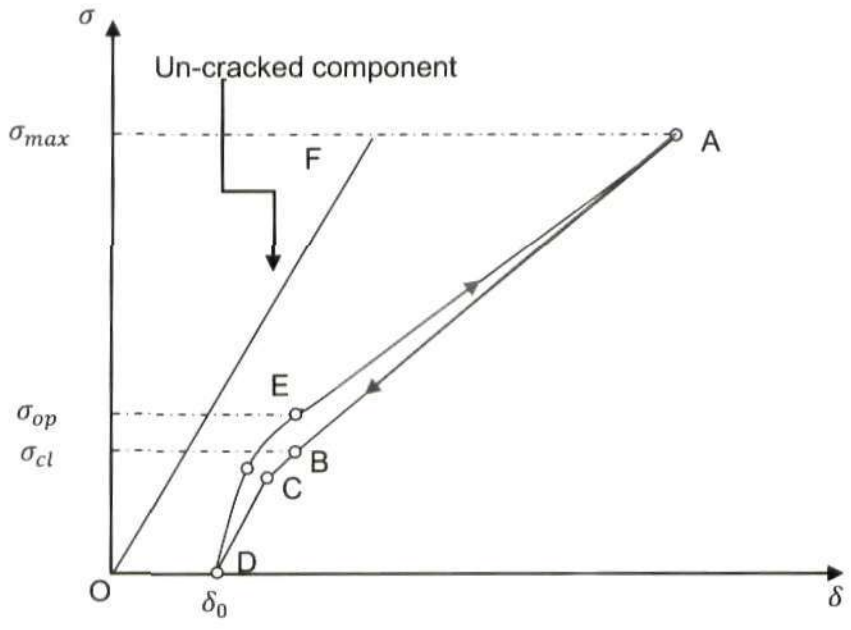

Figure 3.2 Schematic illustration of the relationship between externally applied stress vs. displacement given by strain gauges when crack closure presences in a fatigue crack. The difference between opening stress σ_{op} and closing stress σ_{cl} is also indicated.

Most authors consider the transition point as the lowest point at which the plot becomes linear (point E in Figure 3.2). Some authors draw two tangents for the upper part and the lower part of the load vs. crack opening displacement curve respectively, as shown in Figure 3.3 (a). The point of intersection of the two tangent lines gives the load at opening, and it is a kind of median stress between the crack fully open and the crack fully closed. Some investigators follow the variation of the slope approach, according to which the upper part of the load vs. crack opening displacement curve is obtained by regression analysis [159]. Subsequently, going down the curve, the local averaged slopes are obtained for each point by considering a number of neighbouring points on both sides of the data point, and the criterion for identifying the opening load is a deviation of 5% from the slope of the upper part in the curve. Other methods

for determining the closure load include representing the upper section of the load vs. crack-opening displacement curve (segment 1 in Figure 3.3 (b)) by a linear function and the lower part (segment 2 in Figure 3.3 (b)) by a second order polynomial. The coefficients for both approximations are determined by a regression analysis. A requirement is that the coordinates and the slopes of the linear part and the second order part should be equal for both parts at the tangency point. The tangency point is chosen as the point with minimum error in the regression.

Obviously, the different evaluation procedures may result in different opening values. It has been reported from a statistical evaluation, that even for an individual load vs. displacement curve, significant differences in the opening values may be obtained, depending on the chosen procedure, and other variables such as the interval size, the number of data pairs per interval, or the amount of hysteresis and data scatter in the load vs. displacement curve [160]. The scatter of the opening values determined by these procedures may reach 30% or even more [161].

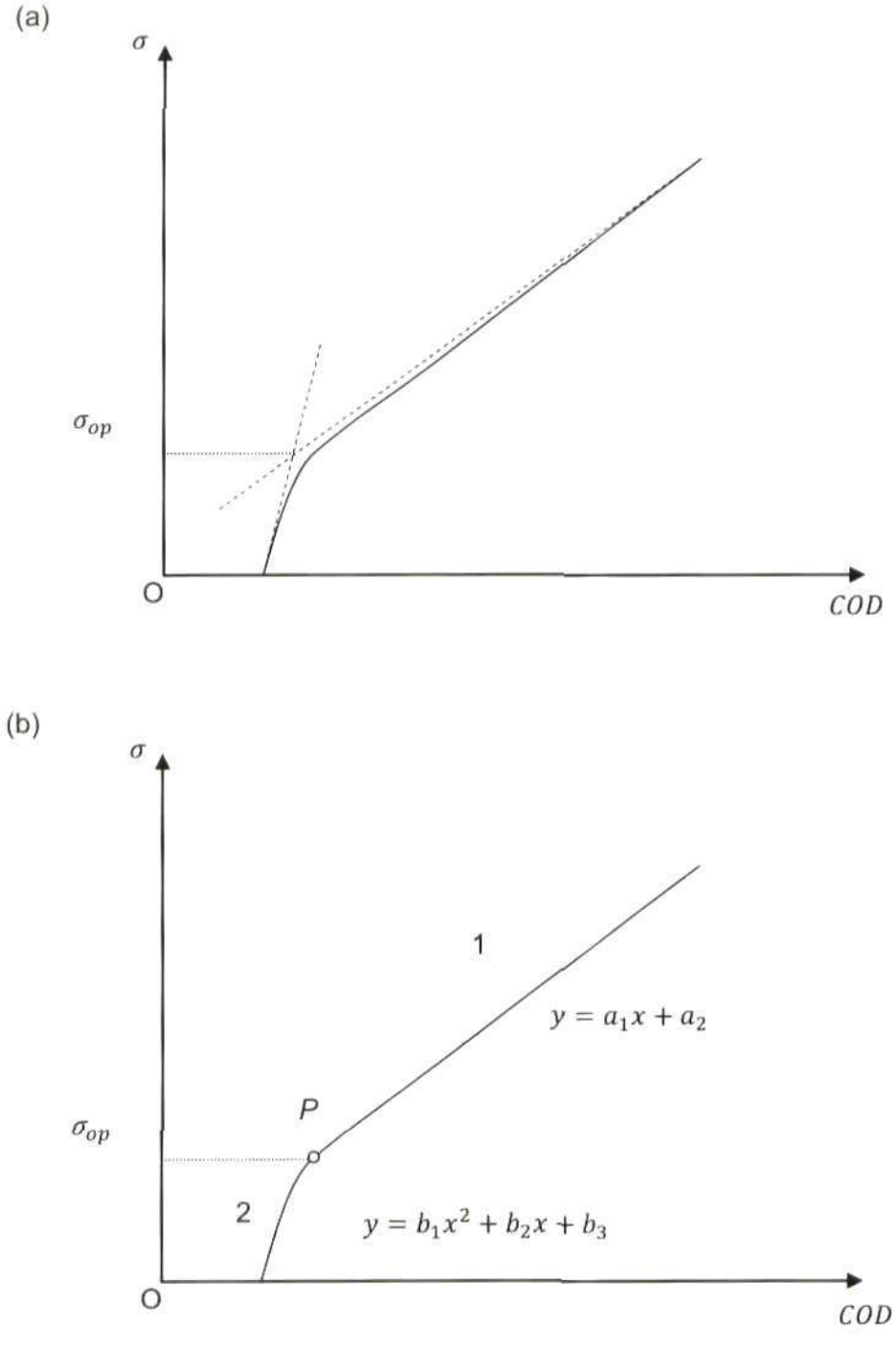

Figure 3.3 Illustration of two methods for determining crack opening stress σ_{op} (a) method of intersection of two tangent lines drawn from the upper and lower linear potions on the curve; (b) method using different degrees of polynomials to fit the whole curves.

When reviewing the literature, it is found that, despite the considerable research that has been conducted on evaluating closure effects with different techniques and many attempts to rationalise the basis of crack closure, crack closure effects are still not fully understood, and there are still unresolved issues related to the mechanisms underlying crack closure and the methods to quantify its effects [65, 140, 162-164]. The variety of experimental techniques used for closure studies which have different sensitivities and accuracies, coupled with different measurement locations relative to the crack tip, render a comparison between literature data almost impossible. In the past forty years, a wide spectrum of uncertain, controversial, anomalous, and contradictory results have been presented in the literature [32] , some of which are listed below.

One controversial issue is the existence and signification of crack closure itself. Some researchers have concluded that it is not significant [48], and that crack growth rates are only dependent on the stress ratio [165, 166]; while some found a significant reduction in crack driving force caused by crack closure [146] with a consequent effect on crack growth rate [167, 168]. Vasudevan et al [48, 64] reported that plasticity originating from the crack tip does not induce crack closure in the near-threshold regime. It was also reported that the formation of oxide asperities is a random process that cannot explain the effect of the load ratio in the near-threshold regime. Moreover, the closure contribution from asperities resulting from oxide or corrosion products or surface roughness is less than that expected based on the changes in the slope of the load vs. displacement curve. Finally, they concluded that the crack closure effect may exist, but its magnitude is either small or negligible. They also proposed a model based on dislocation theory, according to which two load parameters must be exceeded simultaneously if crack growth is to occur, namely ΔK and

ΔK_{max}. The authors supported this new hypothesis with experimental data obtained with drop potential techniques and strain gauges in titanium alloy centre-cracked and compact tension specimens. Huang et al [150], argued that crack closure is not as significant as some people had thought in fatigue crack shielding. On the contrary, Suresh and Ritchie [167, 168] showed that roughness-induced closure is a strong function of the degree of surface roughness and is consistent with observations of the role of coarse grain sizes in reducing near-threshold growth rate at low load ratios. They attribute the significant influences of grain size, yielding strength, and crack size on near-threshold crack growth behaviour to a differing contribution from roughness-induced crack closure. Kondo et al [169] studied the critical crack size that causes retardation of short fatigue crack by single overload. They found that crack closure has a complex dependency on crack length, yield strength of material and the baseline value of stress ratio. Bowman et al [146] reported a result that showed a significant reduction (40%) in the load range due to crack closure, while Fleck and Smith [170] showed that the fatigue crack is closed for 20% of the load cycle in the plane strain regions of a BS 4360 50B steel specimen.

Another issue is controversy regarding the stress value which best characterises closure. Due to the hysteresis during a fatigue cycle, the deviation from linearity occurs at different points during loading (σ_{op}) and unloading (σ_{cl}), with σ_{op} being often 15% greater than σ_{cl} [171]. There is not full agreement about which of these values should be taken as the lower limit of the effective stress intensity range.

The use of potential drop technique for crack closure measurements is highly debated. Some authors find that the technique is useful, [149, 172, 173].

Anderson et al [173] showed that crack opening stress measured with potential drop proved to be somewhat higher than that made through a compliance-based technique from a strain gauge placed in front of the crack tip. However, others find the results unreliable and the technique invalid, and recommend that the potential drop technique should not be used to measure crack closure for steels in air [170, 174, 175]. The main reason given by these authors is that an insulating oxide film on the crack surfaces prevents the electrical current flow and that electrical but not mechanical contact can occur between points on the crack surface.

Other researchers debate the standard closure assessments, and suggests that the lower limit of the effective stress intensity range lies below P_{cl} [155, 172, 176].

All this controversy was reviewed by James [65] in 1997 and the following reasons were identified as potential sources of ambiguity:

- Discrepancy generated by the use of different experimental techniques. These include differences between compliance methods and other systems, measurements obtained from the surface and through the thickness measurements and positioning of the technique.
- In the case of compliance-based techniques, interpretation given to the variation in the compliance for the characterization of the closure.
- Sensitivity of the closure behaviour to materials, geometry, environment and test methodology.
- Disagreement on the importance and magnitude of plasticity-induced crack closure.

3.4 Concluding remarks

Since the concept of fatigue crack closure initially defined by Elber, numerous investigations have been devoted to this phenomenon Fatigue crack closure has been one of the most intensively studied phenomena associated with fatigue and fracture problems. Fatigue crack closure has been widely applied to study fatigue crack initiation, fatigue crack growth behaviour, mechanisms of crack growth retardation, load interaction, material microstructures, environmental effects and many others. The mechanisms of fatigue crack closure can be categorized into plasticity-induced crack closure roughness-induced crack closure, oxide-induced crack closure, viscous fluid-induced crack closure and phase transformation-induced crack closure.

To estimate the effect of fatigue crack closure, particularly on the behaviours of fatigue crack growth and fatigue life prediction, numerous studies have been carried out to determine fatigue crack opening load or closing load, and effective crack driving force, ΔK_{eff}, using analytical, numerical and experimental methods. Analytical methods are usually based on the Westergaard stress function, William's stress function or Muskhelishvili complex stress functions. Experimental techniques include photoelasticity, thermoelasticity, caustics, Moiré interferometry, electronic speckle pattern interferometry, Image correlation, electric potential drop, compliance techniques etc.

Despite the considerable research that has been conducted on evaluating closure effects with different techniques, and many attempts to rationalise the basis of crack closure, crack closure origins and effects are still not fully understood, and there are still unresolved issues related to the mechanisms of crack closure and the methods to quantify crack closure effects. In the past

forty years, a wide spectrum of uncertain, controversial, anomalous, and contradictory results have been reported.

Chapter 4 Mathematical model, apparatus and methods

4.1 Introduction

This chapter starts with the introduction of a new four-parameter photoelastic model proposed by Christopher et al [51], which was designed to more appropriately describe the shielding effect of the complete plastic zones ahead of the crack tip and along the crack wake. The model will then be employed in the present study to calculate the stress intensity factors and T-stress from experimental data. A detailed description of specimen configuration is then given. In the third part of this chapter, the apparatus and methods adopted in the experimental photoelastic stress analysis and digital image correlation are described, and attention is given to the following issues: mechanical properties and chemical compositions of materials employed, specimen preparation for fatigue testing, equipment and experimental set up, measurement procedure and loading conditions for each specimen subjected to fatigue testing.

The overall aim of the programme was to obtain enough experimental data to be able to explore the way in which the new parameters may be used for life prediction that more explicitly incorporates plasticity-induced crack tip shielding.

4.2 New four-parameter mathematical model

4.2.1 Introduction

Continuum mechanics descriptions of the far-field stresses ahead of a crack are well developed and have proven extremely useful in providing single-parameter (e.g. the stress intensity factor, K) techniques for predicting fatigue crack growth rates, such as Williams' solution, Westergaard's solution and Muskhelishvili's expression for linear elastic crack tip stress field. The stress intensity factor derives from a mathematical analysis of an infinitely sharp crack and essentially characterises the local plastic deformation and crack blunting associated with the growth of real cracks via the similitude concept. Similitude implies that equal stress intensity (and therefore equal plastic zone size and shape) will have equivalent strain fields outside the plastic zone and hence equivalent consequences on crack growth rate. A breakdown in similitude is clearly to be expected where crack tip shielding, particularly plasticity-induced crack shielding, leads to a significant perturbation of the local strain field and hence the driving force for crack growth imposed by the global elastic stress field. There was some considerable scepticism that a phenomenon such as fatigue, which requires cyclic plasticity at the crack tip, could be amenable to prediction by an elastic fracture mechanics parameter such as the stress intensity factor.

In recent years, increasing attention has been focussed on the necessity of a using a two-parameter description of crack tip stresses: namely stress intensity factor K and T-stress. T-stress is thought to be the second important parameter to the process of crack growth besides the well-known governing parameter stress intensity factor K [177-179]. T-stress is the second non-singular term and constant stress acting parallel to crack extension direction in the Williams

series expression for horizontal stress σ_x. The value of T-stress strongly depends on the type of loading as well as on the specimen geometry and crack length. The sign and magnitude of T-stress substantially affect the extent and shape of crack tip plasticity [32, 180]. T-stress could also affect fatigue crack growth rate [181], as T-stress can alter the crack tip triaxiality and hence influence crack tip constraint [32, 177, 179, 180, 182]. Positive T-stress strengthens the level of crack tip stress triaxiality and leads to high crack tip constraint; high crack-tip constraint facilitates crack growth as a result of limited plastic deformation around the crack tip. Negative T-stress reduces the level of crack tip stress triaxiality and leads to the loss of crack tip constraint [179]. This has been proven by experimental work conducted by Tong et al [183], which shows that fatigue crack growth rate in corner notched (CN) specimens is lower than that in compact tension (CT) specimens. This result is consistent with the existence of a negative T-stress in the CN specimen as opposed to the positive T-stress in the CT specimens [180, 184]. Finite element 3D modelling by Roychowdhury and Dodds [185] has indicated that the magnitude of the T-stress influences the closure process through two factors: the stationary crack opening displacement and the residual plastic deformation left in the wake of a steadily growing fatigue crack. They found that if the T-stress was zero then plastic contraction in the thickness direction compensated primarily for permanent deformation in the direction normal to the crack plane; if it was negative then plastic contraction in the in-plane transverse direction (parallel to the crack) contributes the larger share of material flowing into the normal direction (transverse to the crack), and if it was positive then both in-plane directions experienced permanent stretching and the thickness direction alone underwent plastic contraction. Similar work by Kim et al [186] studied the

stationary crack front fields in a thin elastic–plastic plate and varied the T-stress to modify the in-plane constraint level. Their analysis demonstrated a strong influence of T-stress on crack front stress and deformation fields. The size of the near-tip plastic zone, both at the centre-plane and near the free surface, increased as the T-stress deviated from zero. A negative T-stress had a more pronounced influence on plastic deformation with the plastic zone spreading predominantly at an angle of about 45° with the forward direction of the crack plane. For positive T-stress, the plastic zone tilts backward at low load and spreads parallel to the crack both in the forward and the backward direction at higher loads. Moreover, T-stress could affect crack growth resistance or fracture toughness in ductile materials [187] as a high level of crack tip constraint can significantly reduce the plane stress fracture toughness. T-stress can also modify crack paths [188, 189], e.g. straight cracks with negative T-stress stay stable under mode I loading conditions, while positive T-stress deviates the crack off the initial crack plane. A recent paper by Hadj Meliani et al [190] summarises the characteristics and effects of T-stress and these include:

- The value of T-stress is sensitive to loading mode, specimen geometry, and crack sizes. For example, the T-stress increases from high negative value to low negative or positive values when specimen loading mode and geometry change from tension to bending.
- The stress intensity factor over T-stress ratio increases nonlinearly with the crack aspect ratio.
- Sign and magnitude of the T-stress substantially change the size and shape of the plane strain crack tip plastic zone. Irrespective of whether it is positive or negative, the T-stress increases the plastic zone size

comparing with a T-stress free situation. In plane strain, the plastic zone is oriented along the direction of crack extension for $T > 0$ and is in the opposite sense when $T < 0$.

- Fatigue crack growth rate in the Paris law regime decreases with increasing T-stress.
- It has been observed that the T-stress has an influence on crack propagation after fracture initiation. Negative T-stress values stabilise the crack path. In contrast, positive T-stress values induce crack bifurcation.

From those studies, it is clearly necessary to include the T-stress in the solution of the crack tip stress field, in order to try to understand plasticity deformation around a crack tip.

Since the first observation of fatigue crack closure by Elber, several analytical models have been published as reviewed in Chapter 3. Among them, the models proposed by Budiansky and Hutchinson [66], Codrington and Kotousov [135], and Newman [136], were based on Muskhelishvili stress potential functions; however, these models were not presented in a form suitable for fitting to experimentally derived displacement or stress fields [93]. Unlike the previous studies, the mathematical model developed by James et al [16, 93] can be directly fitted to the full-field photoelastic fringe patterns observed on fatigue cracked specimens experiencing crack closure. The origin of the model was many years of research by James [29, 65, 152, 191-193] on fatigue crack closure which led to the realisation that the elastic-plastic interface which existed at the plastic enclave surrounding the crack must exert a 'back-stress' on the elastic field driving growth and that this effect would not be properly captured by traditional techniques for measuring closure. This effect was

therefore likely to underline much of the controversy around closure and its occurrence, including the effects of stress state. The results of the work by Pacey et al [93] provided confirmation that the crack shielding experienced by a fatigue crack included a kind of 'back stress' applied by the total plastic enclave on the crack tip stress field, and that the crack tip shielding effect represents a net effect of the overall plastic enclave on the elastic stresses. The mathematical model in this early work was incomplete, in the sense that wake contact was modelled by a point force and the compatibility requirement at the elastic-plastic interface was not modelled. Following this work and the approach proposed by Nurse and Patterson [92], Christopher et al [51] developed a new mathematical model to better account for and quantify the effect of the total plastic enclave. It assumes that the plastic enclave that exists around a fatigue crack tip and along the fatigue crack flanks shields the crack from the full influence of the applied elastic stress field [51]. Crack tip shielding includes the effects of crack retardation forces that occur by contact across the crack wake, compatibility-induced influences (Poisson's contraction) in the plastic zone ahead of the crack tip, and an interfacial shear stress at the elastic-plastic boundary induced by compatibility requirements. Both of these influences introduce a shielding or 'back stress' on the surrounding elastic field that has to be overcome by the applied tensile stress. Consequently, two additional characteristic parameters were defined in a manner analogous to traditional stress intensity factors, namely a crack retardation intensity factor which captures effects acting perpendicular to the crack, both behind and ahead of the crack tip, and an interfacial shear stress intensity factor which characterises crack retarding forces arising from compatibility influences acting parallel to the crack.

The model was a natural extension of the earlier studies [16, 92, 93]. It provides a more comprehensive description of the shielding effects on the elastic stress field in the cracked objects due to plasticity deformation ahead and behind the crack tip. The underlying hypothesis is that the complete effects of the plastic zone ahead of the crack tip and the plastic wake on fatigue crack growth behaviour can be identified and understood better if the roles of the K-stress, T-stress and shielding stresses on the elastic stress fields near the crack tip are included in the mathematical model [51]. The newly established mathematical model can assist in critically examining various hypotheses regarding the mechanisms and the effect of fatigue crack tip shielding, and hopefully provide new insight into how the effect of fatigue crack closure can be estimated and help to improve understanding of the ambiguities existing in fatigue crack closure studies. The approach initiated in [51, 52] aims to understand better the mechanisms that appear to underlie the process of plasticity-induced shielding. The following section introduces this mathematical model in more detail.

4.2.2 Four-parameter model for stress (Photoelasticity)

The stresses included in the new four-parameter mathematical model are repeated in the free body diagram shown in Figure 4.1, as the diagram is fundamental to understanding the concepts underlying the model. Figure 4.1 schematically illustrates the forces acting on the boundary of plastic enclave and the surrounding elastic material, which were considered when building the new model.

The forces acting at the interface of plastic enclave and elastic field near the crack tip include: F_{Ax} and F_{Ay}, the reaction to the remote load that generates the crack tip stress fields traditionally characterised by the stress intensity factor

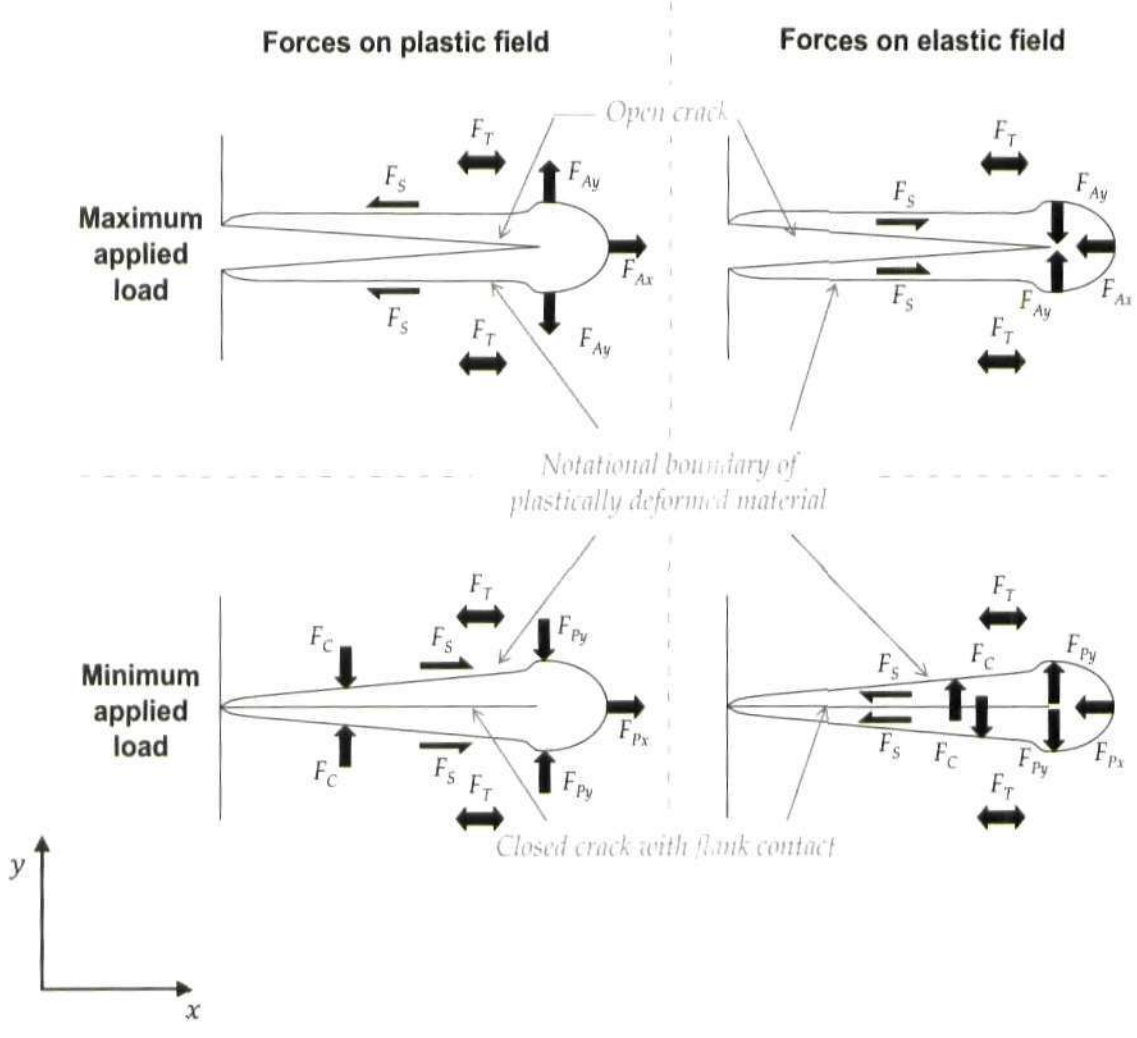

Figure 4.1 Schematic idealizations of forces acting at the interface of plastic enclave and the surrounding elastic material, where F_A is the applied force generating the crack tip stress field characterised by K_I, F_T represents the force due to the T-stress shown in this example as positive, F_S is the interfacial shear force between the elastic and plastic zones, F_C and F_P together create the shielding effect. F_P is the force generated by the constraint of compatibility on the plastically deformed material and F_C is the contact force between the flanks of the crack generated by the interference of the plastic zones along the flanks.([51, 52])

K_I; F_T, due to the T-stress which depends on the remote load for a specific configuration; F_{Px} and F_{Py}, induced by the compatibility requirements on the elastic plastic boundary near the crack tip, resulting from the permanent deformation in the plastic zone around the crack tip extensive in the direction perpendicular to the crack and contractive along the crack due to the effect of the Poisson's ratio; F_S, induced by the compatibility requirements on the elastic-plastic boundary of the crack wakes, as plastic deformation is a constant volume effect, i.e. $\nu = 0.5$, while elastic deformation occurs with $\nu = 0.3$, F_S could change its direction when the crack becomes open from closed state; F_C, is the contact force arising from the plastic wake contact effect transmitted to the elastic-plastic boundary of the crack wake.

In transmission photoelasticity, the relationship between stress fields and the isochromatic data is given by:

$$\frac{Nf}{h} = (\sigma_1 - \sigma_2) = \sqrt{(\sigma_y - \sigma_x)^2 + (2\sigma_{xy})^2}\ , \tag{4.1}$$

where, σ_1, σ_2 are principal stresses; σ_x, σ_y are stresses in x and y direction respectively; σ_{xy} represents shear stress; N is fringe order; h is specimen thickness; f is material fringe constant.

Using Muskhelishvili's potential functions, it can be rewritten as [92],

$$\frac{Nf}{h} = (\sigma_1 - \sigma_2) = \left|\sigma_y - \sigma_x + 2i\sigma_{xy}\right|\ . \tag{4.2}$$

Hence,

$$\frac{Nf}{h} = 2|\bar{z}\varphi''(z) + \chi''(z)| = 2|\bar{z}\,\phi'(z) + \psi(z)|\,, \tag{4.3}$$

where, $\varphi(z)$ and $\chi(z)$ are the two analytical functions in Muskhelishvili's approach, and $\phi(z)$ and $\psi(z)$ are known as Muskhelishvili's potential functions. $\phi(z) = \varphi'(z)$, and $\psi(z) = \chi''(z)$.

Williams' solution for stress fields around the crack tip can be expressed in terms of Cartesian co-ordinates under mode I loading as:

$$\sigma_x = \frac{K_I}{\sqrt{2\pi r}} cos\left(\frac{\theta}{2}\right)\left[1 - sin\left(\frac{\theta}{2}\right) sin\left(\frac{3\theta}{2}\right)\right] + T + O\left(r^{1/2}\right) \quad (4.4a)$$

$$\sigma_y = \frac{K_I}{\sqrt{2\pi r}} cos\left(\frac{\theta}{2}\right)\left[1 + sin\left(\frac{\theta}{2}\right) sin\left(\frac{3\theta}{2}\right)\right] + O\left(r^{1/2}\right) \quad (4.4b)$$

$$\sigma_{xy} = \frac{K_I}{\sqrt{2\pi r}} sin\left(\frac{\theta}{2}\right) cos\left(\frac{\theta}{2}\right) cos\left(\frac{3\theta}{2}\right) + O\left(r^{1/2}\right) \quad (4.4c)$$

where, r and θ are the distance and polar angle measured from the crack tip and crack plane respectively.

Substituting the leading terms in Williams' solution into equation (4.2), the following equation can be obtained:

$$\frac{Nf}{h} = \left|\sigma_y - \sigma_x + 2i\sigma_{xy}\right| = \left|Az^{-1/2} + Bz^{-3/2}\,\bar{z} + Cz^0\right| , \quad (4.5)$$

where,

$$A = -B = \frac{K_I}{2\sqrt{2\pi}},\ A + B = 0\,, and\ \ C = -T$$

The new four-parameter mathematical model was built by adding two new terms into equation (4.5) [51]:

$$\left|\sigma_y - \sigma_x + 2i\sigma_{xy}\right| = \left|Az^{-1/2} + Bz^{-3/2}\,\bar{z} + Cz^0 + Dz^{-1/2} ln(z) + Ez^{-3/2}\,\bar{z} ln(z)\right|$$

$$\frac{Nf}{h} = \left|Az^{-1/2} + Bz^{-3/2}\,\bar{z} + Cz^0 + Dz^{-1/2} ln(z) + Ez^{-3/2}\,\bar{z} ln(z)\right| \quad (4.6)$$

where, z is the complex co-ordinate in the physical plane, $z = x + iy$; x *and* y are co-ordinates in a Cartesian system with the origin at the crack tip; and A, B, C, D, E are unknown coefficients that need to be determined. In this model, an assumption has been made by taking $D + E = 0$ in the analysis in order to give an appropriate asymptotic behaviour of the stress along the crack flank, and $A + B \neq 0$ if an interfacial shear stress exists at the interface of the elastic plastic boundary (if not, $A + B = 0$). It will be mentioned in the last part of this section why A should not be equal to B when an interfacial shear stress is taken into consideration at the interface of the elastic plastic boundary. The $ln(z)$ terms in equation (4.6) encapsulate the wake contact forces across the crack flanks and an explanation of the thinking in the development of the shielding terms and their effects on the other stress parameters is useful.

The $ln(z)$ terms seek to model the extra terms in the Williams solution, where the forces are in an idealised form (i.e. they tend to infinity as the crack tip is approached) which approximate the true behaviour away from the plastic zone of the crack tip. The idealised terms which represent the closure forces are assumed to lie exactly along the boundary of the crack, i.e. ignoring the plastic zone, so that away from the plastic zone of the crack flanks, these extra terms should also approximate the true effect of the closure forces. Clearly, such an approach is quite naive, but the intention was to look for a simple characterisation of the closure forces which could be measured easily.

Since the stresses which appear in the Williams stress solution are of order $r^{-1/2}$, it seems reasonable to posit that the closure forces should also have this *form along the crack flanks in the idealised model. From the photoelastic* images of cracks experiencing closure, it seemed clear that the effects are significant in asymptotic terms (indicated in photoelastic images by a moving of

the end of the fringes away from the crack tip, Figure 4.2; hence it is reasonable that the additional terms should be of a similar asymptotic order to the other forces involved.

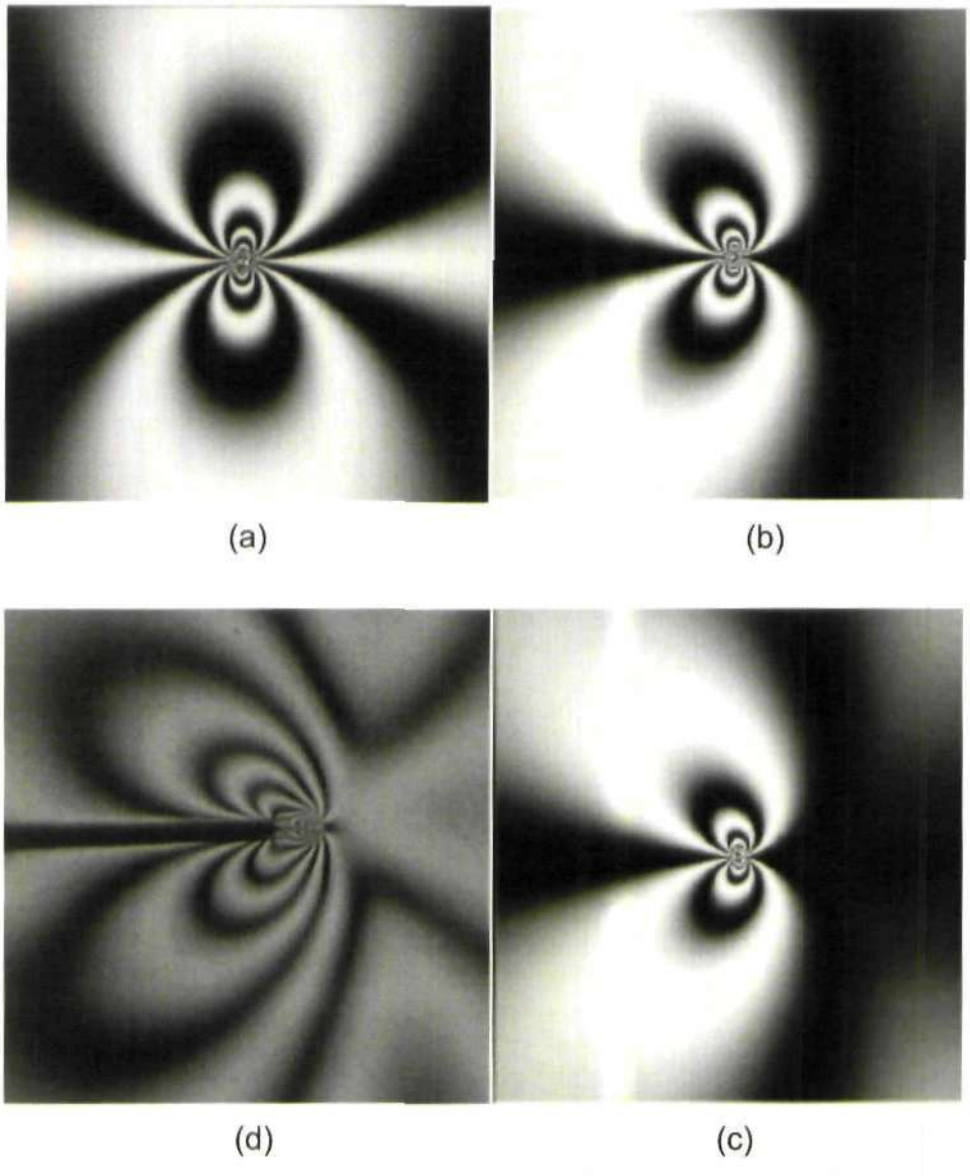

Figure 4.2 Clockwise from top left: Isochromatic fringe pattern modeled using new mathematical model (equation 4.6) for a mode I crack: (a) without consideration of T-stress and retardation intensity, (b) with a positive T-stress and zero retardation intensity, (c) with a positive T-stress and positive retardation intensity (The effect of interfacial shear stresses has been neglected), (After [51]); (d) Photoelastic fringe patterns recorded on a polycarbonate specimen.

In order to produce this growth along the crack flanks, a $ln(r)r^{-1/2}$ term is needed for the component of the closure force normal to the crack flanks. Note that this analysis uses polar coordinates and hence r is always positive, with position ahead and behind the crack tip being denoted by angle θ, relative to the crack plane. If only closure forces parallel to the crack flanks are involved then $r^{-1/2}$ terms are sufficient. However, it seems that the normal force is also significant. The difficulty with such ln terms is that there is no a priori reason why the analysis should stop at $ln(r)r^{-1/2}$ and not consider $ln(r)^2r^{-1/2}$ etc. One possibility for future extension of the model is that higher order terms like this are taken into account. There is a second difficulty with the ln term which is explained below.

This mathematical model describes the elastic stress field around the tip of fatigue cracks which are acting as a blunt plastic enclave in the material subject to Mode I loading. The terms $Dz^{-1/2}ln(z)$ and $Ez^{-3/2}\,\bar{z}ln(z)$ were used to include the shielding effect of the plastic enclave surrounding the fatigue crack on the elastic fields around the crack tip. These are characterised via two parameters, i.e. a crack retardation stress intensity and an interfacial shear stress intensity. Thus, the stress fields on the elastic material can be characterised by four parameters: a stress intensity factor K_F analogous to K_I in classical fracture mechanics, T-stress, interfacial shear stress intensity K_S and a retarding stress intensity K_R. The question is then how to introduce the new parameters into the system in a physical way. Two are clear cut; the normal and tangential components of the crack closure forces as one moves towards the crack tip along the crack flanks should give asymptotically $K_R/\sqrt{r}$ and $K_S/\sqrt{r}$. A closure-free situation corresponds to the case where $K_R = K_S = 0$.

This leaves the original K_I term to re-define. This is much more arbitrary as, mathematically, any expression which reduces to K_I when $K_R = K_S = 0$ would suffice. The original definition of K_I involves the asymptote of σ_y as we approach the crack tip (i.e. σ_y is asymptotically $K_I/\sqrt{r}$). Now, there is only one parameter in the original Williams solution, so K_I could be defined in any number of equivalent ways, and our view was that it would be best to base our definition of K_F on σ_y to give greater acceptance in the fracture mechanics community.

Unfortunately, σ_y involves terms in $z^{-1/2}ln(z)$ as one approaches the crack tip. Since these arose from the closure terms in K_R, it seemed best to remove these and then consider the asymptotics of the remainder to give K_F (i.e. asymptotically we have $K_F/\sqrt{r}$ as the second-order approximation to σ_y once the ln term in K_R is removed). This has the advantage that apart from the subtraction, the remaining definition is close to the one already used in the literature. The disadvantage is that it is quite arbitrary. The author recognises that a better approach would be to use an alternative definition of K_I which works in both the closure-free and plasticity-induced closure cases without modification. A satisfactory way to do this has yet to be found. Nonetheless, the definition adopted for K_F appears to work reasonably well in characterising fatigue crack growth.

The elastic stress fields near the crack tip are then given by:

$$\sigma_x = -\frac{1}{2}(A + 4B + 8E)r^{-\frac{1}{2}}cos\frac{\theta}{2} - \frac{1}{2}Br^{-\frac{1}{2}}cos\frac{5\theta}{2} - C$$

$$-\frac{1}{2}Er^{-\frac{1}{2}}\left[ln(r)\left(cos\frac{5\theta}{2} + 3cos\frac{\theta}{2}\right) + \theta\left(sin\frac{5\theta}{2} + 3sin\frac{\theta}{2}\right)\right] + \mathcal{O}\left(r^{\frac{1}{2}}\right)$$

$$\sigma_y = \frac{1}{2}(A - 4B - 8E)r^{-\frac{1}{2}}cos\frac{\theta}{2} + \frac{1}{2}Br^{-\frac{1}{2}}cos\frac{5\theta}{2} \tag{4.7}$$

$$+\frac{1}{2}Er^{-\frac{1}{2}}\left[ln(r)\left(cos\frac{5\theta}{2} - 5cos\frac{\theta}{2}\right) + \theta\left(sin\frac{5\theta}{2} - 5sin\frac{\theta}{2}\right)\right] + \mathcal{O}\left(r^{\frac{1}{2}}\right)$$

$$\sigma_{xy} = -\frac{1}{2}r^{-\frac{1}{2}}\left[Asin\frac{\theta}{2} + Bsin\frac{5\theta}{2}\right] - Er^{-\frac{1}{2}}sin\theta\left[ln(r)cos\frac{3\theta}{2} + \theta sin\frac{3\theta}{2}\right] + \mathcal{O}\left(r^{\frac{1}{2}}\right)$$

Four parameters are therefore used to characterise the stress fields generated by the forces in Figure 4.1: the classical opening mode stress intensity factor K_F, the shear stress intensity factor K_S, the retardation stress intensity factor K_R, and the T-stress.

K_F is defined from the asymptotic limit of σ_y as $x \to +0$, along $y = 0$, i.e. towards the crack tip from the front along the crack line:

$$K_F = \lim_{r\to 0}\left[\sqrt{2\pi r}\left(\sigma_y + 2Er^{-1/2}ln(r)\right)\right] = \sqrt{\frac{\pi}{2}}(A - 3B - 8E) \tag{4.8}$$

The quantity K_R characterises the direct stresses acting parallel to the crack growth direction and was obtained by evaluating σ_x in the limit as $x \to -0$, along $y = 0$, i.e. towards the crack tip from behind along the crack flank:

$$K_R = \lim_{r\to 0}\left[\sqrt{2\pi r}\sigma_x\right] = \frac{\pi^{3/2}}{\sqrt{2}}(D - 3E) \tag{4.9}$$

The quantity K_S characterises the shear stress on the elastic-plastic boundary, and is derived from the asymptotic limit of σ_{xy} as $x \to -0$, along $y = 0$, i.e. towards the crack tip from behind along the crack flank:

$$K_S = \lim_{r\to 0}\left[\sqrt{2\pi r}\sigma_{xy}\right] = \mp\sqrt{\frac{\pi}{2}}(A + B) \tag{4.10}$$

Where, the '+' sign is taken for $y > 0$, and '-' sign for $y < 0$. Hereby, if an interfacial shear stress exists at the interface of elastic-plastic boundary, i.e. the shear stress intensity factor $K_S \neq 0$, it requires $A + B \neq 0$. If not , $A + B = 0$.

T-stress represents the transverse stress which is added to σ_x as a constant term and is given by

$$T = -C \tag{4.11}$$

The new four-parameter model, as expressed in equation (4.6), has been termed the CJP (Christopher-James-Patterson) model by its originators. It describes the 2D elastic stress fields near the crack tip for a crack which is essentially acting as a plastic notch in the material and relates the stresses with the value of isochromatic fringe order N. One advantage of using this model for the stress field at a fatigue crack tip is that it addresses one of the fundamental questions associated with cracking, that of when a crack and a notch can be considered to be similar in behaviour. It also attempts to answer, at least to some extent, the fundamental question of why fatigue crack growth, a phenomenon which explicitly derives from plastic deformation, can be described by an elastically-derived parameter, i.e. the stress intensity factor. The model also explicitly demonstrates that the constraint concept of the plastic enclave by the surrounding elastic field offers a very rational explanation for the observed differences in plasticity-induced shielding effects between plane stress and plane strain. It therefore offers insights into resolving a number of the controversies associated with research into plasticity-induced crack tip shielding. The definitions for the new and modified stress intensity factors may therefore provide a better solution for prediction of fatigue crack growth rates in

the presence of variable amplitude loading, where plastic zone sizes and hence constraint factors vary from cycle to cycle.

4.2.3 Four-parameter model for displacement (DIC)

Photoelasticity is rather limited in application to metallic materials and although this model works well in describing fatigue crack growth in polycarbonate, it was desired to extend it to describing crack growth in metallic materials. This is possible using digital image correlation (DIC) techniques, which measure displacements on the surface of cracked specimens. The experimental application of both photoelastic and DIC techniques to crack tip stress characterisation has been described in the previous chapters.

The concept of the four-parameter model can therefore be extended to study displacement distribution around a crack in structures or components of a wide range of materials, especially metals. The four-parameter model in terms of displacement fields (perpendicular and parallel to the crack faces) can be derived from Muskhelishvili's stress potential functions,

$$2\mu(u_x + iu_y) = \kappa\varphi(z) - z\overline{\varphi'(z)} - \overline{\chi'(z)} \ ,$$

$$\begin{aligned} 2\mu(u_x + iu_y) = \kappa &\left(-2(B+2E)z^{\frac{1}{2}} + 4Ez^{\frac{1}{2}} - 2Ez^{\frac{1}{2}}ln(z) - \frac{C}{4}z\right) \\ &-z\left(-(B+2E)\bar{z}^{-\frac{1}{2}} - E\bar{z}^{-\frac{1}{2}}\overline{ln(z)} - \frac{C}{4}\right) \\ &-\left(A\bar{z}^{\frac{1}{2}} + D\bar{z}^{\frac{1}{2}}\overline{ln(z)} - 2D\bar{z}^{\frac{1}{2}} + \frac{C}{2}\bar{z}\right), \end{aligned} \qquad (4.12)$$

where, u_x and u_y represent horizontal and vertical displacement respectively, $\mu = \frac{E}{2(1+v)}$; $\kappa = 3 - 4v$ (Plane strain) or $\kappa = \frac{3-v}{1+v}$ (Plane stress).

The stress intensity factor K_F, the interfacial stress intensity factor K_S, the retardation stress intensity factor K_R and the T-stress can be calculated by *equation (4.8-4.11) respectively.*

4.3 Apparatus and methods

4.3.1 Introduction

This section describes two simple experimental programmes designed to investigate the fatigue crack closure behaviour of compact tension specimens and validate the four-parameter mathematical model described in the previous section. One group of experiments applies photoelasticity on polycarbonate compact tension specimens; another group of experiments was conducted on aluminium alloy compact tension specimens and used image correlation. The main goal of the two groups of experiments is to investigate the development of crack closure in specimens under simple loading conditions such as constant amplitude loading without/with single peak overloads with varying load ratio.

It has been reported that fatigue crack closure is influenced by many parameters, such as specimen configuration and geometry, load conditions, the stress state and the environment. It also has been reported that the factor $U = (\Delta K_{eff})/\Delta K$ depends primarily on the load ratio R in Elber's work [62]. For 2024-T3 aluminium alloy specimens, Elber concluded that $U = 0.5 + 0.4R$, $-0.1 < R < 0.7$, which indicated that U is dependent on R. This conclusion is controversial and is questioned by many other investigators. For example, Shih and Wei [172] indicated a definite K_{max} dependence, while McClung [162] compared the influence of applied stress, crack length and stress intensity factor on crack closure, and classified three regimes to describe different closure behaviour. He concluded that no single relationship between crack

opening levels and the fundamental fatigue parameters gives a universal description; load condition is only one of the major factors. Therefore, it is important to investigate the influence of different load conditions on crack closure and employ experimental data collected under varying load conditions to validate the four-parameter model.

4.3.2 Specimens employed

The specimens employed in this study are compact tension (CT) specimens. To maintain consistency, the current study employed the same geometry as in the previous studies [52, 93, 94]. The geometry of the CT specimens studied in the current work is summarised in Figure 4.3. It should be noted that the CT geometry shown in Figure 4.3 represents a non-standard CT specimen geometry in comparison with Ewalds and Wanhill [194] or ASTM Standard E-399-72 [195] (see Figure 4.4). The difference is that it has longer ligament to allow a greater extent of crack growth before complete failure than is possible in standard CT specimens.

For a standard compact tension specimen, the solution for the theoretical value of stress intensity factor K_I proposed by Srawley [196] is given by the following formula:

$$K_I = \frac{P}{tb^{1/2}} \cdot f\left(\frac{a}{b}\right) \tag{4.13}$$

Where P is the load, b is the specimen width, t is the thickness of the specimens, a is the crack length measured from the centre of the pin holes and $f(a/b)$ is a non-dimensional geometry function of (a/b),

$$f\left(\frac{a}{b}\right) = \frac{\left(2+\frac{a}{b}\right)}{\left(1-\frac{a}{b}\right)^{3/2}}\left[0.886 + 4.64\left(\frac{a}{b}\right) - 13.32\left(\frac{a}{b}\right)^2 + 14.72\left(\frac{a}{b}\right)^3 - 5.6\left(\frac{a}{b}\right)^4\right] \tag{4.14}$$

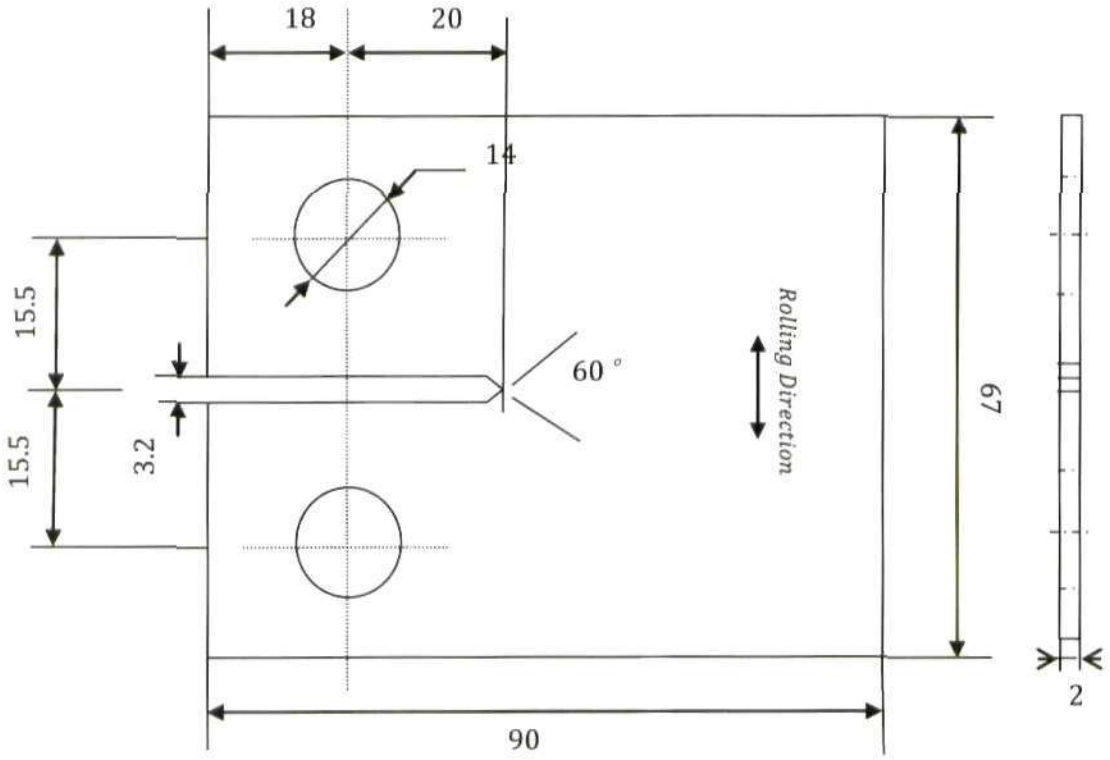

Figure 4.3 Geometry details of polycarbonate compact tension specimens or aluminium alloy 2043-T3 compact tension specimens in this study.

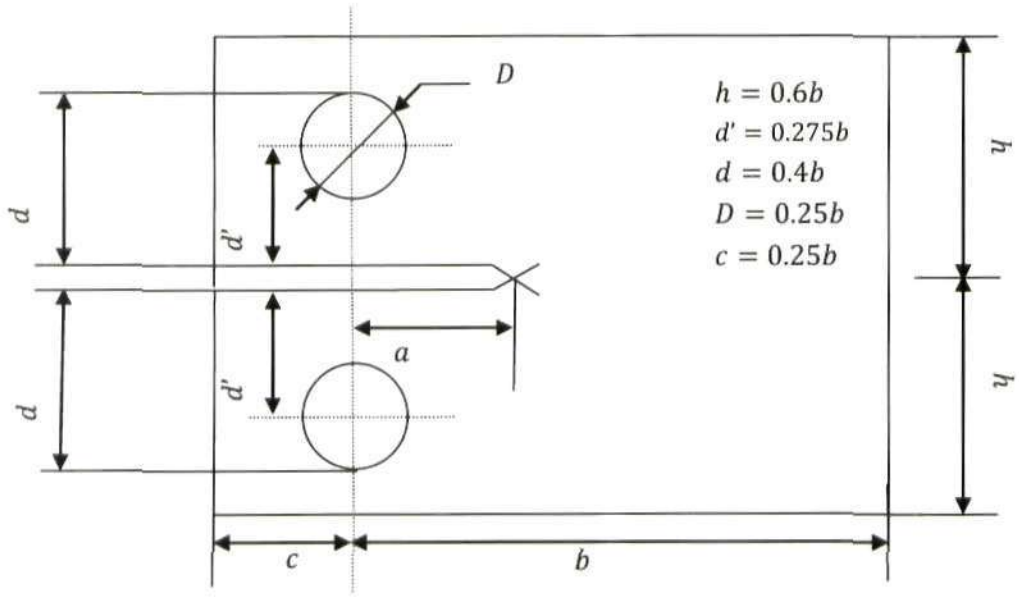

Figure 4.4 Standard geometry of compact tension specimen [195].

For the non-standard CT specimens used in current study, we have $h/b = 33.5/72 = 0.465$ and $/h = 20.9/33.5 = 0.624$, while for standard CT specimens, $h/b = 0.6$ and $d/h = 0.667$. The formula in equation (4.13) is therefore not applicable to evaluate the theoretical stress intensity factor K_I, and so the following more general formula is used [195] :

$$K_I = \frac{P}{tb^{1/2}} \cdot F\left(\frac{a}{b}, \frac{h}{b}, \frac{d}{h}\right) , \tag{4.15}$$

where,

$$F\left(\frac{a}{b}, \frac{h}{b}, \frac{d}{h}\right) = \frac{\left(2+\frac{a}{b}\right)}{\left(1-\frac{a}{b}\right)^{3/2}} \cdot 2 \cdot F_2\left(\frac{a}{b}, \frac{h}{b}, \frac{d}{h}\right),$$

and F_2 is a non-dimensional function of $(a/b, h/b, d/h)$, whose value can be estimated from Figure 4.5.

In particular, if the compact tension specimen is a standard CT specimen, Formula (4.15) is equivalent to (4.13), for

$$F_2\left(\frac{a}{b}, \frac{h}{b}, \frac{d}{h}\right) = 0.443 + 2.32\left(\frac{a}{b}\right) - 6.66\left(\frac{a}{b}\right)^2 + 7.36\left(\frac{a}{b}\right)^3 - 2.8\left(\frac{a}{b}\right)^4 , \tag{4.16}$$

and,

$$F\left(\frac{a}{b}, \frac{h}{b}, \frac{d}{h}\right) = \frac{\left(2+\frac{a}{b}\right)}{\left(1-\frac{a}{b}\right)^{3/2}} \cdot 2 \cdot F_2\left(\frac{a}{b}, \frac{h}{b}, \frac{d}{h}\right) = f\left(\frac{a}{b}\right) . \tag{4.17}$$

In current study, the formula in equation (4.15) was used to calculate the theoretical value of the stress intensity factor K_I for the compact tension specimens shown in Figure 4.3.

Comparison between the two formulae in evaluating the theoretical K_I at various crack lengths for the CT specimen configuration used in this study is presented in Table 4.1.

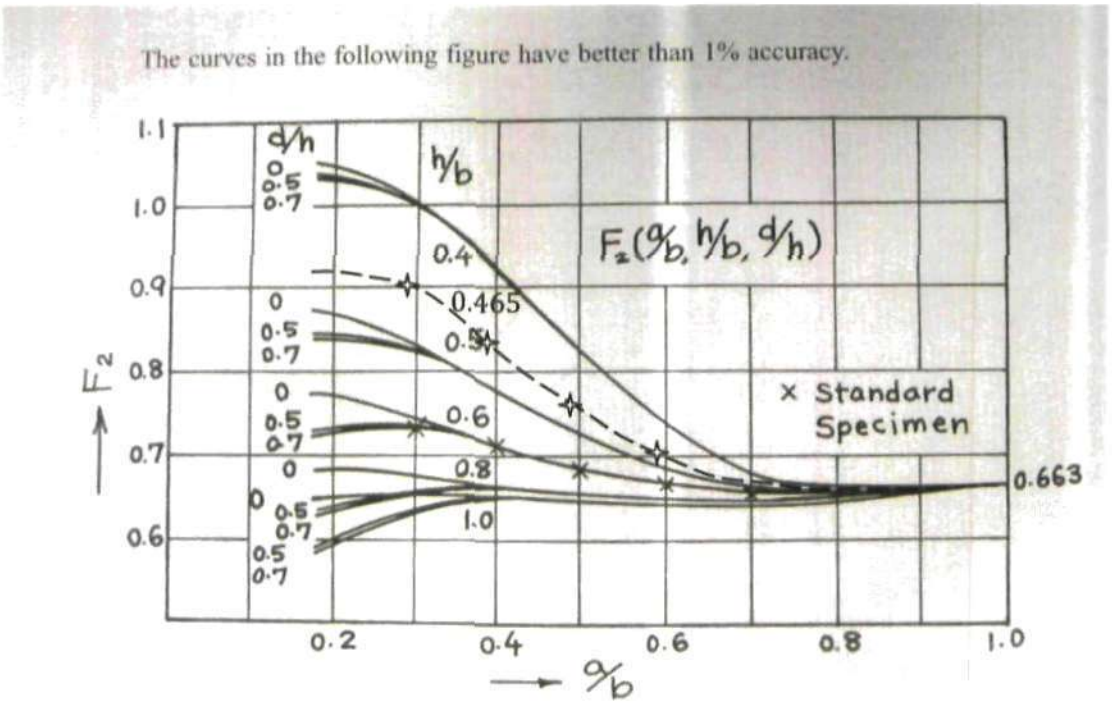

Note that: The dash line for h/b=0.465 was interpolated between the given curves for h/b=0.4 and h/b=0.5.

Figure 4.5 Numerical values of $F_2(a/b, h/b, d/h)$.

crack length a $[mm]$	$\frac{a}{b}$	K_I by Eq. (4.14) $[MPa.m^{0.5}]$	K_I by Eq. (4.16) $[MPa.m^{0.5}]$	Difference $[MPa.m^{0.5}]$	Relative %
24	0.333	1.369	1.643	0.274	20.0
26	0.361	1.471	1.743	0.272	18.5
28	0.389	1.581	1.853	0.272	17.2
30	0.417	1.702	1.975	0.273	16.0
32	0.444	1.836	2.112	0.276	15.0
35	0.486	2.071	2.350	0.279	13.5

Table 4.1 Comparison of the two formulae in equation (4.13) and equation (4.15) with $h/b = 0.465$, *and* $d/h = 0.624$.

4.3.3 Photoelasticity experiments

4.3.3.1 Material employed

For the photoelasticity experiments, compact tension specimens were cut from polycarbonate sheets (GE® Lexan or BAYER Makrolon®). Polycarbonate is a transparent polymer and can exhibit a birefringent character when loaded and observed through a polariscope. It also exhibits sufficient ductility to allow fatigue crack growth to be initiated and controlled [93]. Many researchers have reported that polycarbonate is an ideal model material in fatigue crack closure studies since crack closure effects can be clearly demonstrated in polycarbonate [16, 51, 63, 93, 191]. The physical and mechanical properties of polycarbonate sheets are listed in Table 4.2.

Physical		Mechanical		
Density	Poisson's ratio	Yield strength	Ultimate strength	Modulus of Elasticity
$1.2\ g/cm^3$	0.38	$60\ MPa$	$70\ MPa$	$2.3\ GPa$

Table 4.2 Typical property values of polycarbonate

4.3.3.2 Equipment for fatigue testing

In these experiments, the load frame is an Instron screw-driven uniaxial testing machine (Model 2519-104), with a load cell range from 0-500N. The equipment is controlled by a dedicated desktop computer, see Figure 4.6.

4.3.3.3 Experimental set-up

Figure 4.7 shows a photograph of the experimental setup. It consists of a fatigue load frame with a 500N load cell, a JVC CCD camera (Model KY-F1030) of the resolution $1360 \times 1024\ pixels$, a Pentax magnifying lens, and two

computers (one to control the Instron testing machine, and the other to store digital images recorded by the CCD camera).

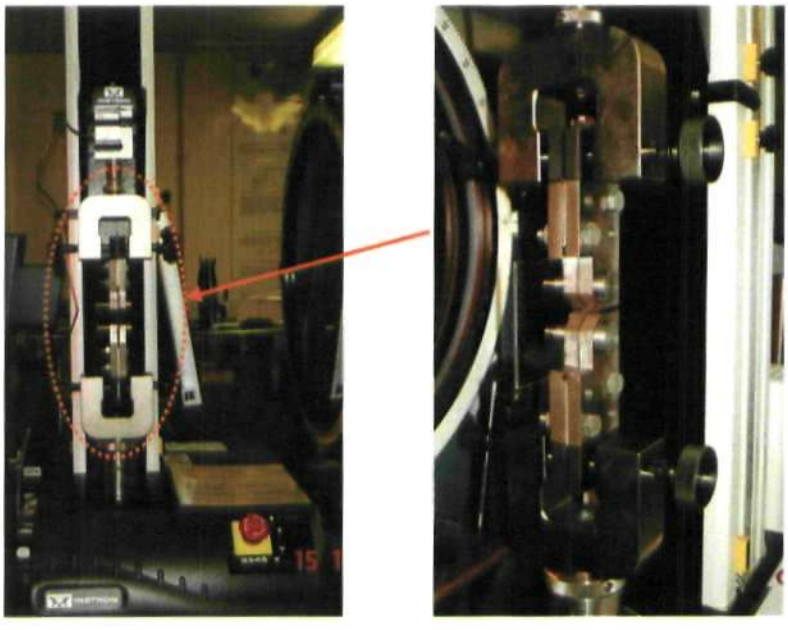

Figure 4.6 Fatigue testing machine employed for cyclic loading of the polycarbonate compact tension specimens.

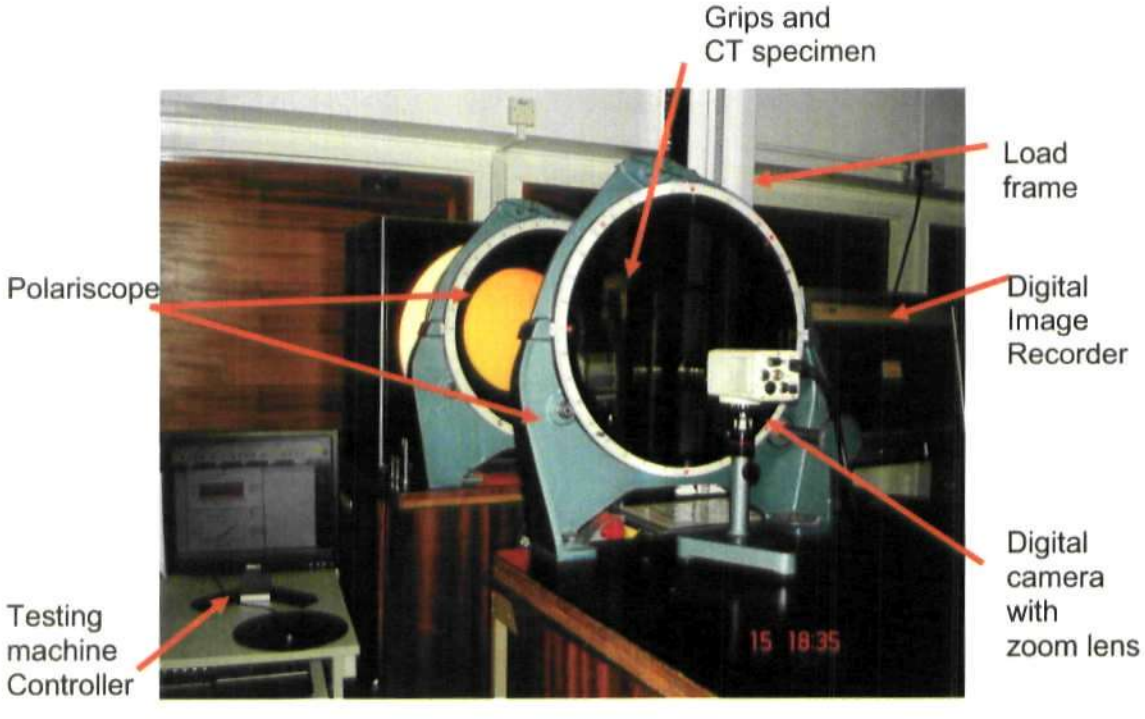

Figure 4.7 Photograph of the experimental setup.

4.3.3.4 Sample annealing procedure: Preparation for fatigue testing

Compact tension samples were machined from 2mm thick extruded polycarbonate sheet. Before subjected them to fatigue testing, the polycarbonate samples were annealed in order to remove residual birefringence which can otherwise be clearly observed in a polariscope, see Figure 4.8. This results from residual stresses induced by extrusion and machining process.

The annealing process consists of two steps: the first is to remove the moisture/bubbles contained in the material, and the second part of the cycle removes the residual birefringence [197].

1st cycle: To remove bubbles contained in the material:

- Raise temperature to 125 °C at 6°C/hour ≈ 17 hours
- Maintain temperature at 125°C for 48 hours = 48 hours
- Lower temperature to 40°C at 5°C/hour = 17 hours

Total time = 82 hours

2nd cycle: To remove the residual birefringence in polycarbonate samples:

- Raise temperature to 145 °C at 7°C/hour ≈ 17 hours
- Raise temperature to 155°C at 1°C/hour = 10 hours
- Maintain temperature at 155°C for 5 hours = 5 hours
- Lower temperature to 145°C at 1°C/hour = 10 hours
- Lower temperature to 40°C at 7°C/hour = 15 hours

Total time = 57 hours

It is worth mentioning that: (a) residual oil on the surfaces of polycarbonate samples should be removed where appropriate; (b) polycarbonate samples are

laid on a glass plate in the oven. To avoid additional residual stresses induced by samples sticking to the glass plate during the process of annealing (as shown in Figure 4.9), a piece of fibreglass paper can be inserted between them. After annealing, only those polycarbonate samples that still have flat surfaces and no obvious residual birefringence remaining were used in the fatigue tests.

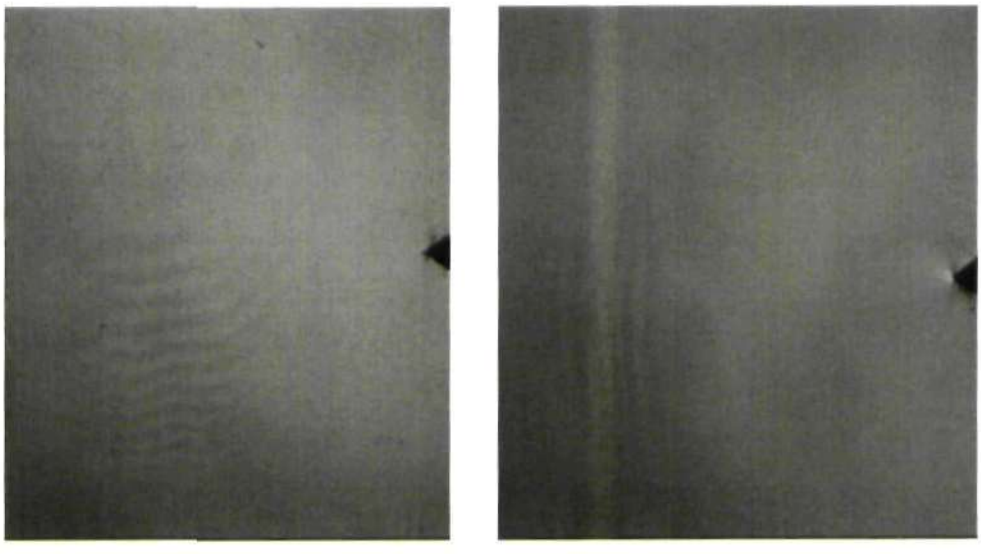

Figure 4.8 Residual birefringence in polycarbonate samples before annealing observed via the circular polariscope in dark-field arrangement.

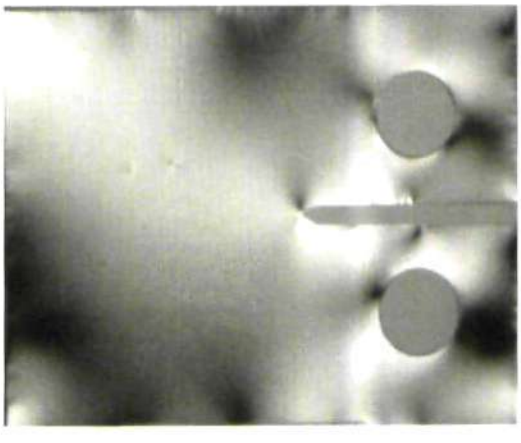

Figure 4.9 An annealed polycarbonate specimen observed in the circular polariscope (transmission): it shows unevenly distributed residual stresses induced by the specimen sticking to the support (glass plate) in the annealing process.

4.3.3.5 Fatigue testing procedure

The aim of the experimental programme is to ascertain the ability of the four-parameter model to predict fatigue crack growth through validating it against full-field photoelastic isochromatic data. This was done by investigating the effect of the load ratio $R = P_{min}/P_{max}$ on the closure behaviour, i.e. on the values of the new stress intensity factors, for polycarbonate compact tension specimens under constant amplitude loading with or without peak overloads. In order to select the appropriate loads to be used in the fatigue tests, five specimens were tested under different loading conditions. Following these tests, the maximum tensile load P_{max} was chosen to be $120\,N$, and kept constant in all the subsequent tests, leading to a steady increase in the value of opening mode stress intensity factor K_I as the fatigue cracks grew. Three different load ratios were chosen $R = 0.1$, $R = 0.3$, and $R = 0.5$. The choice of the minimum load ratio $R = 0.1$ took into account that there may be slack in the Instron load chain (grips/pins/specimens) and that the test machine is less accurate at lower load levels (close to zero). The load frequency in fatigue testing was not greater than $1HZ$ for all the specimens, aiming to allow fatigue cracks to undergo enough cycles to develop plasticity along the crack flank and around the crack tip. The rate of crack propagation for all the polycarbonate specimens was above $10^{-8}\,m/cycle$.

The present experimental programme consisted of two sets of tests. The first set was performed on unannealed polycarbonate specimens due to a failing to achieve usable annealed polycarbonate specimens in the early stage of the study. The second set of tests was performed on annealed polycarbonate specimens, as explained previously. Table 4.3 presents a list of the polycarbonate specimens used for fatigue testing.

Specimen reference	CA-loading [N]		Ratio R	20% Overload		Frequency [Hz]	Annealing	Material
	P_{max}	P_{min}		a [mm]	N			
PCCT-1	120	12	0.1	-		0.1	No	Bayer
PCCT-2	120	12	0.1	24.8	22000	0.5	No	Bayer
				27	24000			
PCCT-2*				29.3	26000			
				31.2	27500			
PCCT-3	120	60	0.5	25.4	359635	1.0	No	Bayer
				26.4	399635			
				29.3	466255			
PCCT-5	120	12	0.1	-		0.5	Yes	Lexan
PCCT-10	120	12	0.1	31.4		0.5	Yes	Lexan
PCCT-6	120	36	0.3	-		0.5	Yes	Lexan
PCCT-11	120	12	0.1	-		0.5	Yes	Lexan
PCCT-12	120	36	0.3	-		0.6	Yes	Lexan
PCCT-13	120	60	0.5	-		0.9	Yes	Lexan

Table 4.3 List of CT specimens in fatigue test and loading conditions

For the annealed polycarbonate specimens as listed in Table 4.2, the CT specimens were placed on the Instron screw-driven load frame, which was positioned inside a circular transmission polariscope, as illustrated in Figure 4.7. As the constant amplitude tension-tension cyclic loading was applied to the specimen, fatigue crack growth rate measurement was performed using the digital camera which took a sequence of images at each crack length. All the digital images were transferred to the computer by wire. When the fatigue crack grew to a suitable crack length after a number of fatigue cycles, the cyclic loading was paused, followed by the photoelasticity study in the following load cycle. A fatigue cycle was divided into several load steps, as illustrated in Figure 4.10. In the loading part, starting from P_{min}, the load P was increased by an increment of $6\,N$ step by step, and was held for 60 seconds after each

increment. Once the load P reached the maximum value, it was then reduced by $6N$ step by step until the load value of P_{min} was again reached.

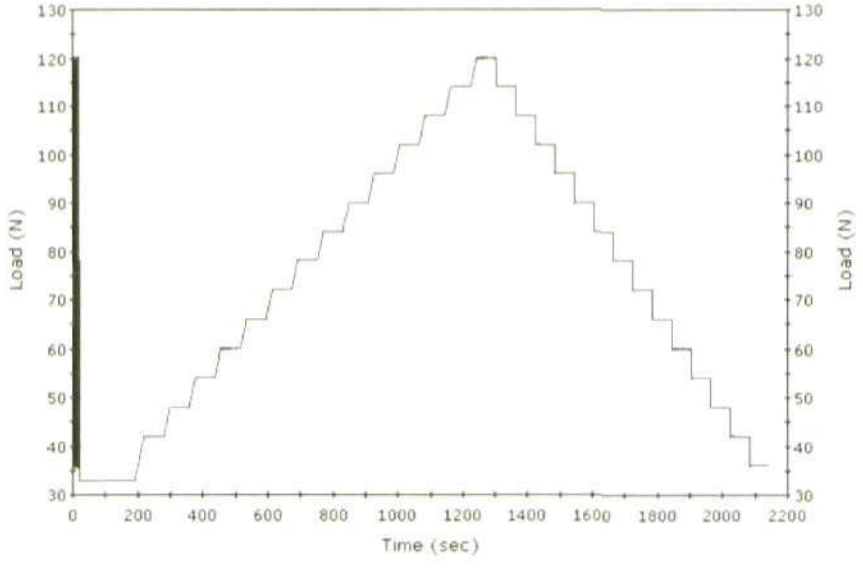

Figure 4.10 Scheme of one load cycle divided into 29 steps ($P_{max} = 120\ N$, load ratio $R = 0.3$), in each of these steps, six images of photoelastic fringe patterns were collected.

In each load step, photoelastic fringe patterns were recorded with the JVC digital camera and the Pentax magnifying lens using the six-step phase-shifting method developed by Patterson and Wang [198]. The arrangement of the circular polariscope and details of this method are shown in Figure 4.11 and Table 4.4. In this method, the light intensity maps are related to the relative retardation α and the isoclinic angle θ. The method requires six images, each obtained under different angular orientations of the analyser and the output quarter-wave plate.

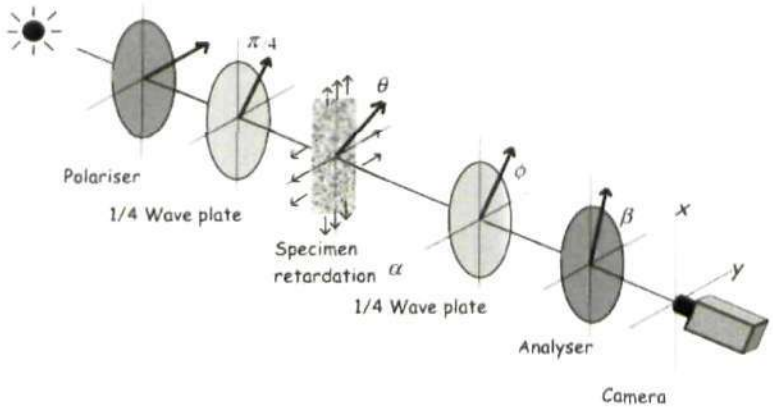

Figure 4.11 Schematic diagram of a circular polariscope (transmission with right circularly polarised light input) showing the angular orientations of the elements. The fast axis of the polariser is taken as the reference axis [199].

Image reference	φ	β	Light intensity
i_1	0	$\pi/4$	$i_m + i_v cos\alpha$
i_2	0	$-\pi/4$	$i_m - i_v cos\alpha$
i_3	0	0	$i_m - i_v sin\alpha \cdot sin2\theta$
i_4	$\pi/4$	$\pi/4$	$i_m + i_v sin\alpha \cdot cos2\theta$
i_5	$\pi/2$	$\pi/2$	$i_m + i_v sin\alpha \cdot sin2\theta$
i_6	$3\pi/4$	$3\pi/4$	$i_m - i_v sin\alpha \cdot cos2\theta$

Table 4.4 Six-step scheme of digital transmission photoelasticity [198]

In Table 4.4,i_m is the stray light term for transmission polariscope; i_v is the light intensity observed when all optical axes in a transmission polariscope are parallel; α is the phase difference, or relative retardation; β is the angle between the fast axis of the analyser and the reference axis; φ is the angle between the fast axis of output quarter wave-plate and reference axis; $\theta$is the isoclinic angle: angle of fast axis of specimen to reference axis.

A typical set of six-step phase-shifted images for an annealed polycarbonate specimen are shown in Figure 4.12.

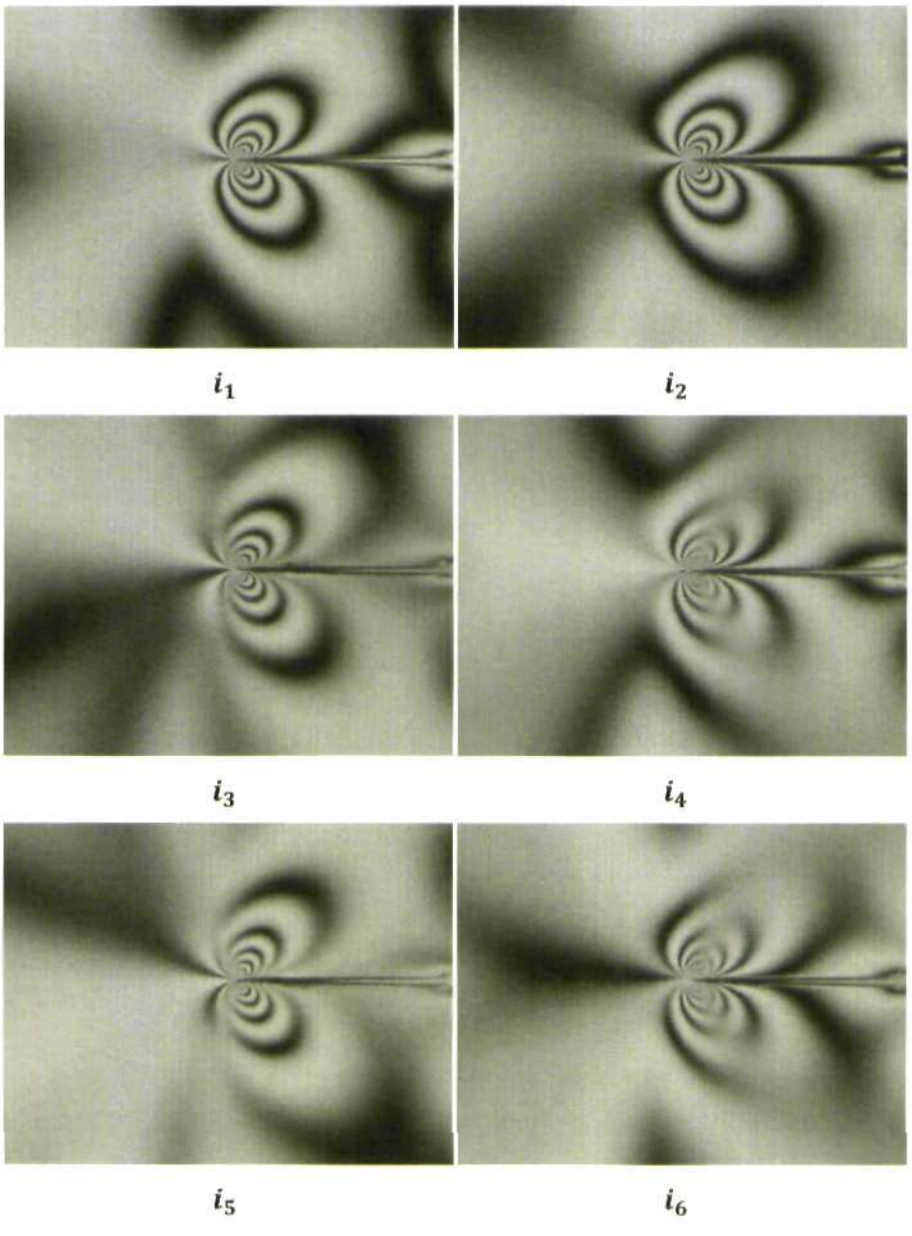

Figure 4.12 Six-stepped photoelastic fringe patterns recorded in PCCT-5 (annealed CT specimen) with the fatigue crack length $a = 35.0\,mm$. (Loading condition: $P_{max} = 120\,N$, $R = 0.1$, Frequency = $0.5\,Hz$).

After all six steps of the photoelastic data in the cycle were recorded, the specimen was subjected to further fatigue cycling. The length of the fatigue crack and the crack growth rate were then measured again. After a further number of fatigue cycles, the fatigue test was interrupted and photoelastic fringe patterns were recorded once again. This procedure was repeated several times before the end of the test.

To analyse the data, the program RICO (Regularisation Isochromatic phase map computation) developed by Siegmann et al [200] in 2008 was employed to obtain an unambiguous distribution of the unwrapped relative retardation α and the map of unambiguous isochromatic fringe order N for each set of six step phase-shifted images during one load step, which were then fitted to the four-parameter mathematical model [51].

For non-annealed polycarbonate specimens, i.e. PCCT-1, PCCT-2, and PCCT-3, the fatigue cracks grew in these specimens also under constant load amplitude ($P_{min} = 108\,N$ for PCCT-1 and PCCT-2, $P_{min} = 60\,N$ for PCCT-3) with maximum tension load $P_{max} = 120\,N$. The load ratio R was 0.1 for PCCT-1 and PCCT-2, 0.5 for PCCT-3. The loading frequency was $0.1\,HZ$, $0.5\,HZ$, $1.0\,HZ$ for PCCT-1, PCCT-2 and PCCT-3 respectively. In one fatigue test, after the polycarbonate specimen underwent a number of fatigue cycles and the fatigue crack grew to a crack length of interest, the cyclic loading was paused and the specimen was removed from the testing machine. Thus an underload was introduced by removing the specimen from the load frame. The length of the fatigue crack was measured using an optical microscope (Olympus BX60M, Soft Imaging System) and a confocal laser scanning microscope. This method of measuring accurate crack length will be described in detail in section 4.3.3.6. After the measurement of crack length, the specimen was returned to the testing frame and subjected to one specified load cycle, which was divided into several load steps. During the load cycle, the opening mode stress intensity factor K_I was increased in an increment, $0.1\,MPa.m^{1/2}$ by each step. After each increment, the load was held for 80 seconds while a computer recorded the photoelastic fringe patterns, as seen through a CCD camera (Panasonic WV-BP100) with the Pentax magnifying lens. Once the stress intensity factor K_I

reached the maximum value according to the maximum load P_{max} and the current crack length a, it was then reduced by the same steps. After the fringe patterns in the cycle had been recorded, the specimen was subjected to the fatigue cycle again for about 2000 cycles, equivalent to a crack increment of some $0.9\sim1.8\,mm$. The cyclic loading was then again paused, the specimen was removed from the testing machine, the length of the fatigue crack was measured and photoelastic data was collected during the applied load cycle. This procedure was repeated several times until the crack length grew to around $33\,mm$. Next, the program CoPA developed by Siegmann and Patterson [201] in 2004 was employed to obtain unambiguous isochromatic fringe data for each set of six step phase-shifted images, which were then fitted to the four-parameter mathematical model [51].

The algorithm used in RICO is more robust than that in CoPA, which allows the relative retardation to be obtained directly from the isochromatic map without demodulating the isoclinic angle in advance, for detailed information please refer to reference [200]. This technique avoided the ambiguity problems arising from the unclear definition of the isoclinic angle related to the direction of one of the principal stresses and problems induced by the isoclinic-isochromatic interactions in complex photoelastic models that exist in the generation of unambiguous distributions of isochromatic and isoclinic data when using CoPA to process photoelastic images.

A typical set of six-step phase-shifted images for an unannealed polycarbonate specimen are shown in Figure 4.13.

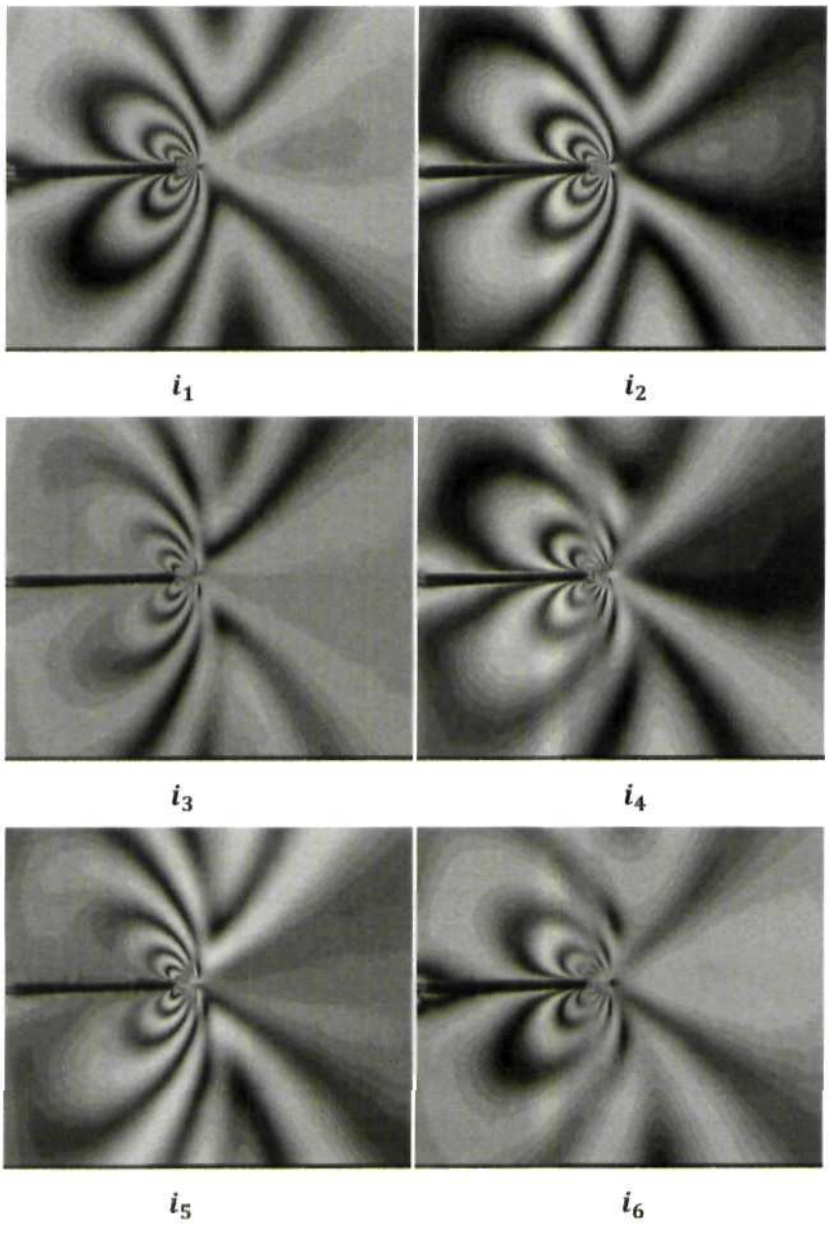

Figure 4.13 Six-stepped photoelastic fringe patterns recorded on PCCT-1 (unannealed CT specimen) with the fatigue crack length $a = 32.44\,mm$. (Loading condition: $P_{max} = 120\,N$, $R = 0.1$, Frequency = $0.1\,Hz$)

It should be mentioned again that the first set of three polycarbonate specimens, PCCT-1, PCCT-2, and PCCT-3 were tested in the year of 2008 *without undergoing the annealing process because of difficulties encountered in* obtaining usable annealed polycarbonate specimens at that time. In those experiments the photoelastic fringe patterns were recorded with a monochromatic CCD camera (Panasonic WV-BP100 with a resolution of $704 \times 576\ pixels$) and a Pentax magnifying lens ($12.5 \sim 75\ mm$), and the CoPA program developed by Siegmann and Patterson [201] in 2004 was employed to obtain unambiguous unwrapped isochromatic fringe data for the specimens with the exception of PCCT-3 for which experimental photoelastic data was processed with the RICO software. The second batch of specimens, however, were subjected to annealing cycles prior to fatigue loading, and photoelastic data was collected by a JVC digital camera of the Model KY-F1030 (Resolution: $1360 \times 1024\ pixels$) with a Pentax magnifying lens, and fringe patterns for the second batch of specimens were processed by using the newly-developed program 'RICO' by Siegmann et al [200] in 2008.

The interfaces for the program CoPA and RICO are shown in Figure 4.14 and Figure 4.15 respectively.

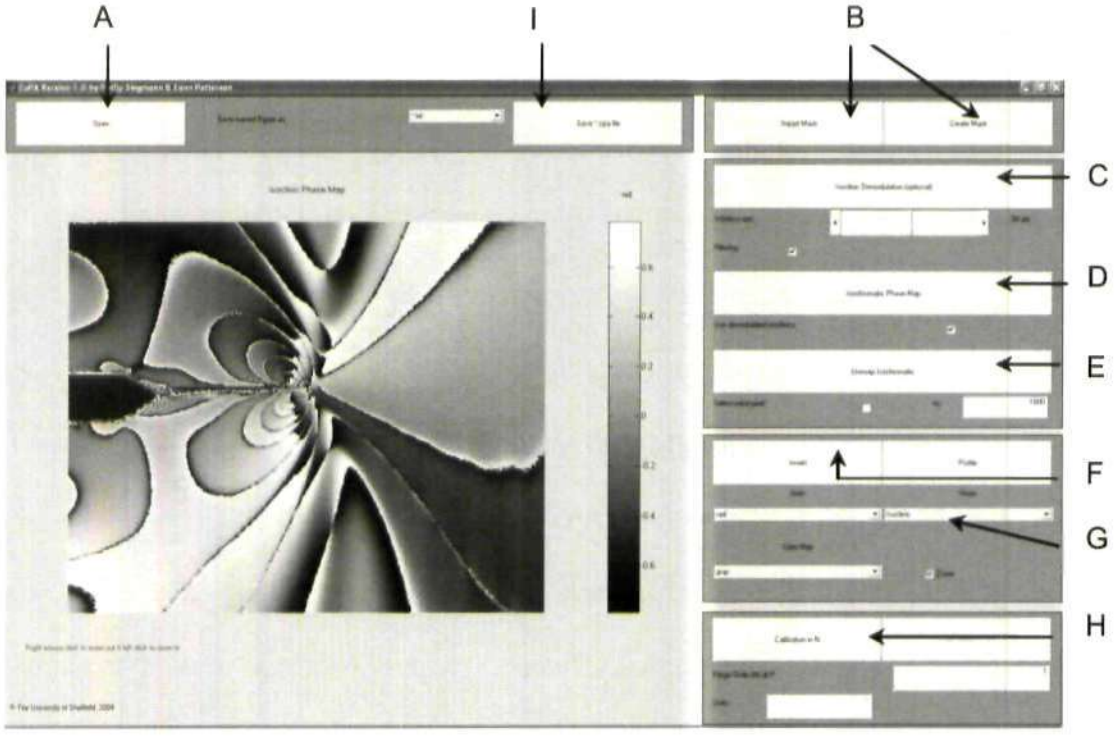

Figure 4.14 Graphical user interface window for the program CoPA.

A: Open a '.six' file

B: Import a '. bng' mask created in CatchSix or create a mask

C: Demodulate isoclinic data

D: Create relative retardation map

E: Unwrap fringe order

F: Invert fringe order map if necessary

G: Select data in figure

H: Calibrate fringe order

I: save data as a '.txt' file

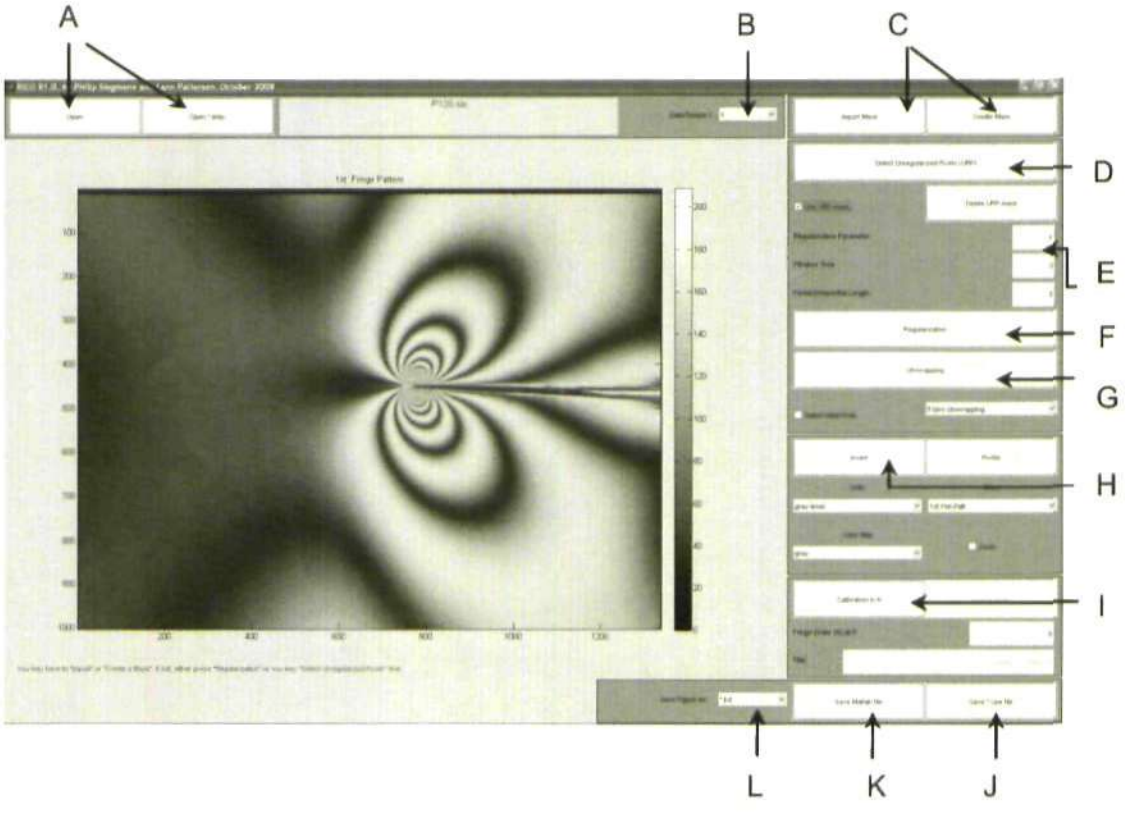

Figure 4.15 The MATLAB Graphical user interface (GUI) for the RICO program.

A: Open a '.six' file or six '.bmp' images, or '.cpa' file created by RICO

B: Data resize to reduce the resolution of the data to reduce the processing time

C: Import a '. bng' mask created in CatchSix or create a mask

D: Create a URP mask by selecting unregularised pixels

E: Set the three parameters used for the regularisation process

F: Regularize

G: Unwrap

H: Invert data map if necessary

I: Calibrate fringe order

J: Save data as a '.cpa' file

K: Save MATLAB file

L: Save data in '.txt' ,'.eps', '.tif', or '.jpg'

Another program 'CatchSix' was used to capture the six-step phase-shifted images and package them in a '.six' file, which can then be read into the CoPA program or RICO program. The graphical interface is shown in Figure 4.16.

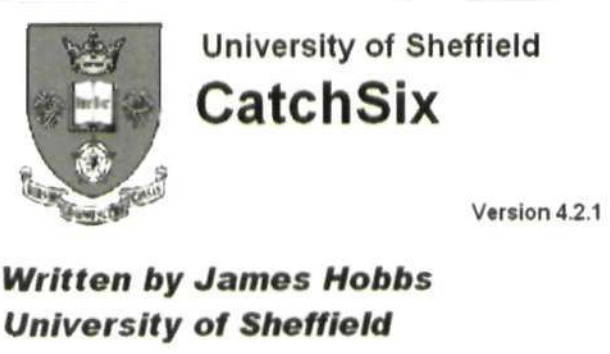

(a)

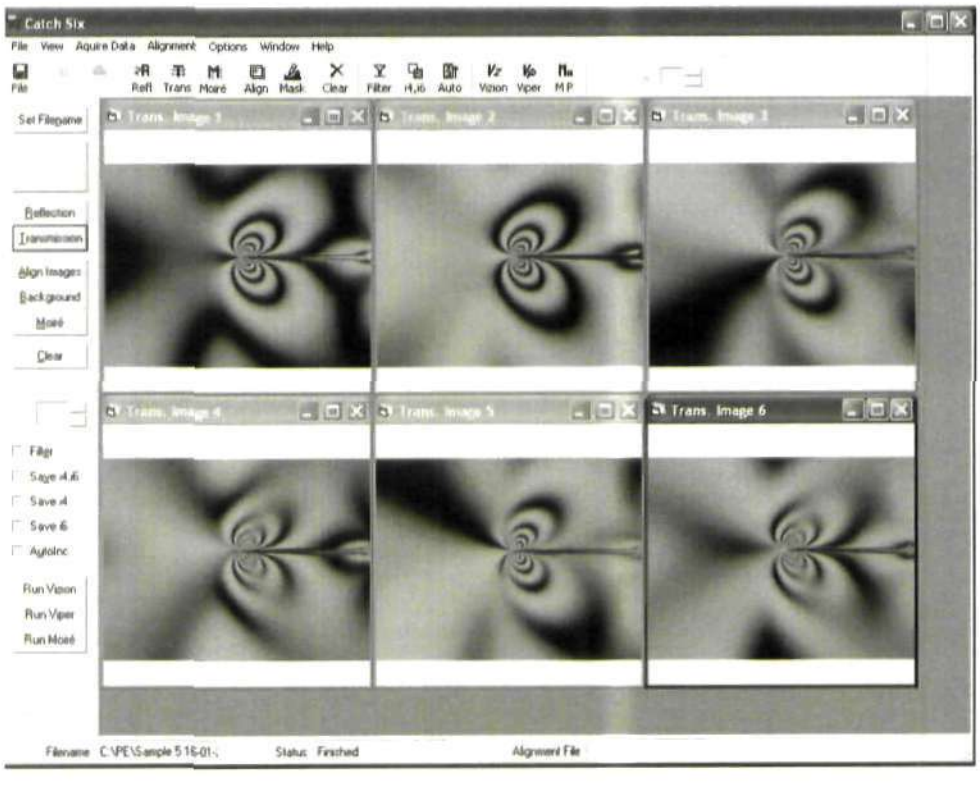

(b)

Figure 4.16 CatchSix (a) Front window (b) Graphical user interface for the CatchSix program.

A schematic description of the experimental program is shown in the flow chart presented in Figure 4.17.

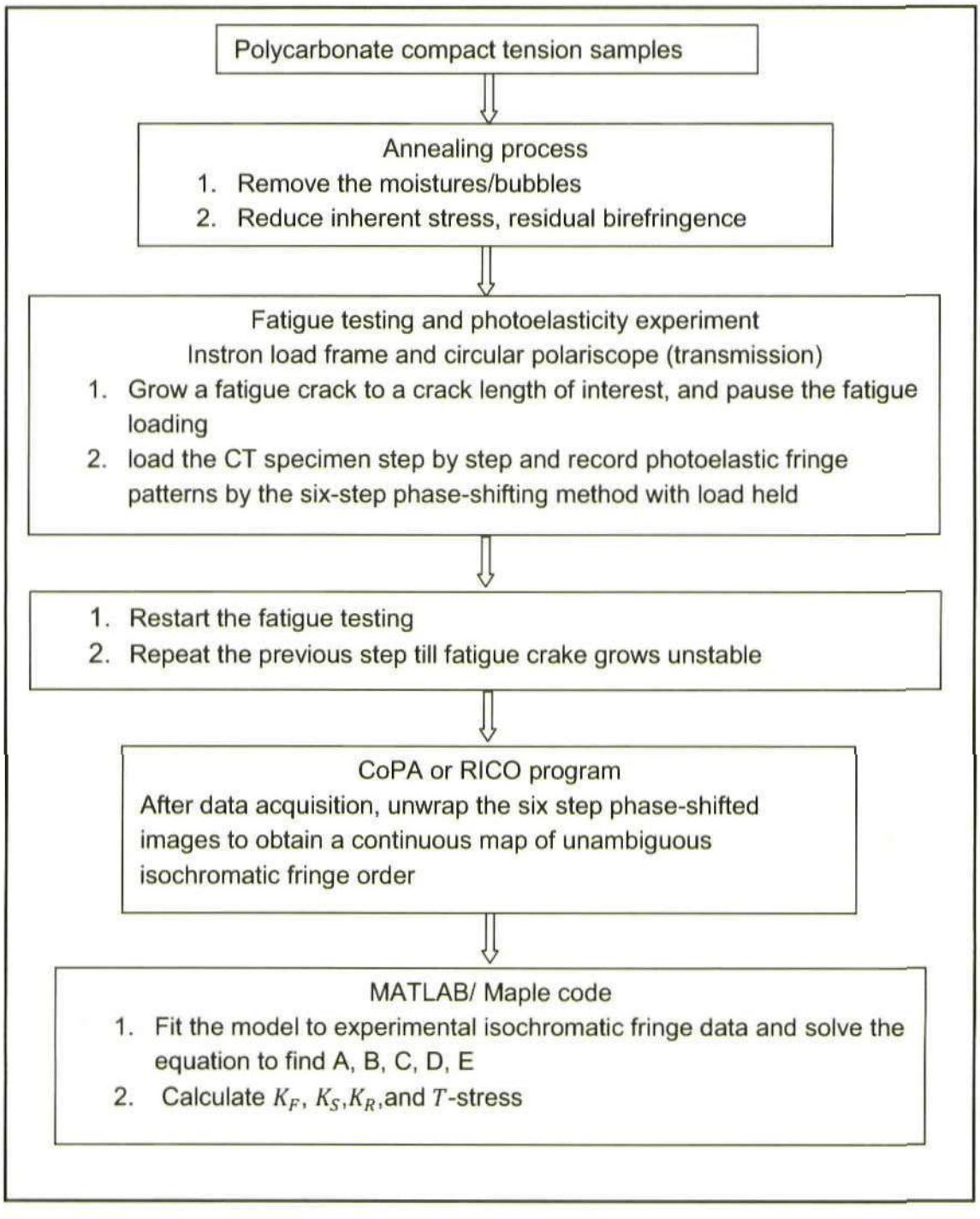

Figure 4.17 Flow chart describing the photoelasticity experimental programme.

4.3.3.6 Crack length measurement

Accurate crack length measurement is important for theoretical K calculation. *Crack length can be measured directly from photoelastic images taken under* the maximum applied load where fatigue cracks are thought to be fully open. However, those photoelastic images cannot provide enough precision for crack length measurement due to the low resolution camera used in this study. It is certainly hard to identify the crack tip only from those photoelastic images, see Figure 4.18 (a). Apparently, it can be seen from Figure 4.18 (a) that the fracture process zone and the plastic zone ahead of the crack tip are large, showing that identifying the crack tip is not an easy task. Moreover, fringes in these zones are disordered which complicates the task. Furthermore, even if the photoelastic images are not to be used for crack length measurement, the location (coordinates) of the crack tip on these photoelastic images is still required when fitting the mathematical model to the isochromatic fringe data. Therefore, prior to crack length measurement, it is necessary to study and find out how to locate the crack tip accurately. It seems that this problem, in part, relates to the way the polycarbonate crazes and fatigue cracks develop, with the craze running in a zone ahead of the crack, and the crack then either running on one side of the craze or the other, or going through the middle, as shown in Figure 4.18 (b). Therefore, the crack front shape/curvature can provide some important information for the identification of the crack tip position, which might let one find an average position through the specimen thickness. Optical microscopy, confocal laser scanning microscopy (CLSM) and scanning electron microscopy (SEM) were used to assist in crack front shape and crack tip identification.

(a)

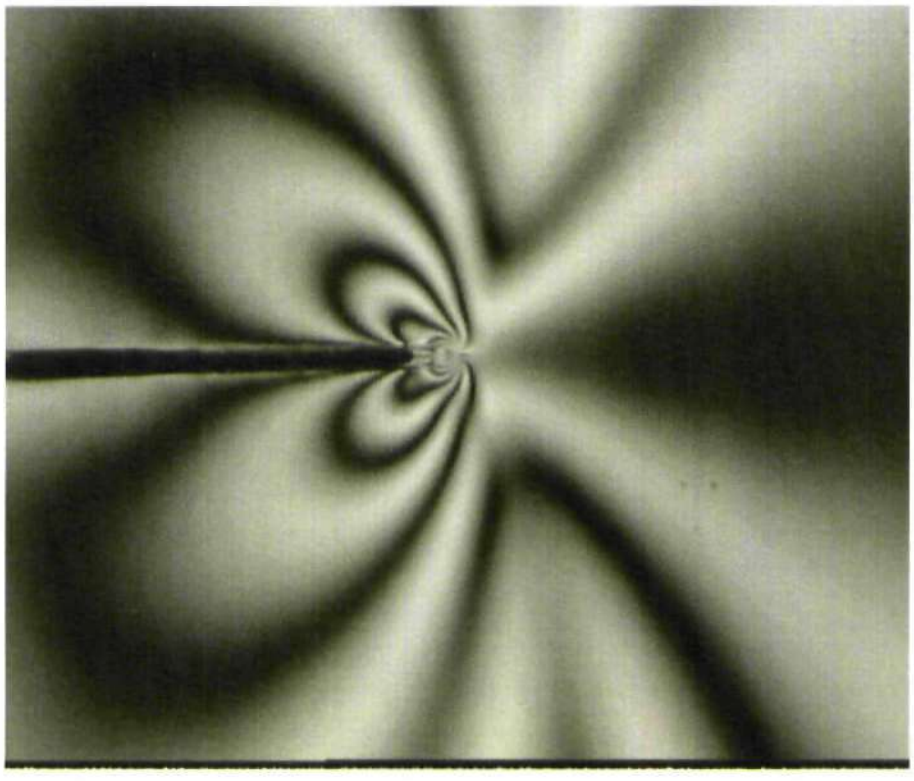

(b)

Figure 4.18 (a) A photoelastic image of the specimen PCCT-1 recorded in dark-field circularly polarised light; (b) An image focusing on the fatigue crack tip in PCCT-1 taken by the Soft Imaging System (Olympus BX60M), with the fatigue crack length a of $32.44\ mm$. (PCCT-1 : $P_{max} = 120\ N$, load ratio $R = 0.1$, frequency = $0.1\ Hz$)

In the current study, this problem was resolved through the following test: grow a fatigue crack in a CT specimen with the maximum load $120\ N$ and load ratio 0.1. After every $2\ mm$ of growth, a single 20% peak overload spike was applied to the specimen. Each time this spike overload is applied, the specimen was removed from the test machine and optical and laser scanning microscopy

images of the crack tip were taken. This enabled a direct comparison of the actual surface crack extension with the indication from an optical photograph. The marks of overloads on the specimen were shown clearly when observed through circular polariscope and confocal laser scanning microscope, see Figures 4.19-4.21. Once the crack was around $34\ mm$ long, the specimen was pulled apart. Typical CLSM images of the fracture surface are given in Figures 4.23-4.25. Then the crack tip position could be measured at seven points through the thickness and an average crack length was obtained. This relationship between crack front shape and crack length was applied to all subsequent specimens as the crack front shape remains fairly constant. This method hence helps to identify the crack front from photoelastic images.

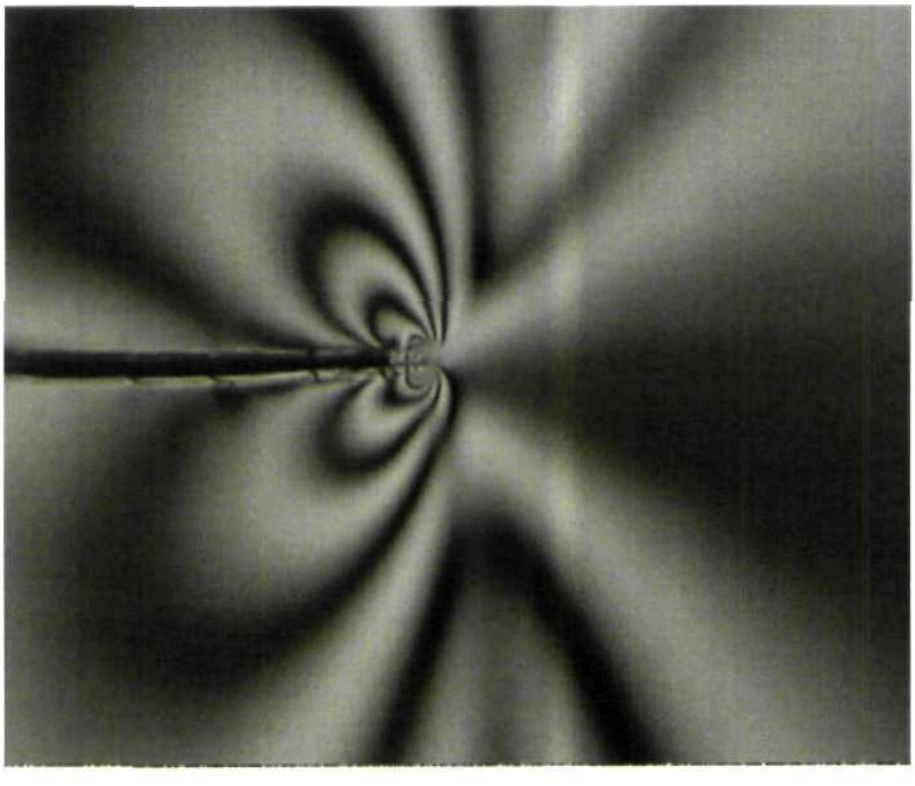

Figure 4.19 An optical image of fringe pattern on PCCT-2* in dark-field circularly polarised light. (PCCT-2*: $P_{max} = 120\ N$, load ratio $R = 0.1$, frequency = $0.5\ Hz$)

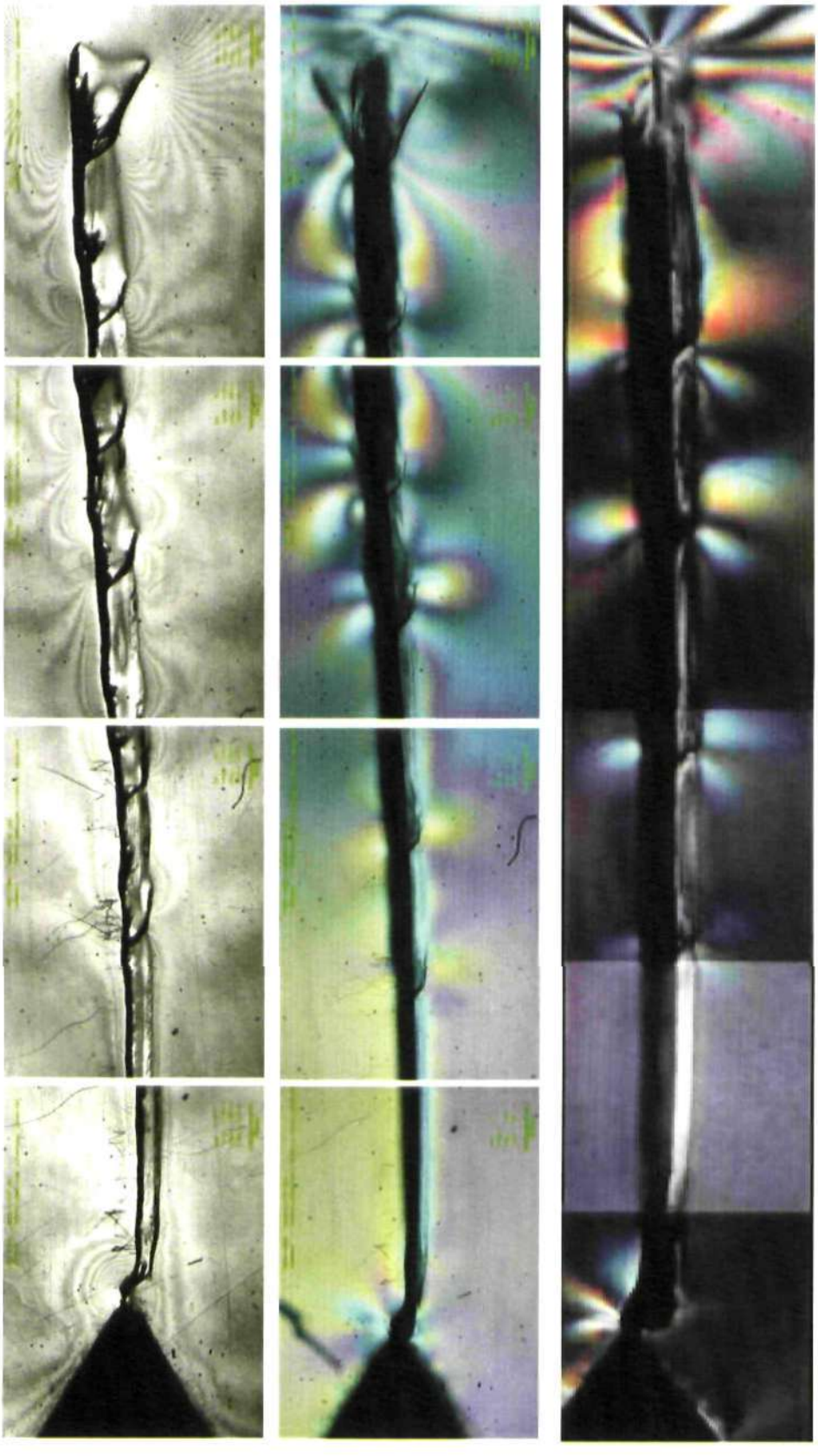

Figure 4.20 Images for a crack with length a of $33.2\ mm$ in the specimen PCCT-2* obtained using confocal laser scanning microscope (Left) Density images, (Middle) Colour images; (Right) in an optical microscope.

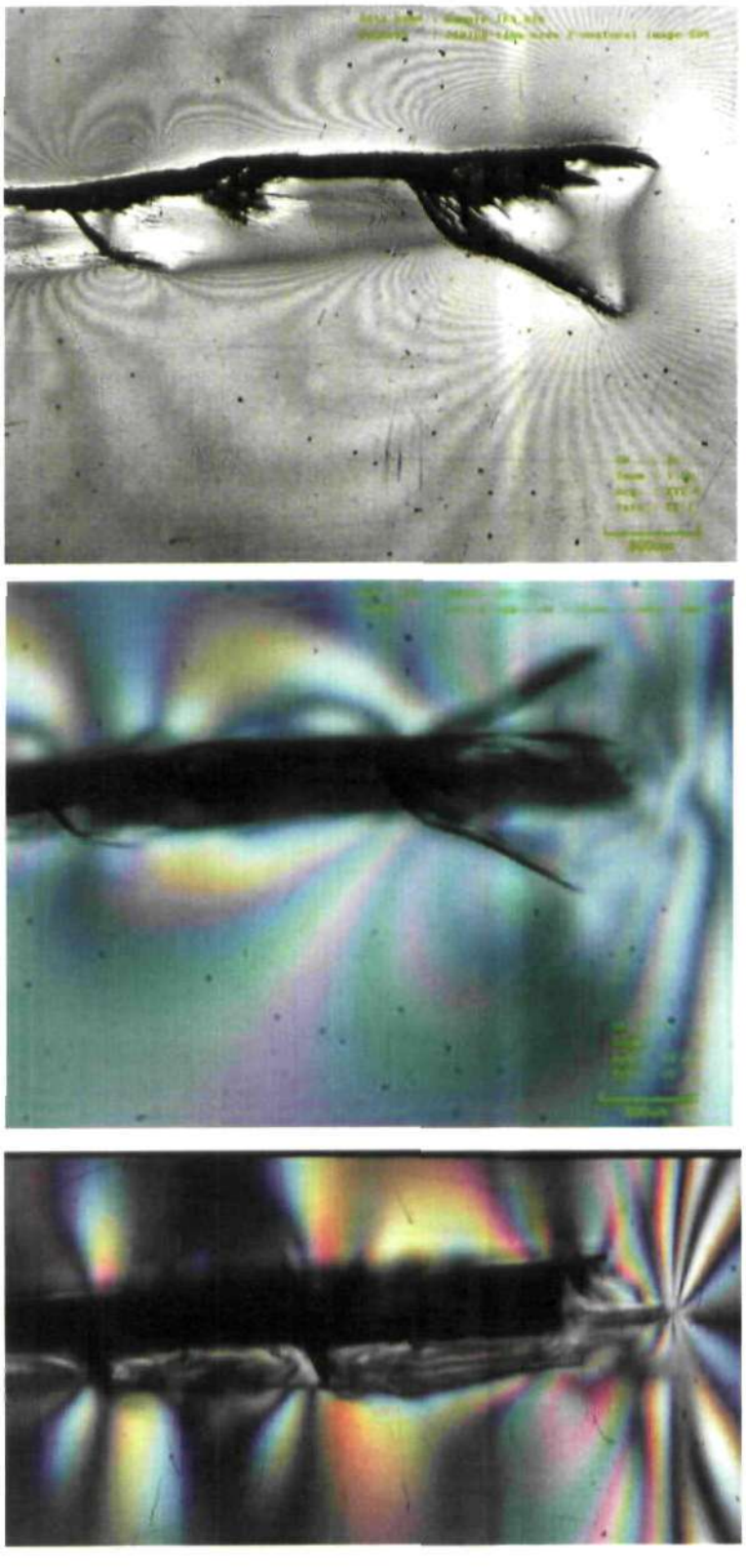

Figure 4.21 A close-up view around the tip of a crack with a length of $33.2\,mm$ in the specimen PCCT-2* using confocal laser scanning microscope (Top and Middle) and in an optical microscope (Bottom).

Figures 4.19-4.21 shows typical optical micrographs of the fatigue crack in the specimen PCCT-2* taken using CLSM. As can be seen, a zone of damaged material surrounds the crack and there are transformed bands along the crack flanks. These images enable us to identify and measure the width of transformed material/craze width (equal to plastic zone) as a function of the increase in crack length (Figure 4.22) and provide help for valid data selection from photoelastic fringe data. This will be discussed in more detail in the next chapter.

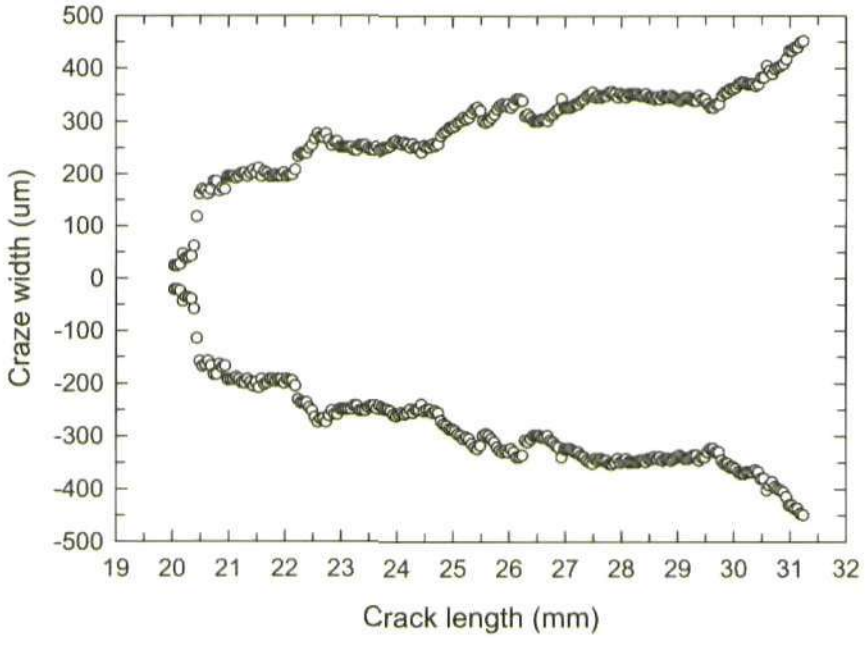

Figure 4.22 Increasing extent of transformed material (craze width) with the crack length ('+' and '-' width value just means different side).

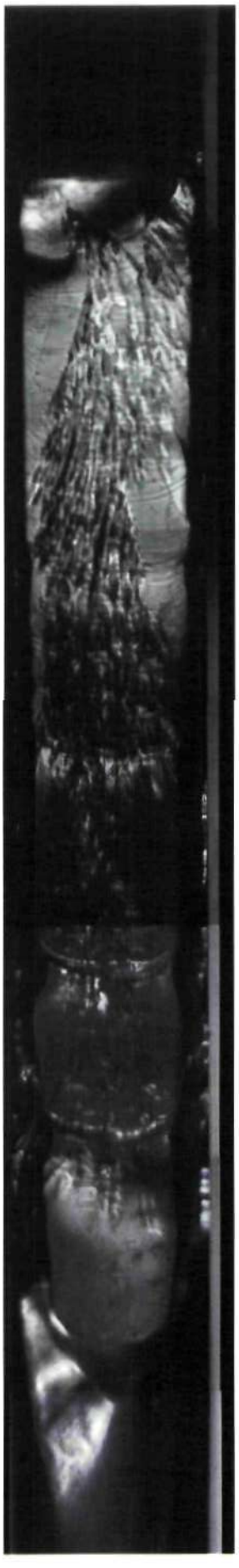

Figure 4.23 A view of f the fracture surface of the specimen PCCT-2* using Confocal Laser Scanning Microscopy (CLSM).

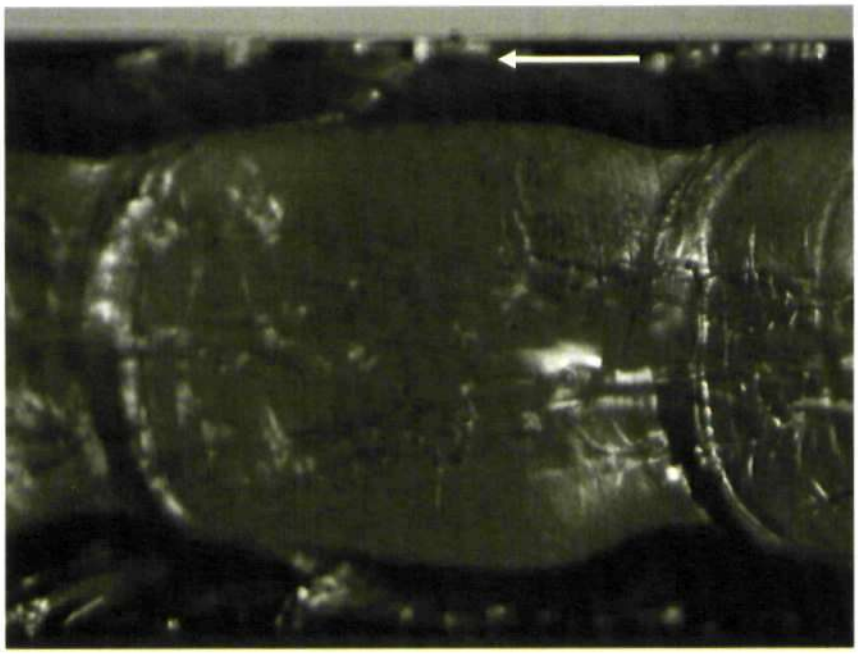

Figure 4.24 A typical view of beach marks on the fracture surface of the specimen PCCT-2* in confocal laser scanning microscope at high magnification. The horizontal arrow indicates the direction of crack propagation.

(a)

(b)

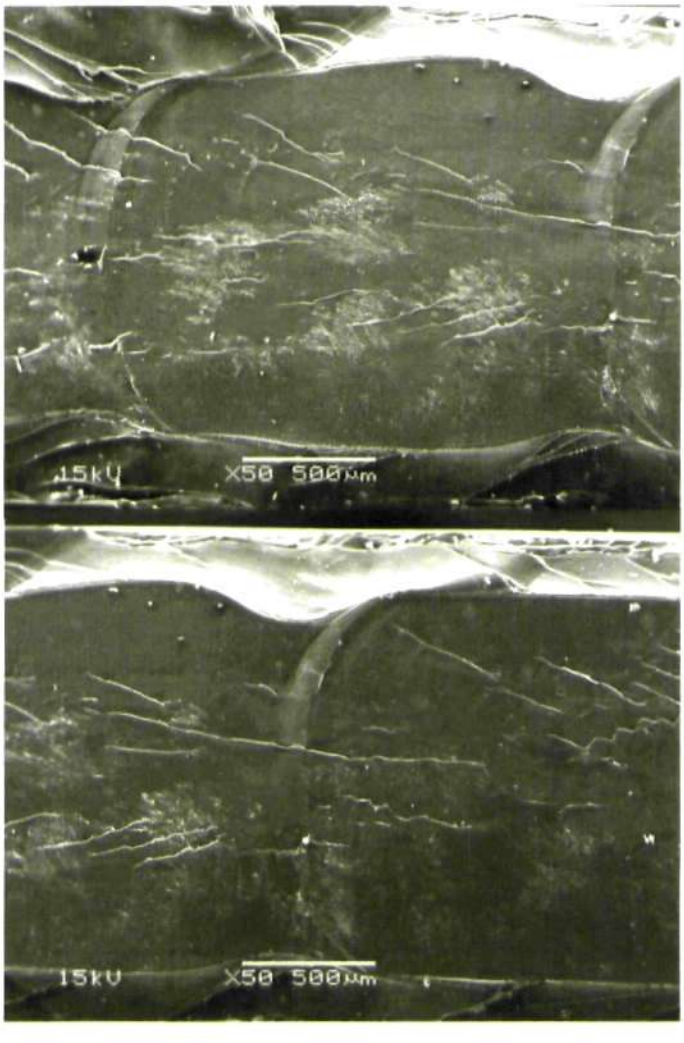

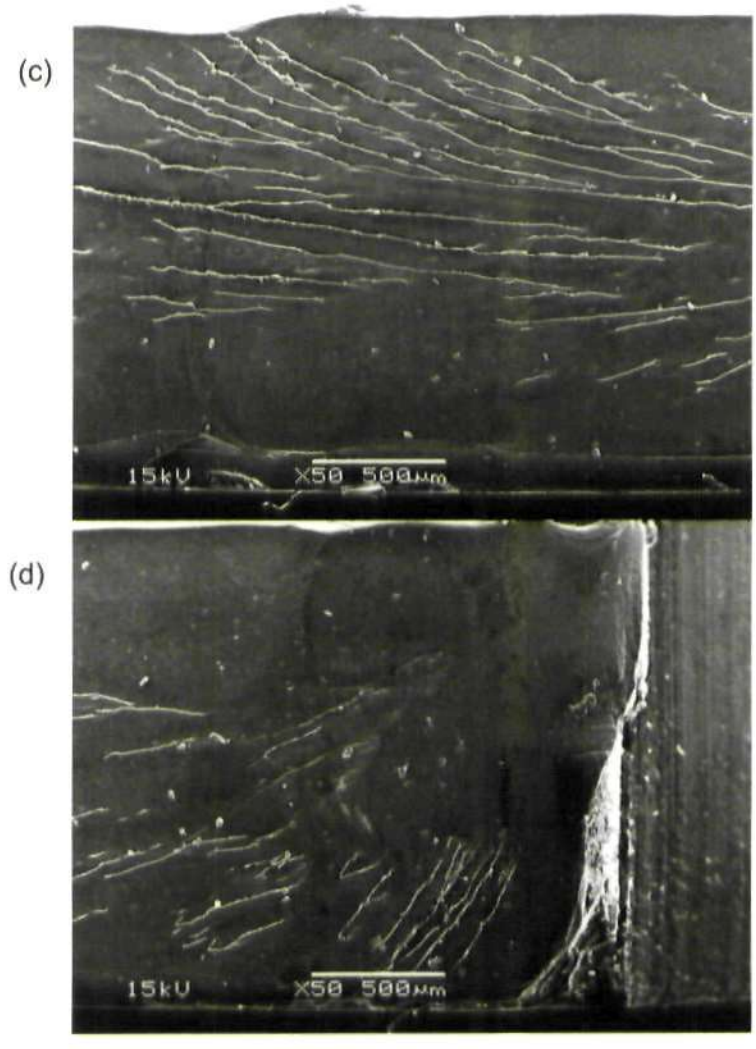

Figure 4.25 (a-d) Scanning electron micrographs of the fracture surface of PCCT-2*.

Figures 4.23-4.25 show micrographs of the fracture surface of the specimen PCCT-2*. The fracture surface is rather rough similar to the observations in the literature, indicating the discontinuous nature of fracture process. Filaments can be observed at short crack length (Figure 4.25). These images clearly show beach marks which indicate the crack front position each time an overload spike was applied. The crack front shape varies considerably through the specimen thickness. In the middle of the specimen thickness, the crack front shape seems like a parabolic curve; while near the specimen surface area, it appears that material in this region has undergone necking.

Typical fractographs of the curved part of the crack tip front and edges near the specimen surface are shown at higher magnifications in Figure 4.26 and 4.27. The boundary between the middle plane area and near-surface regions is sharp and well defined (Figure 4.26). Higher magnifications clearly reveal the characteristics of the craze-dominated fracture process (Figure 4.27). Non-flat fracture surface topography at a micro-level is also noticeable, indicating various inhomogeneities of the material structure and mismatch (imperfect fit) between the mating fracture surfaces at discrete locations where crack closure would occur. In the present experimental study, all the specimens are manufactured with a thickness of $2\,mm$ and are assumed to undergo plane stress deformation. It seems that this assumption does not hold true, from the direct comparison between the middle region and near-surface region on the fracture surface. The crack front shape formed after the application of an overload apparently indicates that crack grows faster in the middle plate (plane strain) than the region near surface (plane stress). It is in agreement with the conclusions found in the literature [144, 179] that the middle plane which tends more towards plane strain deformation experience a higher tensile stress because of the higher effective yield strength, and has a lower fracture toughness and higher crack growth rate than near-surface regions. Moreover, a larger plastic zone near the surface implies that more crack closure happens in near-surface regions. It is therefore obvious that an overload gives an instantaneous crack extension in the original crack growth direction in the middle plane. Nevertheless, 'necking' happens in the region near the surface, indicating that an overload makes more material introduced into the near-surface region undergoing plane stress deformation. In the plane stress condition, the plastic zone size is larger than in the plane strain condition. So, regions with a larger plastic zone after the applied overload have higher values

of residual strain than central regions and this is a major cause of the constraint/compatibility-induced shielding phenomenon. Crack growth rates slow down to a minimum value over a crack growth increment of about half the forward plastic zone size left by the overload. This reflects the larger crack tip plastic regions compared with the previous crack growth state which cause higher crack closure levels and reductions in effective crack driving force. This phenomenon is termed 'delayed retardation'. Finally, the crack accelerates to a stabilized value which is approximately equal to the pre-overload crack growth rate, as the crack advances to near the boundary of the overload plastic zone. Figure 4.23 also indicates that deeper 'necking' happens during post-overload, and then gradually disappears as the crack growth rate returns to normal. Moreover, as the crack length increases, 'necking' becomes deeper following overloads, and the width of the curved middle crack front region decreases and becomes narrower, see Table 4.5.

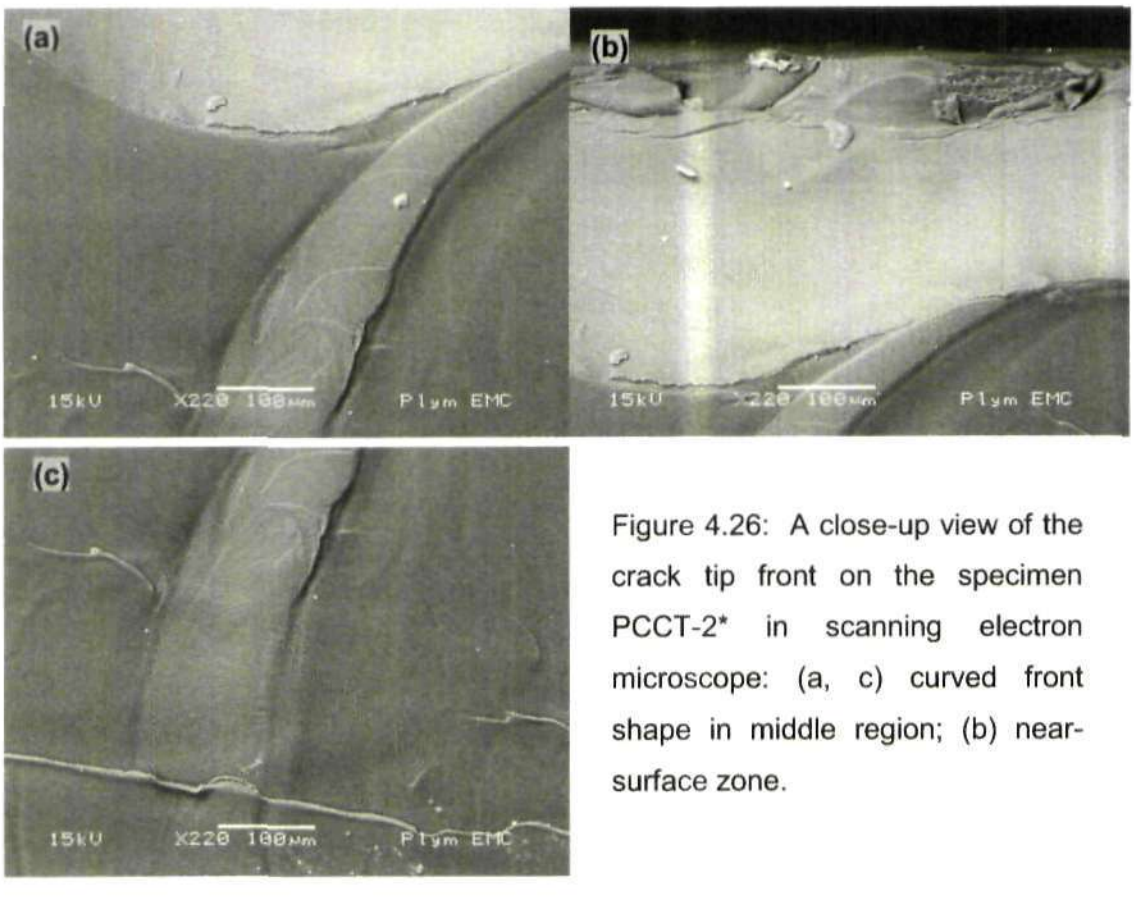

Figure 4.26: A close-up view of the crack tip front on the specimen PCCT-2* in scanning electron microscope: (a, c) curved front shape in middle region; (b) near-surface zone.

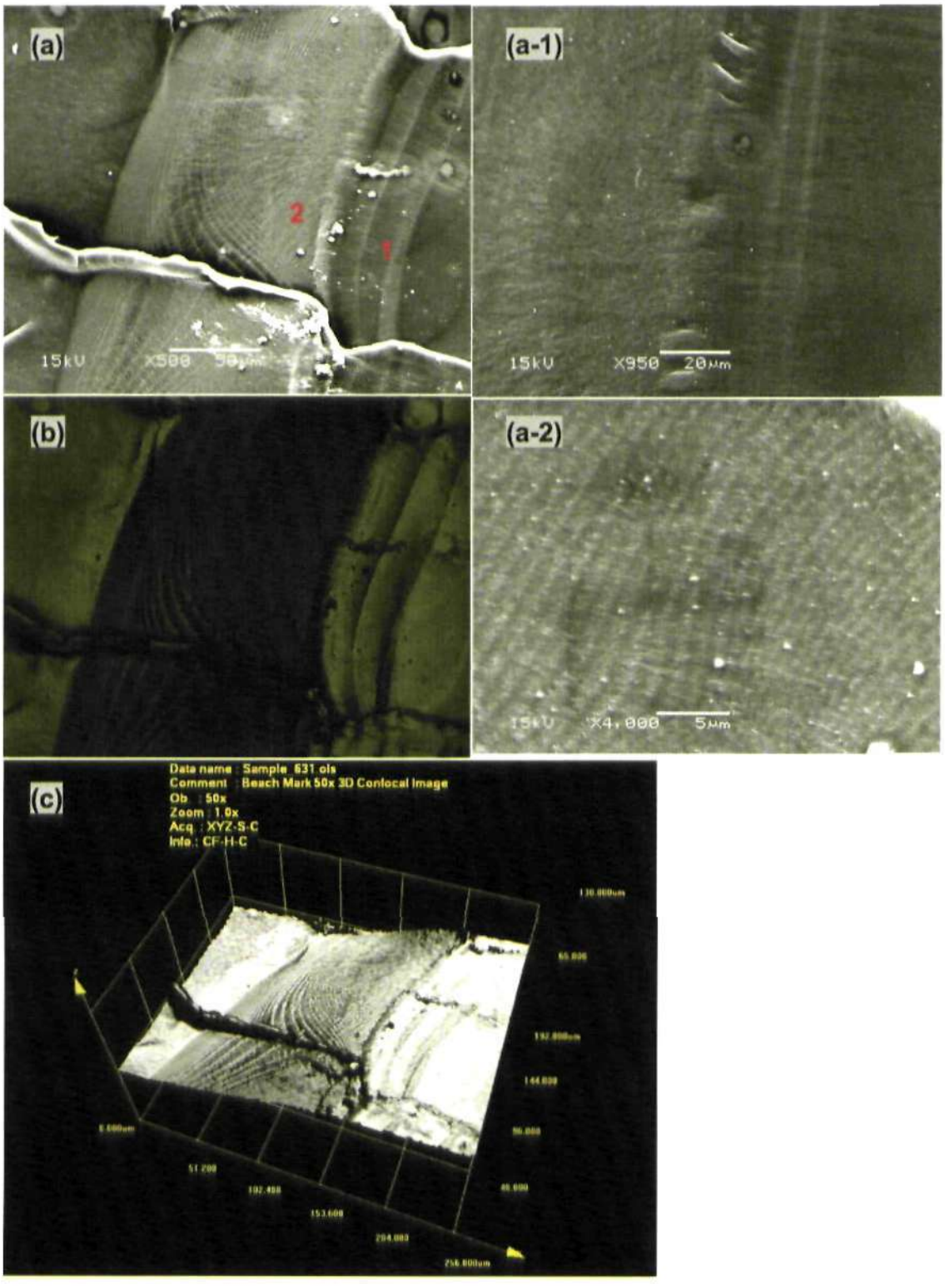

Figure 4.27 Fractography for a crack tip region on the fracture surface of the specimen PCCT-2* (a) taken by scanning electron microscope; (a1-a2) a close-up view of zone 1 and zone 2 at higher magnification; (b)-(c) 3D images using confocal laser scanning microscope.

Crack length	**(mm)**	27.247	29.625	31.563	34.104
Width of the neck (mm)		1.425	1.264	1.208	0.764

Table 4.5 Decreasing widths of 'necking' on the fracture surface of the specimen PCCT-2*

A compilation of crack tip images taken by CLSM, SEM and polariscope, including surface and fracture surface images are shown in Figure 4.28-4.29. This assists in identifying the crack tip location and measuring crack length subsequently. Seven evenly spaced points (T1-T7) were selected along the crack front after each overload was applied, as shown in Figure 4.29. An average crack length was obtained after measuring the crack length at these points through the thickness and crack tip 'T', which represents the average tip position on photoelastic images was then determined (Figure 4.29). As shown in Figure 4.28, the line 1-1 is plotted vertically crossing through the point O indicated in Figure 4.29, i.e. the apparent surface position of the crack tip when overloads were applied. The distance between T1-T5 along each beach mark and the corresponding line 1-1 increases with increase in crack length. The detailed information is reported in Table 4.6. Figure 4.23 and Table 4.6 both show that the crack front shape in the middle plane becomes more curved as *crack grows longer, i.e. crack front curvature becomes larger. Following the* above discussion, it can be seen that this method can provide help to identify the crack tip from optical images not only for accurate crack length measurement but also for the following fitting process.

Crack length (mm)	27.247	29.625	31.563	34.104
Distance to Line 1-1 (mm)				
T1	0.522	0.725	0.745	0.854
T2	0.622	0.750	0.833	0.950
T3	0.719	0.924	0.958	1.402
T4	0.611	0.741	0.833	0.948
T5	0.499	0.672	0.716	0.810
T6,T7	0	0	0	0

Table 4.6 Distance between the points selected along the crack front and line 1-1 on the fracture surface of the specimen PCCT-2* at different crack length where an overload applied.

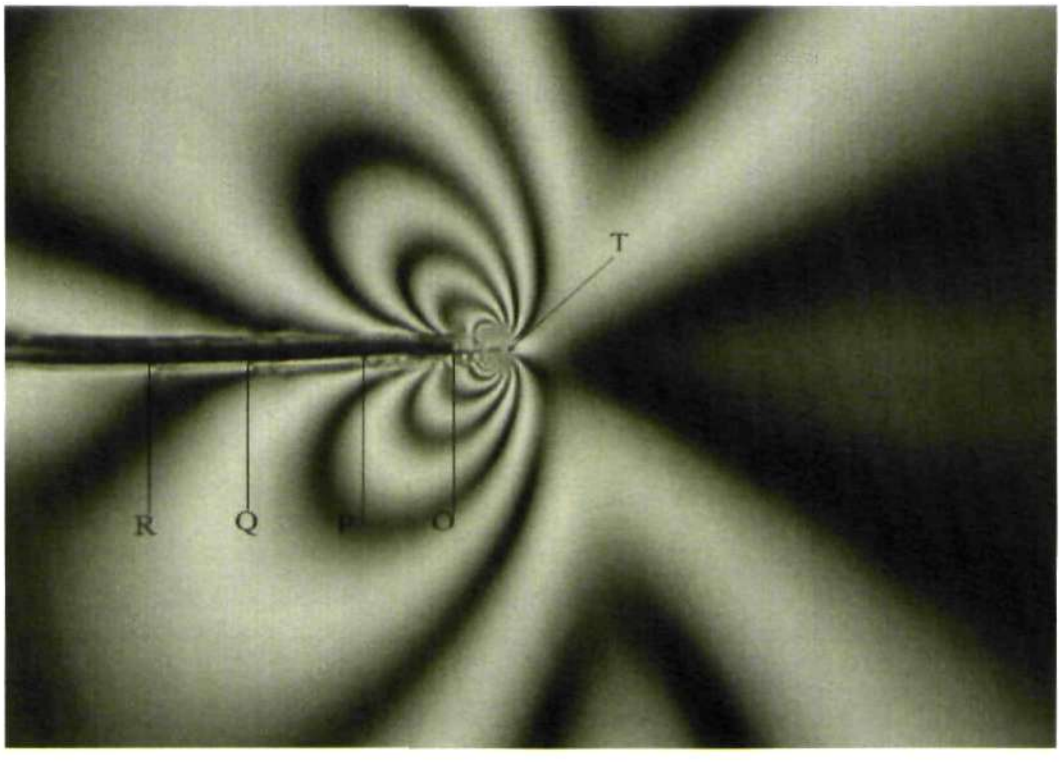

Figure 4.28 Photoelastic fringe pattern image of the specimen PCCT-2* recorded in dark-field polariscope.

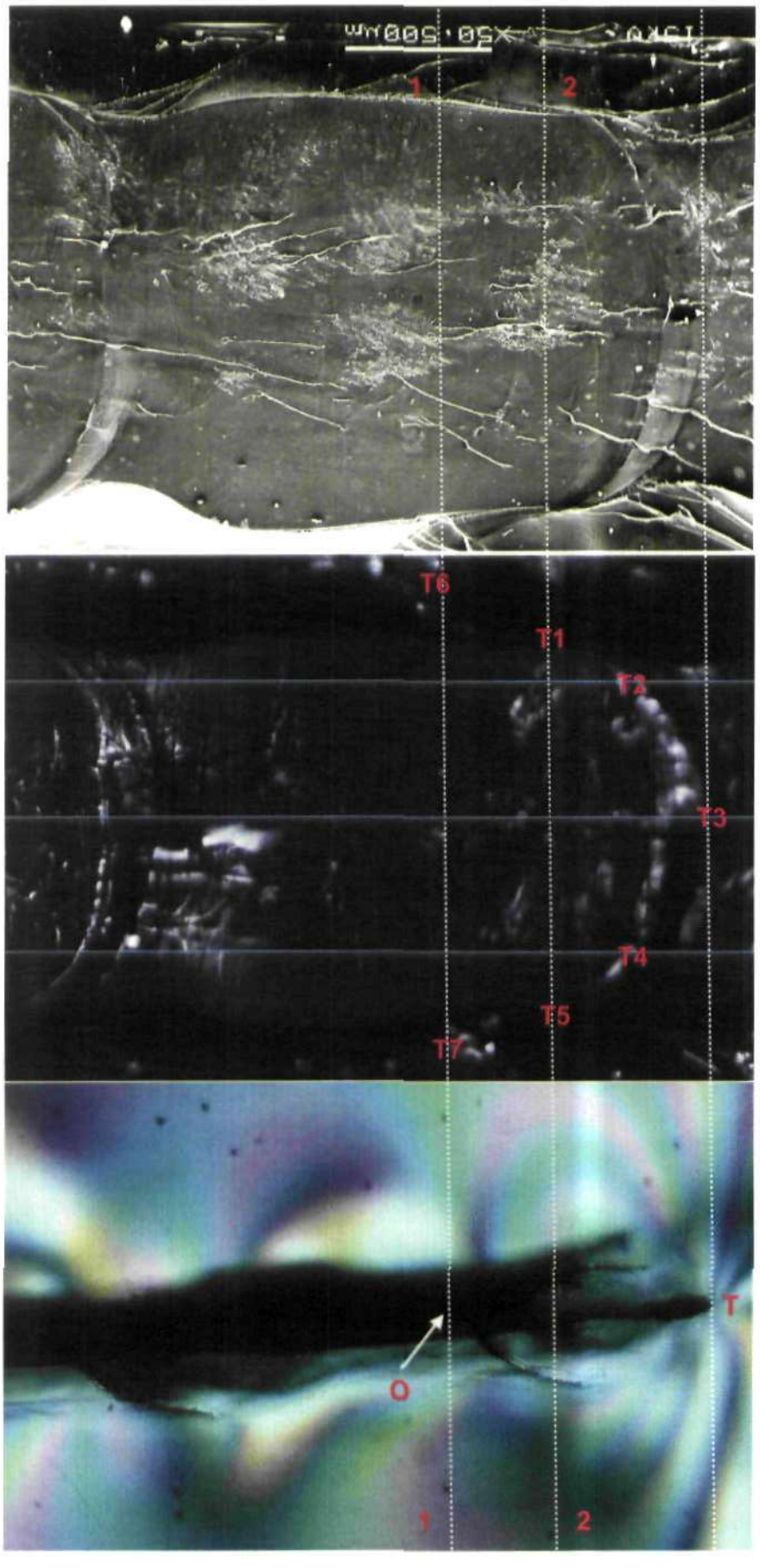

Figure 4.29 Images for the fatigue crack tip of PCCT-2* taken by Scanning Electron Microscope (Top) and Confocal Laser Scanning Microscope (Middle and Bottom), with the fatigue crack length a of 31.2 mm.

4.3.3.7 Calibration

The aim of calibration in photoelasticity experiments is to measure the magnification factor k in $mm/pixel$ (or $1/k$ in $pixels/mm$) which will be required when calculating the three stress intensity factors and the T-stress. The magnification factor was determined by attaching a piece of millimetre graph paper to the front side surface of the specimen, which was placed in the testing machine and subjected to some load to make a photoelastic fringe pattern appear through the polariscope. When the photoelastic fringe pattern was in the focus of the digital camera, one or more pictures were then captured by the camera, as shown in Figure 4.30. After counting the number of pixels in selected distance, the magnification factor could be found in $mm/pixel$. As the graph paper was not fully affixed to the specimen surface, this method could introduce a small error. However, the error was compensated by making a number of measurements at different locations of the graph paper.

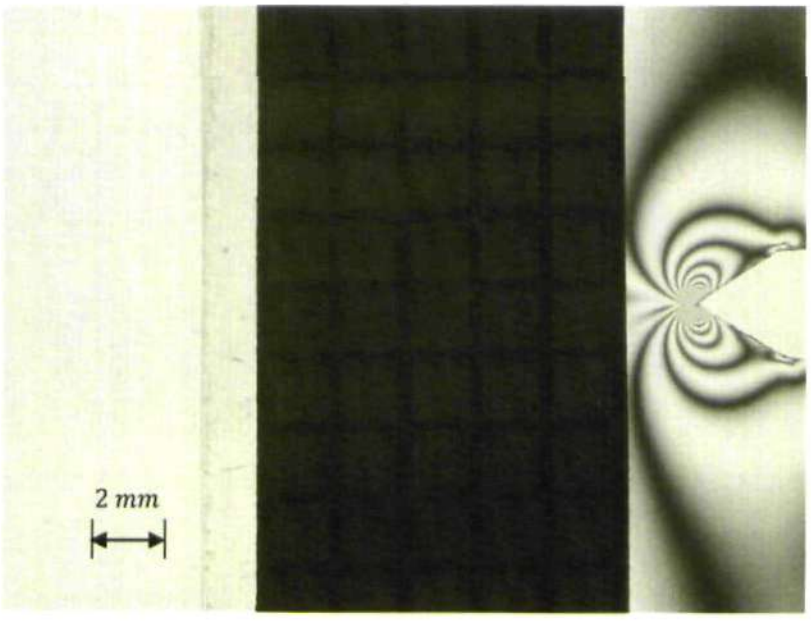

Figure 4.30 Millimetre graph paper attached to the front surface of specimen PCCT-12 for estimating the magnification factor k ; $k = 0.017\ mm/pixel$ in this case.

4.3.4 Digital image correlation

4.3.4.1 Material

The compact tension specimens were machined from an aluminium alloy 2024-T3 sheet (supplied by McMaster-Carr). Al 2024-T3 is commonly used in aircraft and other aerospace structures. Typical chemical composition and mechanical properties of Al 2024-T3 are listed in Table 4.7 and Table 4.8.

Chemical compositions											
Weight %	Si	Fe	Cu	Mn	Mg	Cr	Ti	Zn	Ni	Sn	Pb
2024-T3	$0.50\ max$	$0.50\ max$	$3.8 \sim 4.9$	$0.3 \sim 0.9$	$1.2 \sim 1.8$	$0.10\ max$	$0.15\ max$	$0.25\ max$	$0.05\ max$	$0.05\ max$	$0.05\ max$

Table 4.7 Typical chemical composition for Al 2024-T3

Yield strength	Ultimate strength	Modulus of Elasticity	Shear strength	Poisson's ratio
$345MPa$	$483MPa$	$73.1\ GPa$	$283MPa$	0.33

Table 4.8 Mechanical properties of Al 2024-T3

4.3.4.2 Experimental setup

Figure 4.31 shows a photograph of the experimental setup. The load frame used in this work was an MTS servo-hydraulic material test system, Model 810, with the capacity of 50 KN. The MTS 810 Flextest system was driven with MTS Multi-Purpose TestWare. The Digital 3D Correlation System Dantec Q-400 was used to for the displacement measurements on the Al 2024-T3 CT specimens.

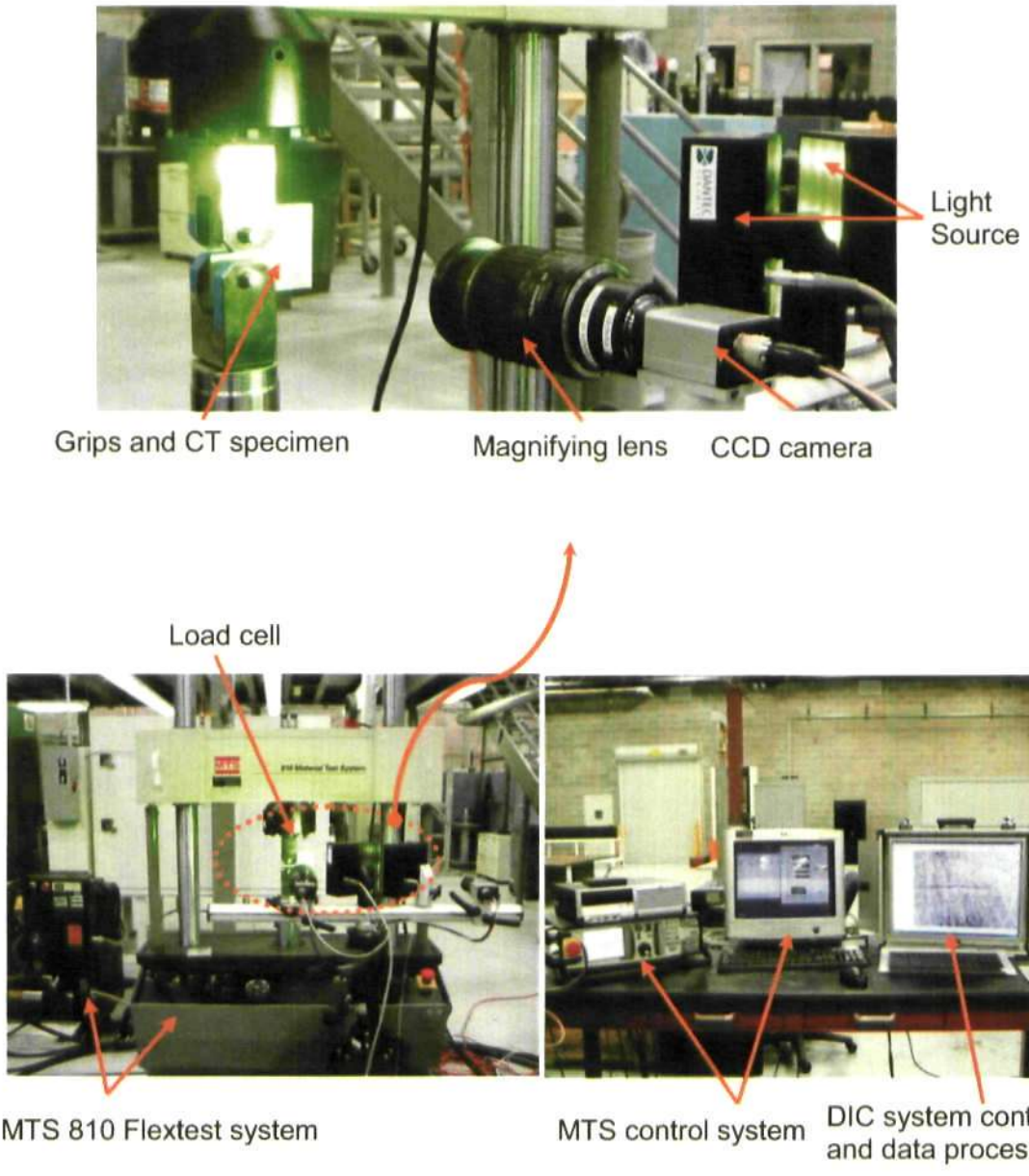

Figure 4.31 Configurations of Instron MTS 810 material test system and Dantec Q-400 system employed in digital image correlation tests.

4.3.4.3 Dantec Q-400 3D digital image correlation system

The Dantec Q-400 system is an optical instrument for true full-field, non-contact measurement of displacements and strains on components and specimens. It can be used on any material without restrictions [101]. The system consists of two $1/2''$ monochrome progressive scan CCD cameras ($1.4\,megapixel$) with lenses, two high intensity LED illumination systems (HILIS), the software

package Istra 4D and a tripod. Figure 4.32 shows the configuration for JAI CV-A1 CCD camera ($1392 \times 1040\, pixels$) in the Dantec Q-400 system with a lens made by Schneider Kreuznach Germany. HILIS is a new and efficient light source that combines the advantages of LED lighting and a high power conventional light source. LEDs provide the high intensity without heating which arises when using conventional lamps of comparable intensity. Figure 4.33 shows the illumination head and the power supply. In the present study, the Dantec Q-400 system was used to implement 2D analysis with one CCD camera and two light sources. The experimental setup is shown in Figure 4.31.

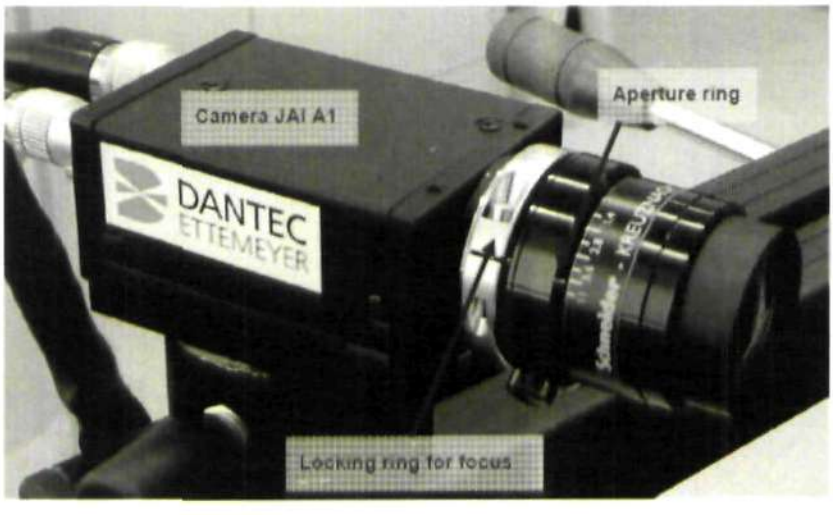

Figure 4.32 Configuration of JAI CV-A1 CCD camera with the lens.

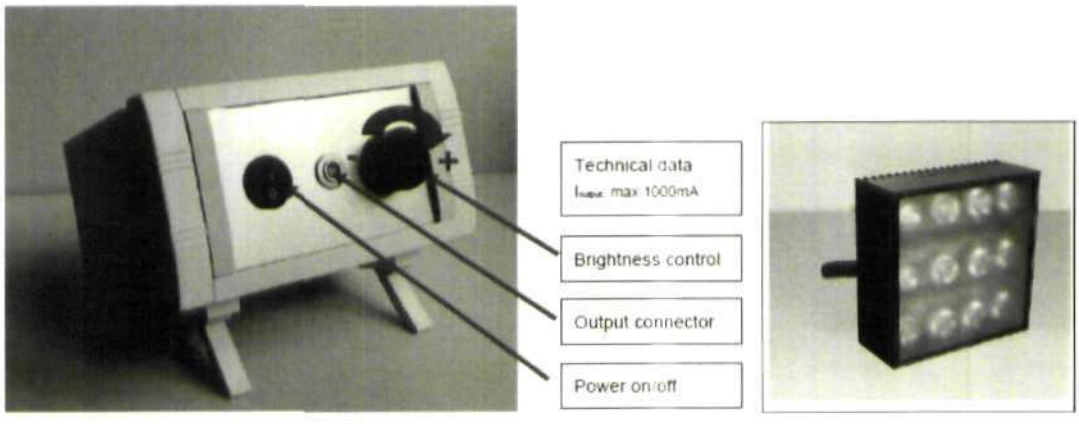

Figure 4.33 HILIS illumination head and the power supply.

The Dantec Q-400 system is controlled by a PC running the software package Istra 4D. Additionally, Istra 4D can process camera images collected by the system. The graphical user interface for Istra 4D can be seen in Figure 4.34.

4.3.4.4 Calibration

In order to evaluate the object geometry from captured digital images, the system setup has to be calibrated to determine the following parameters:

1. Intrinsic parameters, such as focal length of the lenses, principal point of the lenses, radial distortions of the lenses, tangential distortions of the lenses.

2. Extrinsic parameters, such as the translation vector and rotation matrix.

The quality of the measurement relies on exact knowledge of the intrinsic and extrinsic parameters in the system. The calibration is easily done by taking images of a calibration panel under different perspective views.

To perform the calibration, a calibration target is held in the field of view of the camera. The software identifies the corners of the squares in the calibration pattern and marks detected corners with circles. The orientation of the calibration target is recognized by three additional circles in the centre of the pattern. If the software is able to determine the orientation of the target, a blue arrow is drawn in the live image from the central circle to the circle in the neighbouring square, see Figure 4.35. The system automatically captures an image, whenever a sufficient number of corners are detected in the camera. After each exposure, the intrinsic and extrinsic parameters plus a quality parameter 'Residuum' are automatically calculated online and are displayed for the camera. At the end of the procedure, the values for the calibration parameters need to be saved as a calibration file '.isprp', which is required for a subsequent evaluation.

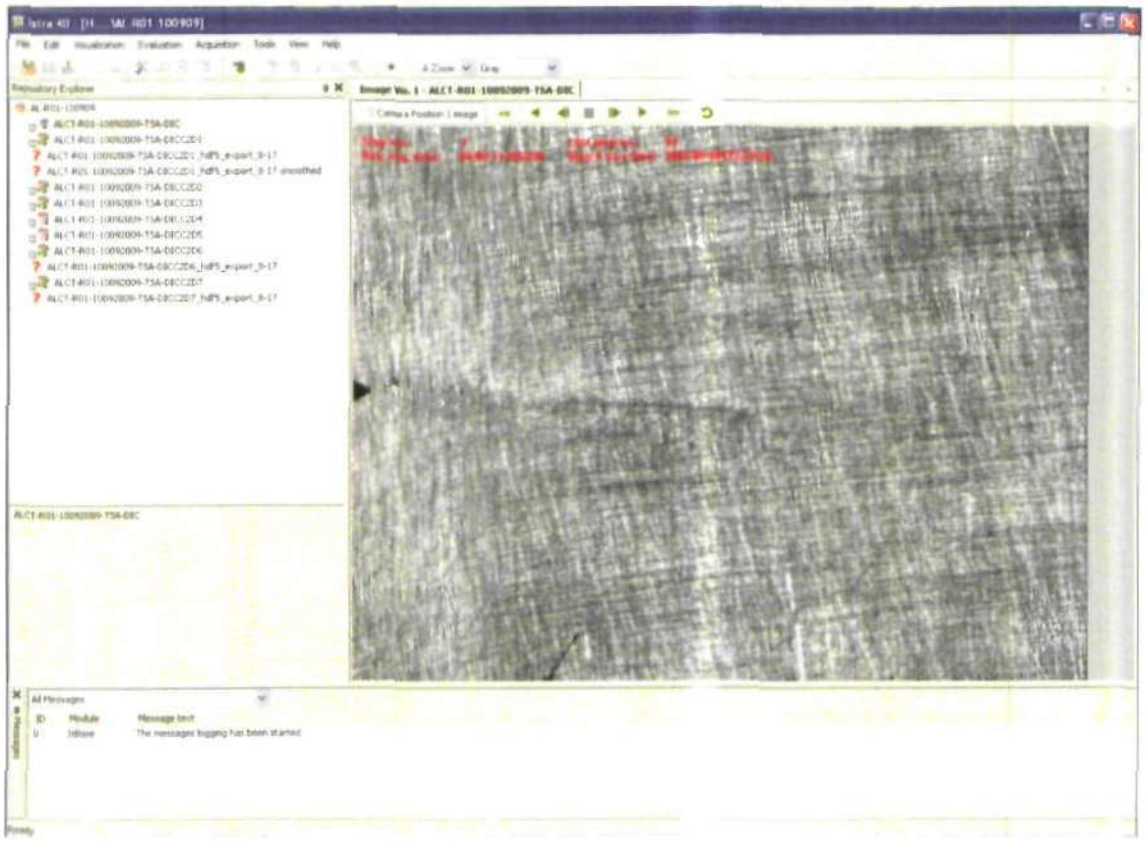

Figure 4.34 The graphical user interface for Istra 4D software.

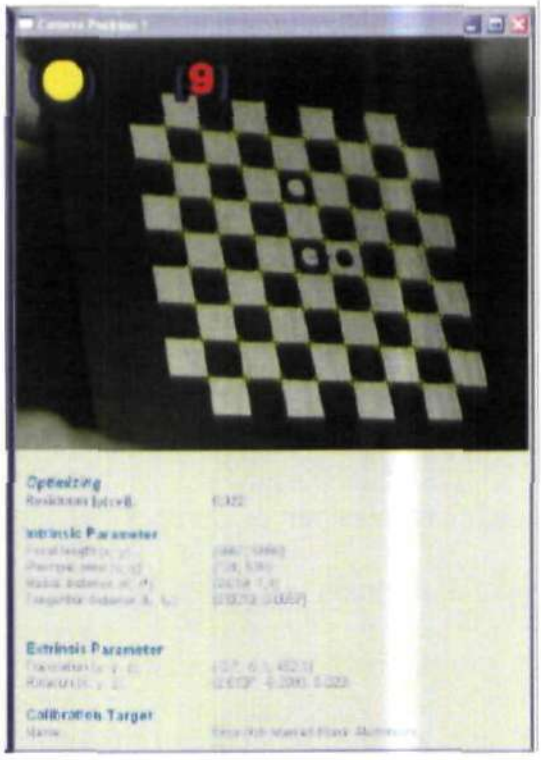

Figure 4.35 View of the calibration panel with the camera.

Additionally, another parameter that needs to be identified is the magnification factor k in $mm/pixel$. The method for finding the magnification factor is similar to the method used in the photoelasticity experiments, by attaching a piece of millimetre graph paper to the front side surface of an Al 2024-T3 CT specimen, as shown in Figure 4.36. The same problem, as in photoelasticity experiments appears when using this method to determine the magnification factor, due to the fact that the graph paper not fully affixed to the specimen surface and the distances from the camera to the specimen surface and to the millimetre graph paper are not exactly the same. This could be overcome by engraving some marks on the surface of the specimen near the crack tip. However, sufficient accuracy was deemed to be obtained by the former method.

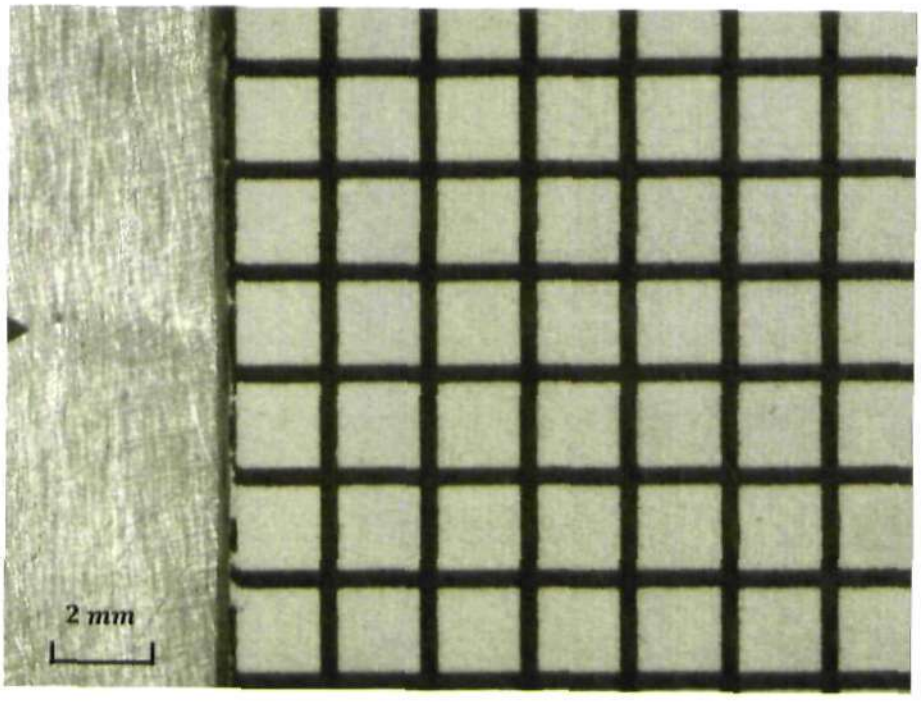

Figure 4.36 Millimetre graph paper attached to the front surface of the specimen ALCT-R01 for estimating the magnification factor k, $k = 0.013\ mm/pixel$ in this case. Image size is about $17.6\ mm \times 13.2\ mm$.

4.3.4.5 Surface preparation

In the current work, a network of randomised scratches of varying orientation, width and depth on the surface was introduced to provide the stochastic surface marking pattern needed for the image correlation. This was created by scratching the specimen surface to be inspected with waterproof silicon carbide sandpaper. The preferred polishing method is using machine polishing [202], although manual polishing was also found to work [94]. Manual polishing can also achieve the requirement that the sample to be optically inspected must have a matt finish rather than shiny. Followed the process given in the references [94, 202], surface texture preparation for all the aluminium alloy CT specimens in the current study was carried out by manual polishing.

Applying a scratch pattern on the specimen surface is beneficial in achieving a smaller size of imaging feature. This allows the use of a smaller facet size which permits a higher spatial resolution. However, the image contrast achieved by scratching the surface instead of applying a speckle pattern to the surface is poorer and local reflections inevitably arose at the surface. In general, it is observed that uncoated surfaces lead to reflective locations and full saturation of the camera CCD. Therefore, the lighting set up for the DIC experiments is arranged carefully and adjusted to minimise the possible reflections. It is recommended that DIC images are viewed under the grayminmax palette which can help in identifying where the saturated locations exist and then assist one to adjust the lighting. Moreover, reflective regions can be eliminated from the correlation process whenever reflections are identified in images [203]. An example of surface finish used for image correlation purposes is shown in Figure 4.37.

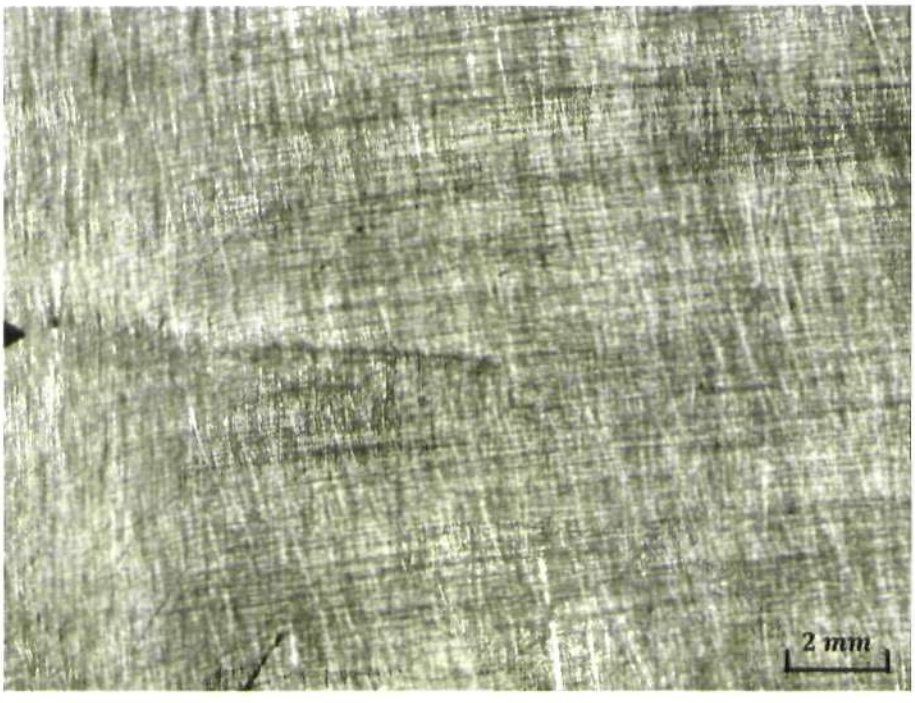

Figure 4.37 Random patterns of scratches applied to the surface of the specimen ALCT-R01.

4.3.4.6 Experimental procedure

The experiment procedure in image correlation tests is similar to that in photoelasticity. A flow chart and a list of Al 2024-T3 CT specimens tested in this work are presented in Figure 4.38 and Table 4.9.

Specimen reference	CA-loading $[N]$		Ratio	Frequency $[Hz]$
	P_{max}	P_{min}	R	
ALCT-R01	1200	120	0.1	10
ALCT-R03	1200	360	0.3	10
ALCT-R05	1200	600	0.5	10

Table 4.9 List of Al 2024-T3 CT specimens tested for image correlation purposes and loading conditions.

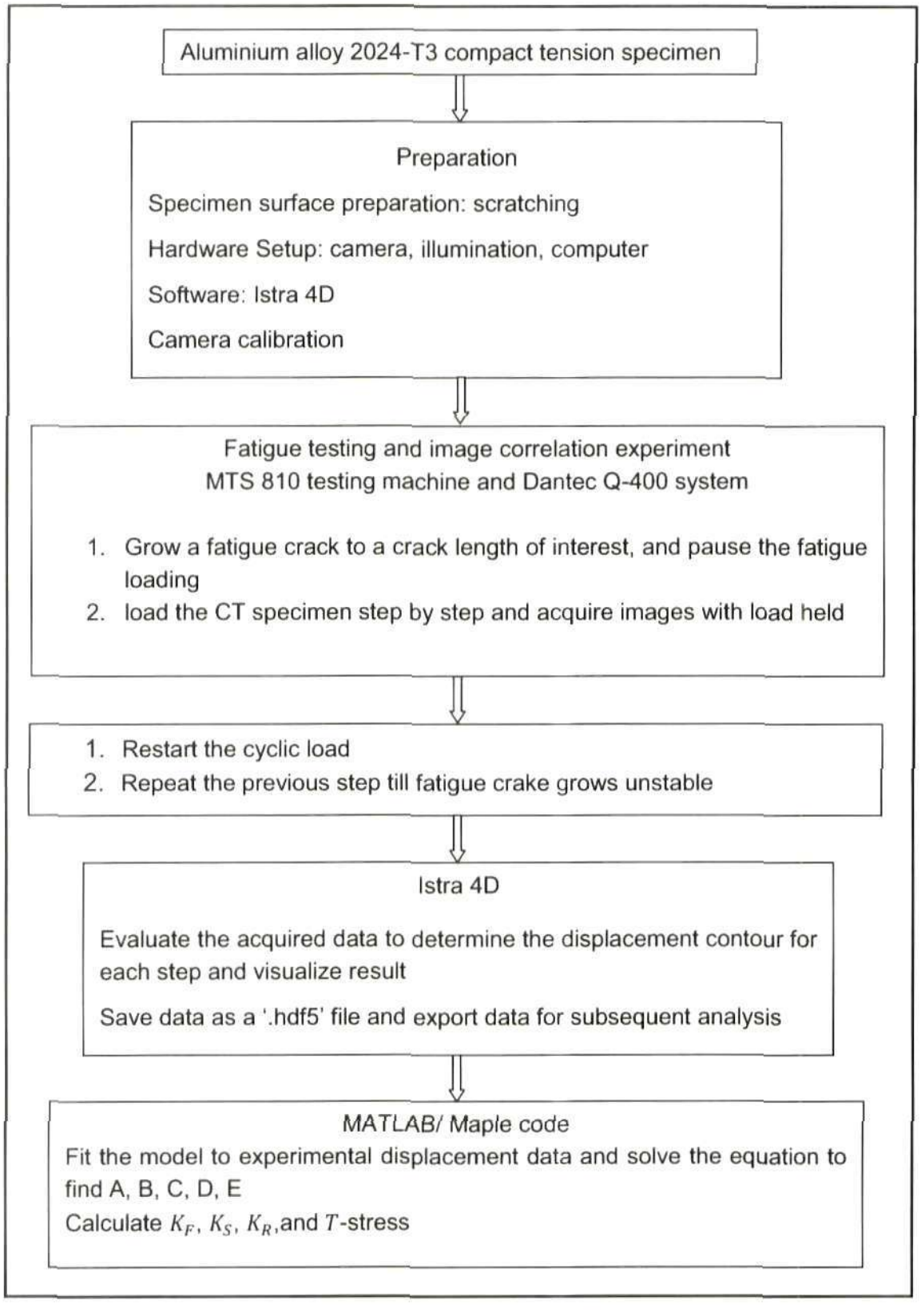

Figure 4.38 Flow chart of the sequence of measurement in the present image correlation tests.

Chapter 5 Photoelasticity experiments and results

5.1 Introduction

This chapter reports the whole process for analysing experimental photoelastic data for real fatigue cracks in polycarbonate compact tension specimens. Initially, the chapter presents the crack growth data obtained from representative polycarbonate CT specimens. Subsequently, the work described in this chapter studied how to collect valid data for the model to provide the best quality fit and hence solution for the stress intensity parameters. The chapter then discusses the way to locate the coordinates of the crack tip which was employed in this work. Finally, the values of the four stress parameters K_F, K_R, K_S and T inferred from experimental photoelastic data by the mathematical model are reported for the polycarbonate CT specimens.

5.2 Crack growth data

Crack length and number of applied fatigue cycles were recorded during fatigue crack growth. This section reports some crack growth data for two sets of CT specimens. The first set of specimens was not annealed prior to the fatigue test; this data comprises three specimens PCCT-1, PCCT-2 and PCCT-3. Crack length for these three specimens was measured with an optical-microscope (Olympus BX60M Soft Imaging System). The second selected set comprised three annealed polycarbonate specimens, including PCCT-11, PCCT-12 and PCCT-13. Crack length was estimated using the crack tip horizontal coordinate obtained from photoelastic images. For detailed information on loading conditions for those specimens, please refer to Table 4.2.

Figure 5.1 shows the crack growth data for the three unannealed polycarbonate CT specimens PCCT-1, PCCT-2 and PCCT-3 tested under constant amplitude loading with $R = 0.1, f = 0.1\,HZ$, $R = 0.1,\ f = 0.5\,HZ$, $R = 0.5, f = 1.0\,HZ$ respectively. Figure 5.2 shows the crack growth data for the three annealed polycarbonate specimens PCCT-11, PCCT-12 and PCCT-13 fatigue tested with $R = 0.1, f = 0.5\,HZ$, $R = 0.3, f = 0.6\,HZ$, $R = 0.5, f = 0.9\,HZ$ respectively. The rate of crack propagation for the three annealed specimens was plotted as a function of ΔK as shown in Figure 5.3. Since the maximum load P_{max} was kept constant at $120N$ for all the specimens, fatigue tests performed at high load ratio, i.e. a lower range of applied load/stress intensity showed a lower rate of crack propagation and a longer fatigue life, as expected. The data also indicate that load amplitude has a greater effect on the fatigue crack propagation rate than does loading frequency.

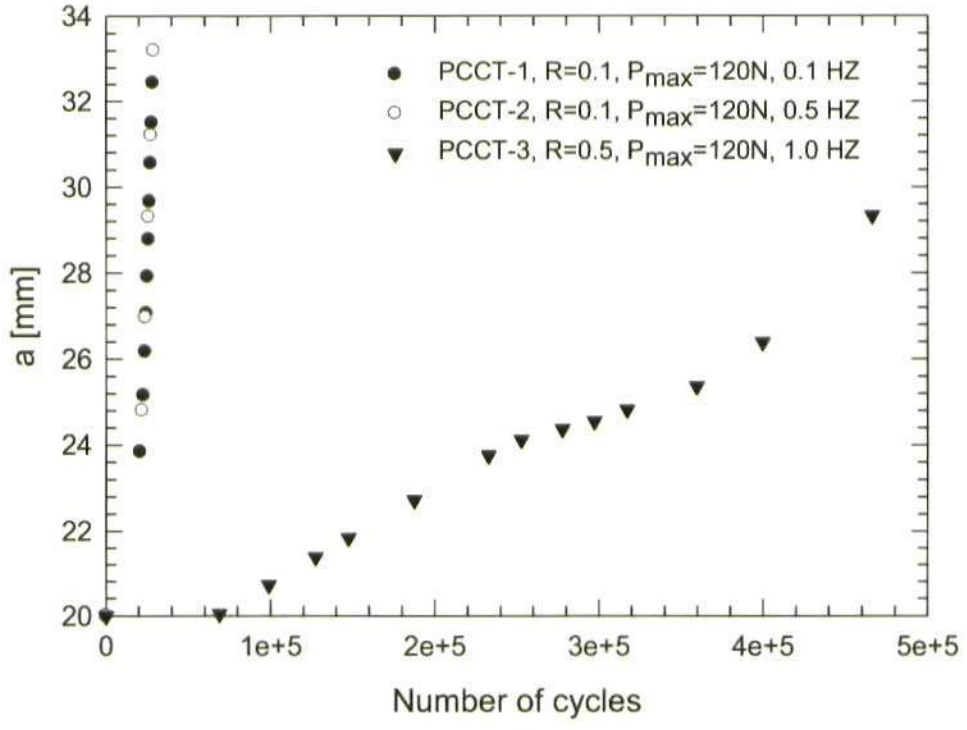

Figure 5.1 Crack lengths versus number of cycles for non-annealed polycarbonate specimens PCCT-1, PCCT-2, and PCCT-3.

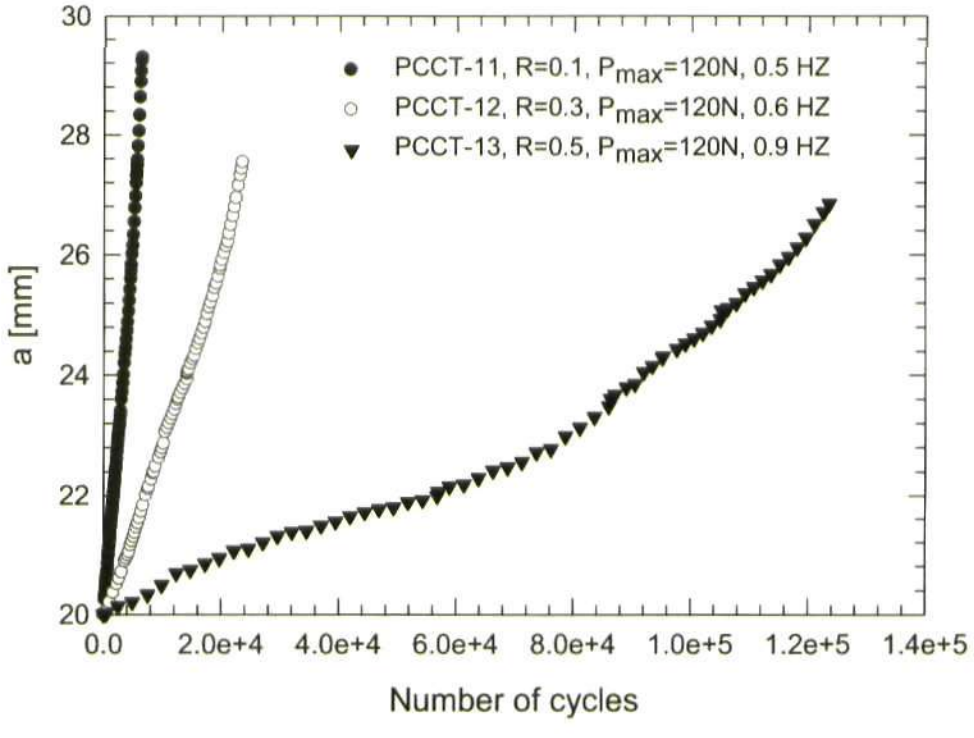

Figure 5.2 Crack lengths versus number of cycles for annealed polycarbonate specimens PCCT-11, PCCT-12, and PCCT-13.

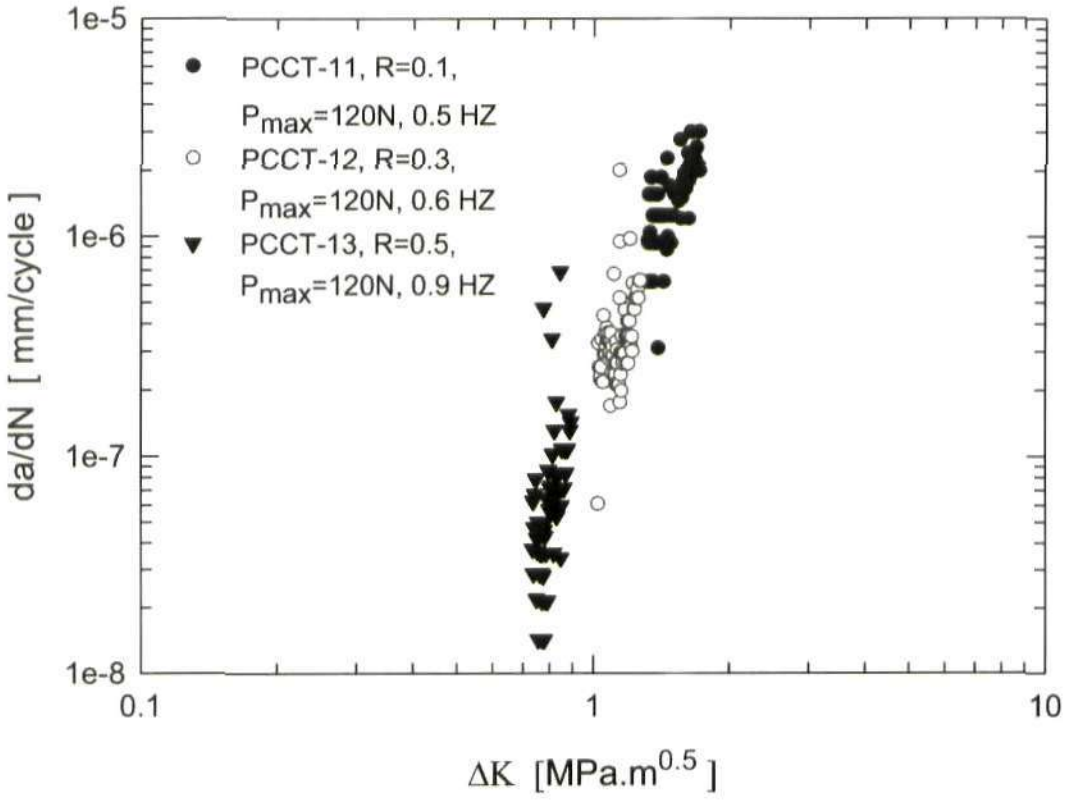

Figure 5.3 Crack growth rate da/dN versus ΔK for annealed polycarbonate specimens PCCT-11, PCCT-12, and PCCT-13.

Figure 5.4 shows the crack growth data for the three specimen tested under the same load ratio $R = 0.1$, i.e. PCCT-1, PCCT-2 and PCCT-11. PCCT-1 and PCCT-2 were not annealed prior to fatigue testing while PCCT-11 was an annealed polycarbonate specimen. PCCT-2 was tested under almost the same loading condition with PCCT-1, except that overloads $(144N)$ were applied at different crack lengths, and it had a higher loading frequency. It can be seen from Figure 5.2 that the fatigue crack in specimen PCCT-2 grew slightly faster than that in PCCT-1. This variation, however, is well within the usual scatter observed in fatigue testing. However, when crack length exceeding $31mm$, fatigue cracks on PCCT-2 and PCCT-1 grew at almost the same rate. It was observed that 27,980 fatigue cycles had elapsed when the crack in PCCT-1 was of a length $31.49\ mm$, while it took some 27,500 cycles to produce a crack

in PCCT-2 which was $31.2\ mm$ long. Figure 5.2 also shows that the crack in the annealed specimen PCCT-11 grew faster than those in unannealed specimens PCCT-1 and PCCT-2, especially when the crack was shorter.

Figure 5.5 shows the crack growth data for the two specimens tested at $R = 0.5$. Through this comparison, it was also observed that fatigue crack grows faster in annealed polycarbonate specimens than in unannealed ones. In addition, the crack initiation process required more fatigue cycles in unannealed PCCT-3 than in PCCT13.

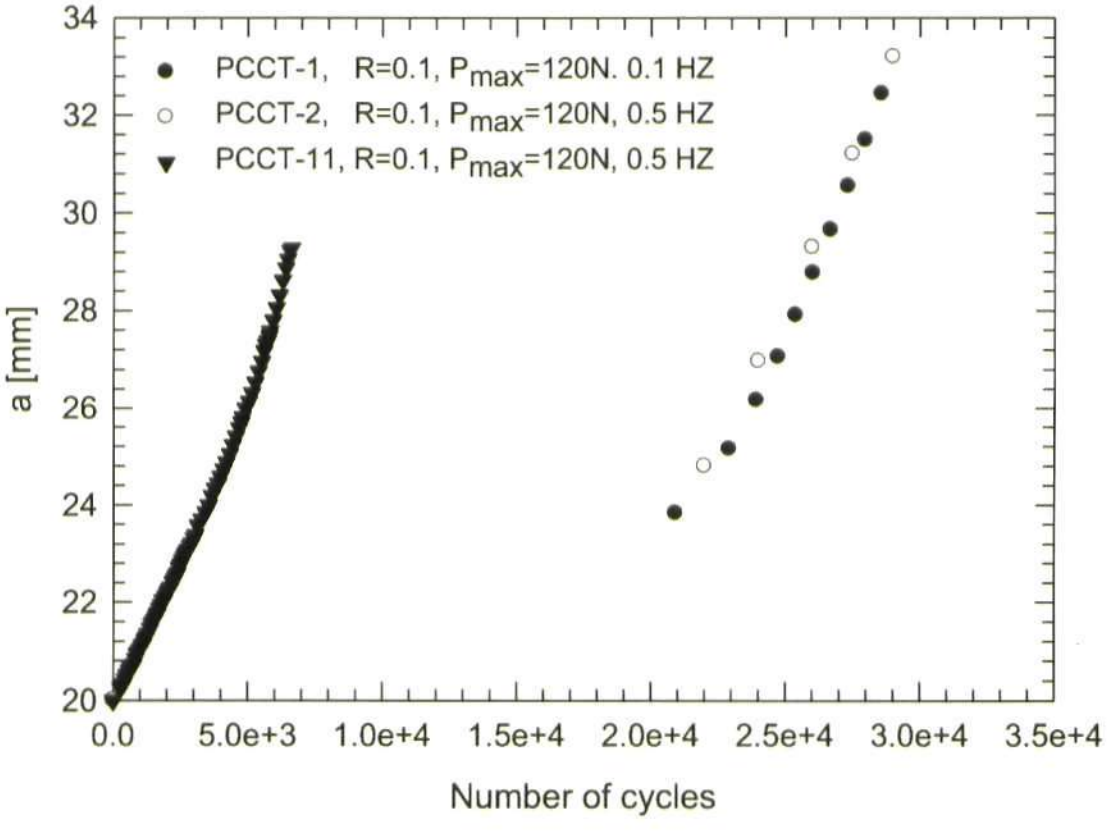

Figure 5.4 Crack lengths versus number of cycles for non-annealed polycarbonate specimens PCCT-1, PCCT-2, and annealed polycarbonate PCCT-11 tested under the same load ratio $R = 0.1$.

As indicated by the data in Figure 5.4 and Figure 5.5, annealing has a significant effect on crack growth behaviour in polycarbonate specimens. It is

believed that this arises because of the removal of residual manufacturing stresses during annealing. Some part of this may, however, arise from other changes to properties of the PC material during annealing. A reduction in the amount of permanent plastic deformation observed in annealed test-pieces during impact has been reported in the work by Adam et al [204]. The current experimental work shows similar observations in the annealed polycarbonate CT specimen, i.e. after annealing the volume of the permanent plastic zone is reduced. The residual stress-induced difference between unannealed polycarbonate specimens and annealed specimens can be seen clearly when viewed in a confocal laser scanning microscope (CLSM) and polariscope (Figure 5.6).

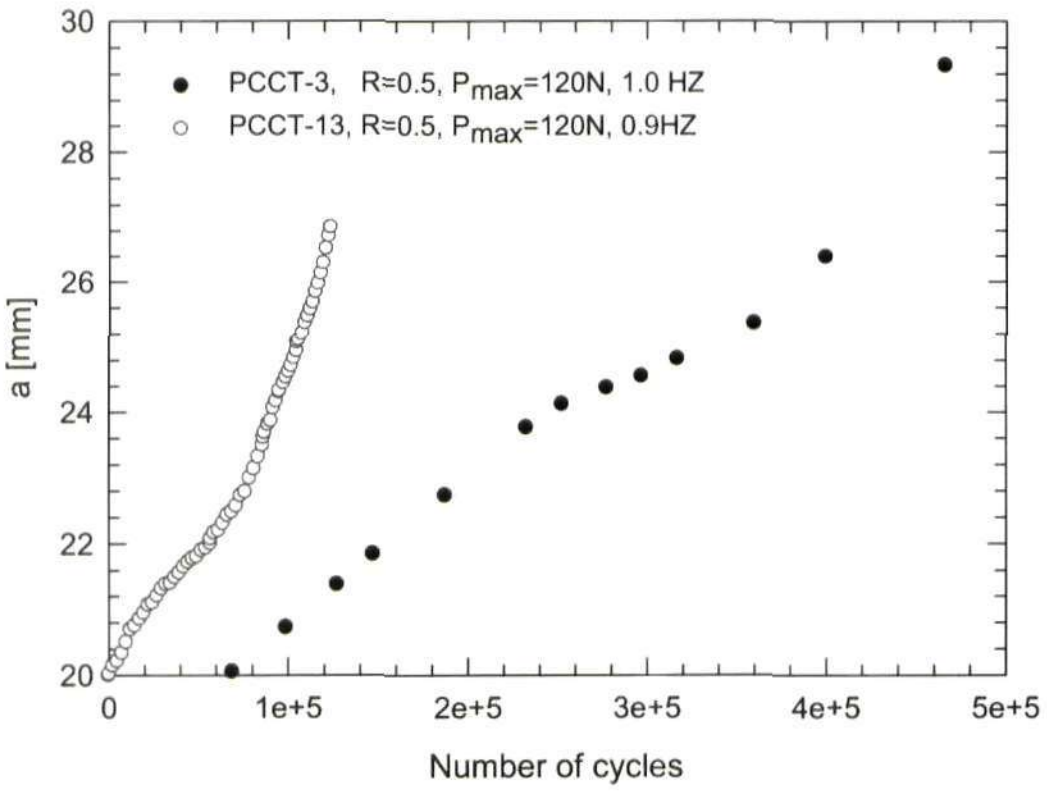

Figure 5.5 Crack lengths versus number of cycles for non-annealed polycarbonate specimen PCCT-3 and annealed polycarbonate PCCT-13 tested under the same load ratio $R = 0.5$.

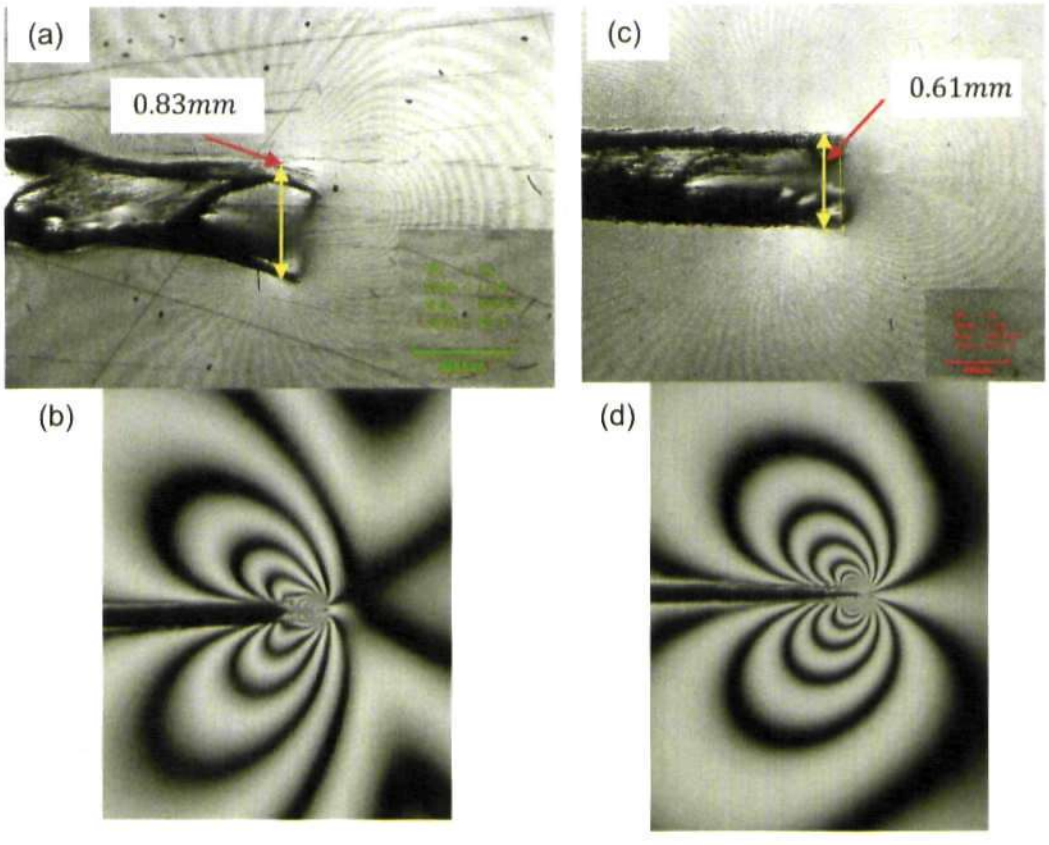

Figure 5.6 Un-annealed polycarbonate specimen PCCT-1: (a) CLSM image for a 32.4 mm crack; (b) photoelastic fringe pattern. Annealed specimen PCCT-5: (c) CLSM image for a 35.0 mm crack; (d) photoelastic fringe pattern.

Figure 5.6 presents the images taken by CLSM and a circular polariscope (dark field). The differences in the size and shape of the plastic enclave and plastic zone in the test-pieces are shown clearly. Figure 5.6(a) shows a crack of length 32.4 mm with a craze width (equivalent to plastic zone size) of 0.83 mm in the unannealed specimen PCCT-1; while Figure 5.6(b) shows a longer crack of length 35.0 mm with a smaller craze width of 0.61 mm in the annealed specimen PCCT-5. Additionally, the figures also indicate that annealing of polycarbonate led to the formation of a straighter and thinner band of plastically deformed material, compared to a more diffuse band in unannealed specimens; this makes identification of the crack tip from optical images of the fringe pattern

more difficult in unannealed specimens. Following from the above discussion, it is reasonable to expect that the reduction in volume of the plastic zone after annealing would lead to lower fracture toughness in the polycarbonate material. Consequently, fatigue cracks are likely to grow faster in annealed polycarbonate specimens than those in untreated specimens. This is fully in agreement with the data in Figures 5.4 and 5.5. Furthermore, it is also reasonable to expect that greater permanent plastic deformation in the annealed material would induce higher crack closure levels under cyclic loading. Further experimental studies on these specimens would be required to provide the proof for this.

5.3 Operational features of the image process programs

CoPA and RICO were used to extract isochromatic fringe data from photoelastic images in the present work. CoPA was developed in 2004 by Siegmann et al [201], and is an earlier work on demodulisation and unwrapping. It was combined together with a regularisation algorithm in the newly-developed program RICO in 2008 by Siegmann et al [200]. In the earlier stage of the present work, difficulties had been experienced in using CoPA to acquire correctly unwrapped isochromatic map. Poorly unwrapped isochromatic maps were obtained. One example is shown schematically in Figure 5.7. It can be seen that the resultant isochromatic map was not continuous and there are regions with discontinuous data. As a result, the size of zones containing valid and usable data points was reduced. It is one of the reasons that fringe order data used in the fitting process were collected only from inside of one specific fringe in order to avoid poorly unwrapped zones (inside the zone bounded by the red solid line in Figure 5.7). In general, poor unwrapping starts from the furthest isochromatic fringe that does not form a closed loop surrounding the

crack tip within the field of view, as indicated by the zones inside the white dashed line.

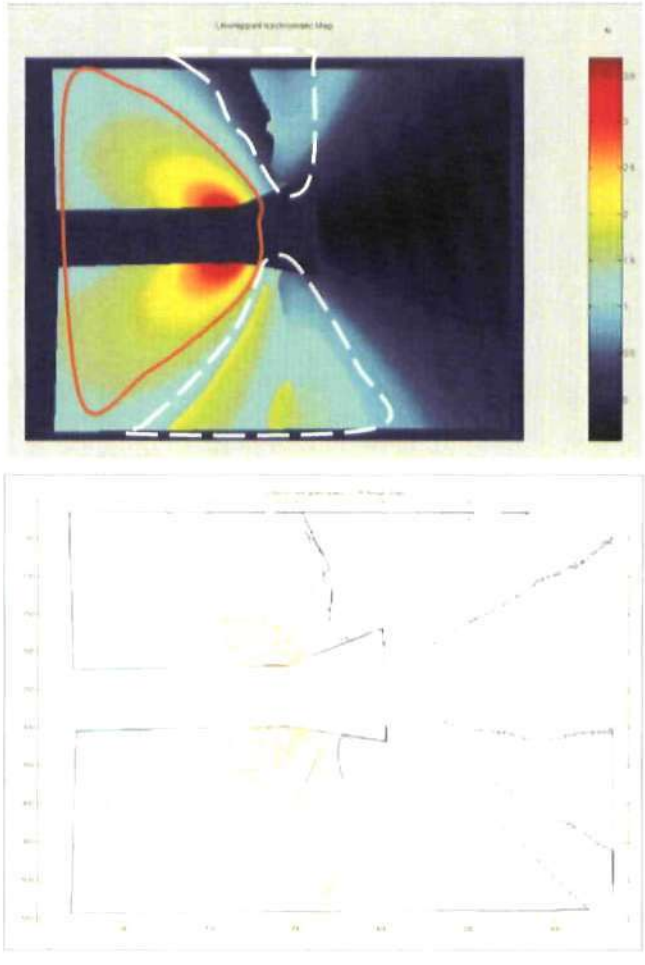

Figure 5.7 Resultant unwrapped isochromatic map. Specimen PCCT-1, crack length $a = 31.49\ mm$, $K_I = 1.3\ MPa.m^{0.5}$ (Load condition: $P_{max} = 120\ N$, $R = 0.1$, frequency = $0.1\ Hz$).

In addition, different initial pixels selected to start demodulating isoclinic data or unwrapping isochromatic data may yield different unwrapped isochromatic maps.

As mentioned in Chapter 4, RICO is a more robust program compared to the CoPA program. RICO has a graphical user interface written in MATLAB, as shown in Figure 4.14 and was used to process photoelastic data in the second stage of the present work. However, RICO has a slower processing time

compared to CoPA. If one set of six-stepped phase-shifted images in the original size of 1360×1024 pixels was processed by RICO, the processing time is no less than 3 hours. So, in practice, photoelastic images were resized by a factor of 0.5 before reading into RICO with the resolution reduced to be half that of the original data.

Figure 5.8 presents a flow chart describing the steps involved in extracting isochromatic data from photoelastic images recorded with six-stepped phase-shifting method using the program RICO. The example was taken from specimen PCCT-11, images taken at $108\ N$ with the crack length of $27.6\ mm$. The three parameters used in the regularisation process are the regularisation parameter L_u, the windows size w and the partial differential length. In this case, $L_u = 2$, $w = 5\ pixels$, $5\ pixels$ were set for them respectively. Normally, the value of the regularisation parameter varies with the fringe density, i.e. a higher fringe density requires a higher value. The viable value in the current study lies between 1 and 3.5. The value of window size is dependent on the signal to noise ratio and fringe density, i.e. higher noise and lower fringe density need a larger value. The viable value in the current study lies between 2 and 5. The partial differential length has the same dependence on noise and fringe density as the window size, and the integer values used in the present work lie between 2 and 5.

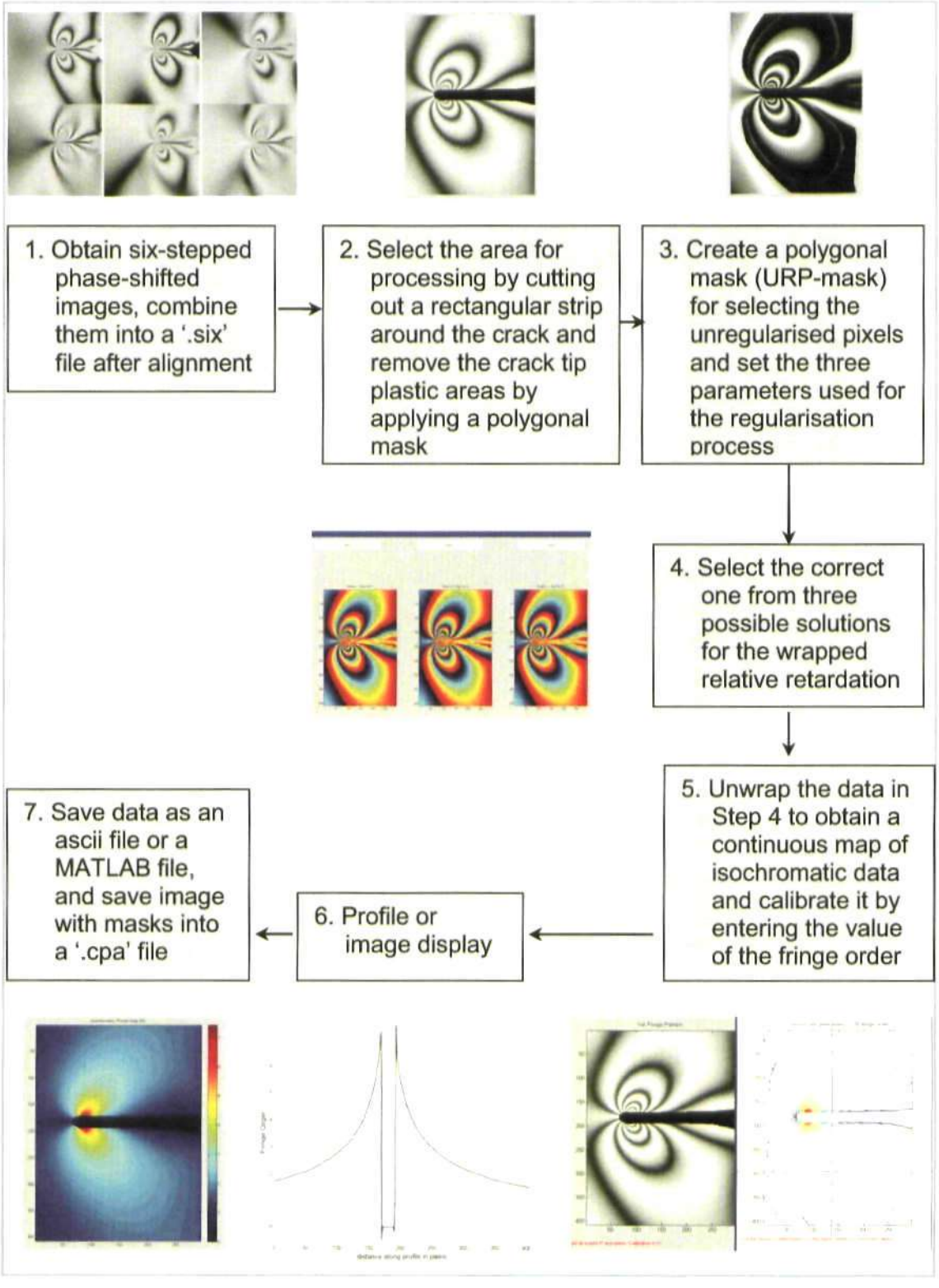

Figure 5.8 Flow chart describing the steps of extracting isochromatic data from photoelastic images recorded with six-stepped phase-shifting method by using the program RICO. (From specimen PCCT-11, images taken at 108 N with the crack length of 27.6 mm)

In step 1, the photoelastic data to be processed with CoPA or RICO should be as good as possible. When obtaining the photoelastic data, special attention should be given to the following points: ensuring the correct arrangement of the polariscope for each of the six images as well as the order in which they are taken; using the maximum range of intensity levels for the camera CCD but without saturating the CCD; also, do not change any of the parameters of the image acquisition system (focal length, aperture, exposure time, gain level, etc.) while capturing the six images or move the relative position of the specimen and the image acquisition system.

In step 2, the crack tip plastic areas should be masked out of the image. The quality map (which is discussed below) can help to identify the areas that should not be included in the following regularisation process. The quality map for the example is shown in Figure 5.9. It can be appreciated that the white areas near the crack tip and along the crack flanks correspond to the damage zones and to regions of plastic deformation. These areas should be masked out of the fringe pattern in the areas that are not well-defined. Additionally, some areas (nonlinear region) where the fringe patterns are blurred or distorted, and where fringes come together or overlap should be removed too. For correct regularisation, the data used should be of a high quality without fringe overlap [205]. The phenomenon of blur or distortion, and fringes coming together or overlapping might happen in three main instances: (i) the optical characteristics of the material are altered due to the plastic deformation; (ii) the fringe density is too high for the camera resolution; (iii) the stress or strain distribution is not constant along the light path.

In step 3, the aim of setting an URP-mask is to select the pixels which are not to be regularised in the regularisation process. The URP-mask should be created

by carefully following the correct slope which has to be continuous with the expected behaviour of the relative retardation. Appropriate values of the three parameters required in the regularisation process can be found through several iterations of this sequence, which makes the regularisation process hugely time-consuming.

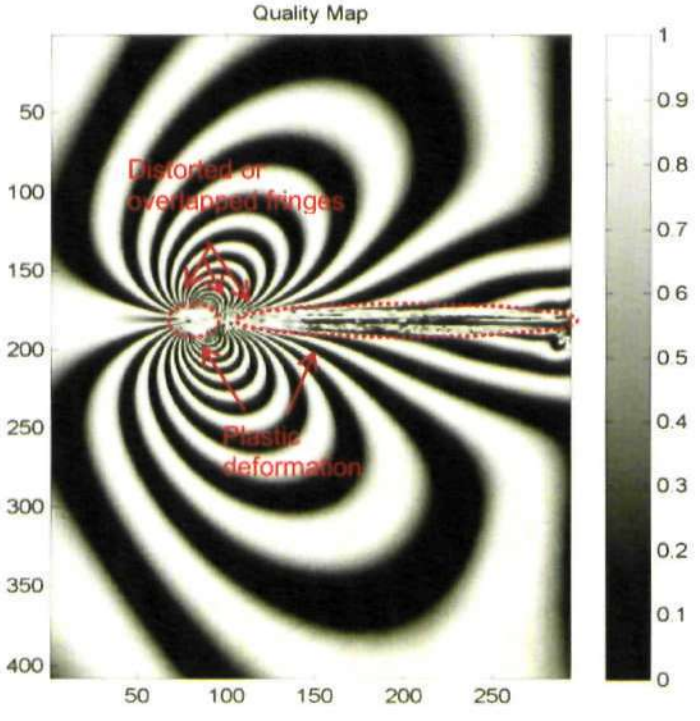

Figure 5.9 Quality map indicating the areas that should be masked out in the regularisation process.

In step 5, unwrapped isochromatic phase maps were calibrated by assigning a half order or an integer value of the fringe order to the point chosen for calibration. To help in determining the absolute fringe order number at a selected point, a colour image was captured in dark field conditions with a white light source at either minimum load or maximum load. This was then used to infer the fringe order to aid the calibration process. White light is composed of all wavelengths in the visual spectrum and is generally used for interpreting full-field fringe patterns (complementary colours) seen by the observer. The

complete colour sequence, the relative retardation and the numerical fringe order for each colour were presented in Table 5.1 and Figure 5.10. The colour image taken at the minimum load $P_{min} = 12N$ was used to aid in the calibration process of the unwrapped isochromatic phase maps at each load step for specimen PCCT-11 with the crack length of $27.6\ mm$, as shown in Figure 5.11.

Colour	Approximate relative retardation (nm)	Fringe order
Black	0	0
Gray	160	0.28
White	260	0.45
Pale Yellow	345	0.60
Orange	460	0.80
Dull Red	520	0.90
Purple(Tint of Passage)	575	1.00
Deep Blue	620	1.08
Blue-Green	700	1.22
Green-Yellow	800	1.39
Orange	935	1.63
Rose Red	1050	1.82
Purple(Tint of Passage)	1150	2.00
Green	1350	2.35
Green-Yellow	1440	2.50
Red	1520	2.65
Red/Green Transition	1730	3.00
Green	1800	3.10
Pink	2100	3.65
Pink/Green Transition	2300	4.00
Green	2400	4.15

Table 5.1 Isochromatic fringe characteristics

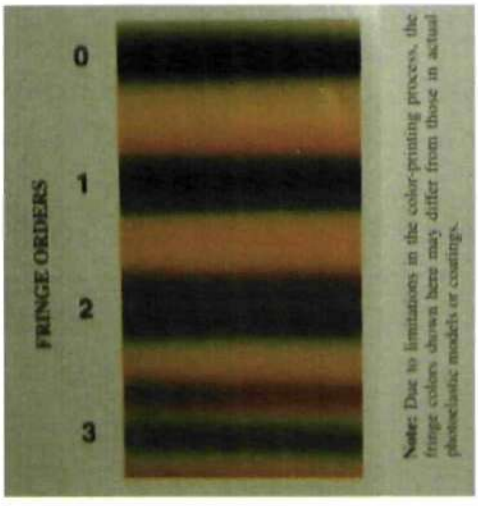

Figure 5.10 Colour scale (VISHAY® PhotoStress Tech Note)

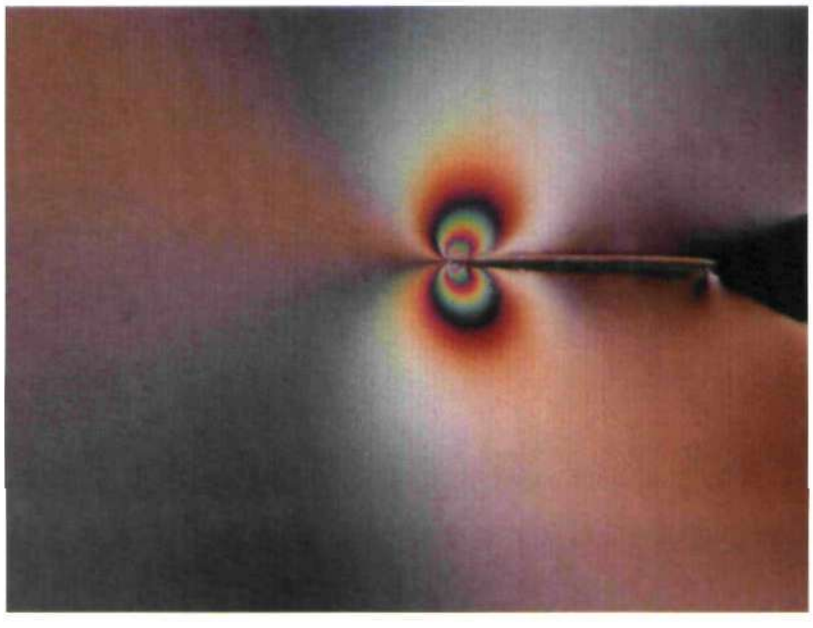

Figure 5.11 The colour image taken at the minimum load $P_{min} = 12\,N$ in dark field with white light source used to calibrate the unwrapped isochromatic phase maps in each load step for specimen PCCT-11 with the crack length of $27.6\,mm$.

5.4 Method

The fitting process fits all the experimental data points in the map of isochromatic fringe order N to the new four-parameter mathematical model (expression (4.6)) through minimising the following error function:

$$J = \iint \delta(x,y)\left(|\xi|^2 - \left|\sum_i a_i\eta_i\right|^2\right)^2 dxdy \tag{5.1}$$

where $\xi = N$ and represents the experimental photoelastic isochromatic data; $\eta_m = \sum_i a_i\eta_i$ represents the new four-parameter model, i.e. $\eta_1 = z^{-1/2}$, $\eta_2 = z^{-3/2}\bar{z}$, $\eta_3 = z^0$, $\eta_4 = z^{-1/2}\ln(z)$ and $\eta_5 = z^{-3/2}\bar{z}\ln(z)$, where a_1, a_2, a_3, a_4, a_5 are real coefficients and $a_5 = -a_4$; $\delta(x,y)$ is a switching function, the value of which is either one or zero depending on whether the corresponding pixel in the selected data or not.

By differentiating the error function and letting $^{\partial J}/_{\partial a_k} = 0$, the following is obtained:

$$\sum_i L_{ik}a_i - \sum_{ijl} M_{ijlk}a_i a_j a_l = 0 \tag{5.2}$$

where,

$L_{ik} = \iint Re(\eta_i\overline{\eta_k})|\xi|^2\,dxdy$ and $M_{ijlk} = \iint Re(\eta_i\overline{\eta_k})\,Re(\eta_j\overline{\eta_l})dxdy$

The coefficients appear as nonlinear terms in expression (5.2), and a Newton-Raphson iteration scheme was used to find a solution which was employed in calculating the constants in expression (4.6) as follows:

$$A = \frac{fk^{1/2}}{h}(a_1 - a_4 lnk), \quad B = \frac{fk^{1/2}}{h}(a_2 - a_5 lnk)$$

$$C = \frac{f}{h}a_3, \qquad D = \frac{fk^{1/2}}{h}a_4, \qquad E = \frac{fk^{1/2}}{h}a_5 \tag{5.3}$$

where k is the photographic magnification factor.

Expression (5.2) was solved by using the library 'NLPSolve' in Maple with default values. Finally, the stress intensity factors and T-stress defined in

expressions (4.8-4.11) were then evaluated. For more detailed information, please refer to the reference paper [52].

5.5 Definition of the region of validity of the model

5.5.1 Introduction

It is known that the accuracy of the solutions is dependent on the quality of fit of the four-parameter photoelastic model to the data points. Thus, before fitting the mathematical model to the unwrapped isochromatic data, attention should be given to the manner used in data collection to ensure that only valid data is collected as input into the fitting process. An important issue that has to be accounted for is the fact that in a real fatigue crack there is always some plasticity ahead of the crack tip whilst the model is based on linear elastic fracture mechanics (LEFM) and incorporates the influences of plasticity through boundary stresses applied at the elastic-plastic boundary.

In a crack with a small plastic zone three regions can be identified, as shown in Figure 5.12: a region of large strain and plasticity, where the linear elastic fracture mechanics model adopted is not valid; a region dominated by the elastic crack tip stress field, that is described by the model; and a region far away from the crack tip that is dominated by the remote stress distribution which the model does not describe. To avoid any plasticity effects and ensure the validity of the model, data points immediately ahead of the crack tip and far away from the crack tip are excluded. Data points should be collected from the second region that is dominated by the crack elastic stress field which represents the predominant regions in crack growth.

5.5.2 Preliminary study

According to the study conducted by Schroedl et al [206] , the region for data collection to calculate stress intensity factors using isochromatic data could be restricted to a core region or annulus centred at the crack tip. The boundaries of this region can only be defined qualitatively as an inner limit, to prevent data being collected from too close to the crack tip where nonlinear and three dimensional effects exist, and an outer limit where the crack tip stress equations no longer describe the state of stress in the vicinity of other singularities (pin-loading) and free boundaries [92].

The inner limit and the outer limit of the data collection zone are dependent on the crack length and the boundary conditions (i.e. they are problem dependent). The inner limit of data collection suggested by Schroedl et al [206] is a radius of 5ρ to 10ρ from the crack tip, where ρ is the notch root radius, if a notch is used to simulate the crack [206]. The outer limit proposed by Nurse and Patterson [92], is an extent of the furthest isochromatic fringe that forms a closed loop surrounding the crack tip within the field of view as shown in Figure 5.13, and other fringes that appear in view but which are not part of a closed loop are not used for data collection purposes.

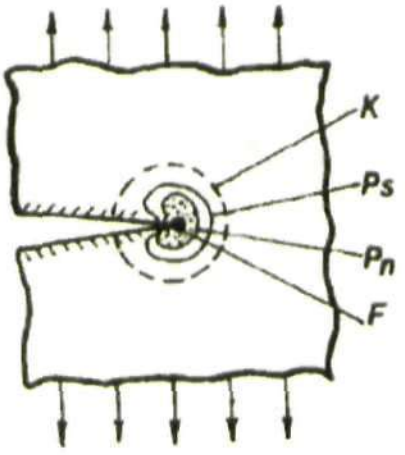

Figure 5.12 Schematic of stress zones (A Shukla and Alexander Blake, 1996): K, stress intensity zone; Ps, plastic zone (plane stress); Pn, plastic zone (plane strain); F, fracture process zone.

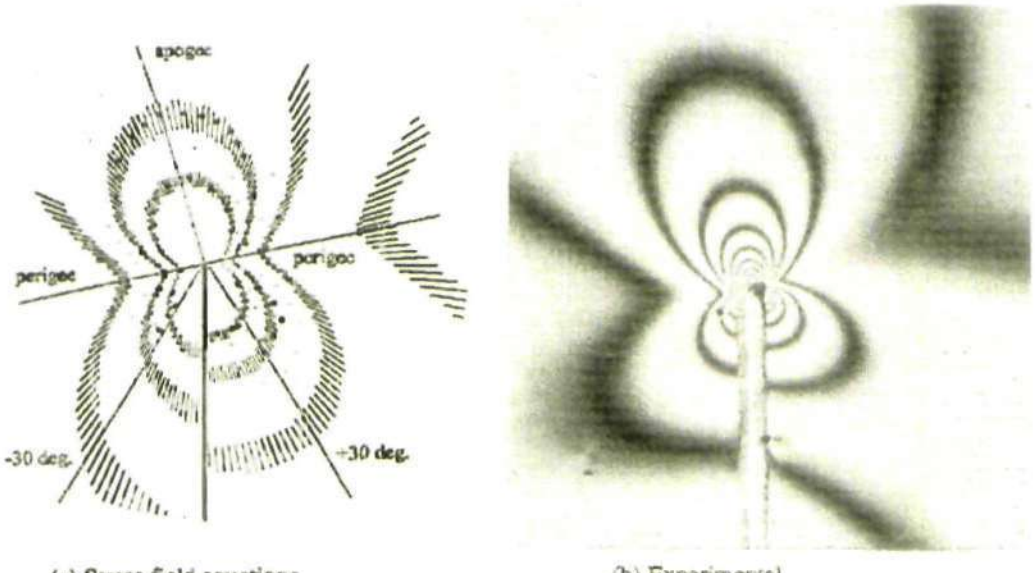

(a) Stress field equations. (b) Experimental.

Figure 5.13 Isochromatic fringe patterns for crack of length $a/w = 0.315$ in a four-point bend specimen [92].

The studies on the limit of data collection zone conducted by Schroedl et al. [206] and Nurse and Patterson [92] provided guidance for the present work. However, before setting the inner limit and the outer limit of data collection region, it is essential to study the distribution of the fringe patterns observed through the circular polariscope on the polycarbonate CT specimens.

Fringe patterns on different polycarbonate CT specimens tested under different load ratios are different, but for the CT specimens tested under the same load ratio, the fringe patterns seem similar. So, one example was selected to study the distribution of the fringe patterns on the entire range of CT specimens, PCCT-5 tested under the load ratio of 0.1, see Figure 5.14. Figure 5.14 gives two images showing the complete set of fringe patterns on the specimen PCCT-5 with a crack length of $35\,mm$. The fringe patterns were recorded in the circular dark-field (top) and light-field (bottom) polariscope (transmission). The absolute fringe order (integer and half order) for most fringes on the fringe patterns have been marked.

Figure 5.14 reveals the precise nature of the fringe patterns for the polycarbonate CT specimens tested under cyclic loading with load ratio $R = 0.1$. The shape of fringe patterns is thought to be mainly affected by the following factors: the specimen geometry, the external boundary conditions and crack tip singularities.

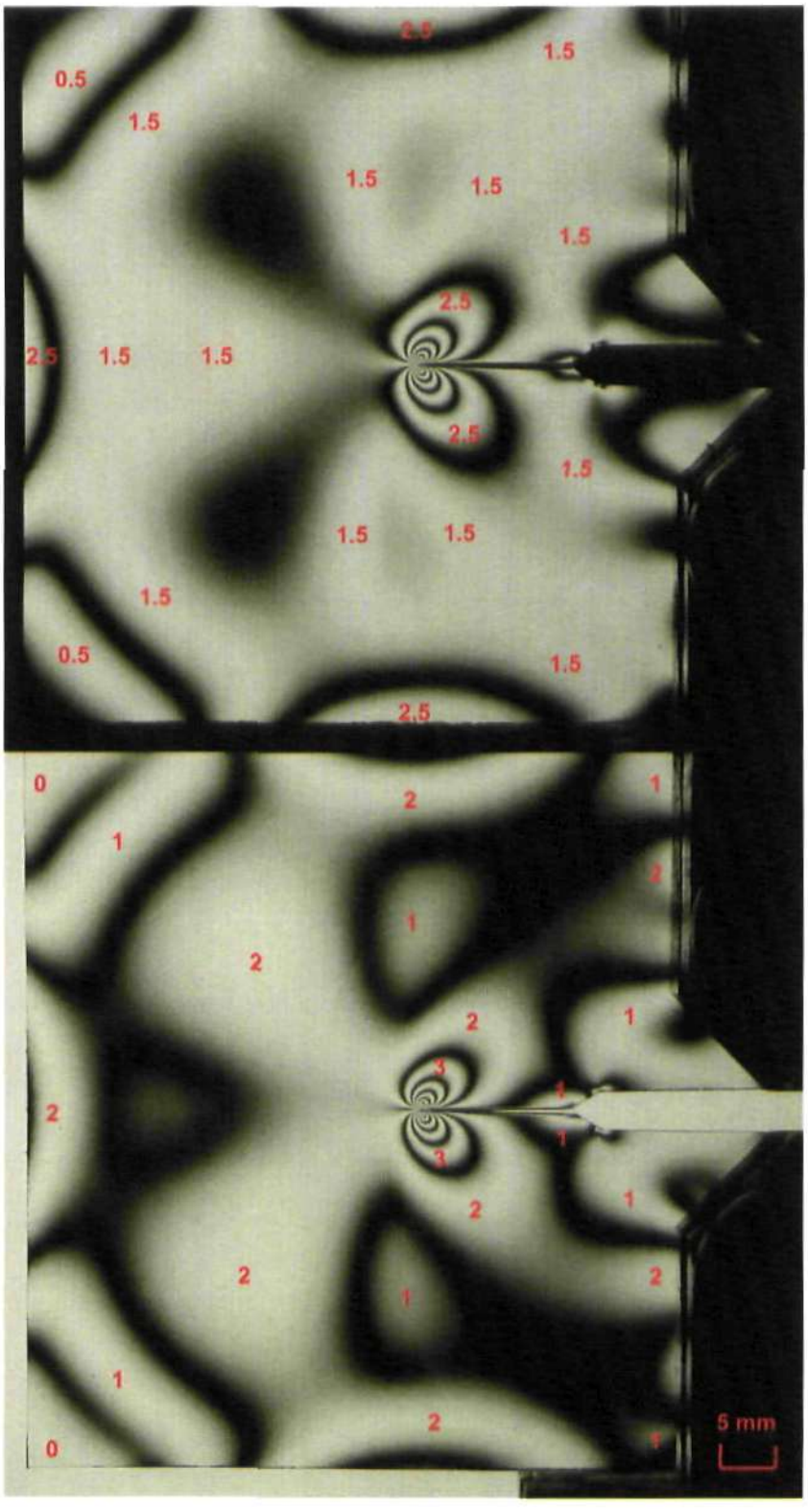

Figure 5.14 Fringe patterns observed in dark-field (top) and light-field (bottom) circular polariscope on specimen PCCT-5 with a crack length of $35.0\ mm$ at $P = 120\ N$ (Loading condition: $R = 0.1$, $P_{max} = 120\ N$, $0.5\ HZ$).

Hence, the entire fringe pattern can be divided into three parts: Zone A, Zone B and Zone C, as shown in Figure 5.15.

In the Zone A, the boundary effects are pronounced and the fringe pattern and stress distribution were affected mostly by the external specimen boundaries rather than the crack. So, it is reasonable to exclude data in Zone A.

In the Zone B, the value of the fringe orders is approximately constant around 2. Data was not collected from Zone B. Furthermore, Zone B could be recognized as a transitional area between Zone A and Zone C.

In the Zone C, it is easy to see that the effect of crack singularities is distinct.

Data used in the next step (the fitting process) will be therefore collected only from this Zone C. But the outer fringe loops in Zone C where the external boundary effects may be pronounced should also be excluded. In this region, it can be observed that all the fringes form a closed loop surrounding the crack tip with the fringe order increasing when approaching closer to the crack tip.

The above discussion outlines the preliminary analysis used to identify the data collection zone through studying the distribution of the fringe patterns on the CT specimen. Three regions have been identified with different fringe distribution. This analysis can serve as a guide when selecting the valid isochromatic fringe data. The following section will outline a further study on the data collecting rules employed in this thesis.

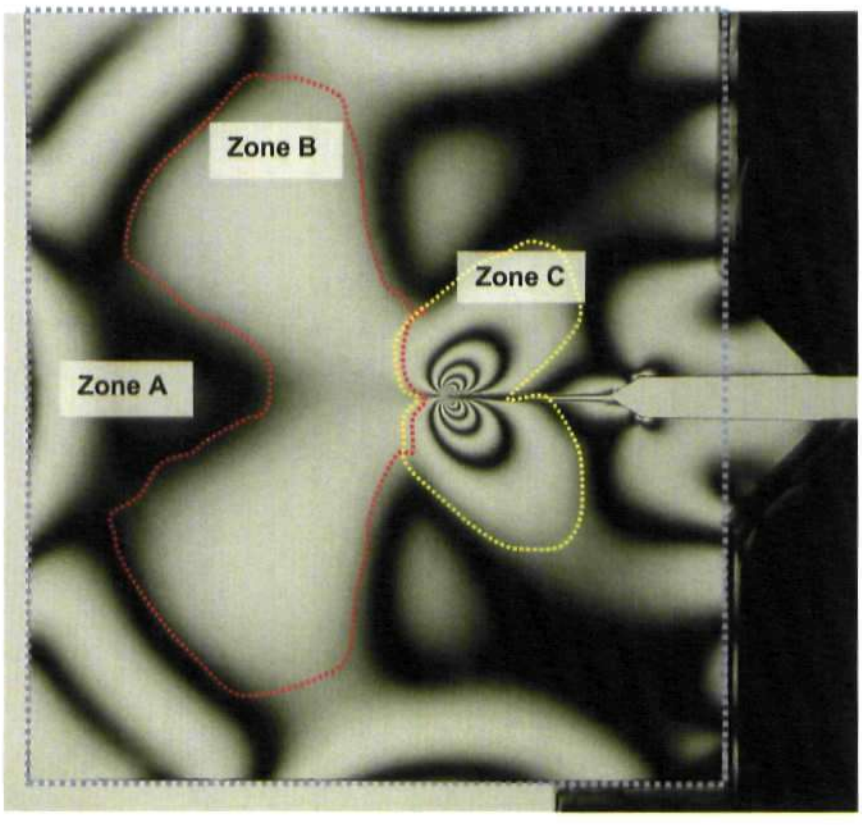

Figure 5.15 The entire fringe pattern is divided into three parts: Zone A, Zone B, Zone C. In different part, fringe pattern has different shape and was affected by different factors, i.e. external boundaries or crack singularities.

5.5.3 Data collection zone

According to the previous section, data should be collected from Zone C, see Figure 5.15. The data collection zone can be defined by two limits, i.e. the inner limit and the outer limit.

The inner limit of data collection was a rectangular strip, as illustrated in Figure 5.16. The width of the rectangle and the distance from the crack tip to the short edge of the rectangle is equal to twice the plastic zone size. The plastic zone size in this study was estimated using the approach proposed by Dugdale [132] for plane stress, given by

$$r_p = \frac{\pi}{8}\left(\frac{K}{\sigma_{ys}}\right)^2 . \tag{5.4}$$

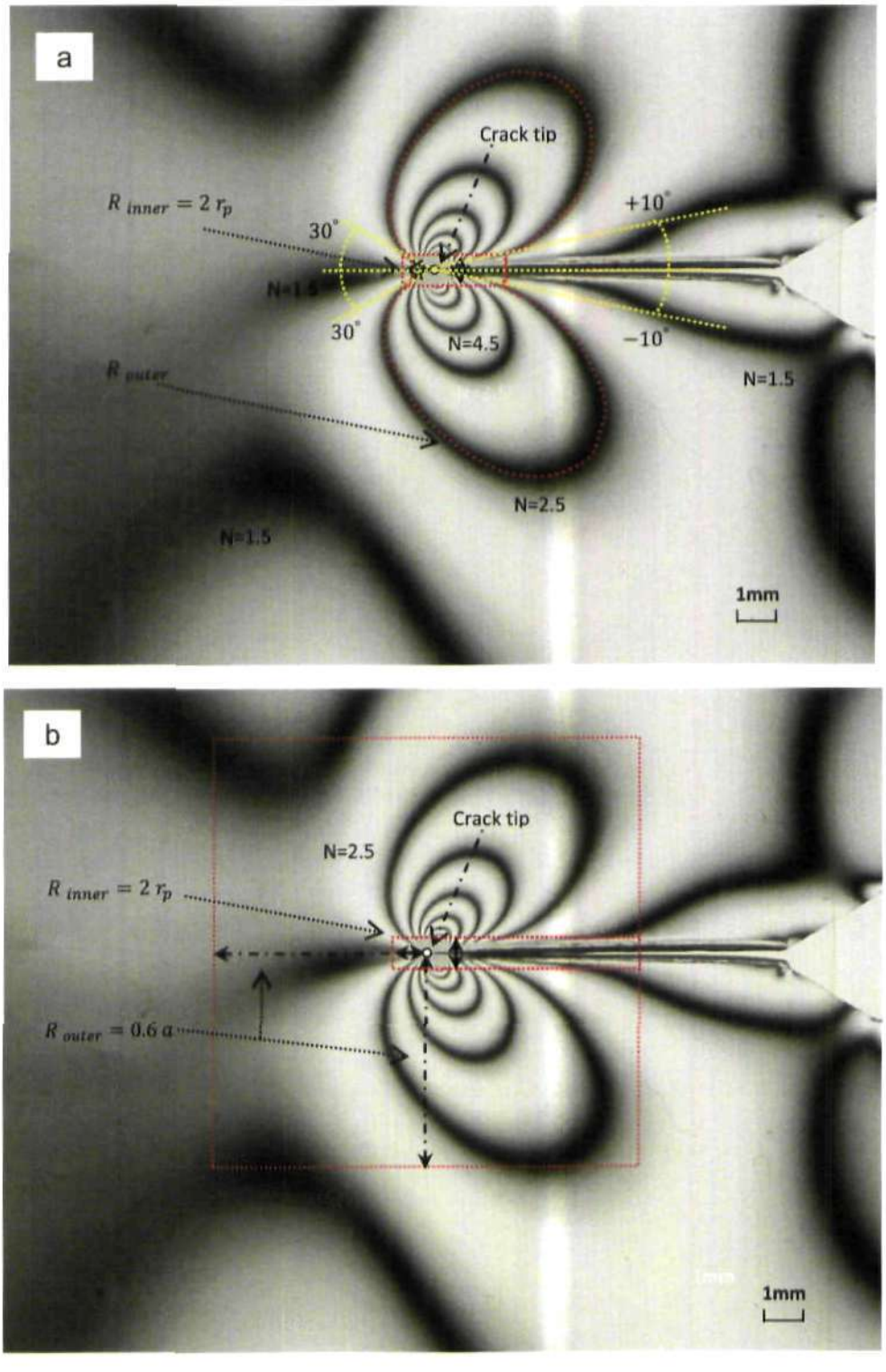

Figure 5.16 Schematic illustration for the valid region of data collection used to calculate stress intensity factors and T-stress. The valid data region is defined by two limits, i.e. the inner limit and the outer limit. The inner limit is a rectangle with the width and the distance from the short edge to the crack tip of twice the Dugdale plastic zone size r_p. The outer limit is: (a) the extent of one fringe with the order of 2.5; (b) bounded by a rectangle with the length and width of $0.6\,a$ ('a' is the crack length). Fringe pattern observed in light field on the specimen PCCT-11 with the crack length of $29.3\,mm$ at $P = 120\ N$ (loading condition: $R = 0.1$, $P_{max} = 120\,N$, $0.5\,HZ$).

The plastic zone width (equivalent to the crazed region) in polycarbonate specimens can be directly visualised by confocal laser scanning microscopy (CLSM). Figure 5.17 shows three CLSM images for the $35\ mm$ crack in the specimen PCCT-5. Figure 5.17(a) gives a standard optical image showing the photoelastic isochromatic fringes around the crack tip. It is difficult to detect the forward and lateral extent of the plastic zone, or identify the crack tip in this image. In contrast, Figure 5.17(b) clearly shows those regions around the crack where surface displacement has occurred. Figure 5.17(c) is the 3D visualization of Figure 5.17(b). It demonstrates an interesting interference phenomenon caused by imaging through the thickness of the PC specimen; the crazed material stands out proud of the surface compared with the uncrazed polymer. It has been reported that there are voids inside the crazed region with the void contents up to 45% in polycarbonate; the existence of voids gives the crazed region a lower density and a lower refractive index [207]. Therefore, this phenomenon is believed to be due to the change in refractive index of the crazed regions. The change in refractive index can, in conjunction with the 3D imaging capability of modern CLS microscopes, provide images in which the crazed region is apparently elevated out of the surface as a contiguous block of material. The crazed region's width and extent ahead of the surface crack tip can then be easily measured. This approach can provide a check on the Dugdale plastic zone estimate and on the chosen inner mask size. In this case, the width of the crazed zone is about $0.61\ mm$ at the craze tip, compared with a Dugdale estimate of $0.57\ mm$ for forward extent of the plastic zone. The mask should be applied over a region larger than the size of this width, i.e. $0.61mm$ and of course larger than the estimated Dugdale plastic zone. Considering this

fact, a value of twice the Dugdale plastic zone would be used to set the inner limit in practice.

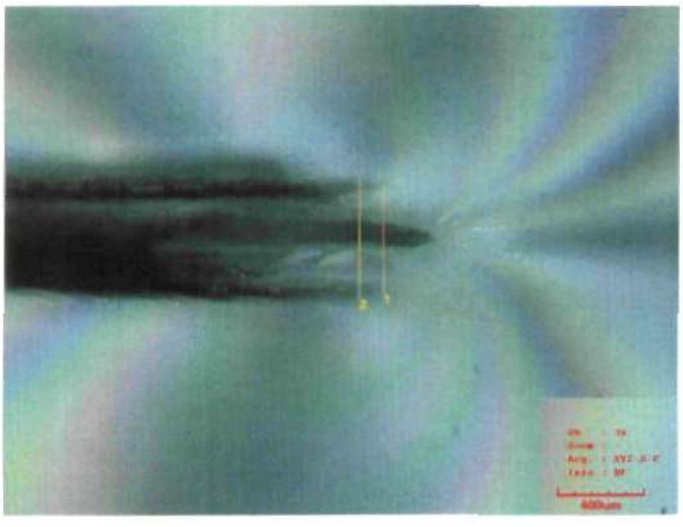

Figure 5.17(a)
Photoelastic isochromatic frnge patterns for a $35\ mm$ *crack in a polycarbonate CT* specimen.

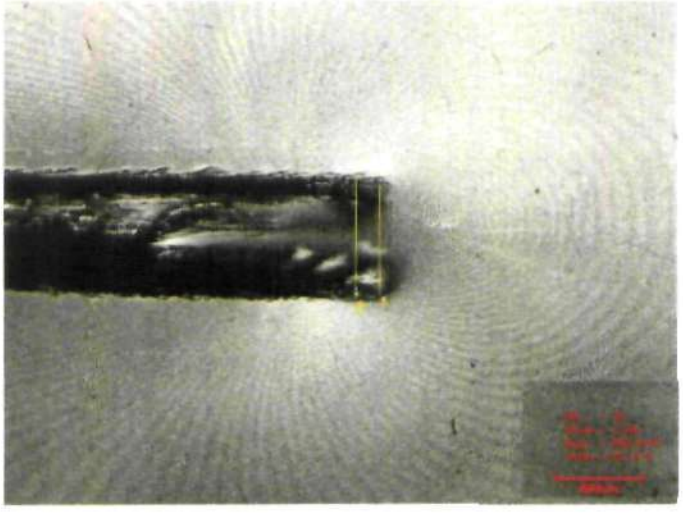

Figure 5.17(b)
CLSM image for a $35\ mm$ crack in a polycarbonate CT specimen which clearly shows the craze extent.

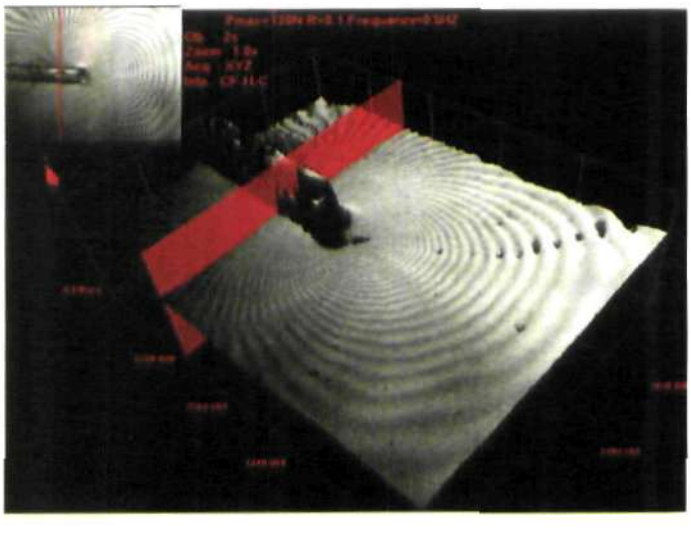

Figure 5.17(c)
3D CLSM image shows clear visualisation of the manner in which the crazed region is 'lifted' out of the surface due to the change in refractive index.

Figure 5.17 The CLSM images for the crack of $35\ mm$ in the specimen PCCT-5.

An interesting interference fringe pattern (Fizeau fringes [208]) can also be observed around the crack tip in Figures 5.17(b) and (c). This interference pattern arises because the CLS microscope is being used in reflection and focussed progressively through the full depth of the specimen. Reflections from the top and bottom surface create an interference pattern that is related to the out-of-plane displacement at the surface, i.e. to the Poisson's contraction associated with the plastic zone. This is analogous to the output from the method of caustics and the change in direction of the fringe pattern behind the crack tip (from pointing forwards to pointing backwards) reflects the shear stress acting along the crack boundary [209]. This provides additional confirmation of the validity of considering a shear stress intensity factor K_S which is one of the novel factors in this new four-parameter analysis of crack tip stresses.

The another reason to set the inner limit to be twice the Dugdale plastic zone size is that when using the MATLAB program RICO to extract the isochromatic data, see Figure 5.9, the inner mask consisting of the plastic region and distorted regions was used and was larger than the Dugdale plastic zone, but less than twice Dugdale plastic zone. The inner limit for data collection zone should be larger than the inner mask. Hence, twice the Dugale plastic zone size was chosen for the inner limit. Larger inner limit could be used, but it is too strict to set a larger inner limit which may severely limit the important data region at lower load levels.

The outer limit can be defined by a fringe loop or bounded by a rectangle as illustrated in Figure 5.16. The following work was done to identify how best to choose the form for the outer limit as either a rectangle or a fringe loop, and involved studying the quality of the fit. The outer limit will then be chosen to be whichever gives the best quality of the fit between the experimental photoelastic

data and the analytical data evaluated from the model. To explain this clearly, one set of six-stepped phase-shifted photoelastic data was selected from the specimen PCCT-11 with the crack length of $29.3\ mm$ under the load of $120\ N$, nominal $K_I = 1.9\ MPa.m^{0.5}$.

Following the work by Nurse and Patterson [92], the discrepancy, or quality of the fit between the experimental isochromatic data and the analytical data is measured through the normalised residual of the fitting, the normalised mean error and the variance,

$$residual \qquad \varrho = \frac{\sum({x_0}^2 - x^2)^2}{\sum({x_0}^2)^2}, \tag{5.5}$$

$$Mean \qquad \mu = \frac{1}{n-4}\sum\frac{x_0 - x}{x_0}, \tag{5.6}$$

$$variance \qquad s^2 = \frac{1}{n-4}\sum\left(\frac{x_0 - x}{x_0} - \mu\right)^2, \tag{5.7}$$

where, x_0 represents the real experimental isochromatic data; x represents the analytical data; n is the total number of data points.

The best solution can be identified as the one which gives smallest value of the normalised residual and the smallest 95% confidence limit, which is defined as [92],

$$(1 + \mu - 2s)K < K < (1 + \mu + 2s)K, \tag{5.8}$$

where K represents K_F, K_R, K_S, T-stress in this work.

5.5.3.1 Outer limit defined by a fringe-loop

The map of the isochromatic data for the example is shown in Figure 5.18. The minimal fringe order on the isochromatic pattern is larger than one. Seventeen different data zones with a fixed inner limit but different outer limits were

considered. Those outer limits were bounded by different fringe loops with fringe order varying from $N = 1.5$ to $N = 5.5$ in increments of 0.25. The results were presented in Figure 5.19 and Table 5.2 with the best solution highlighted in the table.

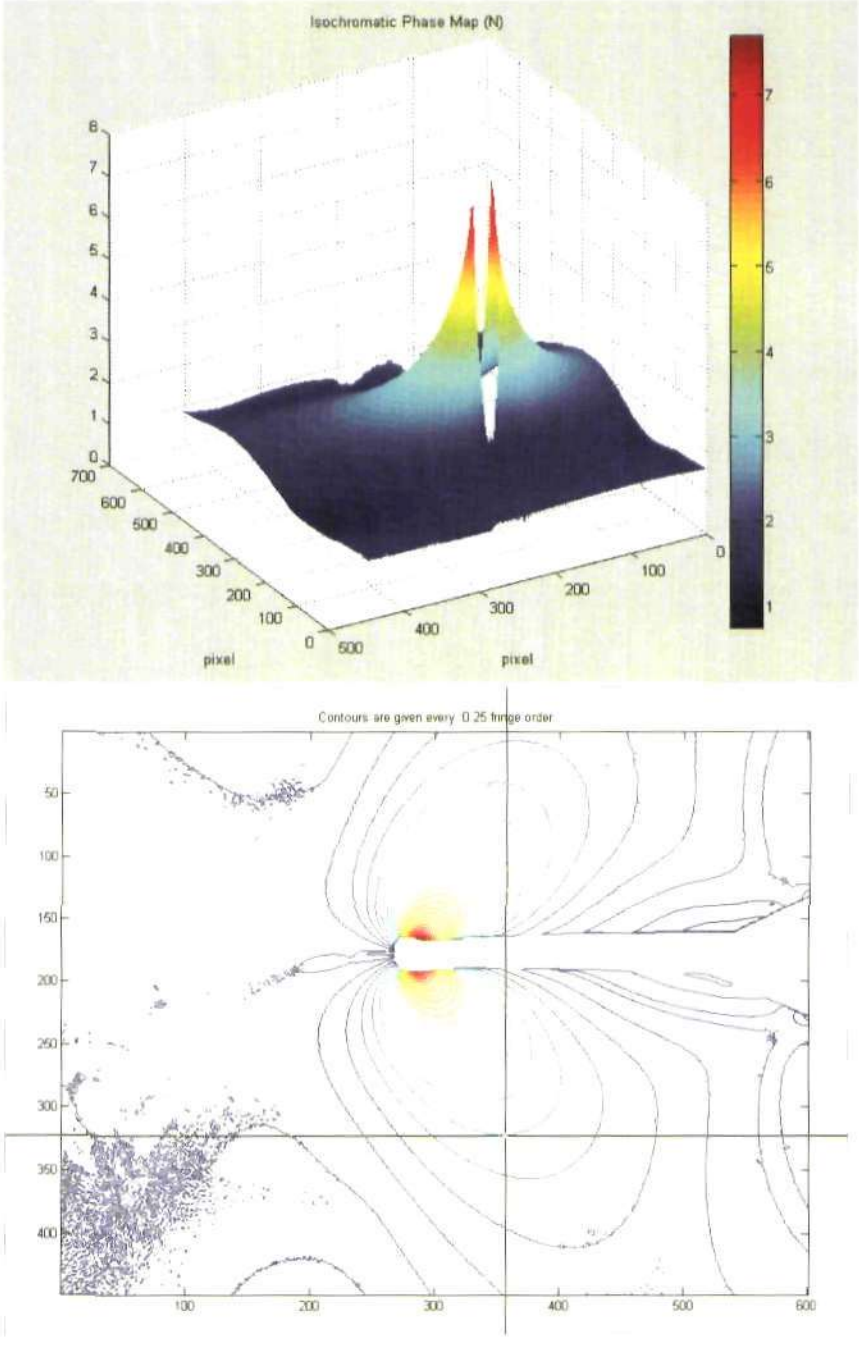

Figure 5.18 The map of isochromatic data for the selected set of six-stepped phase-shifted photoelastic data from specimen PCCT-11 with a crack length of $29.3\ mm$ at $P = 120\ N$ (loading condition: $R = 0.1$, $P_{max} = 120\ N$, $0.5\ HZ$).

Figure 5.19 shows clearly the trend for the quality of the fit for different data zones characterised by a single fringe order defining a fringe loop as the outer limit. Figure 5.19 and Table 5.2 show that most of the values of the normalised residual, mean μ and standard deviation are smaller than 0.004, 0.02 and 0.04 respectively, except those with $N \approx 1.5$ and $N = 1.75$. The highest value for the normalised residual and standard deviation occurred at $N = 1.5$. The results indicate that those isochromatic data with $N < 2$ should be excluded from the fitting process to avoid a poor quality of the fit, as indicated by Zone I in Figure 5.19(a). These fringes do not form a closed loop with regard to the crack tip and reflect the boundary effect clearly as previously discussed. Starting from approximately the fringe loop with $N = 2$, those fringes with $N >= 2$ are closed fringe loops with regard to the crack tip. The quality of the fit becomes better as N increases from $N = 2$ until $N = 3.5$, as indicated by Zone II in the Figure 5.19(a). In the Zone III, the quality of the fit remains good with only small changes as N varies from $N = 3.5$ to $N = 5$. Zone IV also gives good quality fits, but the number of data point is relatively small (less than 1,000). It is thought that to perform a high quality fit, sufficient data points are required to minimise the effect of the noise that exists in the experimental data. Therefore, the 'best' solution should be selected from Zone III with $3.5 \leq N \leq 5$. The value of $N = 4$ represents a good compromise.

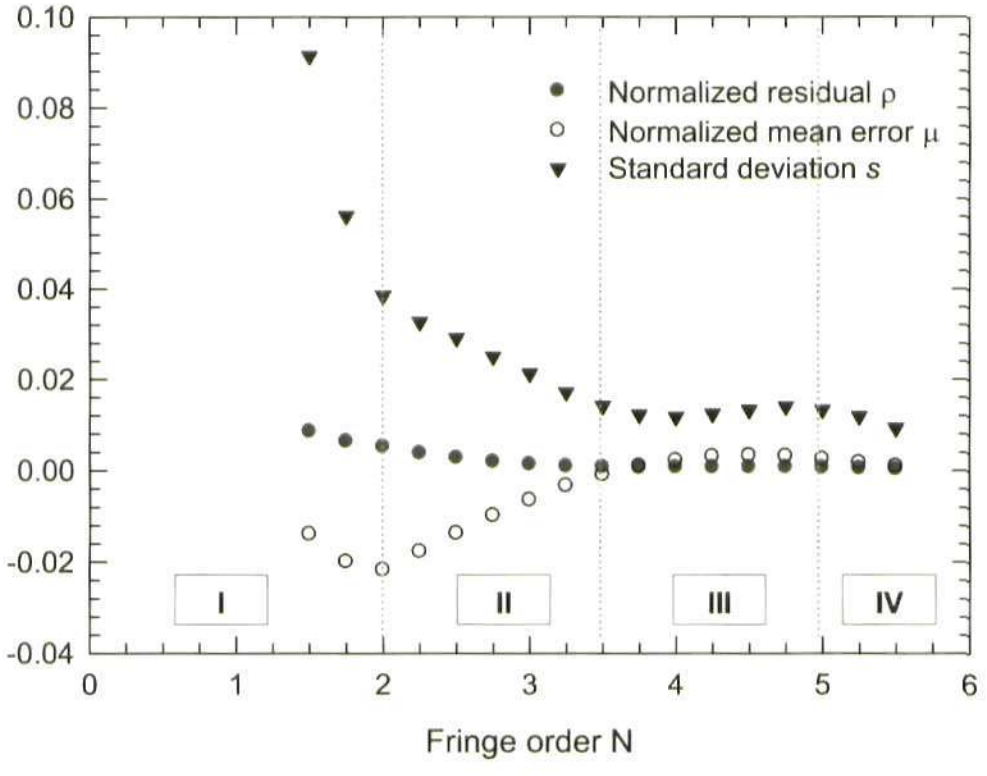
0.10
0.08
0.06
0.04
0.02
0.00
-0.02
-0.04
0
1
2
3
4
5
6
Normalized residual ρ
Normalized mean error μ
Standard deviation s
I
II
III
IV
Fringe order N

(a)

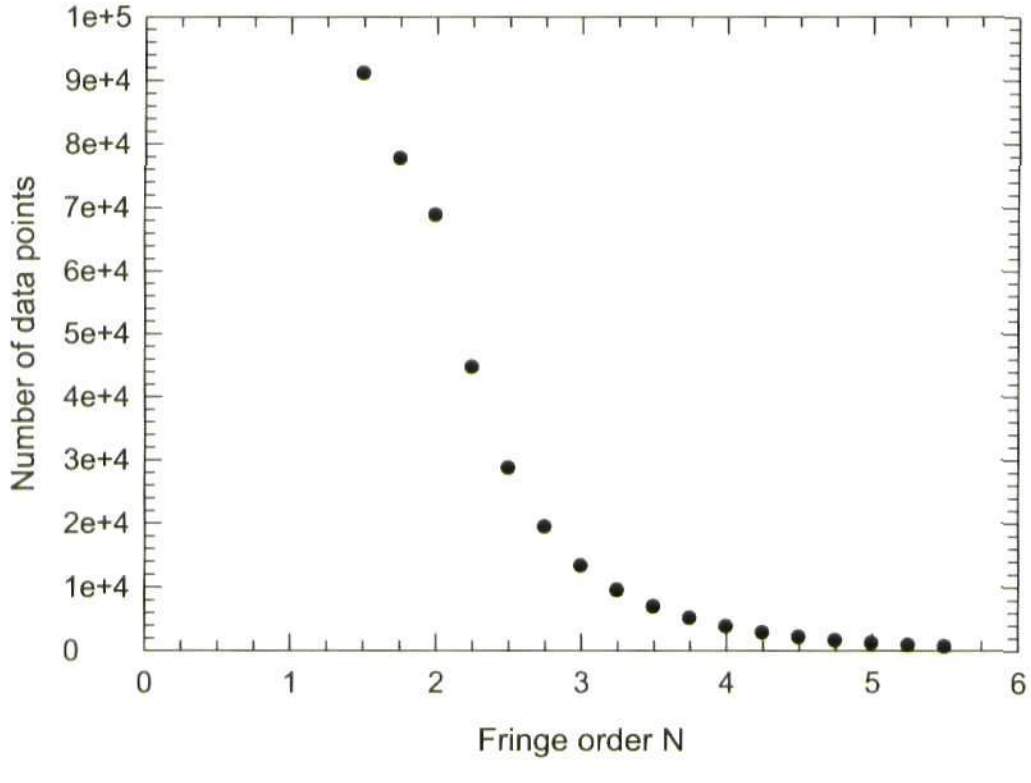
1e+5
9e+4
8e+4
7e+4
6e+4
5e+4
4e+4
3e+4
2e+4
1e+4
0
Number of data points
0
1
2
3
4
5
6
Fringe order N

(b)

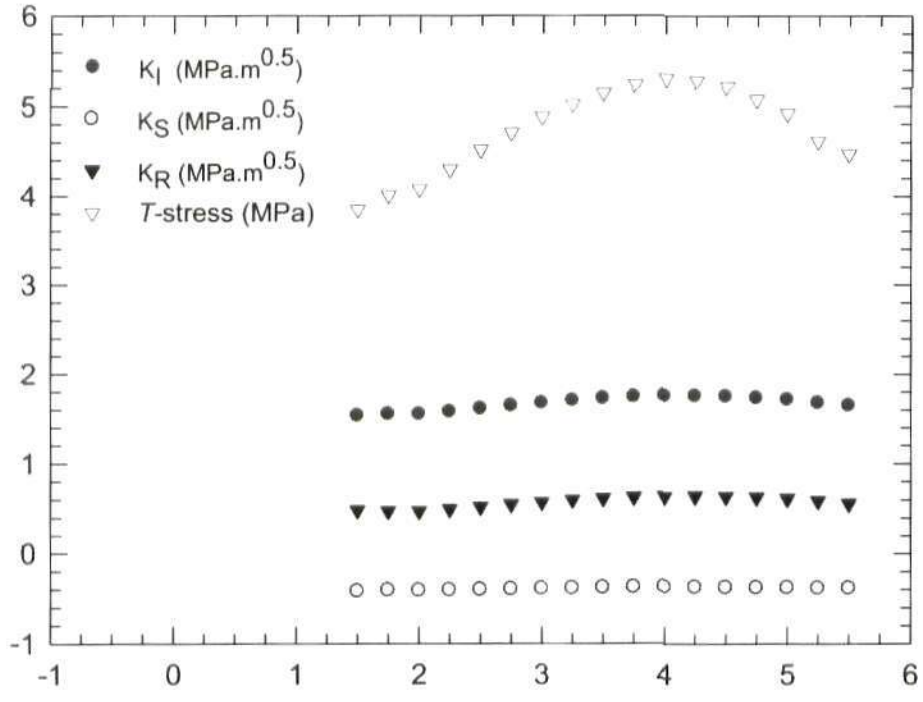

(c)

Figure 5.19 Plotting of the normalised residual, mean error, standard deviation, number of data points and solutions for the four parameters K_F, K_R, K_S, T-stress against fringe order N of the fringe loop defining the corresponding data zone's outer limit.

Fringe order N	Number of data points	residual ϱ	Mean μ	standard deviation s	K_F	K_S	K_R	T [MPa]
					$[MPa.m^{0.5}]$			
1.50	91006	0.00860	-0.0138	0.0914	1.533	-0.420	0.487	3.846
1.75	77598	0.00643	-0.0199	0.0561	1.551	-0.408	0.476	4.008
2.00	68749	0.00521	-0.0217	0.0385	1.550	-0.412	0.476	4.077
2.25	44608	0.00386	-0.0176	0.0327	1.577	-0.409	0.497	4.300
2.50	28590	0.00282	-0.0137	0.0291	1.611	-0.404	0.523	4.515
2.75	19318	0.00200	-0.0098	0.0250	1.644	-0.398	0.549	4.709
3.00	13206	0.00142	-0.0064	0.0213	1.674	-0.392	0.573	4.884
3.25	9413	0.00100	-0.0033	0.0172	1.701	-0.388	0.597	5.021
3.50	**6832**	**0.00078**	**-0.0009**	**0.0142**	**1.725**	**-0.383**	**0.615**	**5.145**
3.75	5048	0.00070	0.0010	0.0122	1.744	-0.378	0.630	5.240
4	3721	0.00070	0.0022	0.0117	1.758	-0.373	0.638	5.310
4.25	2765	0.00076	0.0031	0.0124	1.758	-0.374	0.642	5.285
4.5	2045	0.00080	0.0033	0.0133	1.751	-0.376	0.639	5.220
4.75	1507	0.00081	0.0032	0.0140	1.735	-0.380	0.632	5.075
5	1087	0.00069	0.0025	0.0133	1.716	-0.380	0.615	4.920
5.25	769	0.00052	0.0018	0.0118	1.677	-0.388	0.591	4.616
5.5	538	0.00032	0.0010	0.0093	1.650	-0.385	0.559	4.471

Table 5.2 Results for different data zones with different outer limit defined by fringe order N from processing the set of data from the specimen PCCT-11 with a crack length of $29.3\ mm$ at $P = 120\ N$, nominal $K_I = 1.932\ MPa.m^{0.5}$.

Additionally, values of $\mu \pm 2s$ for the cases with $3 \leq N$ are smaller than 0.05, especially in Zone III ($3.5 \leq N < 5$) where they are less than 0.03 (3%), meaning that solutions vary within a very narrow range $\pm 3\%$ with 95% confidence. The theoretical isochromatic maps predicted by the new model were plotted together with the experimental data for $N = 3$ and $N = 3.5$ in Figure 5.20. As can be observed, Figure 5.20 reveals that theoretical isochromatic maps are practically identical to the experiment inside the data

collection zone, thus indicting a good quality fit between the model and the experimental data.

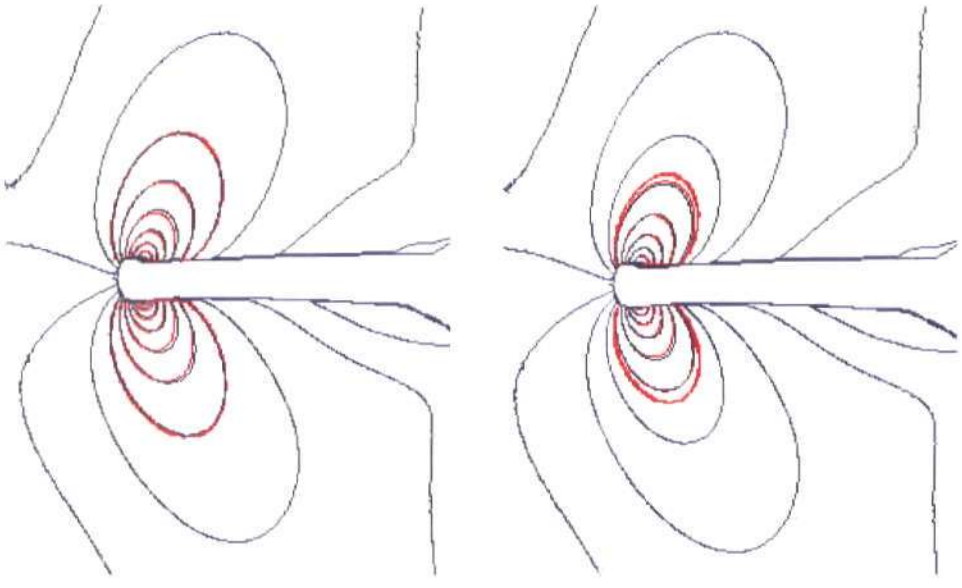

(a) (b)

Figure 5.20 Isochromatic fringe patterns predicted by the model (red solid line) and the actual experimental data (blue solid line) for the crack of length 29.3 mm in the CT specimen PCCT-11: (a) $N = 3$, (b) $N = 3.5$.

5.5.3. 2 Rectangular-shaped outer limit

For simplicity, a special case of a rectangle, i.e. the square was used to illustrate this case. The size of the square is $2R_{outer} \times 2R_{outer}$. R_{outer} is illustrated in Figure 5.16. Seven different data zones were studied with a fixed inner limit but different outer limits. The rectangular-shaped outer limits have different sizes with R_{outer} varying from $0.1a$ to $0.7a$ in increments of $0.1a$ (a represents the crack length, $a = 29.3\,mm$ in this case), see Figure 5.21. The results from processing the set of data are presented in Table 5.3 and Figure 5.22. Table 5.3 and Figure 5.22 show that almost all the standard deviations

have values larger than 0.08, except the one at $R_{outer} = 0.1a$. For $R_{outer} = 0.1a$, the standard deviation is 0.034, which is still higher than those at Zone III shown in figure 5.19(a). It is known that a high standard deviation indicates that the data is spread out over a large range of values. So, poor fit quality occurs when picking experimental data from a rectangular-shaped data zone around the crack tip.

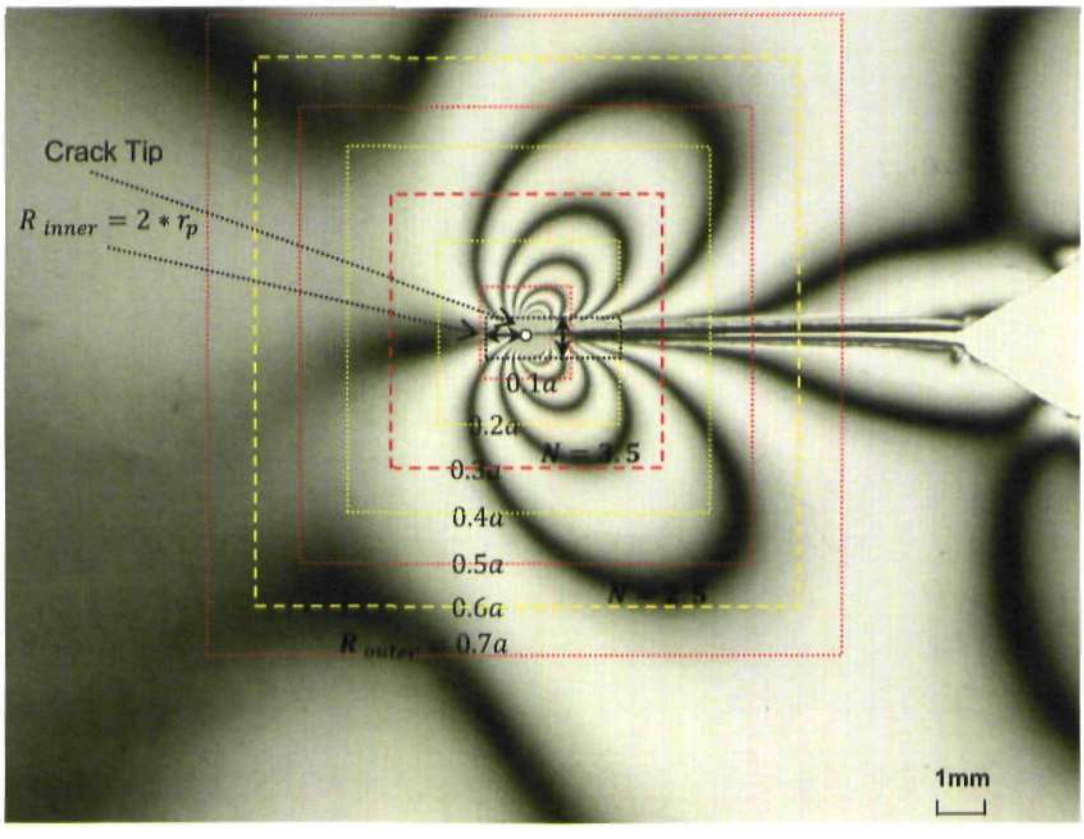

Figure 5.21 Schematic illustrations for the rectangular outer limits with R_{outer} from $0.1\ a$ to $0.7a$ (a is the crack length). Fringe pattern observed in light field on the specimen PCCT-11 with a crack length of $29.3\ mm$ at $P = 120\ N$ (loading condition: $R = 0.1$, $P_{max} = 120\ N$, $0.5\ HZ$).

R_{outer}	Number of data points	residual ϱ	Mean μ	standard deviation s	K_F	K_S	K_R	T $[MPa]$
					$[MPa.m^{0.5}]$			
0.7a	125775	0.0247	0.0475	0.1995	1.437	-0.477	0.583	2.860
0.6a	94342	0.0192	0.0445	0.1885	1.476	-0.465	0.587	3.090
0.5a	64021	0.0138	0.0406	0.1726	1.521	-0.451	0.599	3.346
0.4a	40322	0.0092	0.0353	0.1517	1.571	-0.437	0.619	3.624
0.3a	22007	0.0052	0.0282	0.1224	1.631	-0.423	0.648	3.964
0.2a	9125	0.0021	0.0178	0.0777	1.693	-0.410	0.675	4.410
0.1a	1559	0.0008	-0.0006	0.0344	1.664	-0.404	0.580	4.918

Table 5.3 Results for different data zones with rectangular-shaped outer limit characterised by R_{outer} from processing the set of data from specimen PCCT-11 with the crack length of $29.3\ mm$ at $P = 120\ N$, nominal $K_I = 1.932\ MPa.m^{0.5}$.

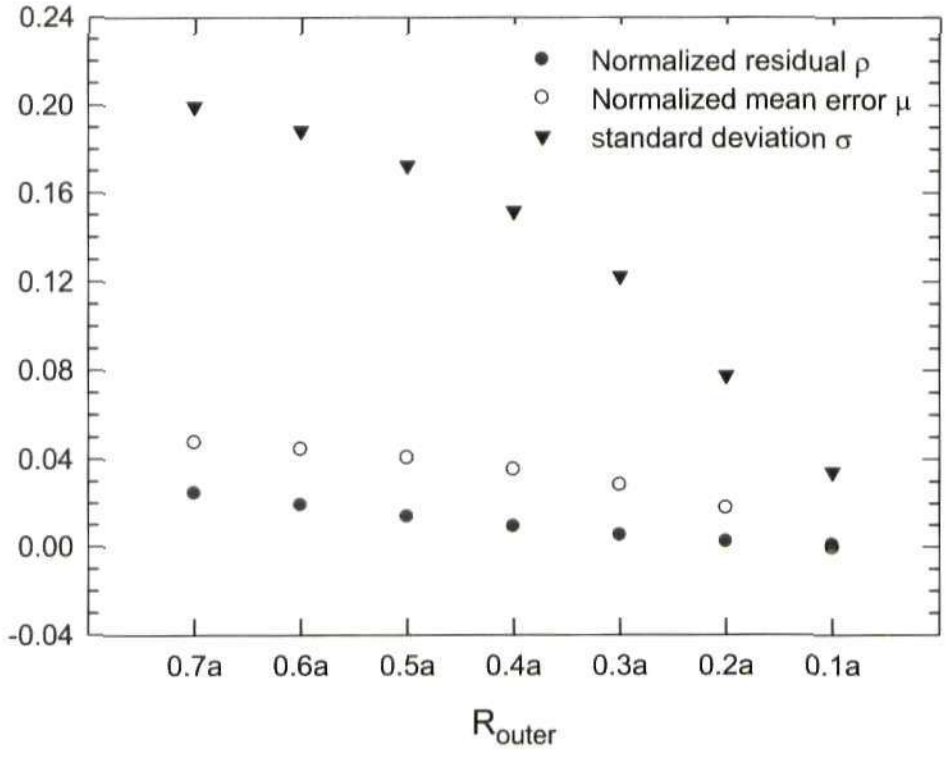

(a)

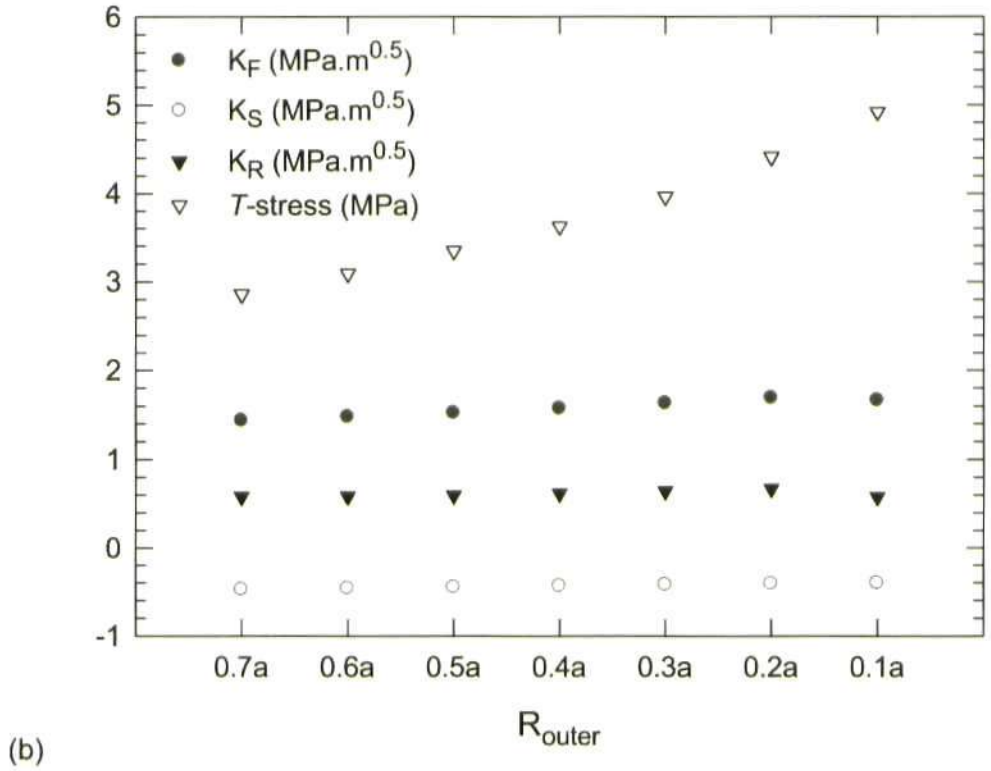

(b)

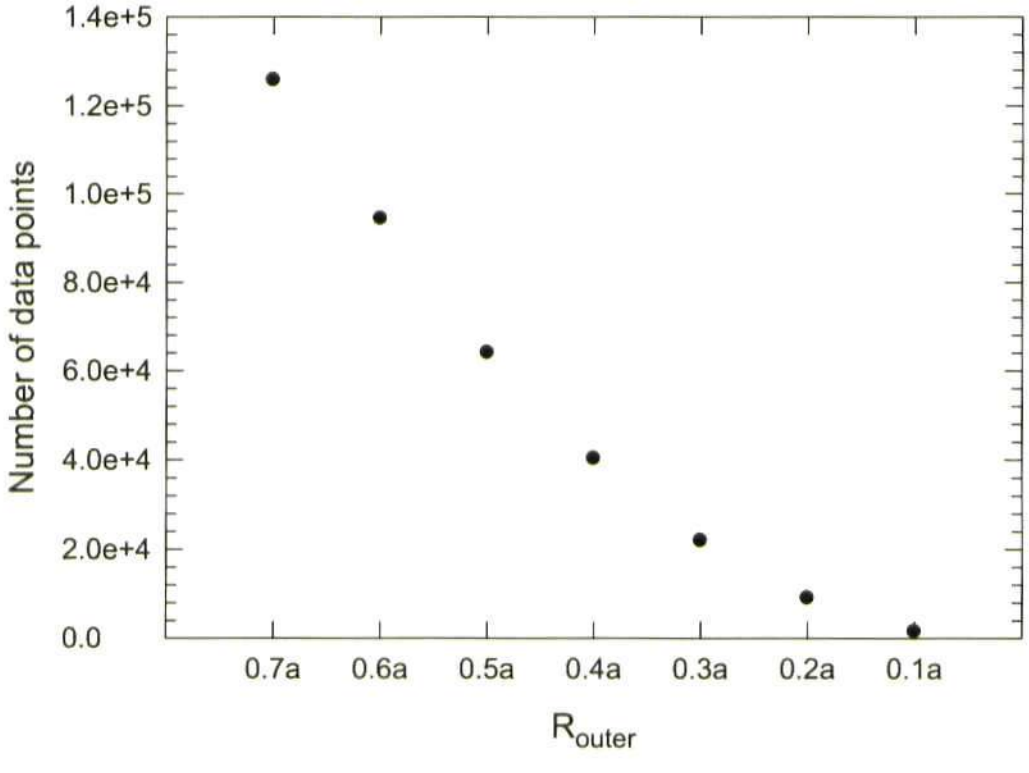

(c)

Figure 5.22 Plotting of the normalised residual, mean error, standard deviation, number of data points and solutions for the four parameters K_F, K_R, K_S, T-stress against R_{outer}.

Comparing the results in Table 5.3 to the results in the previous part listed in Table 5.2, it is obvious that a data zone defined by an 'appropriate' fringe loop provides a good set of data, which can produce a 'best' quality fit and solution.

The following study provides further proof to this conclusion. Figure 5.21 indicates that the data zone bounded by the rectangular with $R_{outer} = 0.6a$ includes all the data points with $N \geq 2.5$. However, as listed in Table 5.2 and Table 5.3, the normalised mean error μ and standard deviation s for the rectangular data zone are 0.0445 and 0.1885 respectively. These values for the zone bounded by the fringe loop with $N = 2.5$ are -0.0137, 0.0291 respectively. Obviously, the quality of the fit for the data zone with the outer limit set as the fringe-loop is significantly better than that for the rectangle-bounded data zone. In order to see which part of the rectangle is responsible for introducing the poor solution, we can calculate the quality of the fit at different regions inside the rectangle. Table 5.4 lists the calculated quality of the fit for different regions inside the rectangle. It shows (1) that the quality for the region I with $N \geq 2.5$ is the best, and the standard deviation is 0.0413; (2) the fitting quality for the regions II, III and IV (outside the region I) is poor, and the standard deviations are larger than 0.2; (3) the poor fit was mainly caused by collecting isochromatic data from the region III in front of the crack tip.

Region	Number of data points	ϱ,	μ,	s
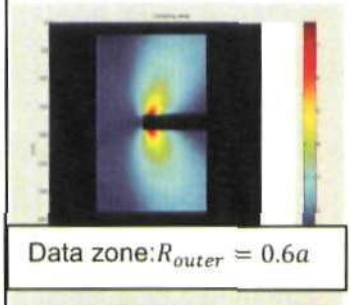 Data zone: $R_{outer} = 0.6a$	94198	0.0019,	0.0445,	0.1885
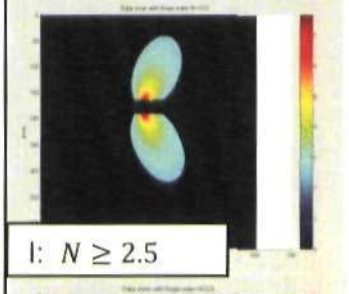 I: $N \geq 2.5$	28573	0.0007,	-0.0024,	0.0413
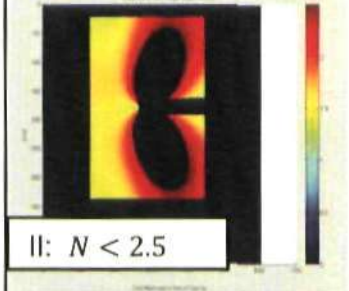 II: $N < 2.5$	65625	0.0048,	0.0648,	0.2211
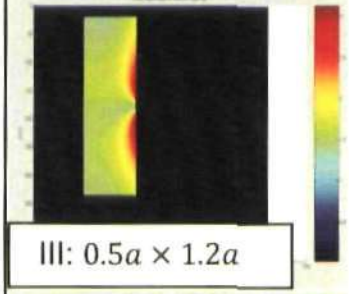 III: $0.5a \times 1.2a$	42500	0.0385,	0.1363,	0.2406
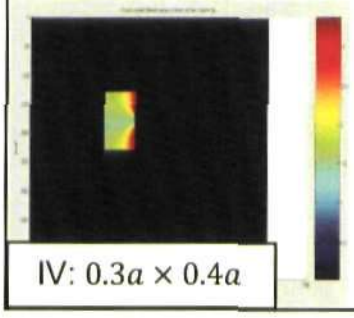 IV: $0.3a \times 0.4a$	7853	0.0023,	0.0588,	0.2078

Table 5.4 Results of the fitting process in different regions inside the rectangle.

5.6 Crack tip location

The coordinates of the crack tip are required when fitting the experimental data to the mathematical model, i.e. they are provided as inputs to the fitting program. For the annealed specimens in the present work, the coordinates of a crack tip were picked up manually, using the following process: a) read and display one of the six-stepped phase-shifted images using the MATLAB program; b) click the point on the image which is regarded as the crack tip via direct observation and at the same time the MATLAB program returns the coordinates of the point. The returned coordinates are its row number i and column number j. So, the crack tip coordinates are $x_{tip} = j, y_{tip} = i$ in pixels with the origin at the upper left corner of the image.

For the example used in the above section 5.3, the crack tip was recognized to be $x_{tip} = 572\ pixel$, $y_{tip} = 356\ pixel$ from the image shown in Figure 5.16 (the magnification factor $k = 0.0178mm/pixel$). As discussed in the previous section 5.3, the valid data zone would be defined by the inner limit $r_{inner} = 2 * r_p$, and the fringe-loop outer limit by fringe order $N = 3.5$. The number of data points is 6,832. Following the procedure introduced previously, fitting the model to the data collected provides the four stress-based parameters.

Incorrectly locating the crack tip might introduce an error to the final calculations. In order to assess the severity of the error arising from the manual crack tip identification, an error analysis was done. The analysis was performed by shifting the crack tip coordinates a small distance. Both x and y coordinates were independently shifted. Table 5.5 lists the results when the crack tip was shifted up, down, left and right by two pixels and four pixels. The correct location of the crack tip was recognized by the minimal normalised mean error

and standard deviation and was highlighted in the Table 5.5. The table also indicates that the solutions do not change much when the crack tip was shifted a bit. Therefore, the method by picking up the crack tip directly from optical images of the fringe pattern was deemed to be sufficiently accurate.

Crack tip coord. [pixels]		K_F	K_S	K_R	T	*Mean*	*Standard deviation*
x_{tip}	y_{tip}	$[MPa.m^{0.5}]$	$[MPa.m^{0.5}]$	$[MPa.m^{0.5}]$	$[MPa]$	μ	s
572	352	1.736	-0.390	0.682	4.827	-0.0019	0.0266
572	354	1.728	-0.386	0.639	5.033	-0.0013	0.0193
572	**356**	**1.725**	**-0.383**	**0.615**	**5.145**	**-0.0009**	**0.0142**
572	358	*1.726*	*-0.384*	*0.623*	5.113	*-0.0011*	*0.0145*
572	360	1.727	-0.389	0.648	4.993	-0.0018	0.0198

Crack tip coord. [pixels]		K_F	K_S	K_R	T	*Mean*	*Standard deviation*
x_{tip}	y_{tip}	$[MPa.m^{0.5}]$	$[MPa.m^{0.5}]$	$[MPa.m^{0.5}]$	$[MPa]$	μ	s
568	356	1.683	-0.408	0.625	5.057	-0.0064	0.0191
570	356	1.673	-0.395	0.579	4.861	-0.0035	0.0159
572	**356**	**1.656**	**-0.387**	**0.545**	**4.569**	**-0.0009**	**0.0142**
574	356	1.631	-0.387	0.519	4.198	0.0015	0.0152
576	356	1.593	-0.394	0.496	3.750	0.0035	0.0189

Table 5.5 Results for different crack tip locations

5.7 Verification of the new model

A set of experimental photoelastic data for a fatigue crack of length $30.3\ mm$ under the nominal applied stress intensity factor $K_I = 1.696\ \mathrm{MPa.m^{0.5}}$ from the specimen PCCT-6 was used to verify the improved accuracy of the new model by comparing it to the results obtained with the classic Williams' solution for crack tip stress. The comparison aimed to see whether the new mathematical model can give a better description of the stress fields in the surrounding elastic

material in real fatigue cracks than does the classic Williams' solution, because the new solution takes into account the influences on the elastic stress fields of the plastic enclave which surrounds the fatigue crack tip.

The two-parameter Williams' solution (expression 4.5), four-parameter Williams' solution (expression 5.9) and the new model (expression 4.6) were fitted to the experimental isochromatic data using the procedure described previously. Results are listed in Table 5.6 and the fit comparisons are presented in Figure 5.2. The best fit was found when using the new four-parameter model, showing that it gives a better description of the real elastic stress fields under the influence of the plastic enclave and crack wake.

$$\frac{Nf}{h} = \left|\sigma_y - \sigma_x + 2i\sigma_{xy}\right| = Az^{-1/2} + Bz^{-3/2}\bar{z} + Cz^0 \tag{4.5}$$

$$\frac{Nf}{h} = \left|\sigma_y - \sigma_x + 2i\sigma_{xy}\right| = A(z^{-1/2} - z^{-3/2}\bar{z}) + B(z^{1/2} - z^{-1/2}\bar{z}) + Cz^0 + D(z + \bar{z}) \tag{5.9}$$

$$\frac{Nf}{h} = \left|\sigma_y - \sigma_x + 2i\sigma_{xy}\right| = Az^{-\frac{1}{2}} + Bz^{-\frac{3}{2}}\bar{z} + Cz^0 + Dz^{-\frac{1}{2}}lnz + Ez^{-\frac{3}{2}}\bar{z}lnz \tag{4.6}$$

Williams' model				**new model**			
2 parameters		**4 parameters**		**4 parameters**			
K_I	T	K_I	T	K_F	K_S	K_R	T
1.563	3.649	1.585	3.976	1.381	-0.321	0.202	3.913
mean	$\mu = 0.0019$	$\mu = 0.0124$		$\mu = -0.0074$			
Std Dev	$s = 0.0418$	$s = 0.0371$		$s = 0.0264$			
residual	$\varrho = 0.0050$	$\varrho = 0.0044$		$\varrho = 0.0025$			

Table 5.6 Comparison between the new model and William's stress solution (Data points=54,228)

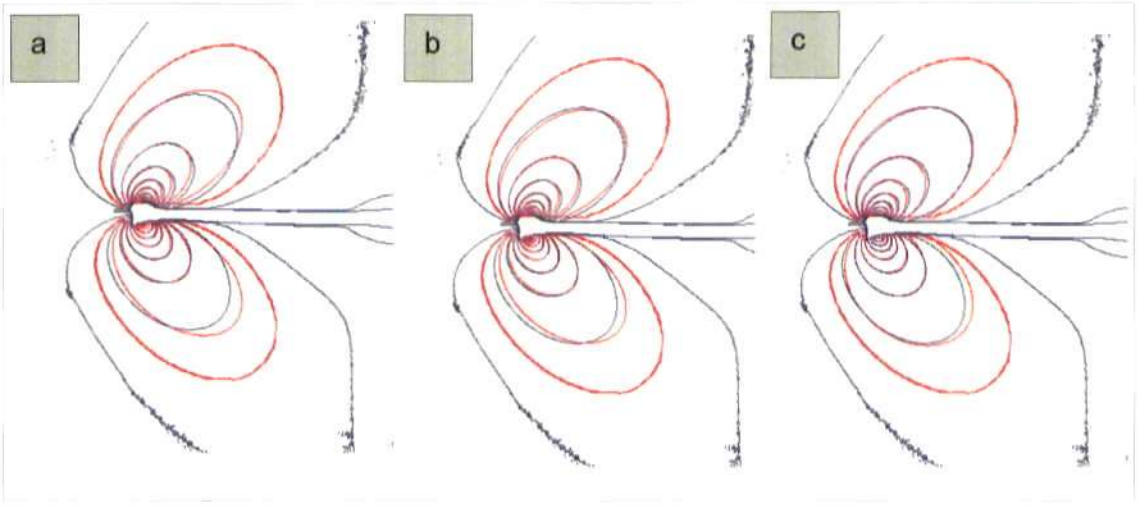

Figure 5.23 Plotting of experimental fringe pattern (blue line) and the fit (red line) predicted by: (a) two-parameter Williams' stress solution; (b) four-parameter Williams' solution; (c) the new model with four parameters which incorporates two terms arising from plasticity-induced stresses. (Fatigue crack of length $30.3\ mm$ in the specimen PCCT-6, nominal applied $K_I = 1.696\ \mathrm{MPa.m}^{0.5}$)

5.8 Experimental results

The experimental values obtained for the stress intensity factors K_F, K_R, K_S and T-stress, which were inferred from isochromatic data using the procedure described previously for the fatigued polycarbonate CT specimens are given in the following sections. Figure 5.24 presents some typical sequences of photoelastic fringe patterns corresponding to load increments of $7N$ over the range from $0\ N$ to $120\ N$ for the specimen PCCT-5 which contains a fatigue crack of length $35.0\ mm$.

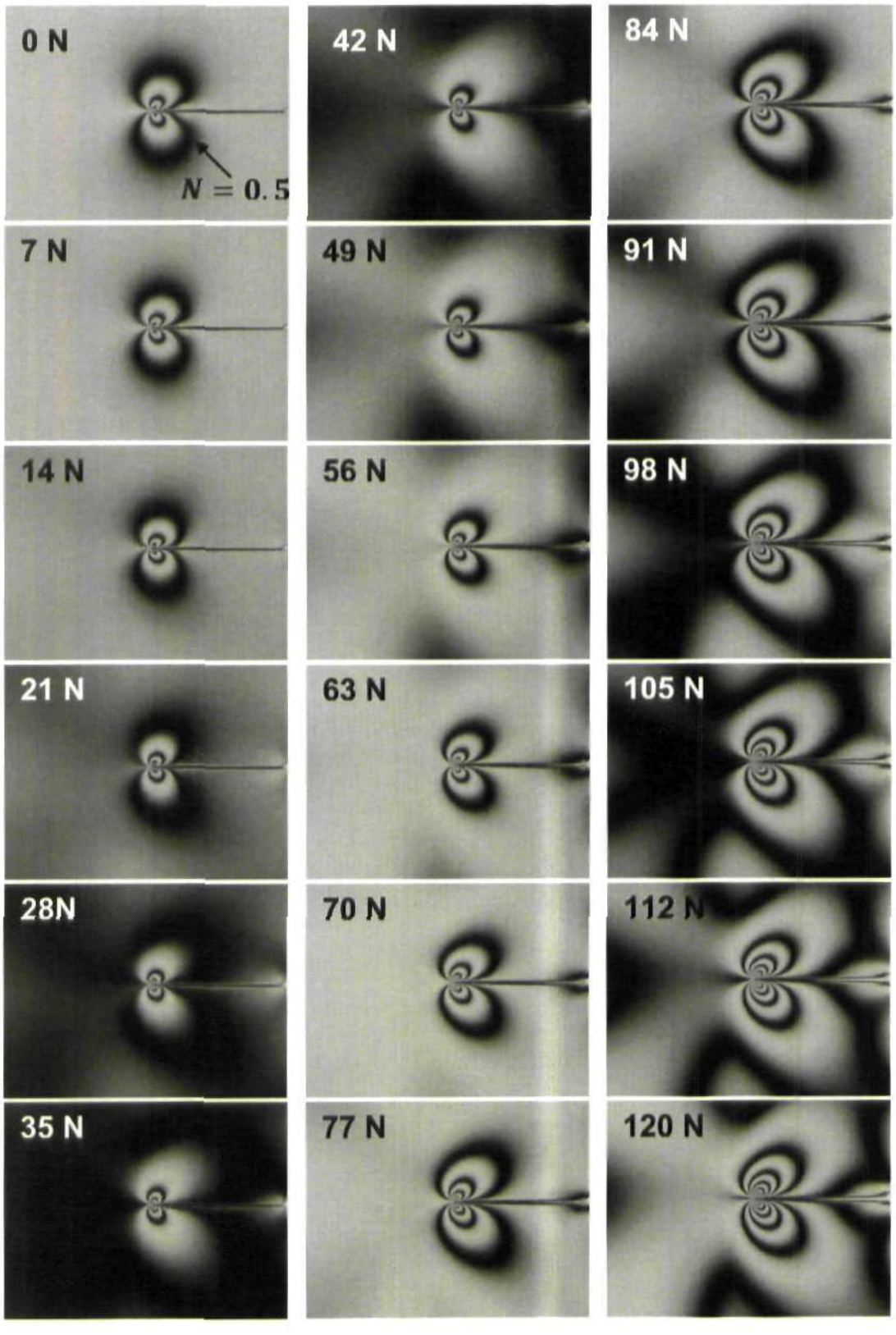

Figure 5.24 Photoelastic fringe pattern (light field) in monochromatic light captured from $0\ N$ to $120\ N$ with the increments of $7\ N$ for the specimen PCCT-5 with a $35.0\ mm$ fatigue crack.

5.8.1 Results for the CT specimens tested under $R = 0.1$

5.8.1.1 Annealed polycarbonate CT specimens

Specimen PCCT-5, PCCT-10 and PCCT-11

These three specimens were tested under the same load condition, i.e. $P_{max} = 120\ N$, $R = 0.1$, Frequency = $0.5\ Hz$.

Figure 5.25 shows the experimental values of K_F, K_R, K_S and T-stress for the specimen PCCT-5. It shows the variation in the three new stress intensity factors for each $7\ N$ incremental load step through a half loading cycle.

In the first four load steps with the nominal applied $K_I = 0{\sim}0.4\ MPa.m^{0.5}$: (a) experimental K_F is higher than the nominal applied load and has a constant value of around $0.4\ MPa.m^{0.5}$ with its minimal value of 0.3 at load step 3 with nominal $K_I = 0.27\ MPa.m^{0.5}$. This can be interpreted as indicating that crack wake contact exists over at least the first 25% of the loading cycle. This is in a very good agreement with experimental photoelastic fringe patterns for the first four load steps as shown in Figure 5.23. Although the shape of those fringe patterns did not change much, careful examination reveals that fringe loops started to shrink inside from load step 2 until load step 3, and then started to expand outside from load step 4. A decreasing fringe pattern indicates energy release and a relatively smaller load exerted by the plastic enclave on the surrounding material near the crack tip. Thus, the experimental value of K_F at load step 3 can be expected to be the minimal. (b) K_R is negative varying between $-0.02\ MPa.m^{0.5}$ and $-0.13\ MPa.m^{0.5}$; and K_s is also negative around $-0.15\ MPa.m^{0.5}$ and decreases as the applied load increases.

From load step 5 with K_I about $0.55\ MPa.m^{0.5}$, experimental values of K_F, K_R, K_S increase steadily as applied load increases. All experimental K_F points fall to

the right of the theoretical K_I curve, i.e. their values are smaller than the corresponding nominal applied K_I value. This is consistent with the occurrence of crack tip blunting inside the fracture process region, as demonstrated in Figure 5.17, and with the concept of the crack acting as a plastic notch. Crack tip blunting in a polymer is likely to arise from local softening of the crazed material and is known to lead to lower applied K_F values than the theoretical K_I, which assumes an infinitely sharp crack. K_R becomes positive and increases as applied K_I increases. K_S remains negative and decreases steadily to $-0.45\ MPa.m^{0.5}$. The observed fairly linear decrease in K_S is likely to be related to the increasing Poisson's contraction as applied load increases. The K_R and K_S terms achieve magnitudes that are respectively 28% and 22% percent of the nominal K_I value which demonstrates the importance of the compatibility-induced stresses generated at the elastoplastic boundary in fatigue crack growth. Additionally, K_R might play a more pivotal role than K_S concerning the observation of its changes as seen in the data plotted.

Figures 5.26 and 5.27 show similar results for a crack of length $31.74\ mm$ in the specimen PCCT-10 and for crack lengths of $25.7\ mm$, $27.6\ mm$, and $29.3\ mm$ in the specimen PCCT-11. The graphs show similar trends to those demonstrated by the specimen PCCT-5 tested under the same load condition (Figure 5.25). Figure 5.28 gives all the results obtained for PCCT-5, PCCT-10 and PCCT-11 in one plot, showing the expected trend for the experimental K_F values of increasing slightly as the fatigue crack length increases. Experimental K_F values were raised a bit more but were still fairly constant at around $0.4\ MPa.m^{0.5}$ in the lower part of the half loading cycle. As crack length increases, values of K_F fall further below the nominal K_I at K values above

$0.4\ MPa.m^{0.5}$, presumably reflecting a slightly increased influence of plasticity on crack tip stresses.

Figure 5.25-5.28 indicate that when the nominal applied K_I is below approximately $0.7\ MPa.m^{0.5}$, K_R is negative and becomes positive when the nominal applied K_I is above $0.7\ MPa.m^{0.5}$. This change may imply that the plasticity-induced shielding is overcome at this point in the loading cycle. Figure 5.29 shows the principal stress fields around a crack when it is only subject to K_R. When K_R is positive, compression exists in front of the crack while tension occurs behind the crack tip. That means that positive K_R would decrease the tension in front of the crack, i.e. it would then reduce the theoretical opening mode driving force K_I to some lower value which then includes the effect of plasticity-induced shielding. This is clearly shown in Figure 5.25. On the other hand, negative K_R would increase the tension in front of the crack and therefore the experimentally calculated K_F is higher than nominal applied K_I during the lower part of the loading cycle as also seen in Figure 5.25.

From the above discussion, it could be stated that (a) when the crack is closed through the existence of wake contact stresses, these would help to increase the effective K_I and consequently the experimentally calculated K_F value is higher than the nominal calculated value. This can be proved visually from the fringe pattern captured at zero applied load, as seen in Figure 5.24, with its experimentally inferred value of K_F of about $0.4\ MPa.m^{0.5}$; (b) when the crack opens, wake contact obviously no longer exists, however the force perpendicular to and acting on the elastoplastic boundary reduces the value of K_I resulting in an experimentally inferred K_F smaller than indicated by the nominal applied load, as seen in Figure 5.25-5.28. That is, the experimental K_F at P_{min} is higher than the nominal applied K_{Imin}, and at the maximum applied

load it is smaller than the nominal applied K_{Imax}. Consequently, the experimentally predicted ΔK_I is lower than the nominal applied ΔK_I, thus the effective crack driving force is reduced by the plastically-induced shielding of the crack tip.

Mathematically, the following interpretation can be argued: considering the definition of K_R, as the limit of σ_x moving along the crack flank towards the crack tip, it is more reasonable to take K_R to be the limit of σ_y moving along the crack flank towards the crack tip for comparison with the traditional definition of K_I, because σ_x and σ_y are equal in magnitude along the crack flanks, i.e. behind the crack tip.

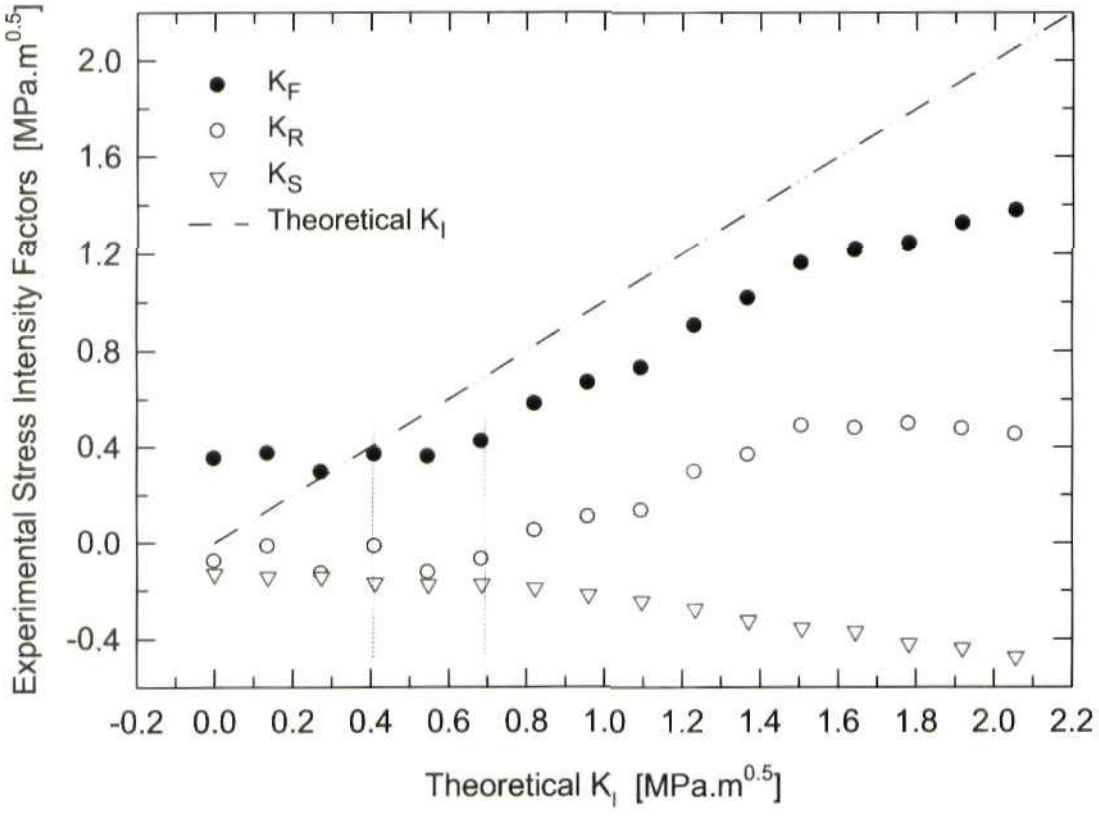

Figure 5.25 Results for K_F, K_R, K_S through a half loading cycle for the fatigue crack of length $35.0\ mm$ in the specimen PCCT-5.

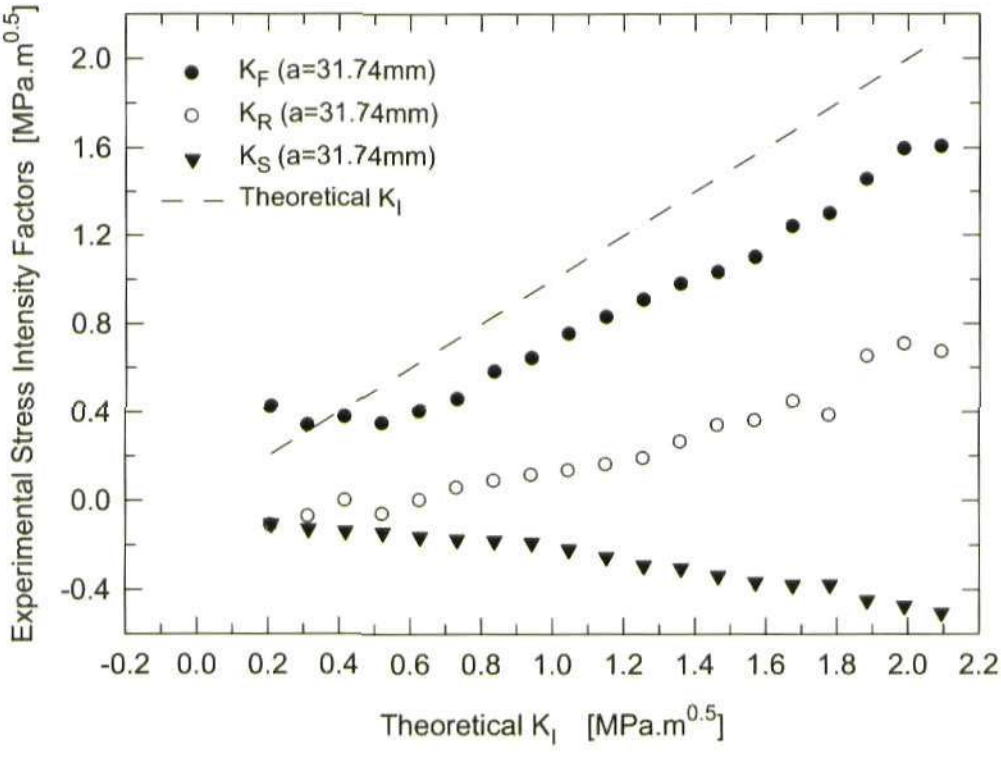

Figure 5.26 Results for K_F, K_R, K_S through a half loading cycle for the fatigue crack of length $31.74\ mm$ in the specimen PCCT-10.

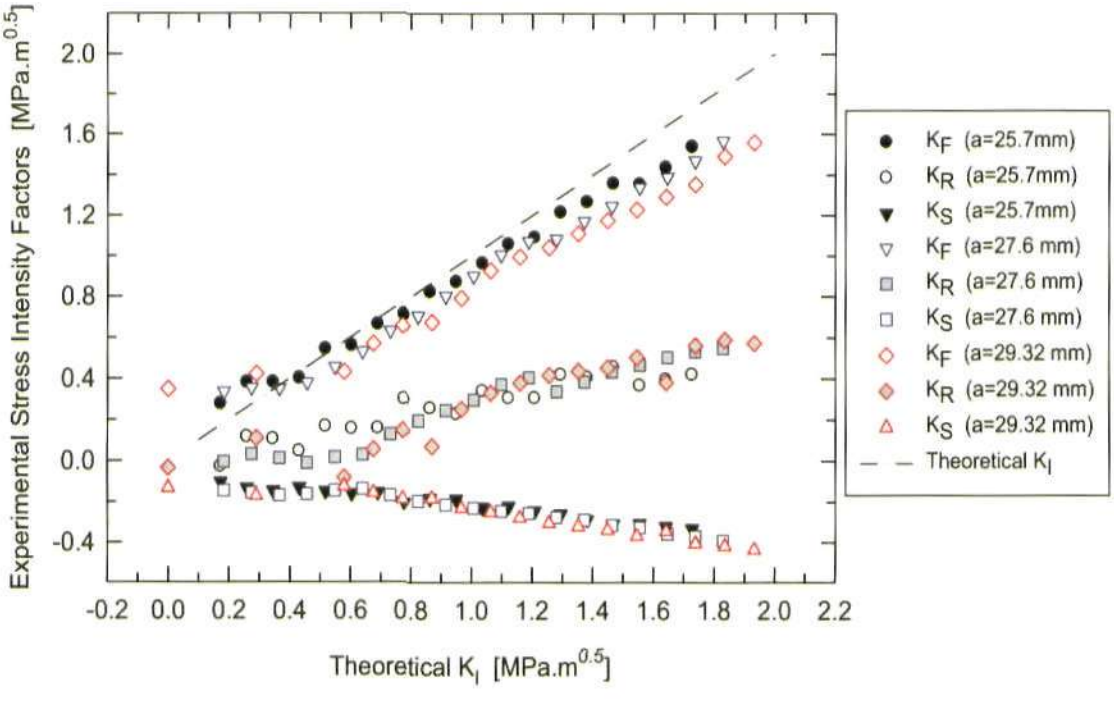

Figure 5.27 Results for K_F, K_R, K_S through a half loading cycle for different crack lengths in the specimen PCCT-11.

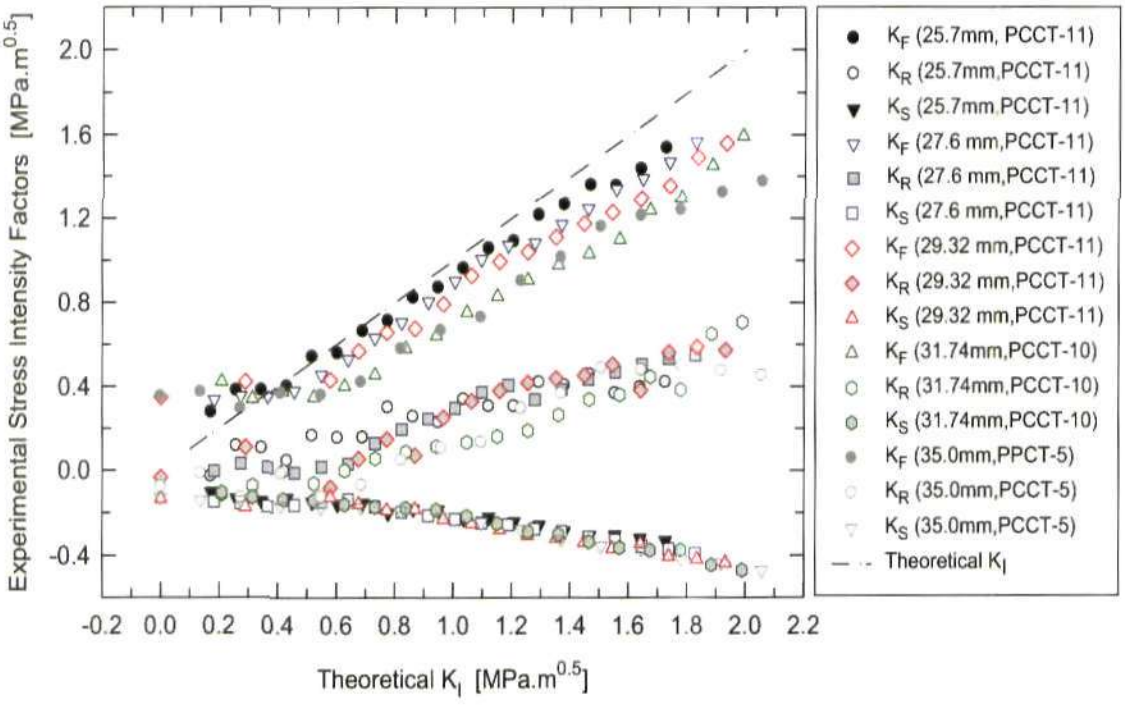

Figure 5.28 Results for K_F, K_R, K_S through a half loading cycle for the fatigue cracks in the specimen PCCT-5 and PCCT-10, PCCT-11.

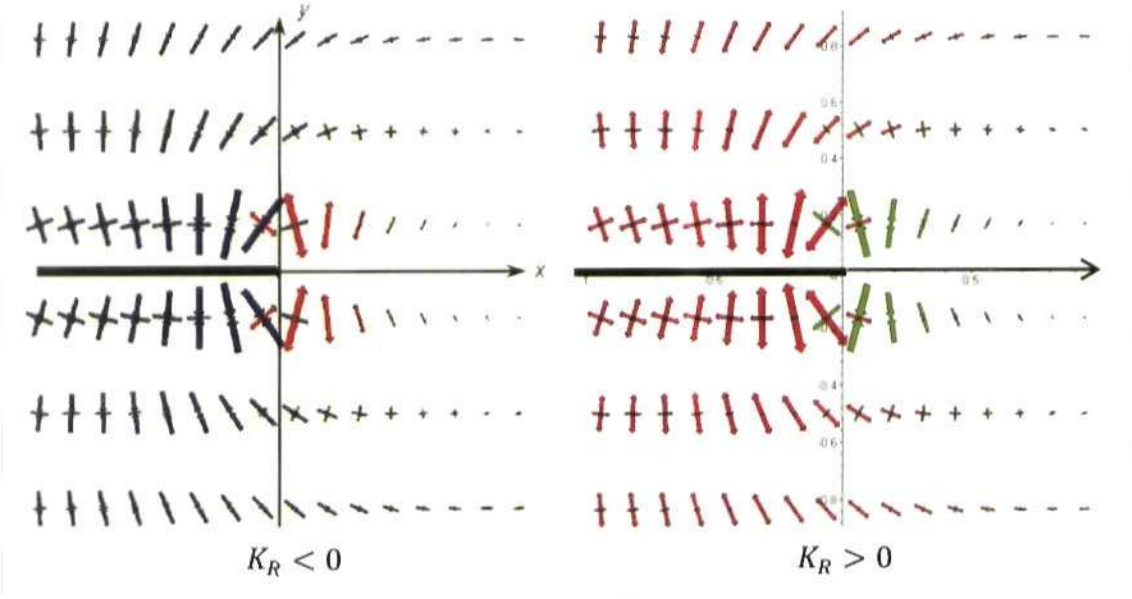

Figure 5.29 Principal stress fields around the crack only subject to K_R due to the presence of a plastic enclave leading to wake contact behind the crack tip, where $K_F = 0, K_S = 0$.

5.8.1.2 Unannealed polycarbonate CT specimens

Specimen PCCT-1

Figure 5.30 shows the experimental results of for K_F, K_R, K_S obtained for the specimen PCCT-1. In a similar fashion to the data discussed above, when the nominal applied K_I is below $0.3\ MPa.m^{0.5}$, the experimental K_F is also higher than that calculated from the nominal applied load and has a constant value of around $0.3\ MPa.m^{0.5}$, the maximum nominal applied K_I is about $1.9\ MPa.m^{0.5}$; K_R is negative ranging from -0.03 to $-0.13\ MPa.m^{0.5}$; K_S is negative decreasing from -0.09 to $-0.15\ MPa.m^{0.5}$ as the applied load increases. When the nominal applied K_I is above $0.4\ MPa.m^{0.5}$, the experimental K_F becomes smaller than the nominal applied stress intensity factor but increases steadily; K_R becomes positive from being negative and increases to around $0.45\ MPa.m^{0.5}$; K_S remains negative and decreasing to $-0.3\ MPa.m^{0.5}$ as the applied load increases. Unannealed specimen PCCT-1 exhibits similar characteristics in the calculated experimental values for K_F, K_R, K_S. However, the difference among the results for different crack lengths is not so distinct as observed in the annealed specimens seen in Figure 5.28, presumably reflecting the variable levels of residual manufacturing stress present in these specimens. Figure 5.31 plots the experimental results for the specimens PCCT-1 and PCCT-5 together for comparison. It shows that in the upper part of the loading cycle, the calculated K_F was lower by about 38% compared with the theoretical value for the $32.44\ mm$ long crack in the unannealed specimen PCCT-1, compared to 31% in the case of the annealed specimen PCCT-5 which however has a longer crack length of $35\ mm$. It can be argued that this difference is due to the wider plastic wake and larger plastic zone observed in the unannealed polycarbonate test pieces (Figure 5.6).

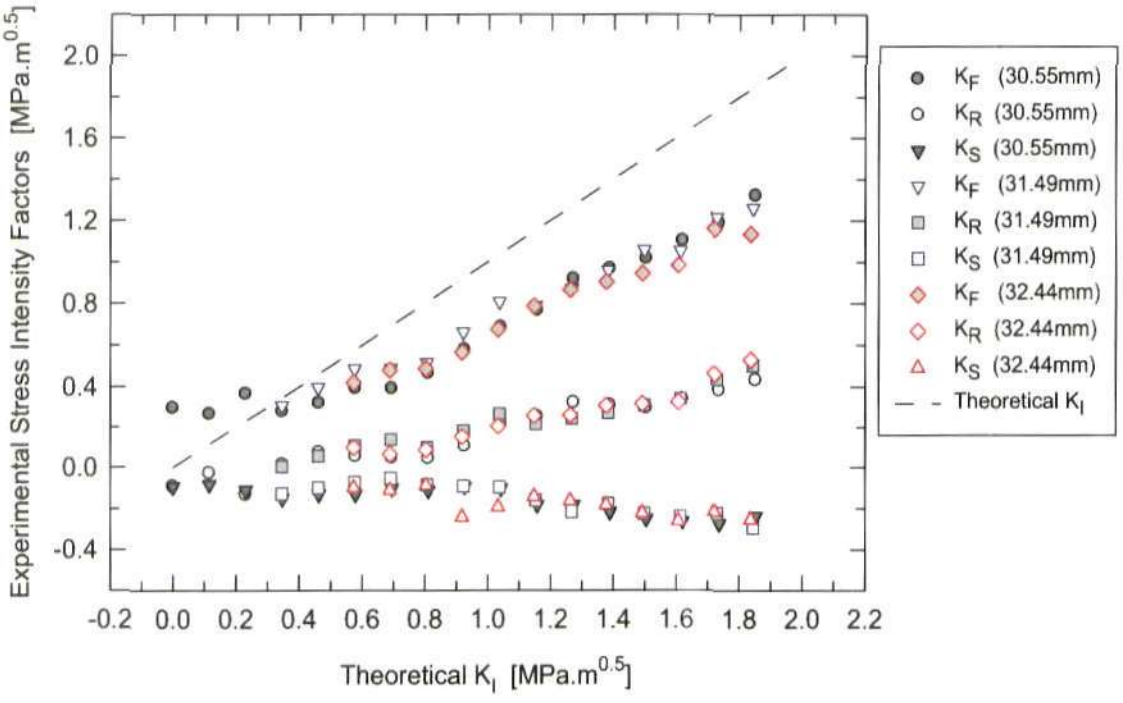

Figure 5.30 Results for K_F, K_R, K_S through a half loading cycle for diferent crack lengths in the specimen PCCT-1.

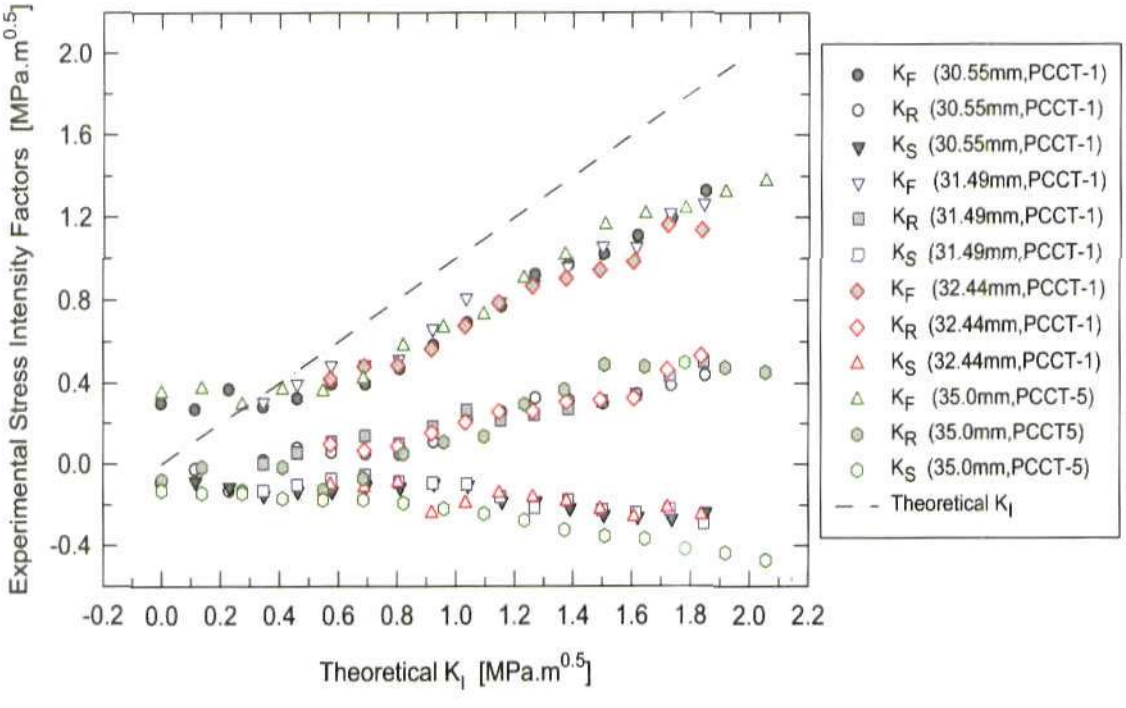

Figure 5.31 Results for K_F, K_R, K_S through a half loading cycle for the fatigue cracks in the specimen PCCT-1 and PCCT-5.

5.8.2 Results for the CT specimens tested under $R = 0.3$

Specimen PCCT-12

The calculated values of K_F, K_R, K_S for the specimen PCCT-12 are plotted in Figure 5.32(a) and together with the results for the specimen PCCT-6 are given in Figure 5.32(b). It can be observed that experimental curves for K_F still fall below the theoretical curve but that the lower load limit in the fatigue cycle is now above the point where the calculated K_I is above the theoretical value, i.e. crack tip shielding is now probably due only to compatibility effects at the elastoplastic boundary and not to wake contact. The maximum calculated K_F is lower by about 15% than the theoretical values for the crack length of $25.5\,mm$, 18% for crack length of $27.48\,mm$ and 22% for the crack of length $30.3\,mm$. This can be interpreted as demonstrating an increasing influence of effective crack blunting by the crack tip plastic zone as the crack length increases. However, when compared to the experimental results for K_F obtained for the specimens tested at $R = 0.1$ under the same maximum load of $120\,N$, there is less of a difference between the theoretical K_I and the calculated K_F in these specimens tested with load ratio of 0.3. This agrees well with the fact that the size of plastic wake and zone and the effect of crack closure decrease as the load ratio R increases. K_R is increasing from $-0.2\,MPa.m^{0.5}$ and becomes positive when K_I is approximately $> 0.7MPa.m^{0.5}$. It is almost the same point observed for the specimens tested with $R = 0.1$ where K_R changed its sign from negative to positive. It is no surprise to see that K_S is almost negative and decreasing to $-0.3\,MPa.m^{0.5}$. Additionally, the maximum absolute values of K_R, K_S are $0.22\,MPa.m^{0.5}$, $0.3\,MPa.m^{0.5}$ respectively both of which are lower than that observed in the specimens tested under $R = 0.1$, which had equivalent values of $0.5\ and\ -0.45\,MPa.m^{0.5}$ respectively.

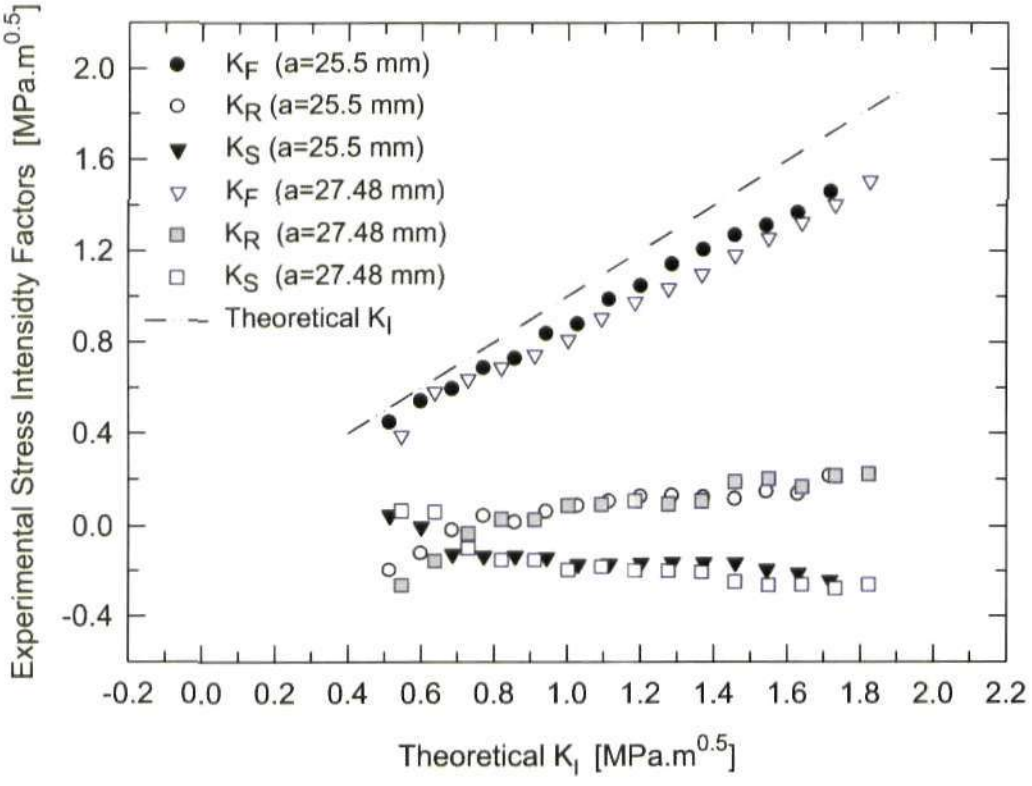

(a)

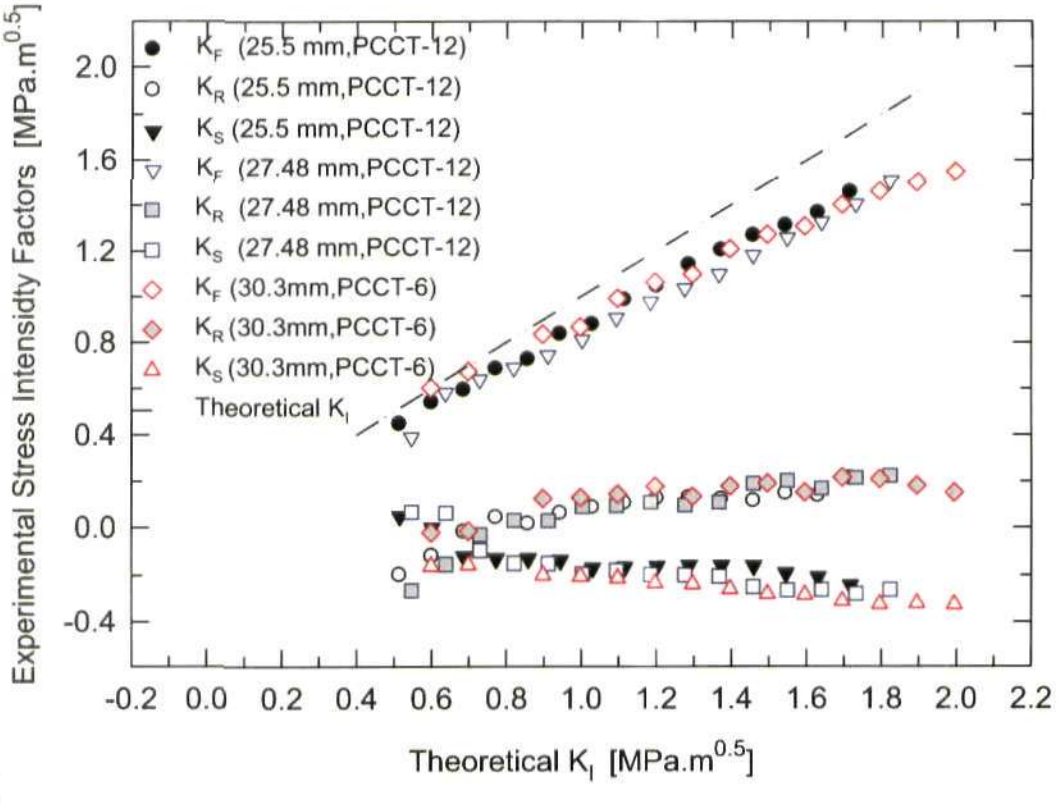

(b)

Figure 5.32 Results for K_F, K_R, K_S through a half loading cycle for different crack lengths in the specimen: (a) PCCT-12; (b) PCCT-6 and PCCT-12.

5.8.3 Results for the CT specimens tested under $R = 0.5$

Specimen PCCT-13

The calculated values of K_F, K_R, K_S for the specimen PCCT-13 are plotted in Figure 5.33(a). Figure 5.33(b) shows the experimental results for the annealed specimen PCCT-13 and the unannealed specimen PCCT-3 together for comparison. It can be observed that experimentally calculated curves of K_F also fall below the theoretical curve. The calculated K_F is lower than the theoretical value by about 11% for a crack of length $25.00\ mm$, 17% for a crack of length 26.89 mm and 23% for a crack length of $29.3\ mm$. However, the difference between theoretical and experimental values in these specimens tested with load ratio of 0.5 is lower than observed with specimens tested at either $R = 0.1$ or $R = 0.3$. K_R is increasing and becomes positive when K_I is about $1.0\ MPa.m^{0.5}$. The calculated K_S is almost negative and decreasing to $-0.25\ MPa.m^{0.5}$ as the nominal applied load increases. Moreover, it is noticed that positive K_S values were observed in some cases in the lower part of the loading cycle as seen in Figure 5.32 and Figure 5.33, and the two K_F stand out as anomalous in Figure 5.33 by being above the theoretical K_I value. This might be due to positive K_S values will help to raise tension stress in front of the crack, as seen in Figure 5.34.

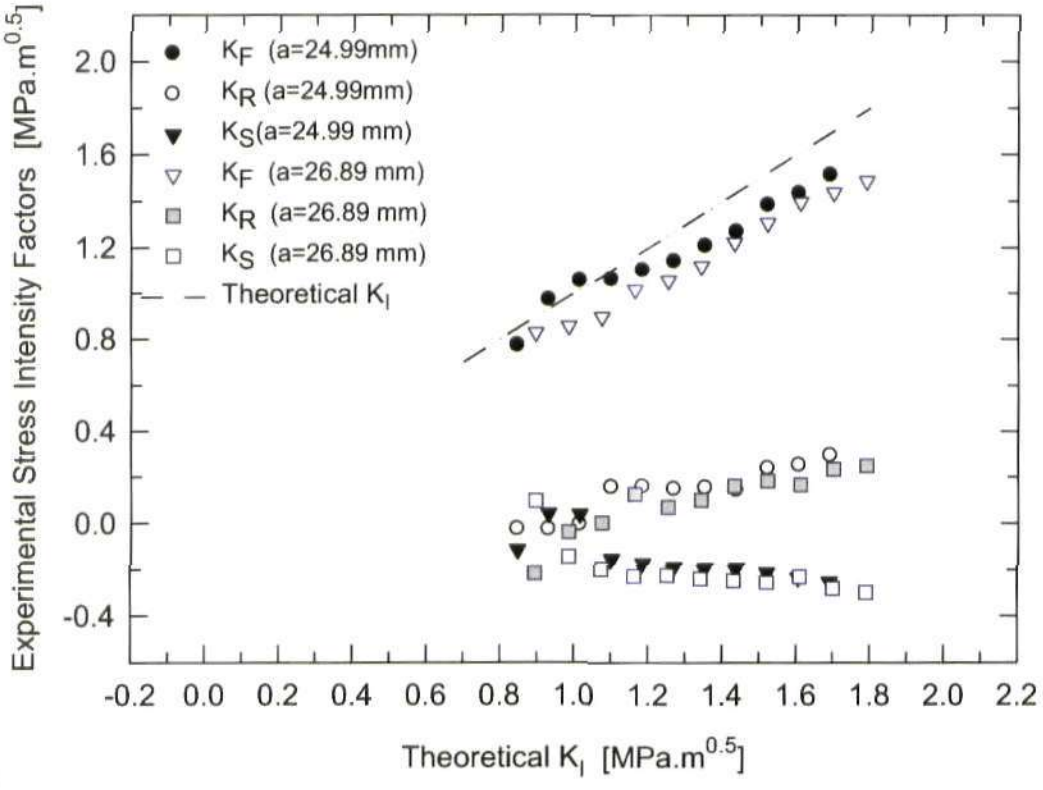

(a)

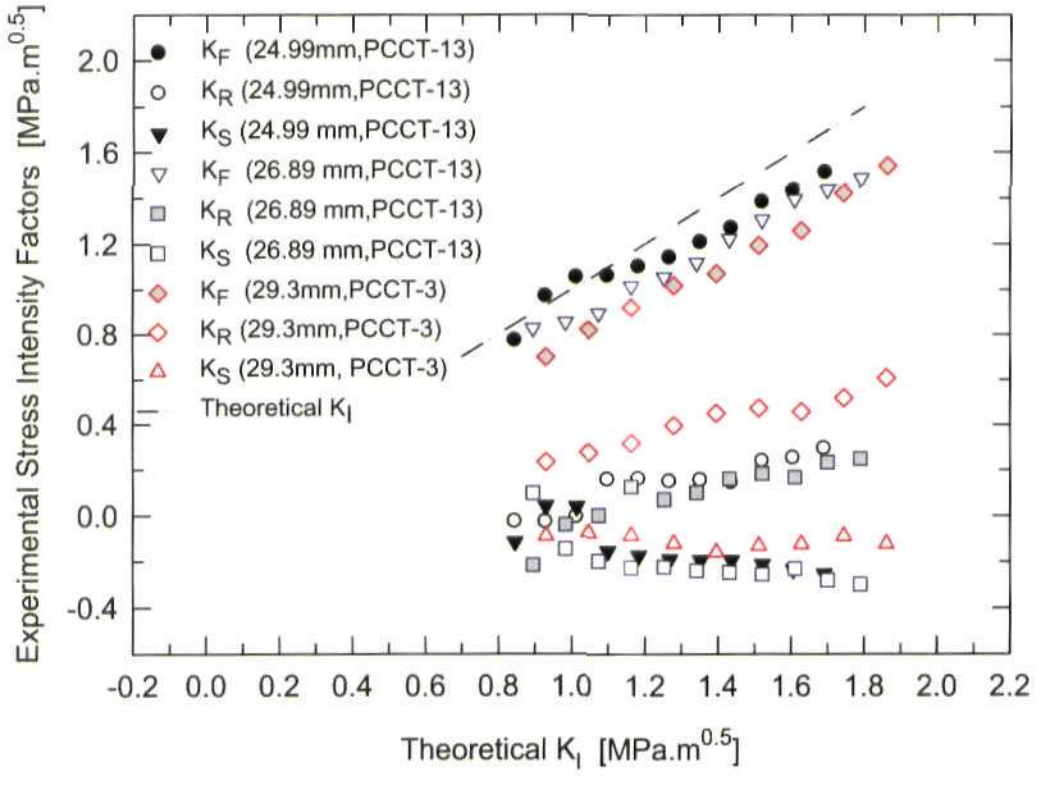

(b)

Figure 5.33 Results for K_F, K_R, K_S through a half loading cycle for the fatigue cracks in the specimen: (a) PCCT-13; (b) PCCT-3 and PCCT-13.

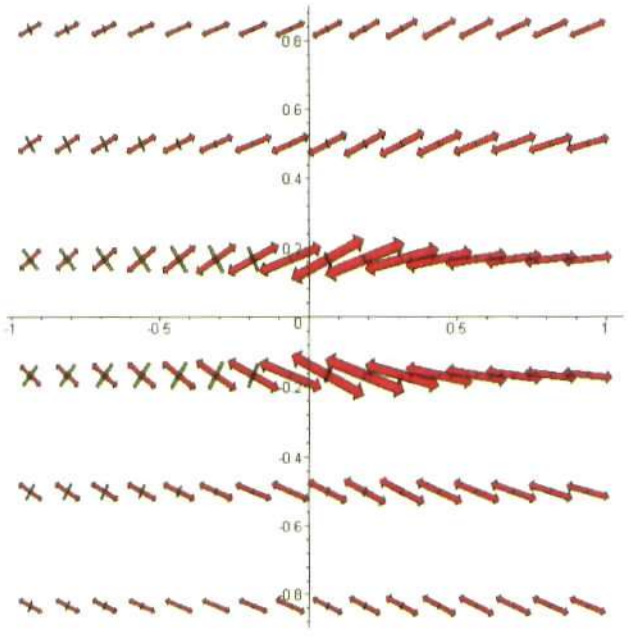

Figure 5.34 Principal stress fields around the crack only subject to a positive K_S where $K_F = 0, K_R = 0$.

Figure 5.35 presents SIF data through a loading half cycle for three tests performed at different stress ratios on CT specimens containing cracks of a similar size, including the specimen PCCT-11 tested at $R = 0.1$, PCCT-12 at $R = 0.3$ and PCCT-13 at $R = 0.5$ (all tested under a maximum value of applied load of $120\ N$). As these cracks are of similar length, the values of K_F are similar for all three stress ratios. However, as might be expected from crack tip shielding arguments related to plasticity-induced closure, the values of K_R are markedly different for $R = 0.1$ at all values of K_I, and somewhat different at $R = 0.3$, particularly in the key region for plasticity-induced shielding where the ratio $K_I/K_{max} < 0.4$. Values of K_S are similar at all three stress ratios with $0.7\ MPa \cdot m^{0.5} < K_I < 1.3\ MPa \cdot m^{0.5}$, except for $R = 0.3$ with positive K_S when the ratio $K_I/K_{max} < 0.4$. The trends shown in Figure 5.35 again appear to be physically meaningful. Further investigations are required to study the correlation of crack growth data da/dN versus ΔK, using the range of stress intensity factor given by combinations of K_F and K_R.

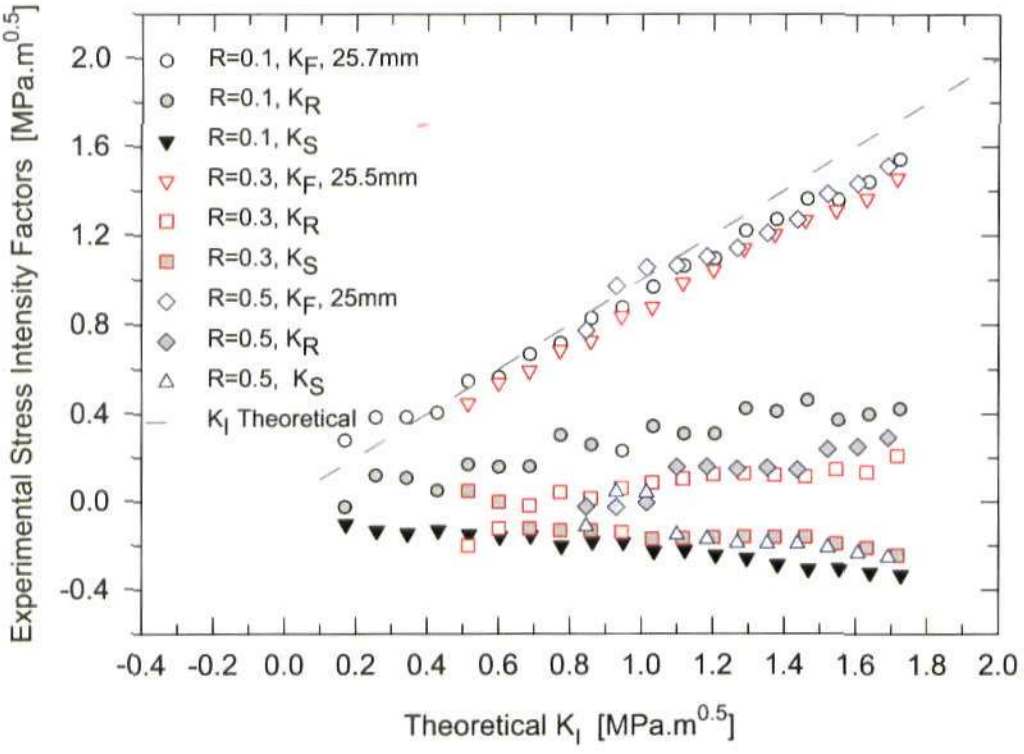

(a)

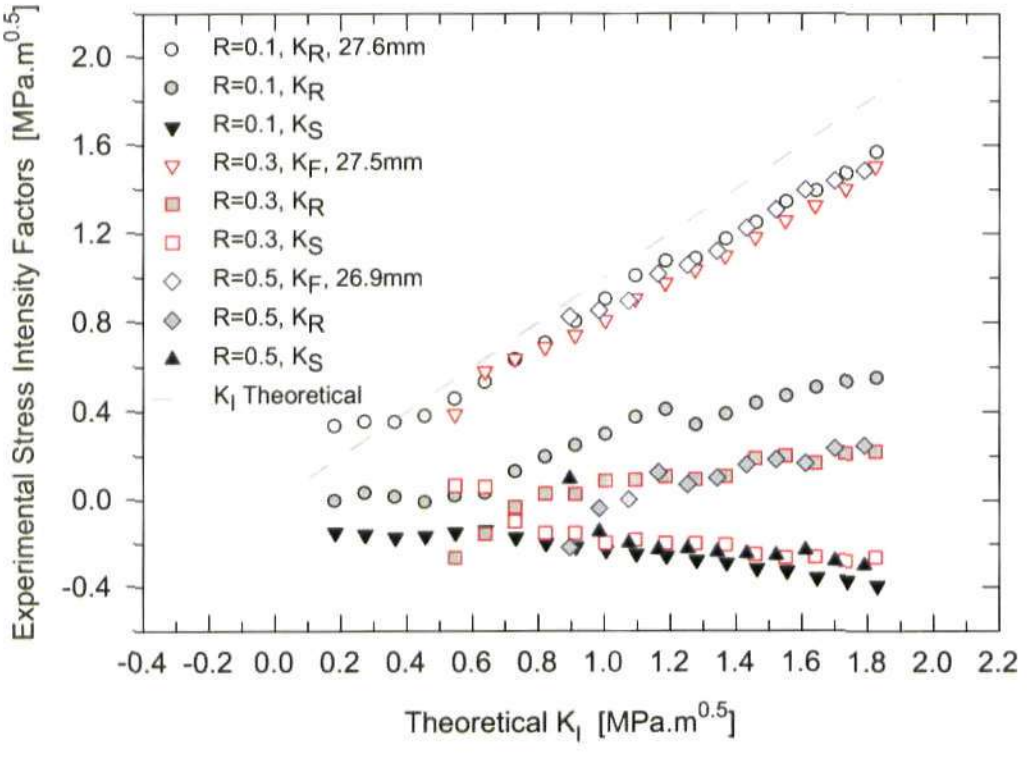

(b)

Figure 5.35 SIFs data for the three specimens: PCCT-11, PCCT-12 and PCCT-13 containing cracks of a similar size tested under load ratio $R = 0.1, 0.3, 0.5$ respectively.

5.8.4 Results for T-stress

Figure 5.36 presents the T-stress versus crack length a data for the annealed specimens PCCT-5, PCCT-10 and PCCT-11 tested with a load ratio $R = 0.1$. The T-stress data shown in Figure 5.36 were all measured at the maximum applied load $120\ N$. Values of T-stress are positive in all cases for these CT specimens and increase with increase in crack length except for the case PCCT-5 with crack length $a = 35.00\ mm$.

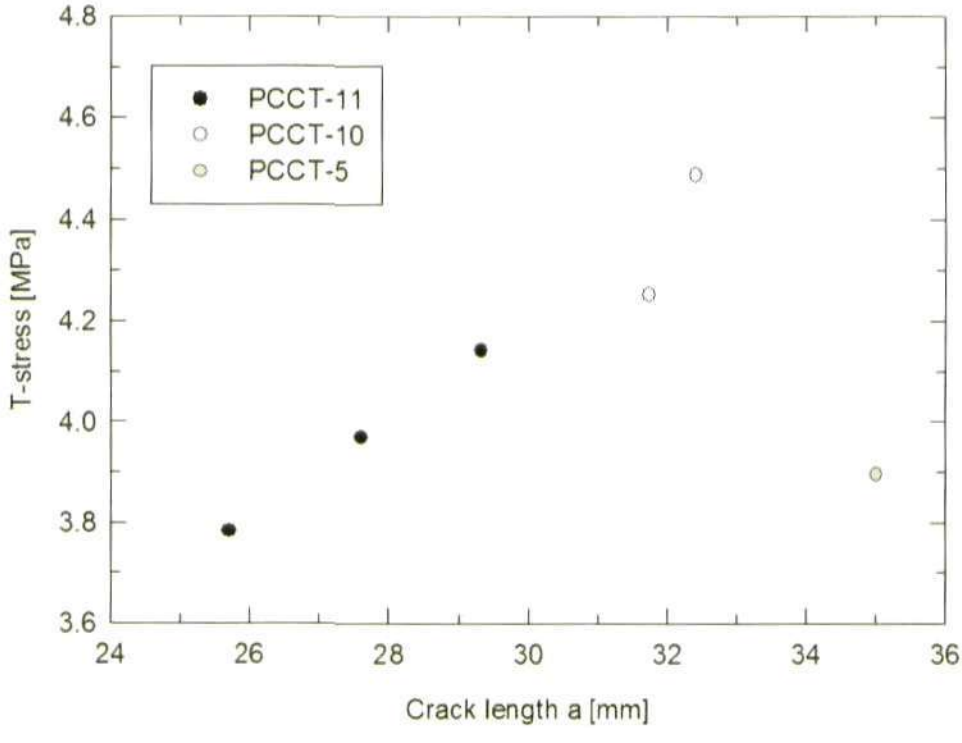

Figure 5.36 The T-stress versus crack length a for the specimens PCCT-5, PCCT-10 and PCCT-11 tested with load ratio $R = 0.1$.

Figure 5.37 presents fringe patterns from the mathematical model for T-stress values going from positive to negative, to show how the T-stress influences fringe patterns. The figure demonstrates the variation in magnitude and shape of fringe patterns over a range of T-stress values from $-10\ MPa$ to $+10\ MPa$. It can be clearly seen that a positive T-stress makes fringe loops lean backwards

(towards the crack flank); negative T-stress lets fringe loops lean forwards (i.e. crack extension direction), while zero T-stress has no influence on fringe patterns with fringe loops being vertical. A change from negative to positive values of T-stress causes the fringes to sweep from forward-facing to reverse-facing. Moreover, there is a more pronounced rotation of the fringe apogee with increase in positive T-stress than is observed with negative T-stress. All the recorded photoelastic images in the present experimental work show similar phenomena with fringe loops leaning backward (e.g. Figure 5.14). This observation of positive T-stress data is in good agreement with the experimental phenomena.

The trend indicated in Figure 5.36 agrees very well with the predictions of T-stress for CT specimens in references [181, 190, 210]. Hadj Meliani et al [190] and Tong [181] both indicate that T-stress increases in CT specimens as a function of increase in crack length. Hadj Meliani et al [190] also pointed out that the value of T-stress varies with distance from the notch tip, being highly negative close to the notch tip and positive further away. Figure 5.38 presents the ratio of T/σ (T is the T-stress, σ is the nominal applied stress) as a function of the ratio a/w (a is crack length, w, the longer distance from the load line to a parallel edge of a specimen) for CT, single-edged notch tension (SENT), centre cracked tension (CCT) and corner-notched (CN) specimens. In this figure, it is obvious that from the plot for CT specimens, T-stresses have positive values and increase as the crack length a increases. For instance, for the case of PCCT-10 with a crack length $a = 31.47\ mm$ and $a/w = 0.44$, the experimental T-stress at the maximum load $120\ N$ is about $4.25MPa$. From Figure 5.38, T/σ is about 5 where $a/w = 0.44$. The nominal applied stress σ is about $0.83\ MPa$.

So T-stress predicted by Figure 5.38 is about 4.15 MPa, indicating that T-stress obtained in the experiment is consistent with the value predicted by Figure 5.38.

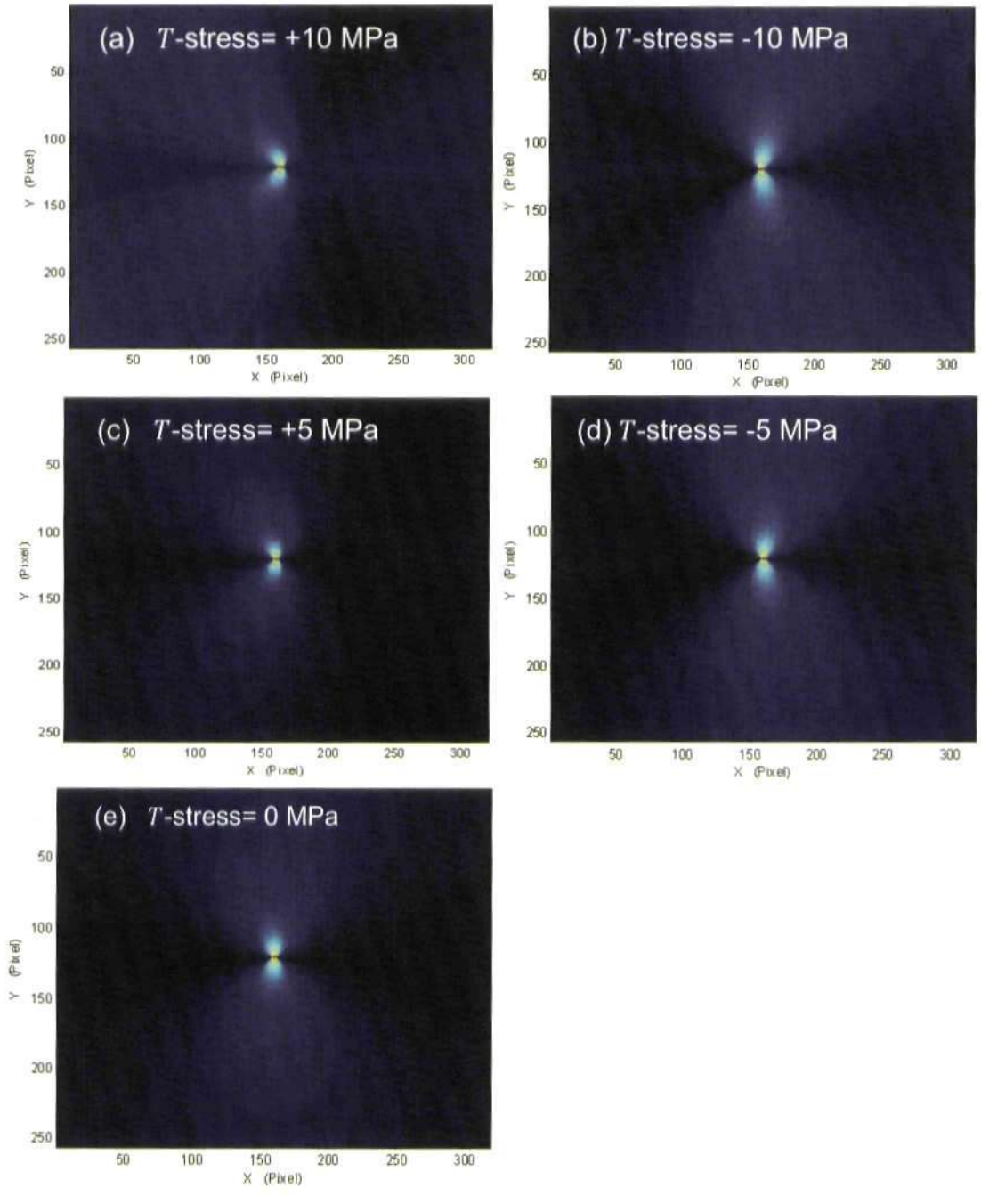

Figure 5.37 Fringe pattern with (a, c) positive T-stress, (b, d) negative T-stress and (e) zero T-stress.

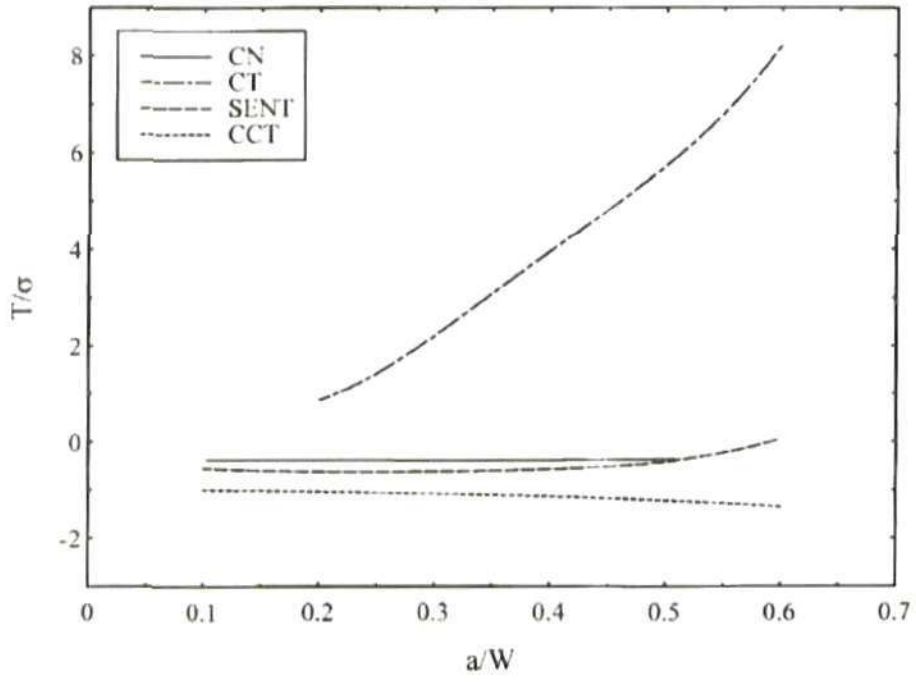

Figure 5.38 T/σ as a function of a/w for CT, SENT, CCT and CN specimens. (reproduced from [181])

Figure 5.39 presents T-stress data throughout a half loading cycle for the specimens PCCT-5, PCCT-10 and PCCT-11 tested at a load ratio $R = 0.1$. It can be seen that values of the T-stress increase through a half loading cycle with increasing applied load in each case. Moreover, the same trend is shown from the T-stress data for those specimens tested at load ratio of 0.3 and 0.5, given in Figure 5.40 and Figure 5.41 respectively. Nevertheless, the T-stress data for the non-annealed specimen PCCT-1 tested at $R = 0.1$ presents different characteristics, as shown in Figure 5.42, with this data remaining approximately constant at $3{\sim}4\ MPa$ over the range of crack lengths between $28\ mm$ and $32\ mm$. Again, it is believed that this reflects the residual manufacturing stresses. It should be noted that in the present work, the change in T-stress with increase in crack length appears to be variable with stress ratio, *test frequency and applied load through a loading cycle. For the specimen* PCCT-1 tested at $R = 0.1$ with frequency of $0.1HZ$, there does appear to be a

trend that the value of T-stress increases with increase in crack length, while the T-stress data obtained for the specimens PCCT-5, PCCT-10 and PCCT-11 tested at $R = 0.1$ with frequency of $0.5\ Hz$ shows a decrease in T-stress as a function of crack length through a half loading cycle, although it has been shown in Figure 5.36 that T-stress increases with the increase in crack length at the maximum applied load. It is noteworthy that previously Roychowdhury and Dodds [185] observed that a reduction in T-stress appears likely to be synonymous with increased plastic deformation perpendicular to the crack plane and this would support the observations of an effect on K_F and K_R of increasing crack length at $R = 0.1$ (Figure 5.28). On the other hand, it has been reported by Tong [179, 181] that stress intensity factors and T-stress are very sensitive to and can be modified by the crack front shape depend on the material parameters, plastic zone and micro-macroscopic fracture process. As the crack grows longer, the size of plastic zone increases rapidly, and crack front constraint decreases rapidly especially near the free surfaces with higher crack closure level, although variation of the T-stress at the mid-plane is relatively smooth and small. Loss of crack front constraint indicates a reduction in T-stress. Moreover, it is regarded that the opening load K_{op} increases as the value of load ratio R increases [144], while increasing K_{op} indicates a lower effective crack driving force and hence a lower crack growth rate, with associated loss of crack front constraint and decreasing T-stress can be expected then. The T-stress data for the specimens PCCT-12 and PCCT-13 tested at $R = 0.3$ and $R = 0.5$ respectively increase as a function of crack length in most cases (Figure 4.40-41).

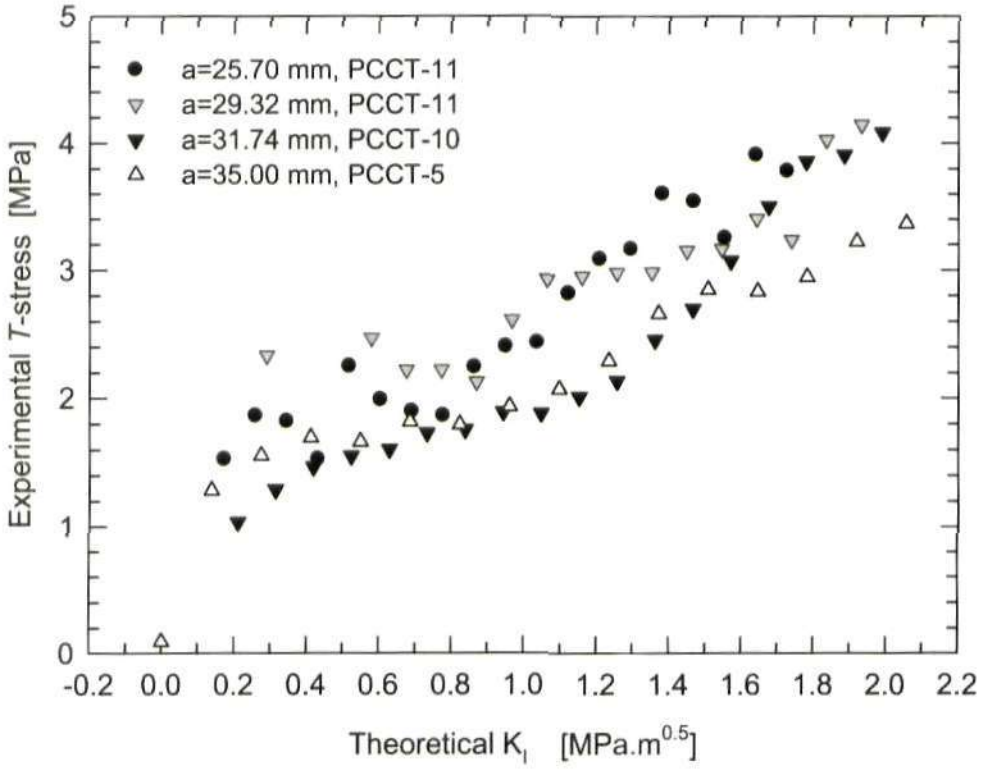

Figure 5.39 Results of T-stress for the specimen PCCT-5, PCCT-10 and PCCT-11. ($P_{max} = 120N$, $R = 0.1$, frequency $= 0.5Hz$)

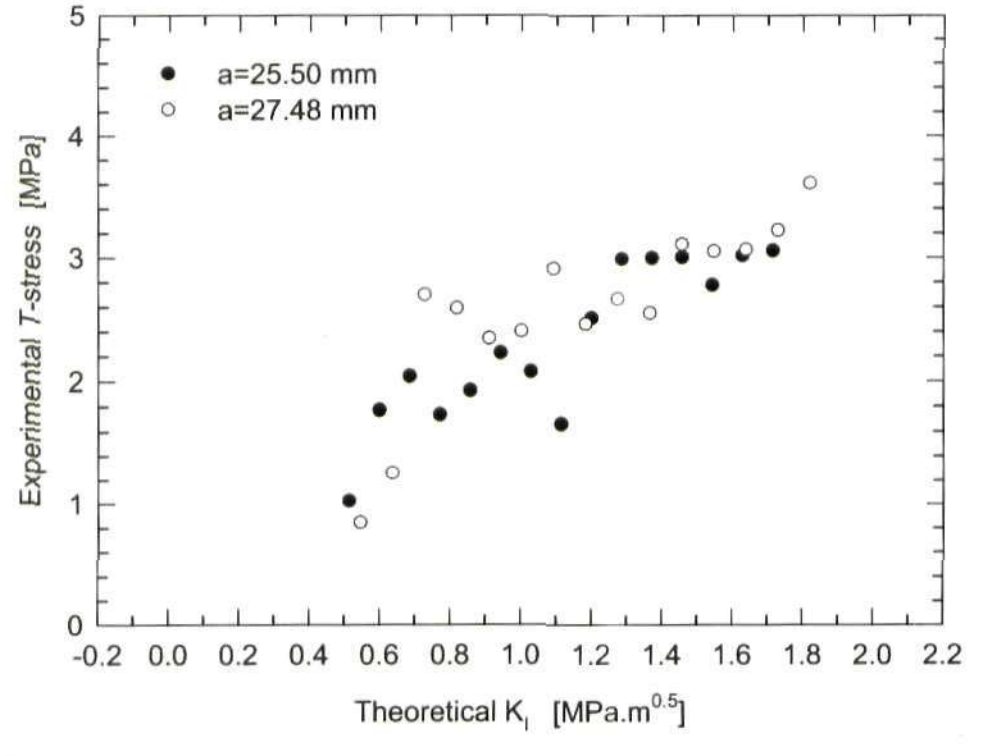

Figure 5.40 Results of T-stress for the specimen PCCT-12 ($P_{max} = 120N$, $R = 0.3$, frequency $= 0.6Hz$)

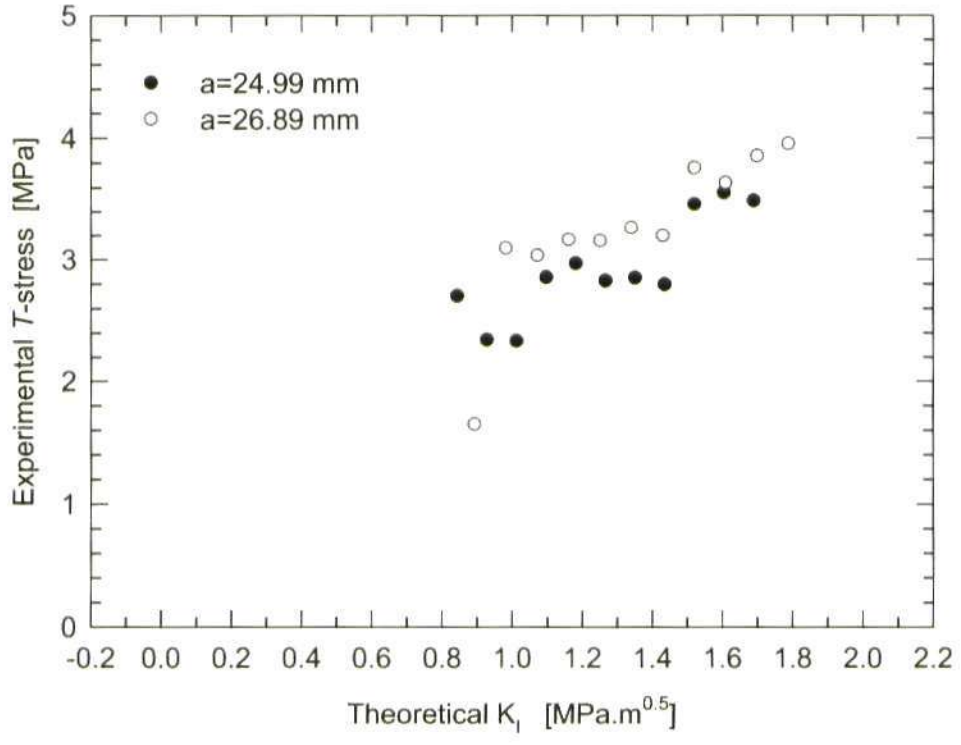

Figure 5.41 Results of T-stress for the specimen PCCT-13 ($P_{max} = 120N$, $R = 0.5$, frequency $= 0.9Hz$)

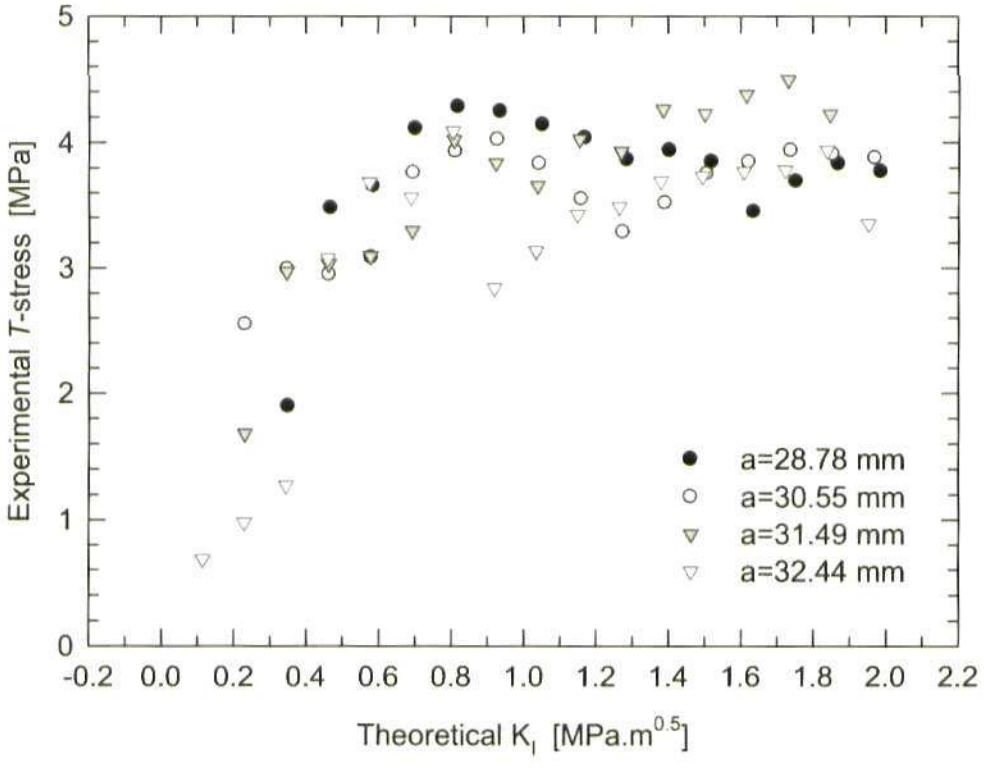

Figure 5.42 Experimental T-stress data for the non-annealed specimen PCCT-1 tested at $P_{max} = 120\ N$, $R = 0.1$ and frequency = $0.1\ Hz$.

5.9 Conclusions

The complete process for analysing full-field experimental photoelastic data for real fatigue cracks in birefringent polycarbonate compact tension specimens and the experimental results obtained with this method have been presented in this Chapter.

Detailed work on the selection of valid data points from experiments was done. It was found that the optimum data collection zone can be defined by two limits, i.e. an inner limit dominated by plastic zone considerations and an outer limit defined by a suitable fringe order. To obtain the best quality fit between the mathematical model and experimental data and hence best solution for the stress intensity parameters, it is recommended that the inner limit is twice the Dugdale plastic zone size and the outer limit is defined by a closed fringe loop with regard to the crack tip which excluding any boundary effects.

Comparison of the new four-parameter model (CJP model) with the classical two and four-parameter Williams solutions for crack tip stresses shows that the CJP model yields a better fit between model and experimental data. This indicates that the CJP model captures the subtleties of local plastic perturbation of the global elastic stress field much better than the purely elastic Williams solutions.

The results for the four new parameters K_F, K_R, K_S and T are reported for CT specimens tested at different load ratios, $R = 0.1$, 0.3 and 0.5. Values of K_F are smaller than the nominal applied K_I in the upper part of a half loading cycle when K_I is greater than a specific number, e.g. $0.4\,MPa \cdot m^{0.5}$ in the case of $R = 0.1$, as expected when crack closure is taken into account by the CJP model. Values of K_F are larger than K_I when $K_I < 0.4\,MPa \cdot m^{0.5}$ where fatigue

cracks are thought to be fully closed and wake contact is occurring. Values of K_R change their sign from negative to positive as the nominal applied K_I increases above about $0.7\ MPa \cdot m^{0.5}$. The trends demonstrated in the results of K_F and K_R are sensible, because positive K_R leads to compression occurring in front of the crack (Figure 5.29) and subsequently reduces the crack driving force. On the other hand, negative K_R would increase the tension in front of the crack and therefore the value of K_F is higher than nominal applied K_I during the lower part of the loading cycle (e.g. Figure 5.25). It is also found that the crack length has less influence on values of the new stress intensity factors (over the limited range of crack length considered) than load ratio R. Values of T-stress increase as a function of the increase in crack length and increase in the applied load during a half loading cycle, except for some cases with longer crack lengths tested at a load ratio $R = 0.1$, where the change in T-stress with increase in crack length appears to be variable with stress ratio, test frequency, shape of the crack front as well as through a loading cycle.

Overall, sensible trends which are interpretable in terms of physically meaningful changes to the plastic enclave surrounding a fatigue crack are observed in the values of K_F, K_R, K_S and T as a function of crack length, stress ratio R, and in the presence of an overload. It is believed that the experimental results demonstrate good repeatability of data between duplicate tests on polycarbonate CT specimens.

The following chapter continues the process of assessing and validating the capability of the model and moves in a coherent way to metallic specimens through the use of experimental digital image correlation (DIC) data.

Chapter 6 DIC experiments and results

6.1 Introduction

This chapter reports the complete process for analysing experimental data obtained via the second technology employed in this thesis, digital image correlation (DIC), for real fatigue cracks in aluminium alloy compact tension (CT) specimens. Initially, the chapter presents the evaluation procedure for extracting displacement information from experimentally acquired DIC data on the aluminium CT specimens and outlines the way of displaying and presenting the displacement field data. Subsequently, the chapter reports the crack growth data observed on representative aluminium alloy CT specimens, before introducing the method for fitting the four-parameter mathematical model to experimental displacement data. This chapter continues by discussing the way to locate the coordinates of the crack tip which was employed in this work, and studies how to define and collect valid data in order to obtain the best quality fit and solution for the stress intensity parameters and the T-stress. Finally, the results of the four parameters K_F, K_R, K_S and T inferred from experimental DIC data are reported for the aluminium CT specimens.

6.2 Experimental DIC data evaluation and displacement field display

DIC data is acquired by following the method previously introduced in Chapter 4 for the aluminium alloy CT specimens. After DIC data acquisition, the next important step is to determine the 2D displacement map/contour of the tested specimens for each single measurement step. Evaluating DIC data is done using the Istra4D program [102] (Figure 4.21). The evaluation process comprises some basic steps listed below.

6.2.1 Evaluation settings

6.2.1.1 Camera calibration settings

This step imports the camera calibration file which contains the camera calibration parameters (intrinsic and extrinsic parameters; for detailed information please refer to the section 4.3.4 in Chapter 4) saved in the camera calibration procedure. It is mandatory to set a calibration file for subsequent evaluation. Without a calibration file, the evaluation process would not be activated in the Istra4D program.

6.2.1.2 Evaluation series generation

A set of evaluation series can be generated by selecting the measurement steps to be evaluated from the acquired experimental DIC data. It is possible to generate multiple sets of evaluation series for one DIC test. Figure 6.1 shows the dialog window through which one can generate the evaluation series of interest. The dialog comprise of two parts: the Data Pool with the complete acquired DIC data on the left-hand side and the Select Data for Evaluation on the right-hand side. The evaluation series contains the evaluation

configurations, the evaluation mask, the start point as well as the evaluated data.

In one evaluation series, it is required to select exactly one of the evaluation steps as the absolute reference denoted by '®' (Figure 6.1). This reference is used for defining the evaluation mask and evaluation grid and serves as the initial step for the subsequent evaluation process. Sub-references denoted by 'R' are recommended for use in the case of large displacements occurring in the test as the evaluation algorithm correlates each step with the absolute reference and the accuracy of the correlation algorithm decreases with larger displacements. However, it is noteworthy that care should be taken in the use of sub-references as an increase in error propagation will happen if too many sub-references are set.

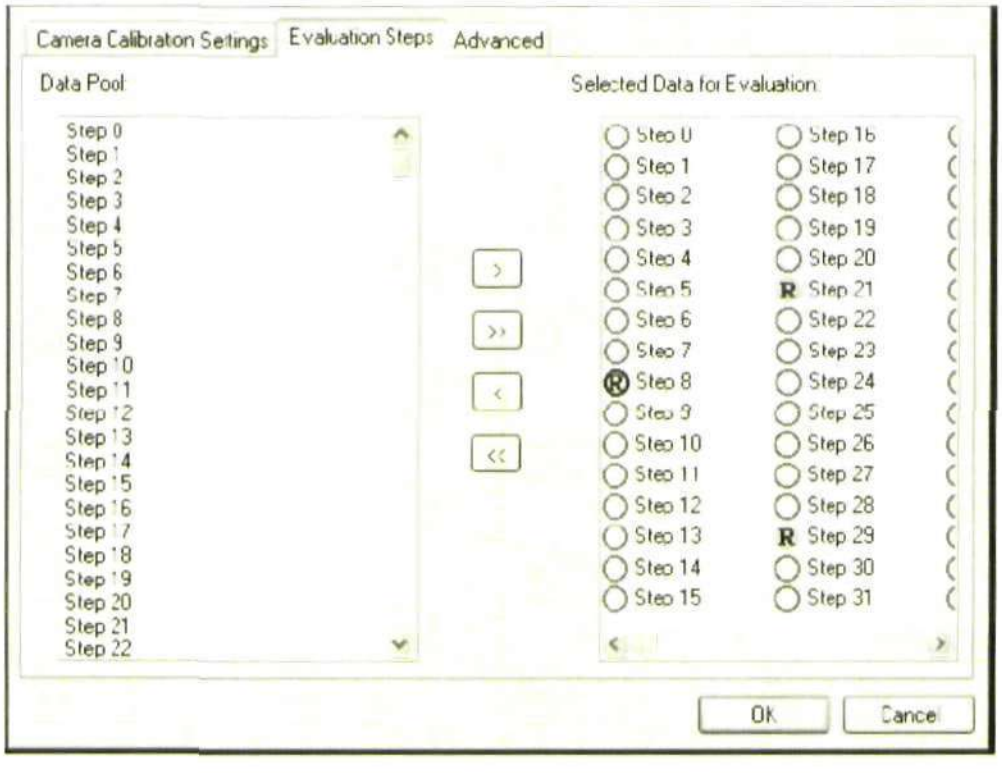

Figure 6.1 Definition of the evaluation series to be evaluated from the complete measurement data in one DIC test.

6.2.1.3 Advanced evaluation parameter settings

Advanced evaluation parameters for configuring the correlation algorithm need to be set through the dialog shown in Figure 6.2. Three individual parameters can be set: grid spacing which defines the evaluation grid, the correlation parameters including facet size, sub-pixel grey value interpolation algorithm and outlier tolerance, and the third one which controls the abort-criterion of the iterative correlation algorithm including correlation accuracy, correlation residuum and 3D reconstruction residuum. The key parameters are discussed in the following paragraphs.

Facet represents a small squared image region in the reference image and all the image points in one facet essentially have the same displacement. Grid point defines the centre of a facet. Both the facet size and grid spacing can limit the spatial resolution. Lower facet size and lower grid spacing can increase the spatial resolution while increasing facet size and grid spacing smooth the data. Accurate displacement measurement requires the facet size to be as small as possible. On the other hand, employing a small facet size (high spatial resolution) means expensive consumption of computing time, and too small a facet which includes fewer features may decrease the correlation accuracy. It is necessary to find a proper facet size and grid spacing that achieves a balance between these requirements. Hence, in the present study, a trial was done by setting different facet sizes and grid spacing for a single evaluation series; this led to selection of an optimum facet size of 17 pixels with a grid spacing of 8 pixels, i.e. 17×17 pixels with about 50% facet overlap. This facet size was employed for all subsequent correlation processes.

In the DIC technique, each digital image is digitised by a camera which converts a continuous intensity field into a digital array of discrete values [211]. Integer

pixel locations in the un-deformed image (reference image) may be at sub-pixel locations in the deformed images. Hence, it is necessary to reconstruct the underlying continuous intensity field before using it in the correlation algorithm. In Istra4D, three algorithms can be selected: Bi-linear interpolation which has lower accuracy but higher speed; Bi-cubic Spline which is more accurate, and Bi-cubic Spline Extended algorithm which has higher accuracy but lower speed. In the present study, the Bi-cubic spline interpolation algorithm is used.

In the outlier tolerance setting, the influence of noise is set to be high which helps to reduce the effect of possible reflections on DIC images. For other parameters, default settings are used.

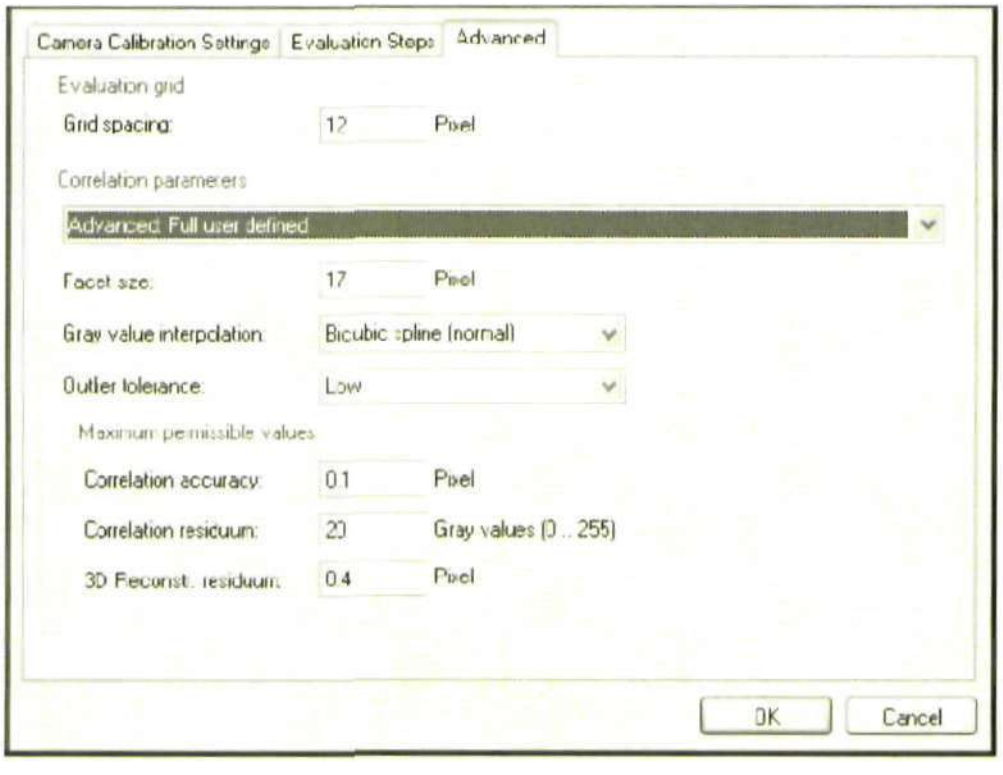

Figure 6.2 Advanced evaluation setup dialog.

6.2.1.4 Definition of evaluation masks

Evaluation masks are used to set the regions of interest in the images, which will enter into the evaluation process. The evaluation mask can be defined

interactively through the Mask editor tool in Istra 4D program, and multiple masks (up to 254) can be created if needed.

6.2.2 Start-point search

The start point is the initial location where the cross-correlation process starts. Each evaluation area must have at least one start point inside it. If multiple evaluation areas are created in the previous step, it is necessary to make sure there is at least one start point set in the interior area.

Start-point search is the first step in the correlation process and is needed to guide the subsequent image correlation. It determines the start-point facet and correlates it firstly with all camera images of the reference step and subsequently from with all other steps in sequence, in order to retrieve the starting point in all frames. Start-point search can be done automatically. The searching results are shown on the interface, and the quality of search for each step is indicated by different colour. A green colour indicates a good quality start-point search and you can move onto the second step of the image correlation process. In case of a yellow or red colour indicator, the start points should be reset.

6.2.3 Image correlation

Once the start-point search is completed with good quality indicator, the program can then run the correlation algorithm automatically. Image correlation is done step-by-step in sequence and the status of the ongoing correlation process is shown on the interface with indicative colour overlying the regions already evaluated, see Figure 6.3, with blue indicating 'best quality' and red 'facet could not be solved'. The indicative colour map can be used to check whether the facet size currently employed is adequate or not. If most of the

already processed regions are denoted by a red colour, the facet size and grid spacing must be reselected. When image correlation has been completed for all steps, the 2D displacement and strain contours will be obtained for each of the evaluation steps.

6.2.4 Displacement field display

When the whole process of image correlation is completed, the full-field horizontal and vertical displacement maps will be obtained. The 2D displacement contour can be visualized in the Istra program, as shown in Figure 6.4. Furthermore, the raw data of the coordinates and displacements can be exported to HDF5 files. The raw data in the format of HDF5 files needs to be converted to ASCII text files which can then be read by MATLAB or Maple to calculate SIFs and T-stress.

Figures 6.4-6.7 give three examples obtained from the three aluminium alloy CT specimens tested under different load ratios in the current study, including the horizontal displacement contour, vertical displacement contour, and total displacement contour. It needs to be mentioned that these displacement field images shown in Figures 6.4-6.7 already have the rigid body motions removed from the displacement data as the mathematical model in current use does not consider any rigid body motions.

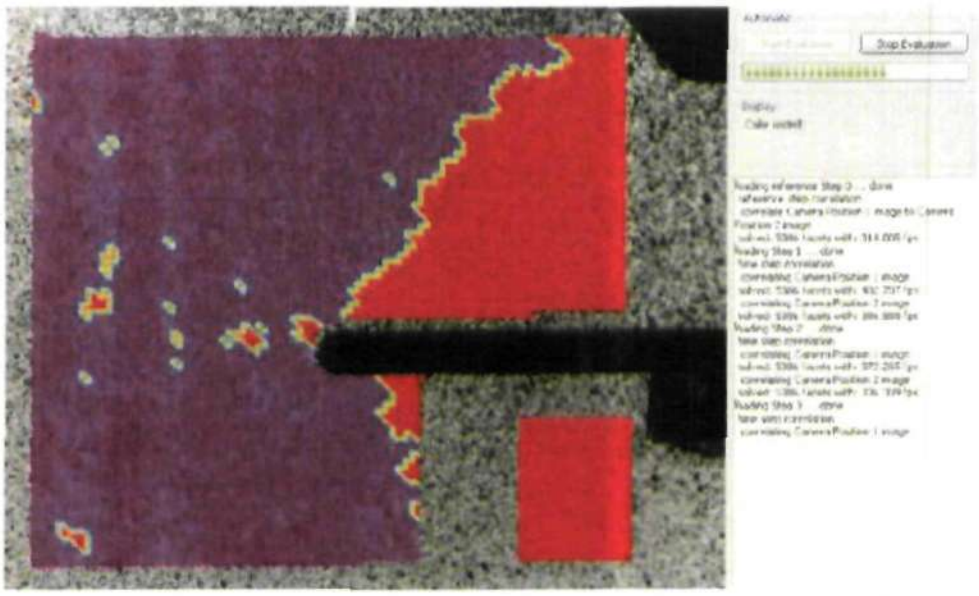

Figure 6.3 Correlation process for one evaluation step with indicative colour: brick red: not yet evaluated; blue/green/yellow/red: indicating the correlation residuum, from left to right, 'best quality' to 'facet could not be solved'.

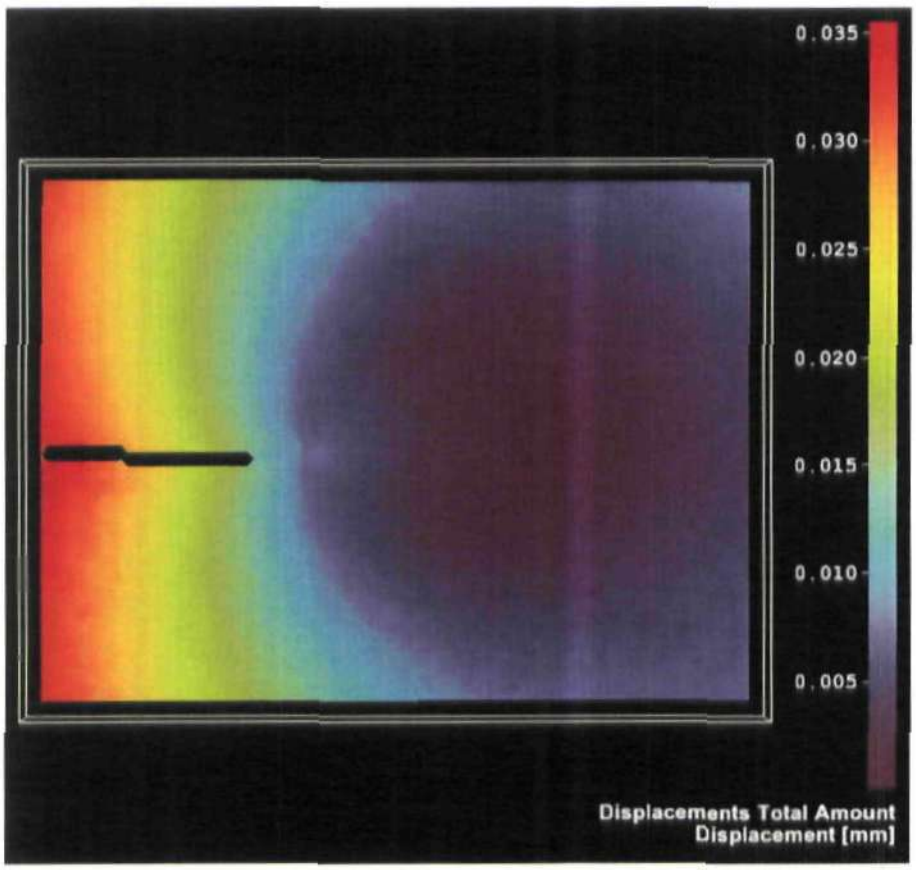

Figure 6.4 Total displacement comprising of both horizontal displacement and vertical displacement for the specimen ALCT-R01 with crack length $a = 26.43\ mm$. (ALCT R01: $P_{max} = 1200N$, $R = 0.1$, frequency=10 HZ)

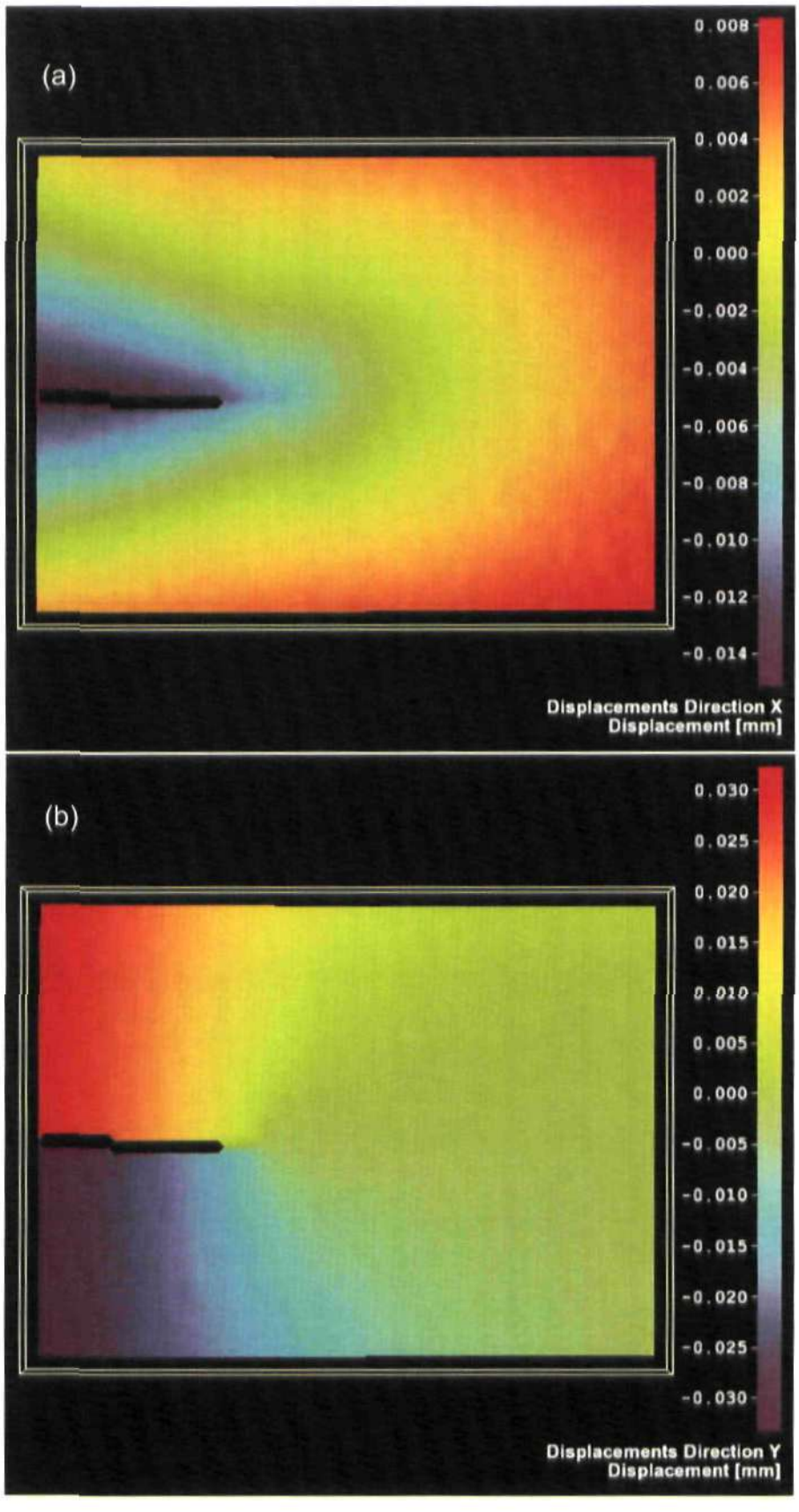

Figure 6.5 Displacement contour: (a) Horizontal displacement; (b) Vertical displacement for ALCT-R01 with crack length $a = 26.43\,mm$. (ALCT R01: $P_{max} = 1200N$, $R = 0.1$, frequency=10 HZ)

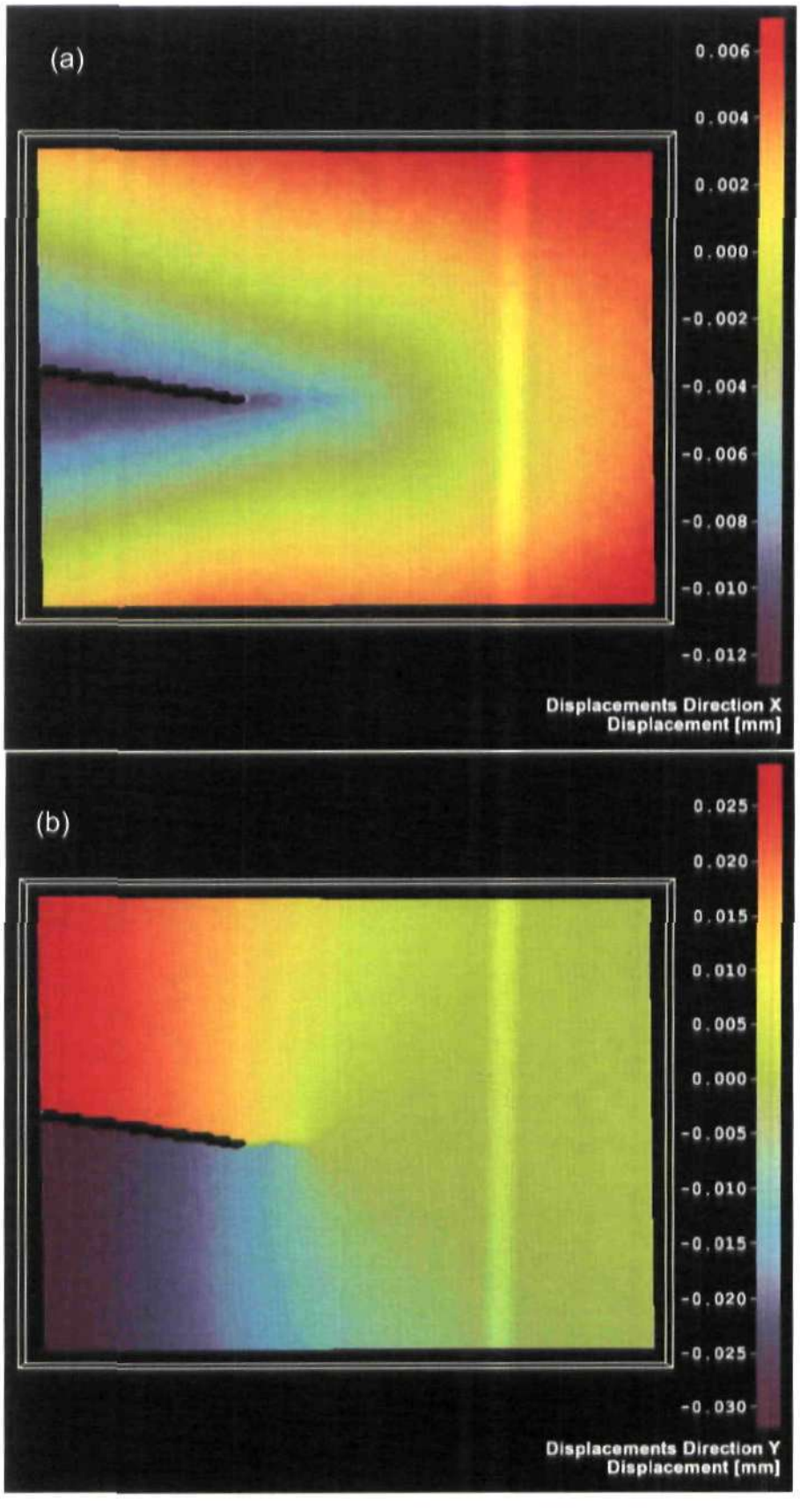

Figure 6.6 Displacement contour: (a) Horizontal displacement; (b) Vertical displacement for ALCT-R03 with crack length $a = 26.97\ mm$. (ALCT R03: $P_{max} = 1200N$, $R = 0.3$, frequency=10 HZ)

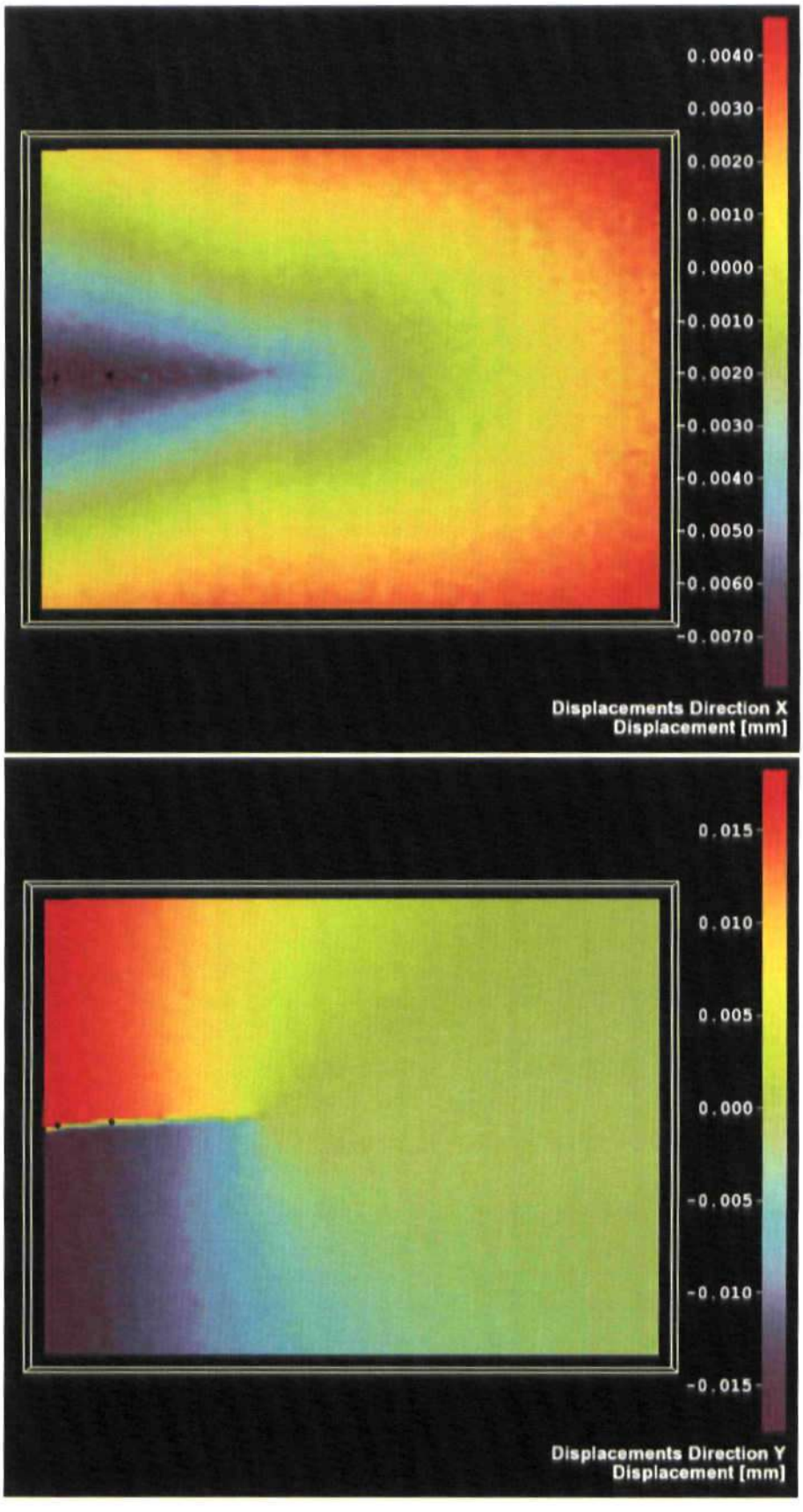

Figure 6.7 Displacement contour: (a) Horizontal displacement; (b) Vertical displacement for ALCT-R05 with crack length $a = 26.40\ mm$. (ALCT R05: $P_{max} = 1200N$, $R = 0.5$, frequency=10 HZ)

6.3 Method of analysis

The new four parameter model (expression 4-12) in terms of both horizontal and vertical displacement fields has been given in Chapter 4. It can be rewritten in the following form,

$$2\mu(u^x + iu^y) = A\mathcal{G}_1(z) + B\mathcal{G}_2(z) + C\mathcal{G}_3(z) + D\mathcal{G}_4(z) \tag{6.1}$$

where A, B, C and D are unknowns, $\mathcal{G}_1(z)$, $\mathcal{G}_2(z)$, $\mathcal{G}_3(z)$ and $\mathcal{G}_4(z)$ are functions dependent on the coordinate z of data points: $\mathcal{G}_1(z) = -\bar{z}^{\frac{1}{2}}$, $\mathcal{G}_2(z) = -2\kappa z^{\frac{1}{2}} + z\bar{z}^{-\frac{1}{2}}$, $\mathcal{G}_3(z) = -\frac{1}{4}\kappa z + \frac{1}{4}z - \frac{1}{2}\bar{z}$, $\mathcal{G}_4(z) = 2\bar{z}^{\frac{1}{2}} - \bar{z}^{\frac{1}{2}}\overline{ln(z)} - 2z\bar{z}^{-\frac{1}{2}} + 2\kappa z^{\frac{1}{2}}ln(z) - z\bar{z}^{-\frac{1}{2}}\overline{ln(z)}$.

For one single point $z_{i,j}$ with horizontal displacement ${u^x}_{i,j}$ and vertical displacement ${u^y}_{i,j}$ (i and j are two indices of a point in the array of displacement grid), the displacement equation is then expressed as

$$2\mu\left({u^x}_{i,j} + i{u^y}_{i,j}\right) = A\mathcal{G}_1(z_{i,j}) + B\mathcal{G}_2(z_{i,j}) + C\mathcal{G}_3(z_{i,j}) + D\mathcal{G}_4(z_{i,j}) \tag{6.2}$$

When expanding to the full-field displacement map with $M \times N$ data points, the equation can be expressed in a matrix format as

$$A_{m\times n}\, x = b \tag{6.3}$$

where x is the vector of unknowns, b is the vector of displacements , $A_{m\times n}$ is the matrix of $\mathcal{G}_1(z)$, $\mathcal{G}_2(z)$, $\mathcal{G}_3(z)$, $\mathcal{G}_4(z)$:

$$A_{m\times n} = \begin{bmatrix} \psi_{11} & \psi_{12} & \psi_{13} & \psi_{14} \\ \psi_{21} & \psi_{22} & \psi_{23} & \psi_{24} \\ \psi_{31} & \psi_{32} & \psi_{33} & \psi_{34} \\ \psi_{41} & \psi_{42} & \psi_{43} & \psi_{44} \end{bmatrix}, \quad x = \begin{Bmatrix} A \\ B \\ C \\ D \end{Bmatrix}, \quad b = 2\mu \begin{Bmatrix} U_1 \\ U_2 \\ U_3 \\ U_4 \end{Bmatrix} \tag{6.4}$$

with $\psi_{m,n} = \sum_{M\times N} Re\left(\overline{\mathcal{G}_m(z_{i,j})} * \mathcal{G}_n(z_{i,j})\right)$, $U_m = \sum_{M\times N} Re\left(\overline{\mathcal{G}_m(z_{i,j})} * (u_{i,j} + iv_{i,j})\right)$

Since, the number of equations equals to the number of unknowns, the equation system always has a unique solution as long as $A_{m\times n}$ is not singular. This equation system can be solved by using LU decomposition.

Similarly to the fitting process for the photoelastic experiments in Chapter 5, the experimental displacement data is fitted to the new model and the unknowns A, B, C, D obtained. The stress intensity factor K_F, the interfacial stress intensity factor K_S, the retardation stress intensity factor K_R and the T-stress can then be calculated using equations (4.8-4.11) respectively.

6.4 Crack tip location

6.4.1 Introduction

The position of the crack tip is always an important factor which not only affects the crack length measurement and theoretical SIF calculation but also has a direct influence on the coordinate system defined through it and is employed by the methodology described in the above section. As with the discussion on the crack tip identification in polycarbonate CT specimens for the photoelastic experiments, it is also impractical to identify the real fatigue crack tip on aluminium alloy CT specimens from the optical images taken by the digital image correlation system in current use. One reason is that the optical resolution provided by the current DIC system is insufficient to allow one to do this. The other reason is that crack tip is an ideal point that exists just in mathematical models; in reality, the crack tip is not a point but a fracture process zone where fracture mechanisms take place, e.g. void nucleation, void growth and coalescence. These, along with plastic blunting make the identification of the precise crack tip position difficult.

To find the crack tip, two methods have been considered in the current DIC study and are described in the following section.

6.4.2 Crack tip coordinates as unknowns in the system of equations

The coefficient matrix $A_{m\times n}$ in the equation (6.3) depends on the crack tip coordinates. If the crack tip coordinates are known, $A_{m\times n}$ is linear and the system of equations is linear. The solution of a linear system of equations is considerably simplified. Nevertheless, if the coordinates of crack tip are unknown, they can be included as unknown parameters in the equations, and then the system of equations becomes nonlinear. The solution of a nonlinear system of equations is much more complicated than for a linear system and can be done only by iterative methods which involve optimising an object function through a number of iterations.

Newton-Raphson technique can be used to solve a nonlinear system of equations using the derivatives of the defined object function [52, 67, 110]. However, the solutions found by this method are very sensitive to choice of initial values. This problem was encountered in the previous computational analysis in photoelastic study and will not be used in this DIC study.

Another technique uses a combination of genetic algorithms and the downhill simplex method. A genetic algorithm is an iterative procedure derived from natural biological evolution [212]. It operates in a similar way by generating a new set of approximations to the solution by selecting the individuals based on the principal of survival of the fittest. The downhill simplex method works as a direct search method by comparing an object function at each vertex of a N-dimensional simplex (geometric figure; N, number of variables to be optimised) and making the simplex change its shape towards the optimum [213]. Unlike

the Newton-Raphson technique, this method does not need any information on the derivatives of the object function. The genetic algorithm is relatively fast in finding the global minimum (close to the optimum) which will be employed as initial values by the downhill simplex method. The downhill simplex method subsequently does the local search by using the approximate solution found by the genetic algorithm as the start point and yields the optimum quickly. The downhill simplex method can solve a nonlinear system of equations itself, though it has high computational cost before an acceptable solution is obtained [214]. The genetic algorithm combined with downhill simplex method does speed up and ensure quicker convergence to an optimum solution [94, 214], but it is still not computationally economic. In the current study, the crack tip is determined a priori from the displacement data which makes the system of equations for the fitting process (equation 6.3) linear and considerably simplifies the problem.

6.4.3 Edge detection method

Edge detection is a fundamental tool for image processing [215]. Edge detection detects physical edges and locates transitions at those points where the intensity gradient of the digital image is a maximum. There exist several edge detection methods, for instance, Candy [216], Sobel [217], and Prewitt [218]. Cracks in an object can be regarded as boundaries or discontinuities which can be detected by applying one of the edge detection techniques to a surface image of the object. This makes it practical to locate the cack tip from DIC images of displacement data. In the current study, the Sobel edge detection method is used due to its simplicity and widespread use. It has also been proven previously that the Sobel edge detection technique gives satisfactory results and is a robust method for crack tip positioning [94].

The Sobel edge detection routine [219] provided in MATLAB in its Image Processing Toolbox was employed in this study. The routine first computes the gradient of change in displacement intensity for each pixel of the digital image by weighting the contribution of its eight neighbours (In the MATLAB Sobel edge detection routine, a 3×3 pixels mask is used and moved over the whole image pixel by pixel as shown in Figure 6.8). The routine then returns edges at those pixels where the intensity gradient is a maximum. Subsequently, the crack tip can be determined from the edges returned by the routine. Figure 6.9 presents an example of running the Sobel edge detection routine on both displacement fields. It is obvious that different edges are returned by the routine resulting in different estimates of the crack tip from the horizontal and vertical displacement fields. This has also been reported in reference [94]. In practice, the displacement which predicts a larger crack length, i.e. larger value of the x component of the crack tip coordinates, is taken as valid. Moreover, under Mode I conditions, in general, it is the vertical displacement field which shows a larger crack length. This is probably due to the fact that vertical displacement in the loading direction is the principal deformation with the value of vertical displacement at a point being about one order of magnitude larger than the horizontal displacement, and crack also seems clearer in the vertical displacement map (Figure 6.7).

P1	P2	P2
P4	P5	P6
P7	P8	P9

Figure 6.8 A 3×3 pixels mask used in Sobel edge detection routine in MATLAB.

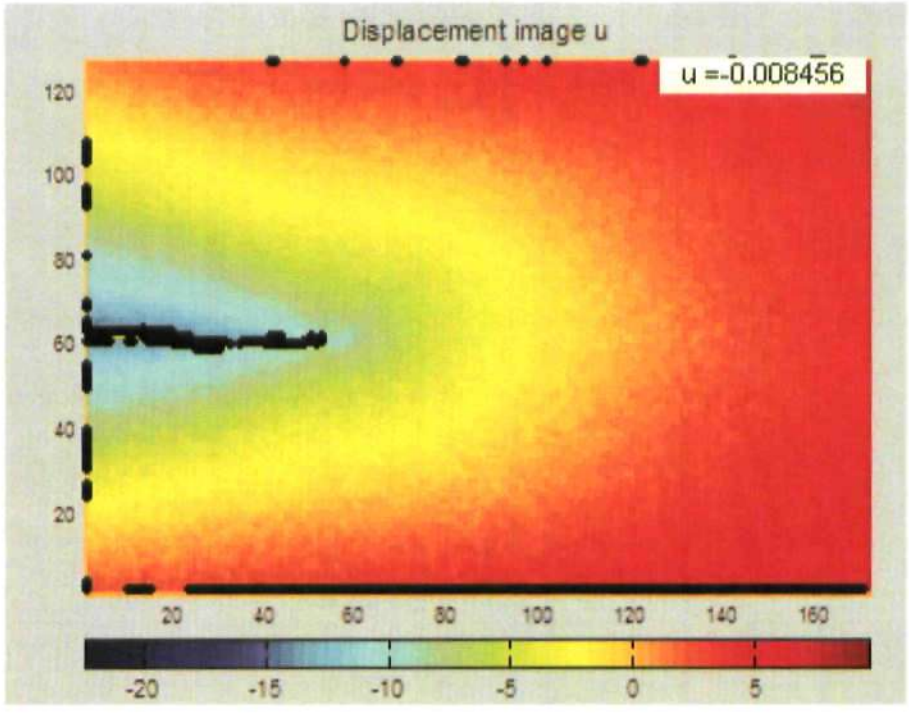

(a)

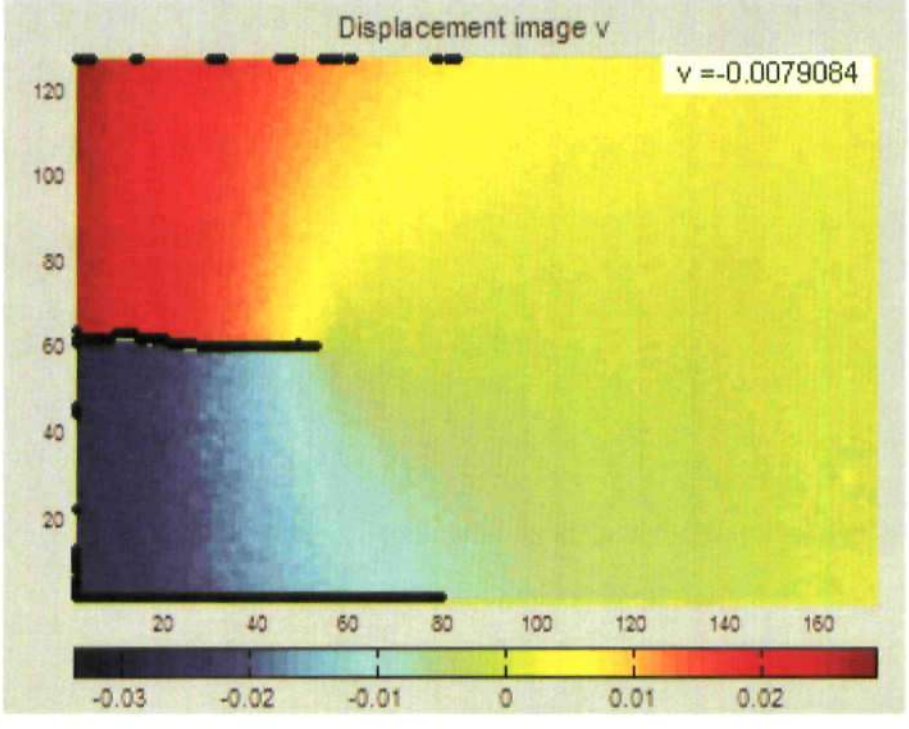

(b)

Figure 6.9 Results of applying Sobel edge detection method to (a) horizontal displacement and (b) vertical displacement of the specimen ALCT-R01 with crack length of $25.35\ mm$ under the maximum load of $1200\ N$. The coordinates of crack tip in pixels predicted by (a) are (54, 61) and by (b) are (56, 61). Thus, vertical displacement predicts a larger crack length, (56, 61) is taken as the crack tip coordinates.

Furthermore, it is recommended that the edge detection routine is applied to the displacement field images recorded at the maximum load to ensure that the fatigue crack is fully open. This is because it is observed that displacement field images taken at small loads (e.g. below $360\ N$ in the specimens tested at $R = 0.1$) are very noisy with a low signal-to-noise ratio which affects the edge detection process. To make this clear, Figure 6.10 presents the results of applying the edge detection routine to the displacement images taken at $240N$ in the same load cycle. Although there always exists noise which affects the results obtained by the edge detection routine, it is still recommended not to use the filter algorithm (an adaptive spline polynomial algorithm) in the Istra program, as smoothing eliminates some effect of the noise but also affects the accuracy of the results. It is observed that using the filtered and smoothed displacement fields for edge detection generally yields incorrect crack tip coordinates in the present work (Figure 6.11).

Moreover, there is always an error in locating the crack tip as it is unlikely that the crack tip is exactly at the intersection of integer pixels. Similarly to the photoelastic study, the sensitivity of the DIC technique to crack tip position is investigated in the following section.

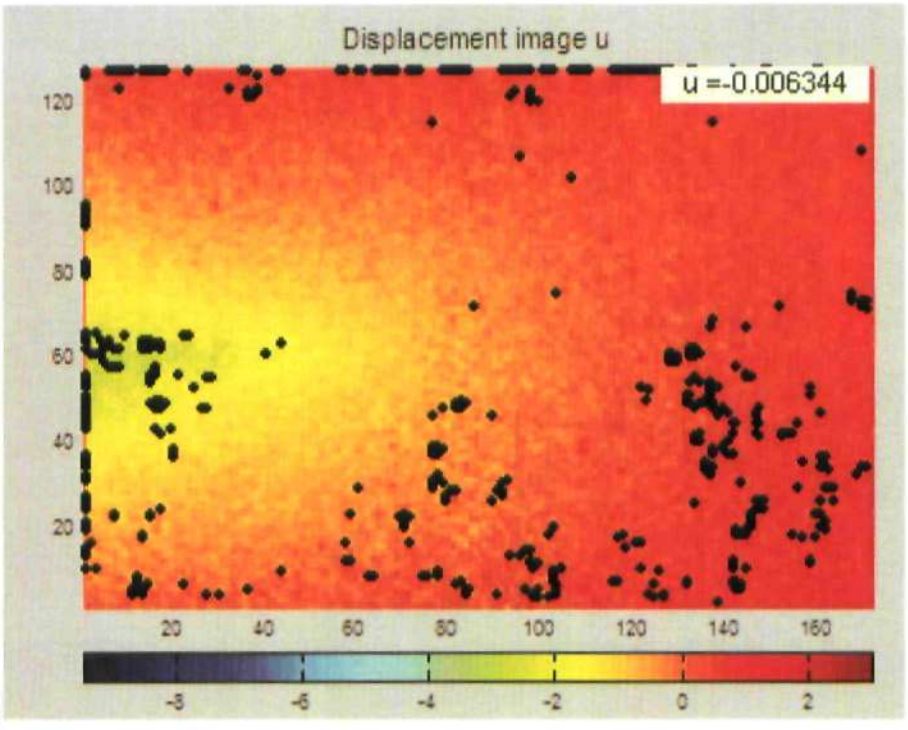

(a)

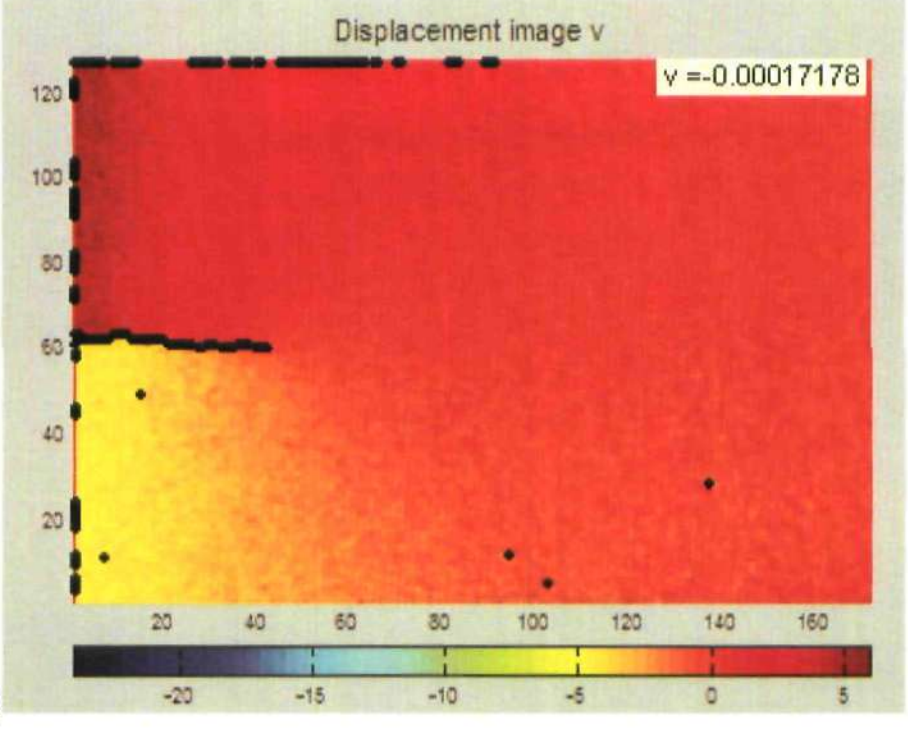

(b)

Figure 6.10 Results of applying Sobel edge detection method to (a) horizontal displacement and (b) vertical displacement of the specimen ALCT-R01 with crack length of $25.35\ mm$ under the maximum load $240\ N$. The crack tip coordinates are (44, 60) by taking the prediction from (b).

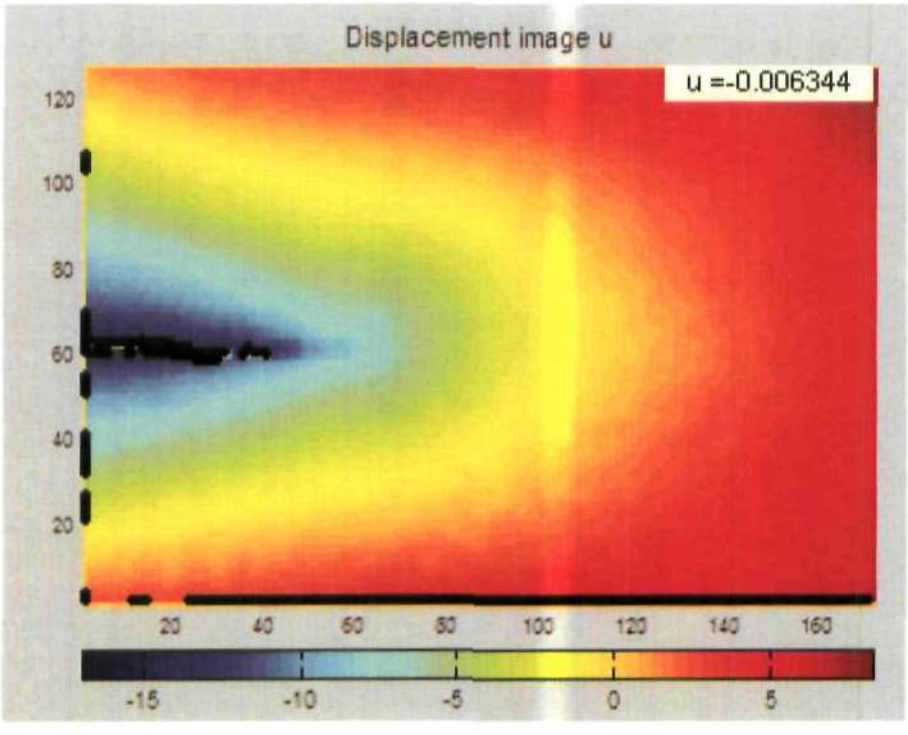

(a)

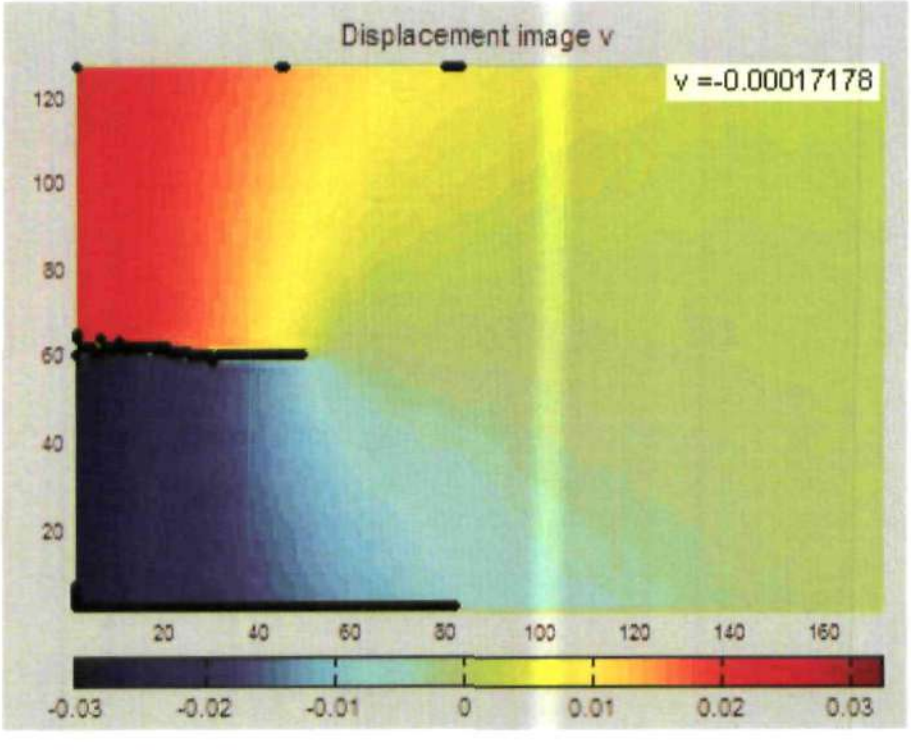

(b)

Figure 6.11 Results of applying Sobel edge detection method to (a) horizontal displacement and (b) vertical displacement of the specimen ALCT-R01 with crack length of $25.35\,mm$ under the maximum load $1200\,N$. Both the displacement fields were smoothed in Istra program. The coordinates of crack tip in pixels predicted by (a) are (42, 61) and by (b) are (51, 61). Consequently, (51, 61) is taken as the crack tip coordinates.

6.4.4 Sensitivity analysis to crack tip position

The sensitivity analysis in this section aims to investigate the errors arising from locating the crack tip position. The analysis is performed by shifting the crack tip coordinates in a horizontal or vertical direction a small distance to assess how much error is introduced in the four parameters $K_F, K_R, K_S,$ and T by incorrectly locating the crack tip.

The two crack tip coordinates x_{tip} and y_{tip} are shifted independently by 0.25, 0.5, 0.75 and one displacement grid point. Displacement data was collected from the regions surrounding the crack tip and the total number of data points was 6,470 (Regarding the way of collecting valid displacement data, please refer to the following section). Following the procedure introduced previously, the model was fitted to valid displacement data, the system of equations was solved and the four unknown parameters obtained.

Figures 6.12-13 present the results for the errors in the four parameters $K_F, K_R, K_S,$ and T when the crack tip was shifted independently either horizontally or vertically. It was observed that shifting the crack tip in the x direction introduces a bigger error into $K_F, K_R, K_S,$ and T compared with those from shifting in the y direction. Errors are generally less than 1% in $K_F, K_R, K_S,$ and T when the crack tip is shifted in the y direction by less than one displacement grid point, as shown in Figure 6.13, except for the case of a single displacement grid point shifting in the y direction which gave errors in $K_R, K_S,$ and T of 7% 39% and 10% respectively (These error values fall outside of the y axis range in Figure 6.13). Errors in K_F are less than 2.5% in all cases when the crack tip is shifted in the x direction less than one displacement grid point, while large errors in $K_R, K_S,$ and T of are observed, as shown in Figure 6.12.

This investigation indicates that errors in the final solution, especially in K_R, K_S, and T, mainly arise from incorrect location of the crack tip in the x direction (usually, underestimated), i.e. in the crack propagation direction. Great attention has been paid to this matter in the current study. In general, the error in locating the crack tip by using the edge detection method is less than one displacement grid point.

Overall, this investigation shows that satisfactory results are obtained by using the Sobel edge detection method to identify the crack tip directly from the displacement field images. It is believed that this methodology is more efficient and robust than using optical instruments to identify the crack tip or including the crack tip coordinates as unknowns. This method is used for identifying the crack tip for the subsequent analysis.

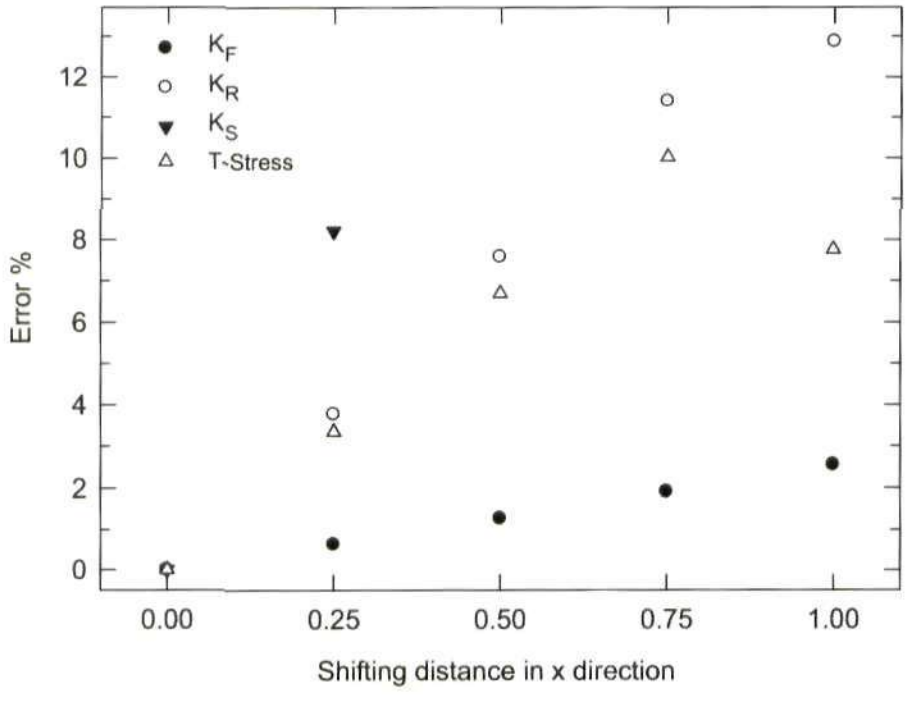

Figure 6.12 Errors introduced by shifting the crack tip in the x direction on the four parameters K_F, K_R, K_S, and T. The magnification factor of displacement grid point is $0.102\ mm/point$.

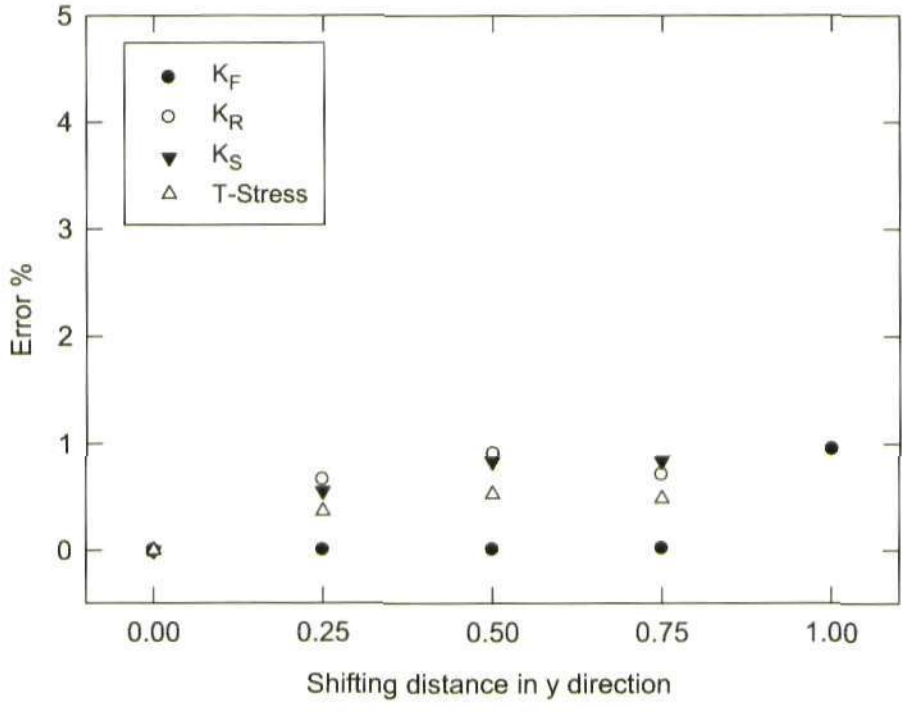

Figure 6.13 Errors introduced by shifting the crack tip in the y direction on the four parameters $K_F, K_R, K_S,$ and T. The magnification factor of displacement grid point is $0.102\ mm/point$.

6.5 Definition of the region of validity of the model

6.5.1 Introduction

As discussed previously in the photoelasticity study in Chapter 5, the accuracy of the final solutions is dependent on the quality of fit of the model to experimental data, namely displacement data in the DIC study here. To produce a good quality fit, one needs to ensure that only valid displacement data is employed as input into the fitting process. As the stress fields studied in photoelasticity are apparently different from the displacement fields in DIC, the investigation on the manner of data collection needs to be done.

Firstly, as the model in current use describes the elastic field, data points immediately ahead of the crack tip and along the crack flanks are excluded to

avoid any plasticity effects and ensure the validity of the model. To achieve this requirement, an inner limit can be used to ensure data inside it is not to be collected. Secondly, data points with a high degree of noise and low signal-to-noise ratio usually close to the borders of displacement field images will also be excluded from data collection (Figure 6.14).

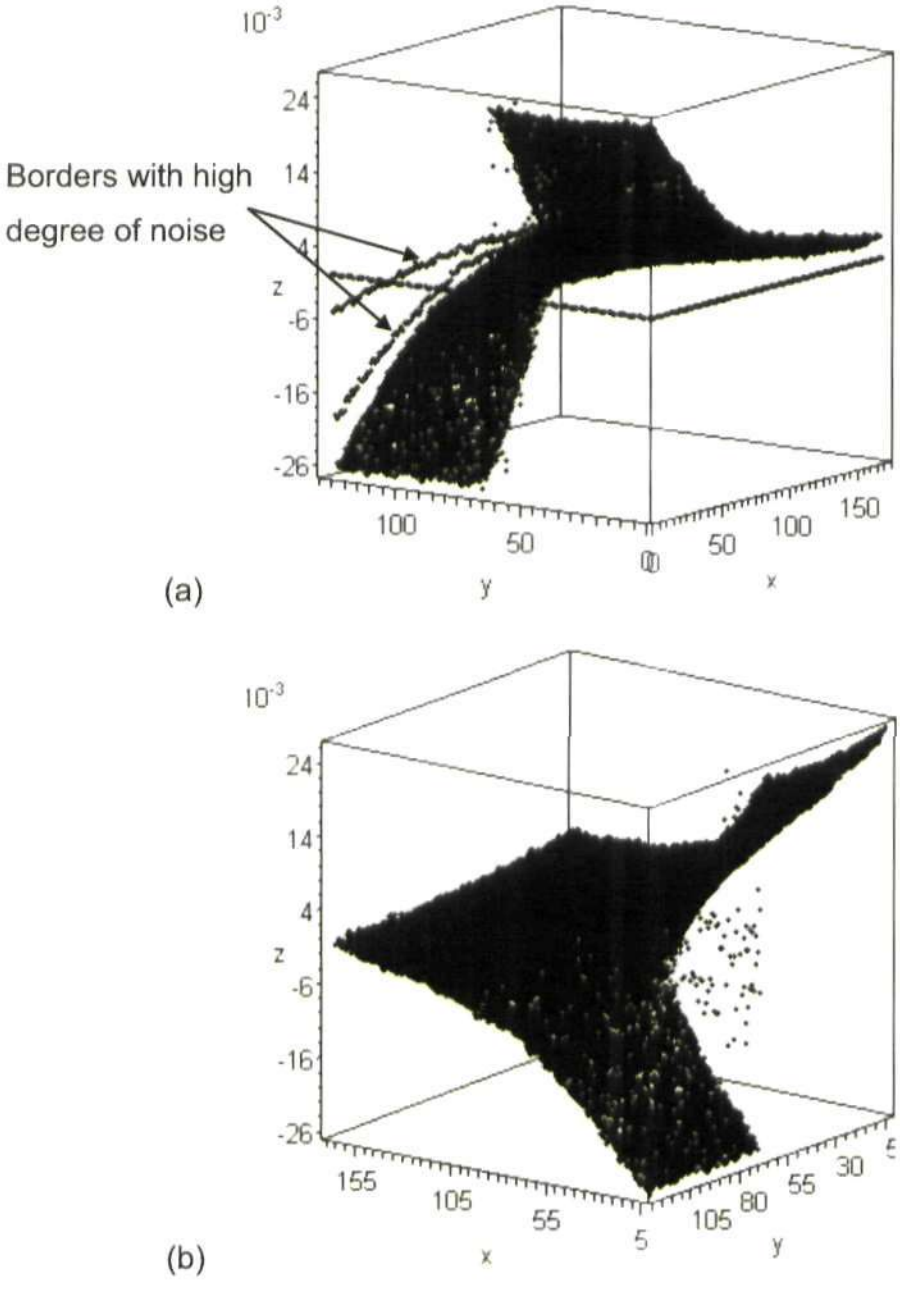

Figure 6.14 Example of a vertical displacement field showing that: (a) data close to the image borders are in high degree of noise; (b) data near the boundaries is removed from the displacement field.

From the displacement contours (Figure 6.9), a trend is observed that the vertical displacement increases as the position moves from the crack tip towards the notch mouth, whilst there is little change in the vertical displacement field ahead of the crack tip. The horizontal displacement in front of the crack tip increases as the position moves away from it towards the right border and also increases towards the top and bottom boundaries. This shows that large vertical and horizontal deformations are happening behind the crack tip and ahead of it respectively. Moreover, the displacement data in these regions has relatively high signal-to-noise ratio [94]. Hence, both horizontal and vertical displacement data are employed and also displacement data from those regions behind the cack tip and ahead of it are collected. This can be done by using outer limits to remove data from the far field. Therefore, a rectangular shaped region with an inner limit and outer limits can be used for data collection.

6.5.2 Rectangular shaped data collection zone

Figure 6.15 shows a rectangular shaped region where displacement data is collected from a vertical displacement image. This rectangular shaped region is characterised by the following parameters: an inner radius R_{inner} defining the data collection zone's inner limit, height H and width $(L1 + L2)$ defining the outer limits. These parameters can be represented by three points $P1, P2$ and $P3$: the distance between $P1$ and the crack tip equal to the value of R_{inner}; the x coordinate of point $P2$ and $P3$ define the width of rectangle $(L1 + L2)$; the y coordinate of point $P3$ defines the height $(2H)$. Therefore, one can control the shape and size of the rectangle through these three points. Moving one of the three points will change the rectangle and consequently the total number of displacement data points employed in the fitting process. The following work

studies the effect of such changes on the final solutions for K_F, K_R, K_S, and T, and the quality of fit found using different rectangular shaped data collection zones, with the purpose of determining a guide for displacement data collection.

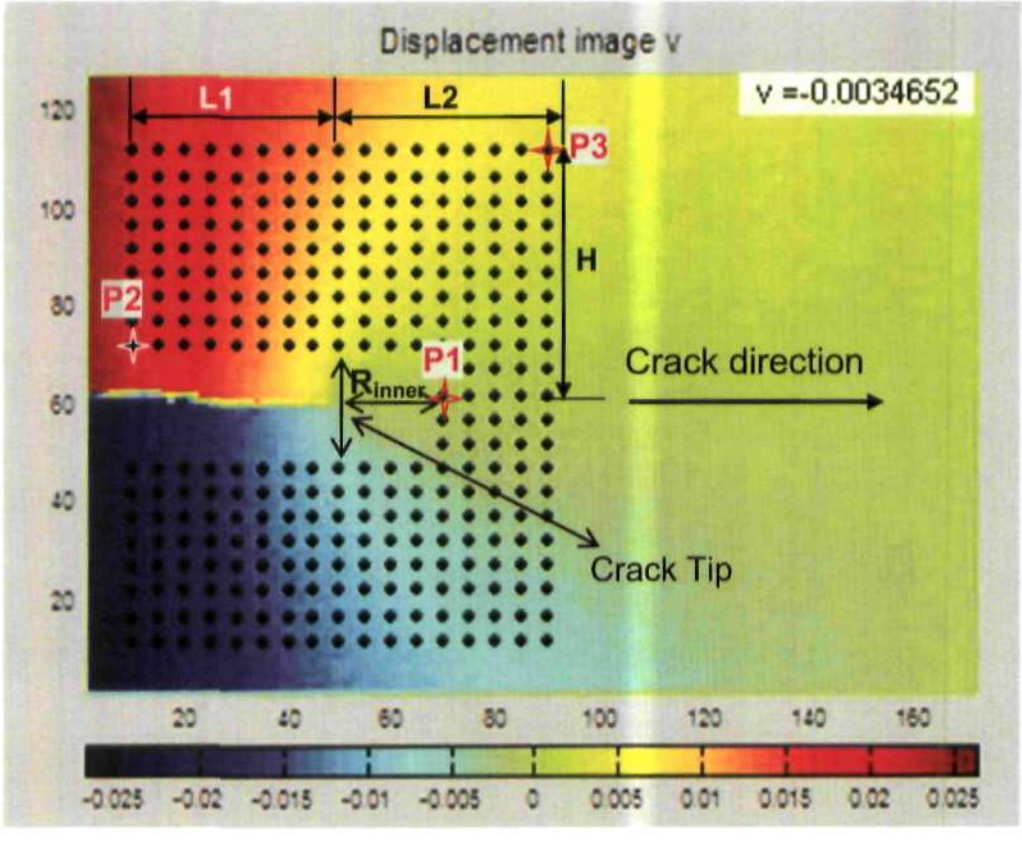

Figure 6.15 Rectangular shaped data collection zone characterised by four parameters R_{inner}, H, $L1$, and $L2$ and three points: $P1$, the distance between P1 and the cack tip equal to the value of inner radius R_{inner}; point $P2$ and $P3$ define the height and width of the rectangle.

The investigation is done by increasing the four parameters R_{inner}, H, $L1$, and $L2$ independently in this sequence. R_{inner} is studied firstly and increased from a value of R_P to $3R_P$, where R_P is the plastic zone size predicted by expression (5.4). The quality of fit is measured by the normalised mean error and standard deviation through expressions (5.6-5.7).

The resulting changes in K_F, K_R, K_S, and T-stress as a function of the ratio of R_{inner} to R_P are reported in Figure 6.16. The values of K_F appear fairly constant, with the biggest difference among them just 0.4%. There is a relatively large discrepancy in the values of K_R , K_s and T-stress with the biggest differences 15.2%, 9.3% and 5.6% respectively. Figure 6.17 presents the results for the calculated values of normalised mean error and standard deviation calculated. It is observed that increasing the inner radius increases the quality of fit with decreased normalised mean error and standard deviation. The value of normalised mean error is smaller than 0.05 in all cases and the value of standard deviation less than 0.08 in most cases except for the one at R_{inner} equal to R_P. This indicates that real plastic zone size is larger than the predicted value of plastic zone size and R_{inner} must be set larger than R_P. Hence, the inner radius is set to be $2R_P$ which not only avoids the plastic effects and ensures the validity of the elastic model but also collects as many data points as possible. Figure 6.18 presents the results for both the vertical and horizontal displacement fields predicted by the model together with experimental displacement data with the inner limit set of $2R_P$. It seems that the predicted data is very close to the real displacement data.

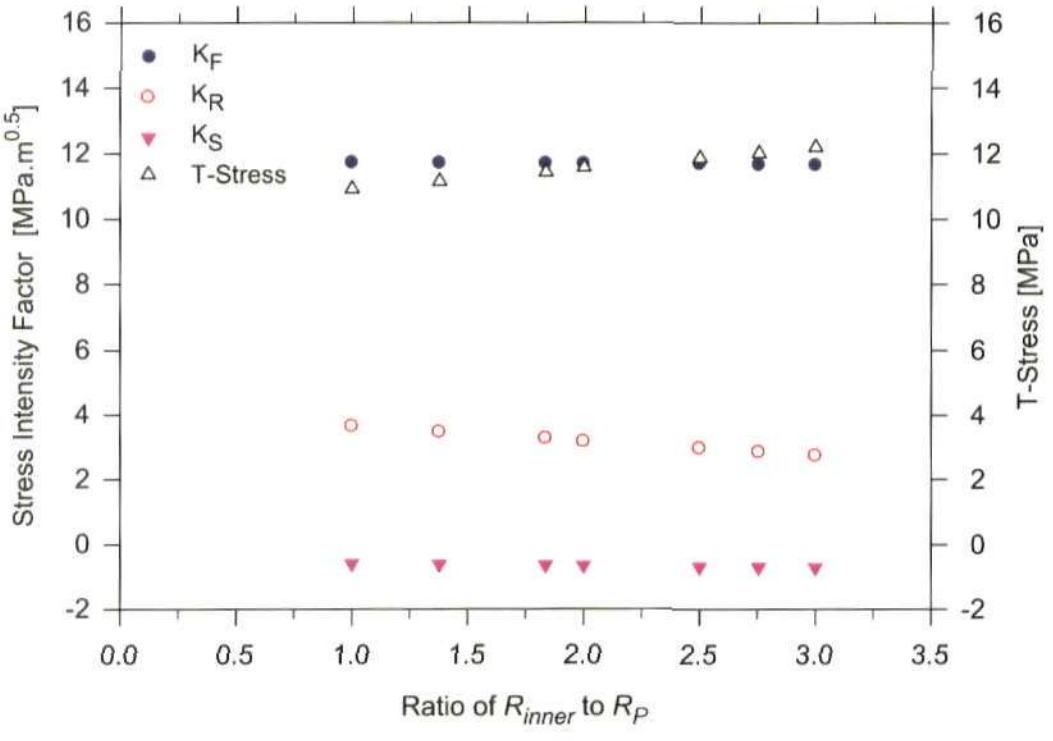

Figure 6.16 Plotting of the solutions for K_F, K_R, K_S, T-stress vs. ratio of R_{inner} to R_P.

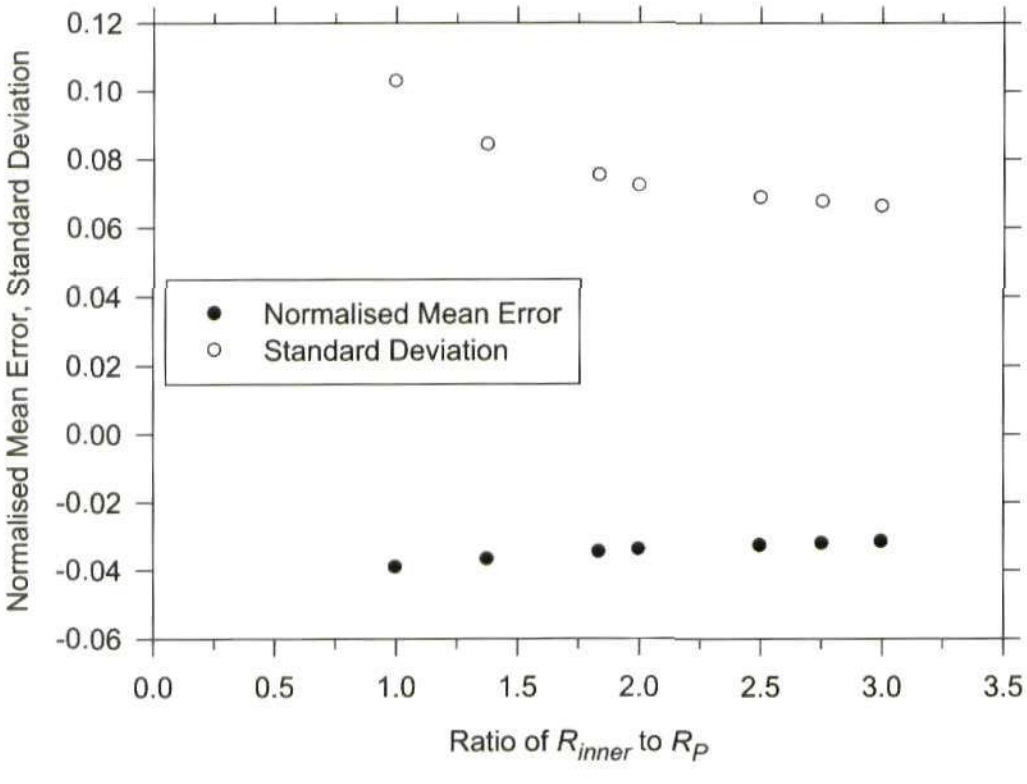

Figure 6.17 Plotting of normalised mean error and standard deviation against ratio of R_{inner} to R_P.

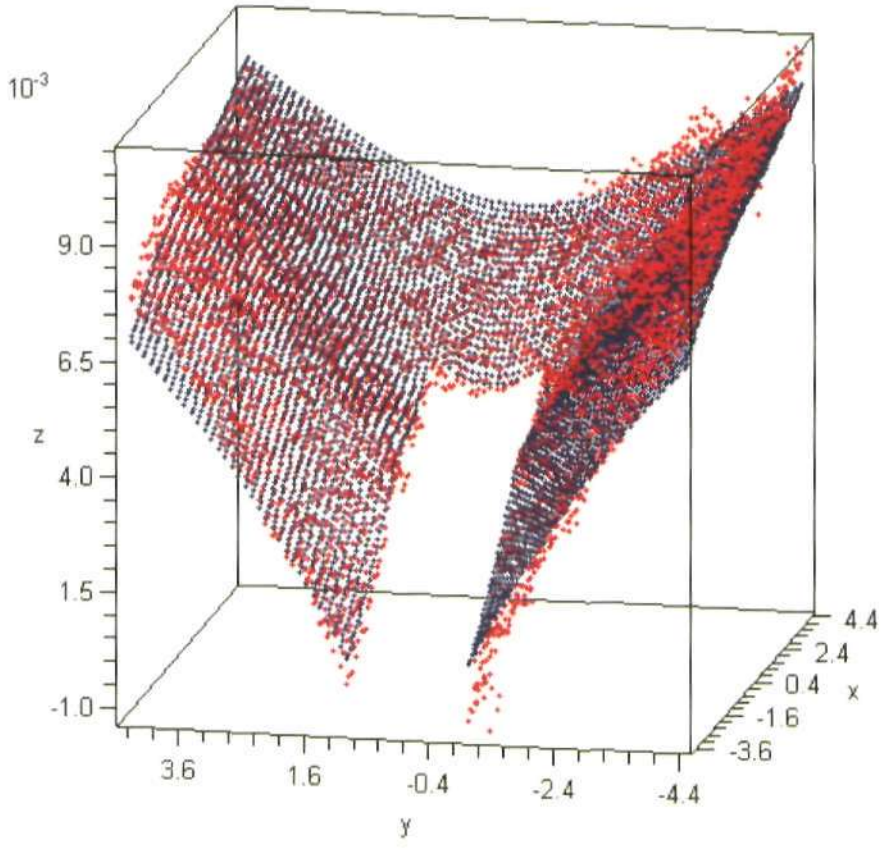

(a)

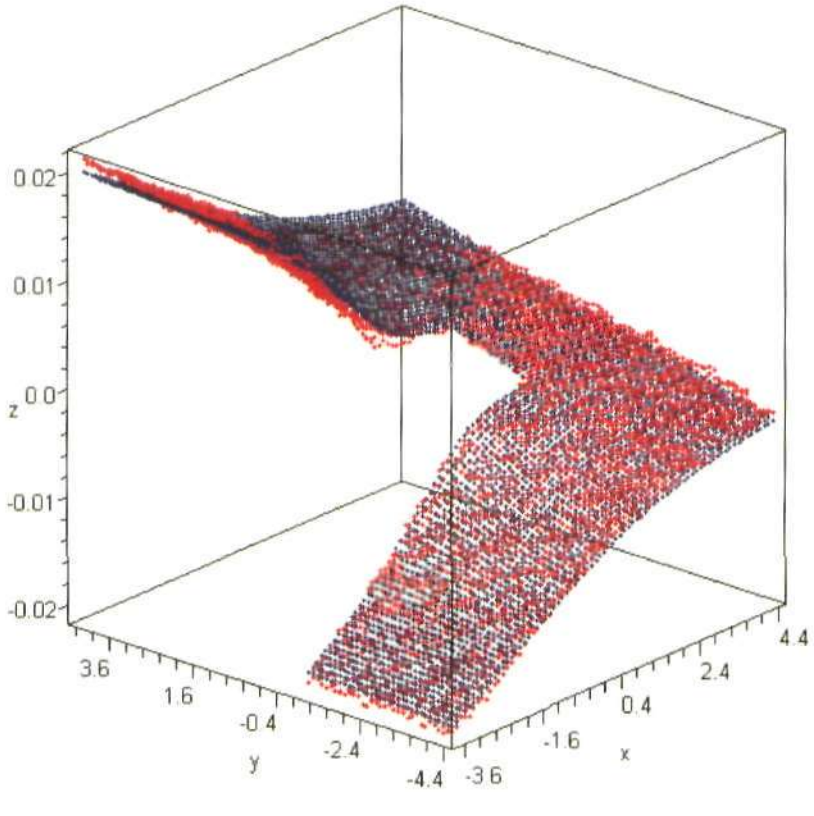

(b)

Figure 6.18 Plotting of (a) horizontal displacement field and (b) vertical displacement field predicted by the model (blue) and the experimental displacement fields (red), with the inner limit set to be $2R_P$. (Units: mm)

The investigation of the influence of the parameters H, $L1$ and $L2$ was done by increasing their value steadily in increment of $0.1a_0$, where a_0 is the crack length measured from the specimen's notch mouth. It is noteworthy that the inner limit found in the previous study as $2R_P$is employed for this investigation into H. Results of the study on H, $L1$ and $L2$ are presented in Figures 6.19-6.22.

Figure 6.22 shows that the value of normalised mean error is less than 3.5% and the value of standard deviation is below 0.08 in all cases (Figure 6.22). This again indicates that the quality of fit is good. As observed previously in Figure 6.16, K_F did not undergo much change, while the value of K_R and T-stress change dramatically over this range of value. It is also observed that from Figure 6.19, there is not much change in K_R and T-stress in those cases with ratio of H to a_0 above 0.7 and 1. Hence, a value between $0.7a_0$ and a_0 is recommended for H. For the subsequent study on $L1$ and $L2$, $H = 0.9a_0$ was employed.

Figure 6.20 also shows that large differences exist among the values of K_R and T-stress over the spanrange of parameters considered. It seems hard to make a firm decision for $L2$ just from this figure. Nevertheless, the normalised mean error appears to increase firstly when the ratio of $L2$ to a_0 is below 0.8, and then decrease when the ratio is above 0.8. This makes sense due to the value of vertical displacement data being almost constant in front of the crack tip while the value of horizontal displacement data increases as distance from the crack tip increases towards the right boundary (Figure 6.9). Therefore, it is recommended that $L2$ is set as long as possible to utilise the horizontal data with high ratio of signal-to-noise ahead of the crack tip and collect as many data points as possible. $L2 = 0.9a_0$ is employed here.

Figure 6.21 presents the results for K_F, K_R, K_S and T-stress against ratio of $L1$ to R_P. A trend is observed that the value of K_F, K_R, K_S and T-stress change little in those cases where the ratio of $L1$ to a_0 is below 0.7. Hence, for $L1$, a value below $0.7a_0$ is recommended, but cannot be chosen too small or it will reduce the total number of data points employed. A lower limit equal to or larger than the inner limit is suggested for $L1$.

In summary, this section gives a detailed investigation of the necessity of identifying a valid data collection zone, which can be rectangular shaped. Through this investigation, the following conclusions can be drawn: (1) the inner limit of a rectangular shaped data collection zone must larger than R_P, with $2R_P$ as a recommended setting; (2) a range of $0.7a_0$ and a_0 is suggested for the height of the rectangle; (3) width $L2$ can be set as long as possible to collect as many data points in front of the crack tip as possible; (4) for $L1$, a value below $0.7a_0$ but larger than the inner limit of the rectangle (about $0.4a_0$) is recommended for use.

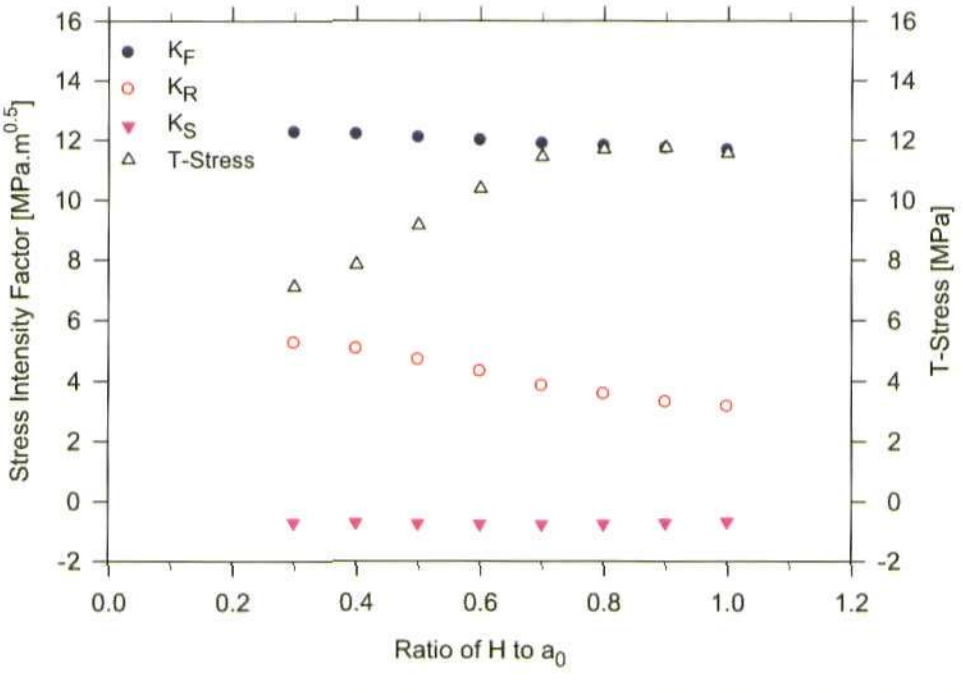

Figure 6.19 Plotting of the solutions for K_F, K_R, K_S, T-stress against ratio of H to a_0.

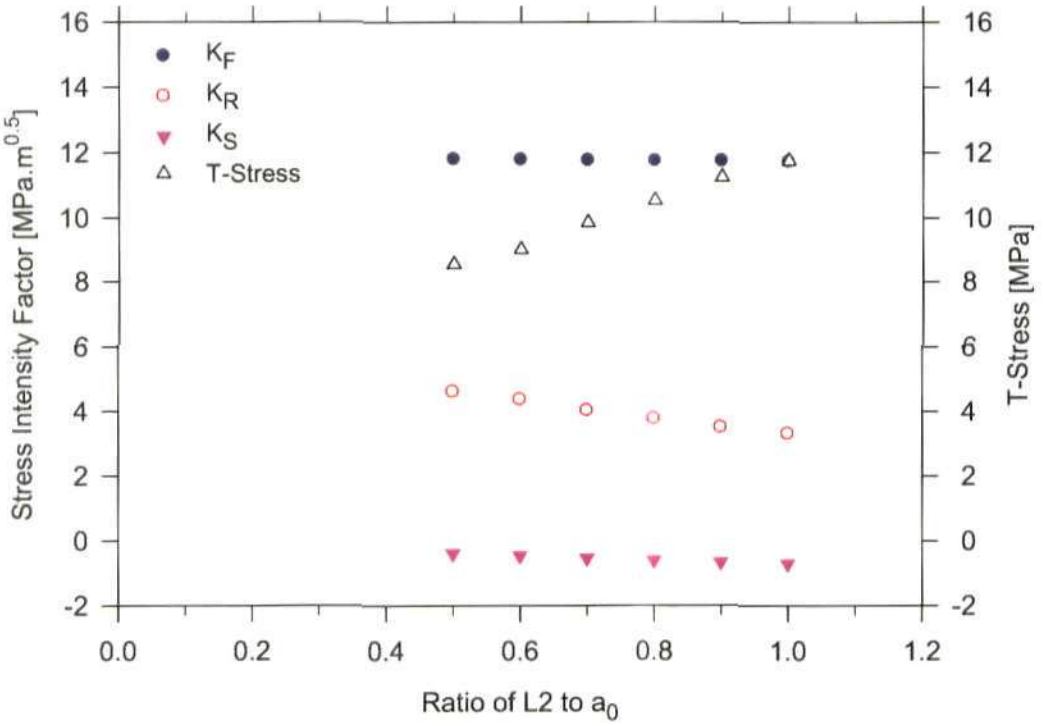

Figure 6.20 Plotting of the solutions for K_F, K_R, K_S, T-stress against ratio of $L2$ to a_0.

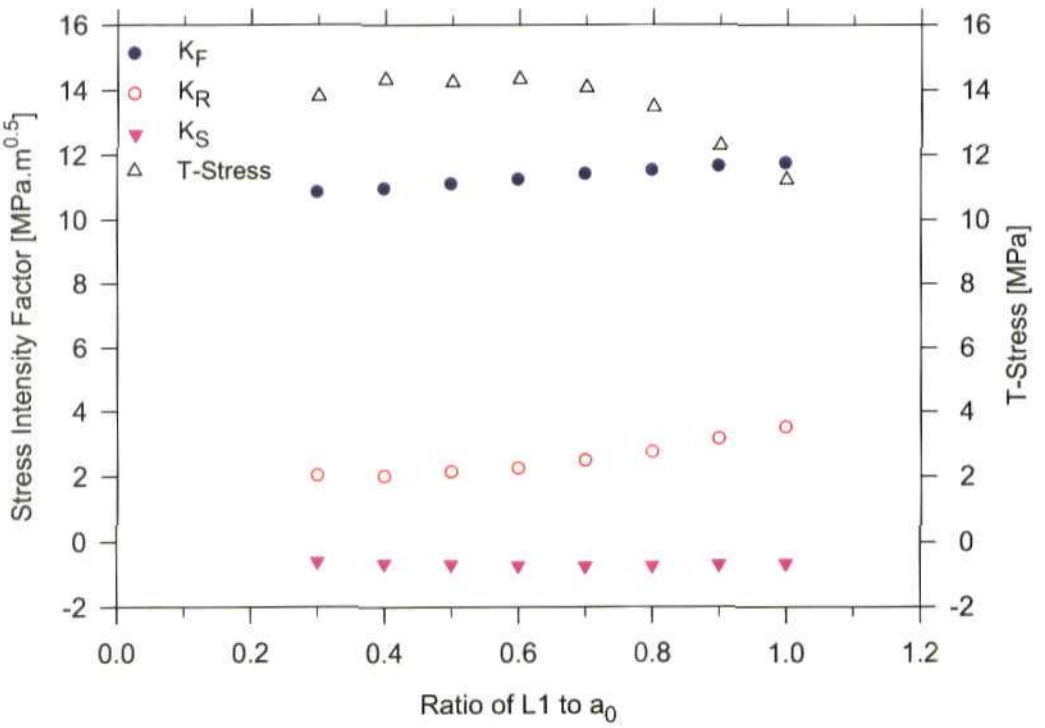

Figure 6.21 Plotting of the solutions for K_F, K_R, K_S, T-stress against ratio of $L1$ to a_0.

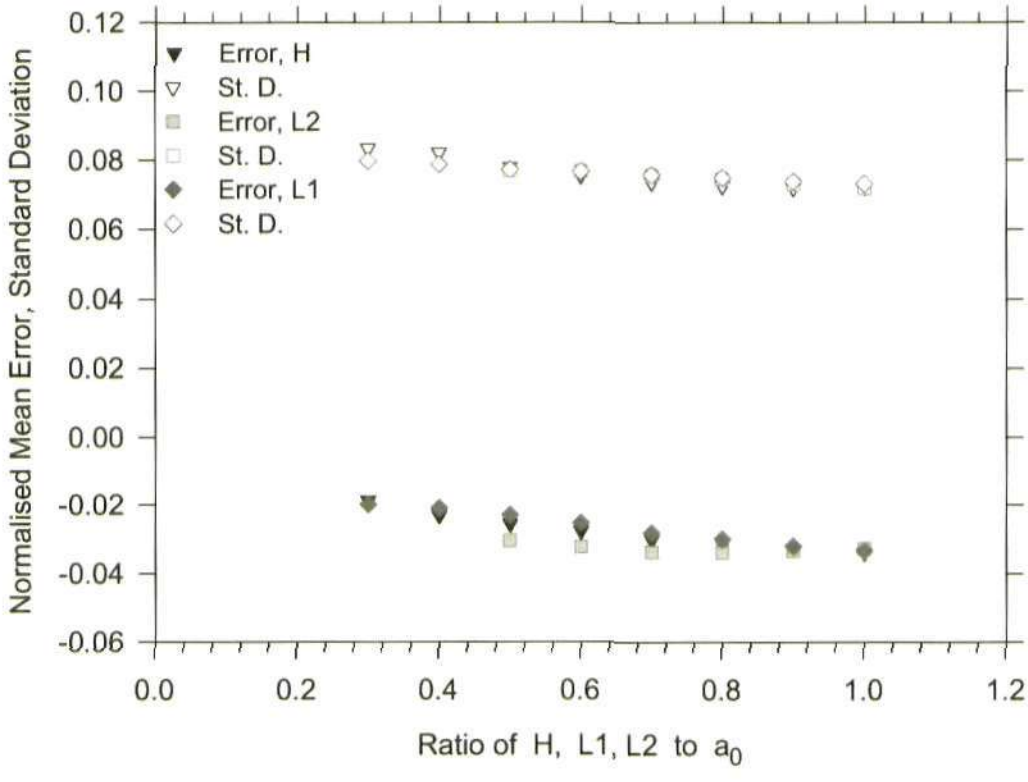

Figure 6.22 Plotting of normalised mean error and standard deviation against ratio of $H, L1, L2$ to a_0.

6.6 Experimental results

6.6.1 Crack growth measurements

Crack propagation was monitored during fatigue tests on the aluminium CT specimens. The total number of load cycles was recorded at which crack measurement was made, and digital images were taken of the crack with the DIC system. As previously described in section 6.4, crack length was estimated using the MATLAB Sobel edge detection method. Figure 6.23 shows representative crack growth data for the aluminium CT specimens tested under constant amplitude loading at $R = 0.1$, $R = 0.3$, $R = 0.5$ respectively. The crack growth rate da/dN as a function of ΔK is plotted in Figure 6.24. From Figure 6.23 and 6.24, it can be seen that for each specimen tested under constant

amplitude loading, the crack growth rate increases with increasing crack length and increasing nominal applied ΔK as expected. Furthermore, since the maximum load P_{max} was kept constant at $1200\ N$ for all the specimens, fatigue tests performed at high load ratio, i.e. a lower range of applied load/stress intensity showed a lower crack growth rate and a longer fatigue life.

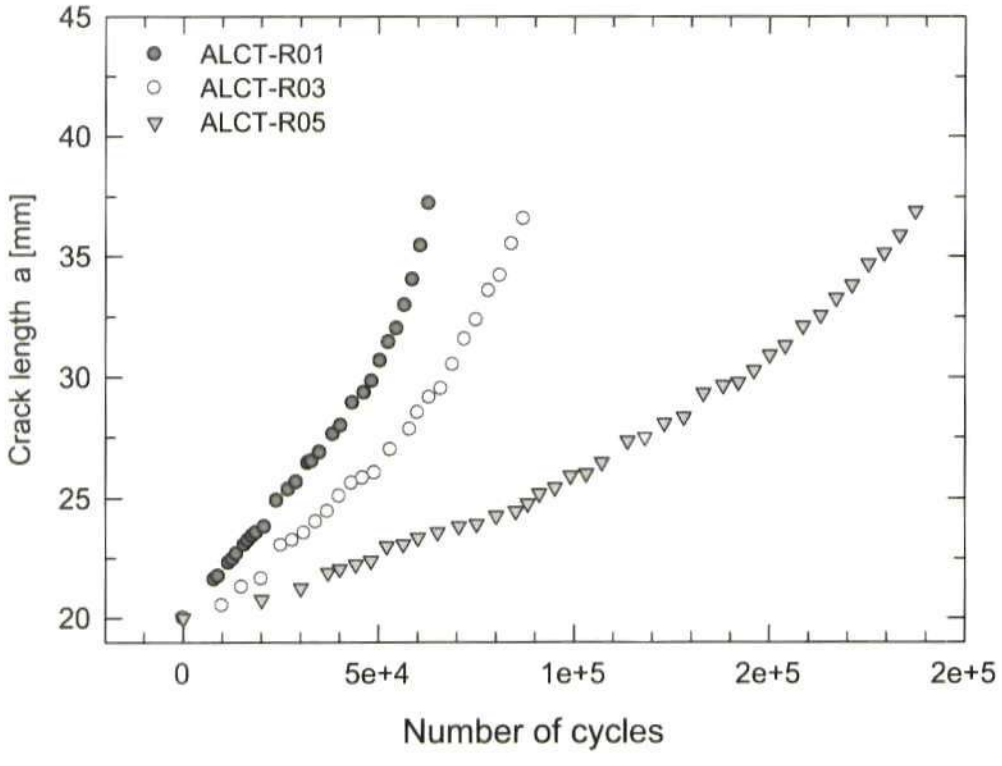

Figure 6.23 Crack lengths as a function of the number of cycles for the aluminium CT specimens tested under constant amplitude loading at $R = 0.1$, $R = 0.3$, $R = 0.5$ respectively, with the same $P_{max} = 1200\ N$ and frequency of $10.0\ HZ$.

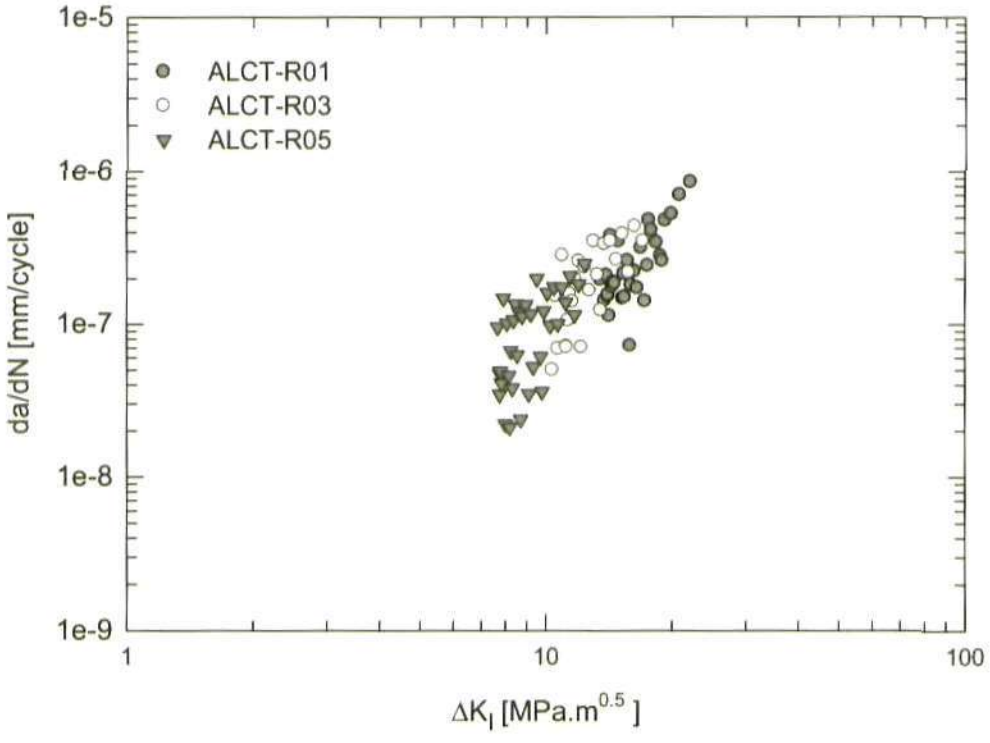

Figure 6.24 Crack growth rate as a function of the range of stress intensity factor for the aluminium CT specimens tested under constant amplitude loading at $R = 0.1$, $R = 0.3$, $R = 0.5$ respectively, with the same $P_{max} = 1200\ N$ and frequency of $10.0\ HZ$.

Moreover, it was observed that the crack in the aluminium CT specimen tested at $R = 0.1$ appeared to grow unstable with its crack path deviating from the original crack path (perpendicular to the tensile load) when the crack grown beyond about $7\ mm$ and never returned to the original crack path. The same phenomenon was observed in the specimens tested at $R = 0.3$ and $R = 0.5$ when cracks grew to about $7.5\ mm$ and $7.9\ mm$ respectively. It was also observed that the cracks initially grew flat at small crack lengths till about $3\ mm$, where they started to grow in a microscopic 'zig-zag' pattern, see Figure 6.25. From a global point of view, the crack has to propagate in its original plane. However, due to the principal stress/strain ahead of the crack occurring at $45°$

from the crack plane, the crack seems to grow in a zig-zag way. Moreover, on the fracture surface, a tunnelling effect was observed due to the crack growing at a relatively high growth rate in the centre of the specimen where there exists higher stress triaxiality. Shear lips were observed near the surface planes where the crack grows at 45° to the tensile load/principal stress due to stress triaxiality varying through the specimen thickness [179, 181].

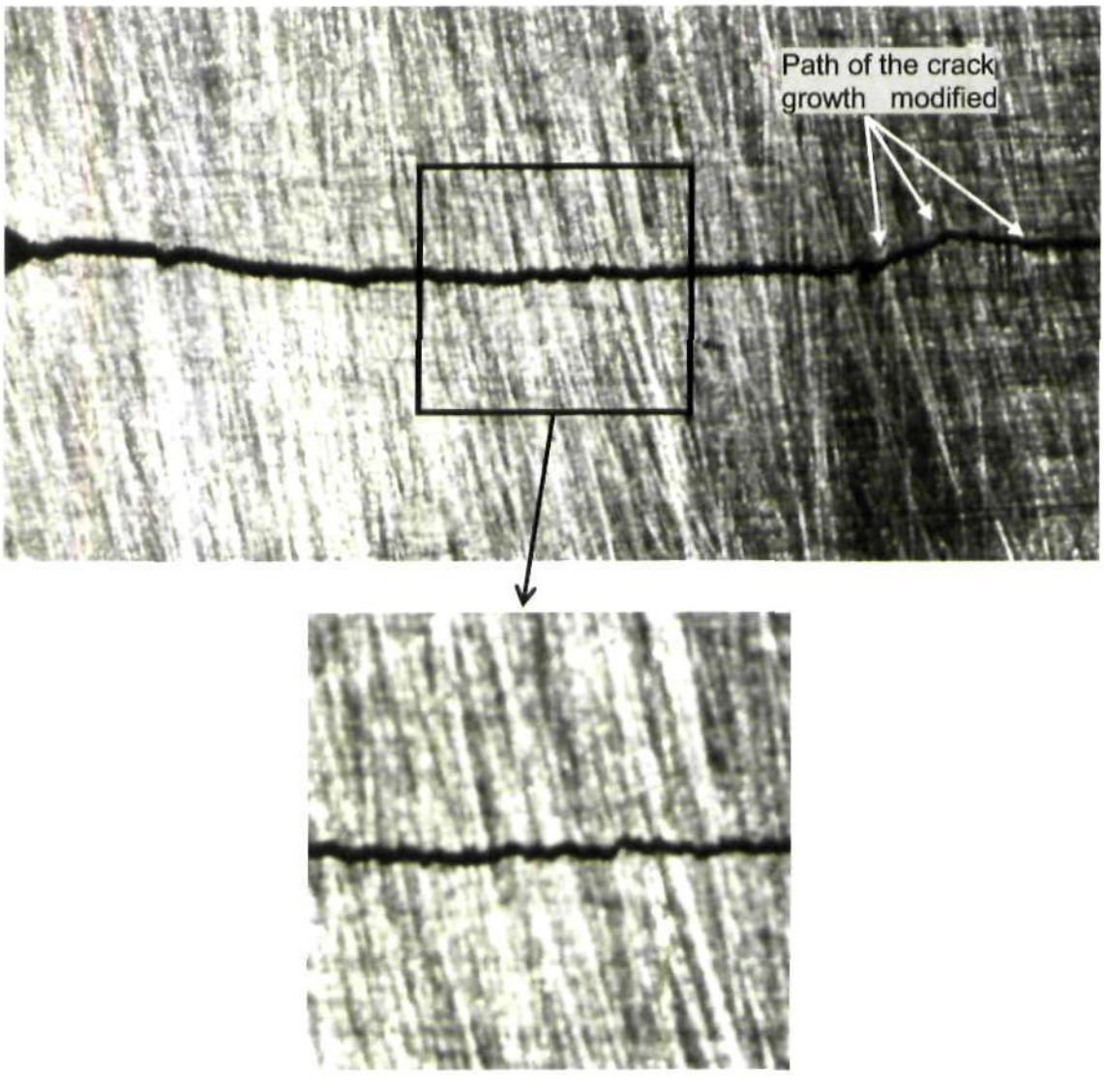

Figure 6.25 (Top): The directional unstability observed at crack length of 27 mm where crack growth becomes unstable with its path deviated from the original crack path; (bottom): microscopic 'zig-zag' behaviour exhibited by the crack.

6.6.2 Results

The experimental values obtained for the stress intensity factors K_F, K_R, K_S and T-stress, which were inferred from displacement data using the methodology described previously for the aluminium CT specimens are given in this section. Figure 6.26 presents a typical sequence of digital images recorded during a half loading cycle with the load increments of $120N$ in each step on the aluminium CT specimen tested at $R = 0.1$. It can be seen from this figure that the crack opens gradually with increasing applied load. Furthermore, the crack flanks appear closed immediately behind the crack tip at the minimum load (top left image in Figure 6.26).

Figures 6.27-6.31 present the DIC experimental results for K_F, K_R, K_S for cracks with different lengths in the aluminium CT specimens tested under constant amplitude loading with $P_{max} = 1200\ N$, a frequency of $10\ HZ$, and a load ratio $R = 0.1$.

Figure 6.27 shows the experimental results for the crack of length $25.67\ mm$ through a half loading cycle. The value of K_F is lower than the corresponding nominal K_I in all cases. The difference between K_F and the theoretical value of K_I decreases with increasing applied load. The biggest difference occurs at the minimum load where the value of K_F predicted from the model is $0.96\ MPa.m^{0.5}$ while the corresponding K_I is $3.44\ MPa.m^{0.5}$. The difference between K_F and K_I in the case of the maximum load is 16.7%. K_R has a positive value in all cases within the range of $1.25 \sim 3.67\ MPa.m^{0.5}$. It increases with increase in applied load when $K_I/K_{max} < 0.4$, following which it deceases slightly and then increases again as the applied load increases. K_S is positive at lower load levels when K_I/K_{max} below 0.4 as observed from Figure 6.27, while becomes

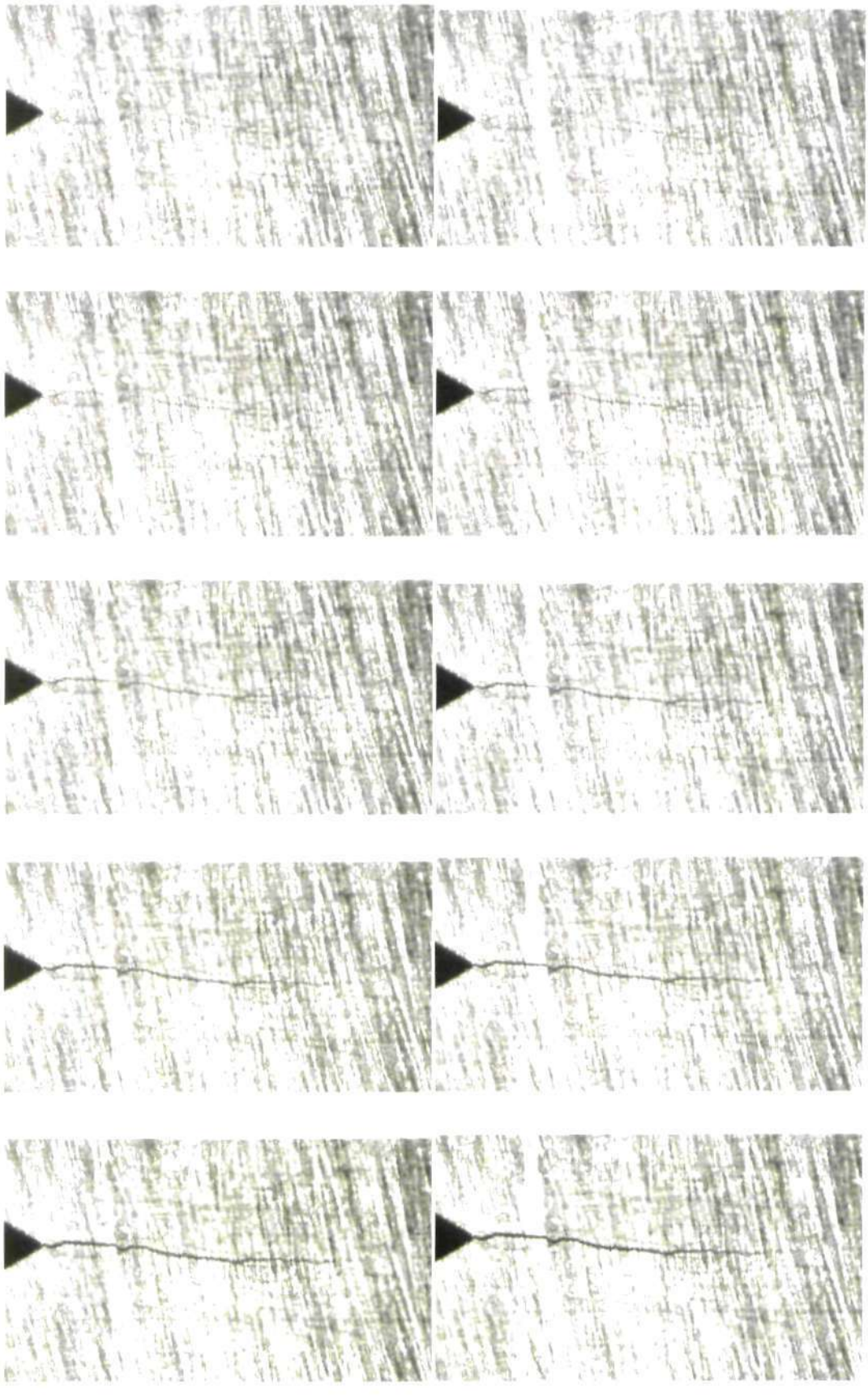

Figure 6.26 A typical sequence of DIC images recorded during a half loading cycle with load increasing from top left ($120\ N$) to bottom right ($1200\ N$) in cerements of $120\ N$ each step.

negative at values of K_I/K_{max} above 0.4. Nevertheless, the absolute value of K_S increases generally as applied load increases.

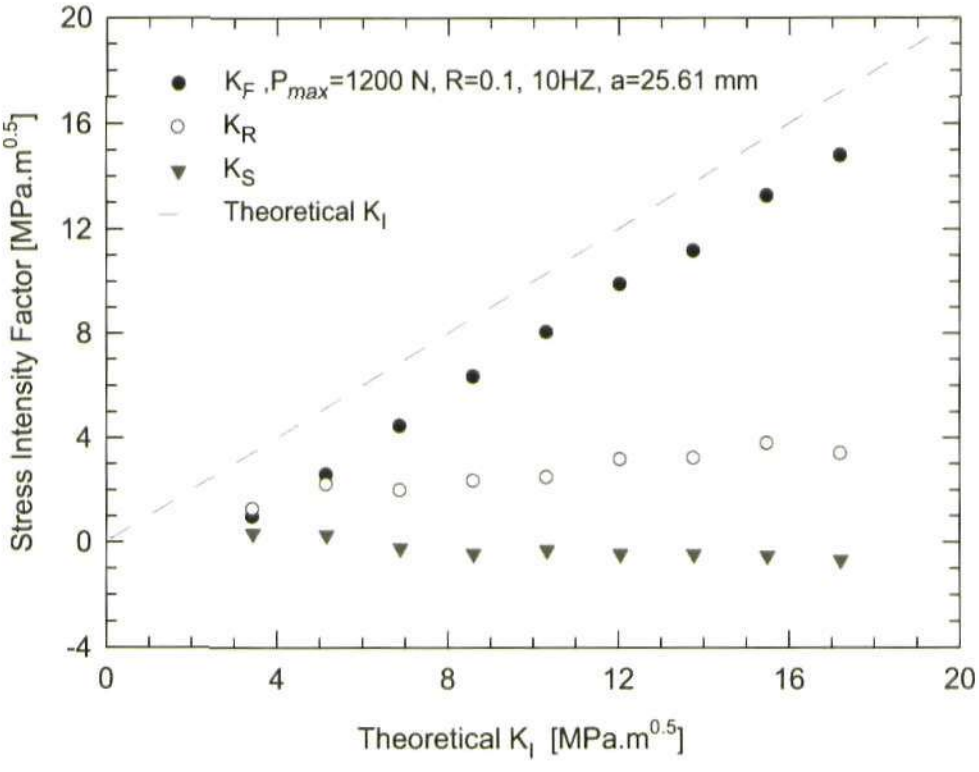

Figure 6.27 Results for K_F, K_R, K_S through a half loading cycle for the specimen tested at $R = 0.1$ with the crack length of $25.61\ mm$.

The experimental results for cracks of other length from $22.7\ mm$ to $27.0\ mm$ are reported in Figures 6.28-6.31. Similar trends for the three parameters K_F, K_R, K_S can be observed in these plots except for the one shown in Figure 6.28 for a crack of length $22.7\ mm$. As can seen in Figure 6.28, the biggest difference between the value of K_F and the theoretical K_I appears to occur at a high load level, contrary to the trend exhibited by the data for K_F for cracks with large crack length. Moreover, the data of K_R seems inconsistent and relatively scatter. This might be due to the displacement data is small in value and there is a low signal-to-noise level for shorter cracks.

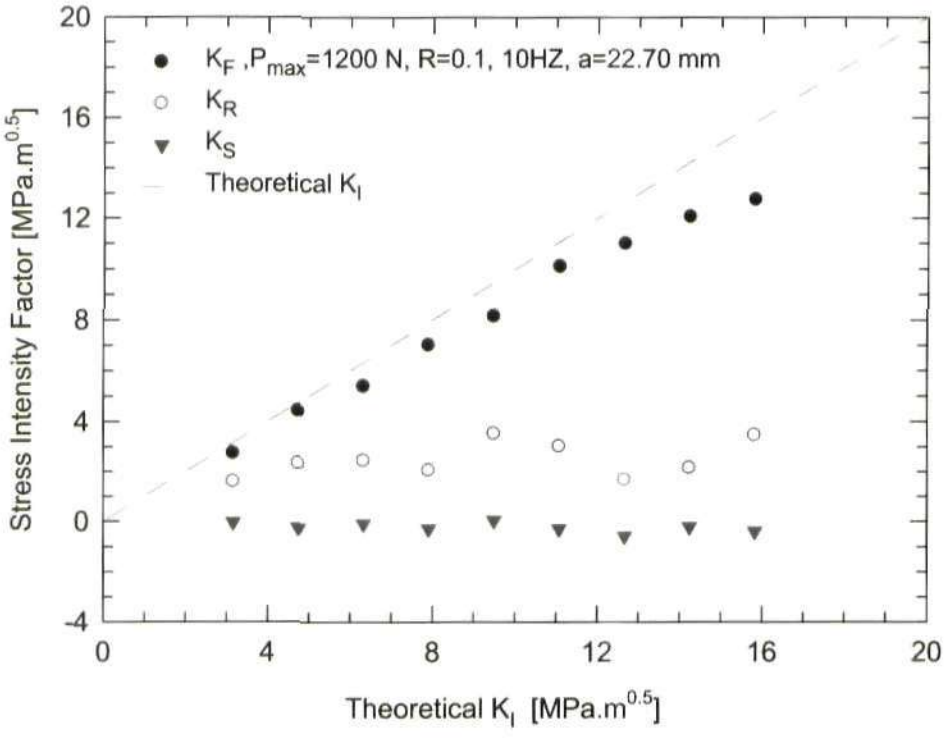

Figure 6.28 Results for K_F, K_R, K_S through a half loading cycle for the specimen tested at $R = 0.1$ with the crack length of 22.7 mm.

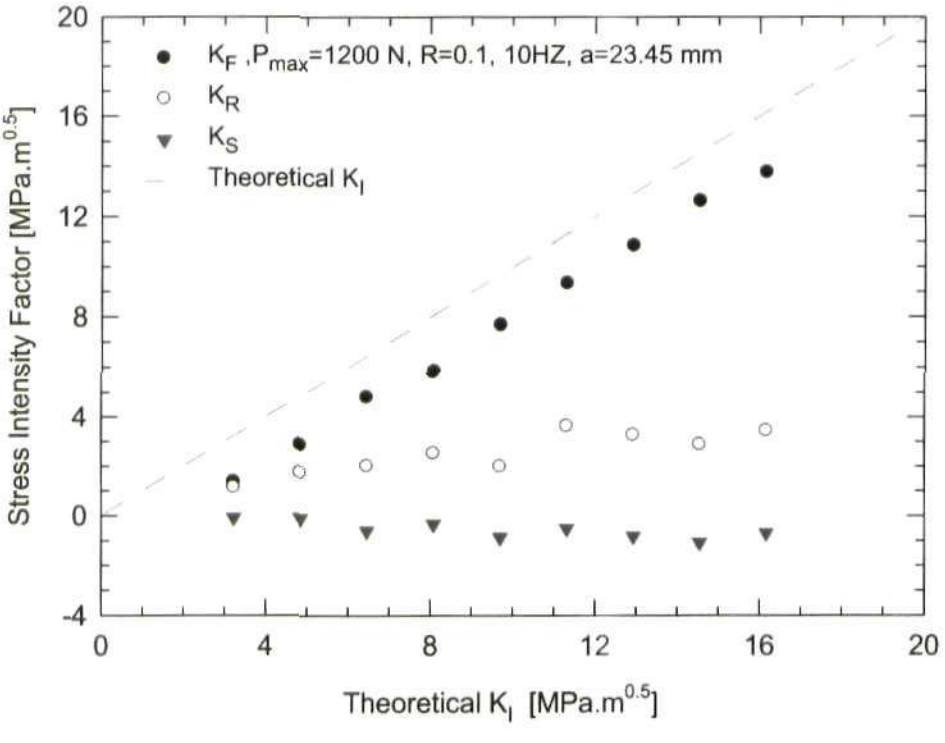

Figure 6.29 Results for K_F, K_R, K_S through a half loading cycle for the specimen tested at $R = 0.1$ with the crack length of 23.45 mm.

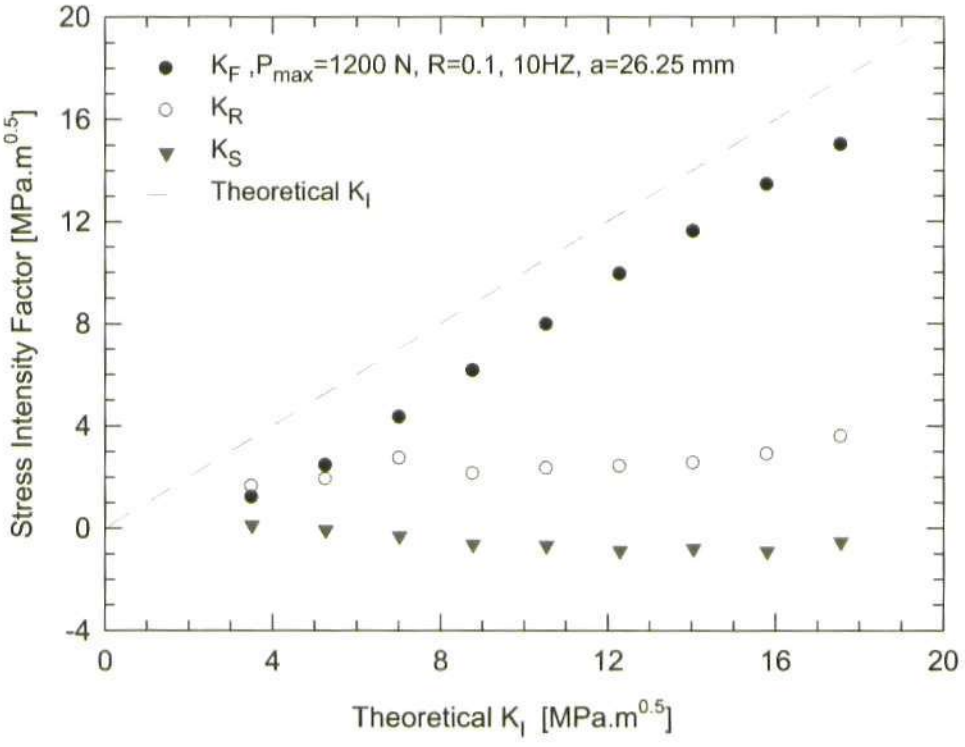

Figure 6.30 Results for K_F, K_R, K_S through a half loading cycle for the specimen tested at $R = 0.1$ with the crack length of $26.25\ mm$.

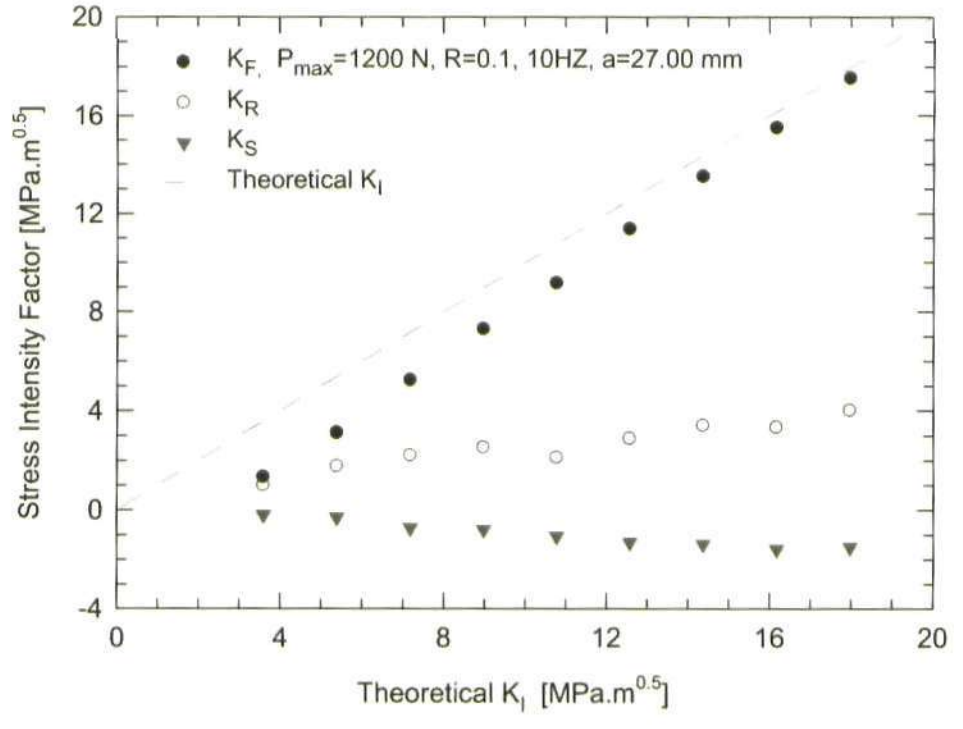

Figure 6.31 Results for K_F, K_R, K_S through a half loading cycle for the specimen tested at $R = 0.1$ with the crack length of $27.00\ mm$.

Figure 6.32 plots the results for T-stress for cracks with crack lengths of $25.61\,mm$, $26.25\,mm$ and $27.0\,mm$. It can be observed that the value of T-stress increases as the applied load increases through a half loading cycle, and also appears to increase with increase in the crack length. The figure also shows that the T-stress has generally positive values except some cases where a negative value is found at lower load levels where the displacement data is close to zero and has a poor signal-to-noise ratio [94]. Hence, in such cases, it is thought that the experimental results are not reliable and would not be considered here. This agrees well with the positive T-stress reported for CT specimens in the previous photoelastic study in this thesis and work done by other researcher, e.g. Cotterell [210]. Furthermore, high positive T-stress at the maximum load implies that there exists a high stress constraint around the crack tip which facilitates crack growth (Figure 6.23) such that cracks grow faster with increase in T-stress. Moreover, as previously discussed in section 4.2.1, T-stress has been related with the directional stability of crack path [188, 189]: straight cracks under Mode I loading conditions grow in a stable fashion and remain straight with negative T-stress, while cracks grow more unstably with crack path deviations from the initial crack plane occurring at positive T-stress (Figure 6.33). In addition, high positive T-stress in CT specimens was *also regarded as an "inherently unstable physical condition" contributing to* crack deviation by Tong [181]. Hence, unstable crack growth can be attributed to the high positive T -stress in specimens experiencing out-of-plane deformation which is not taken into account here. This seems to provide an explanation for the observation that in the current experimental work cracks in CT specimens tested under constant amplitude loading apparently became unstable after propagating about $7\,mm$ from the notch mouth (Figure 6.25)

where out-of-plane deformation might exist at a significant level and the 2D elastic model might not be valid and is not recommended to be used when a crack grows in an unstable fashion.

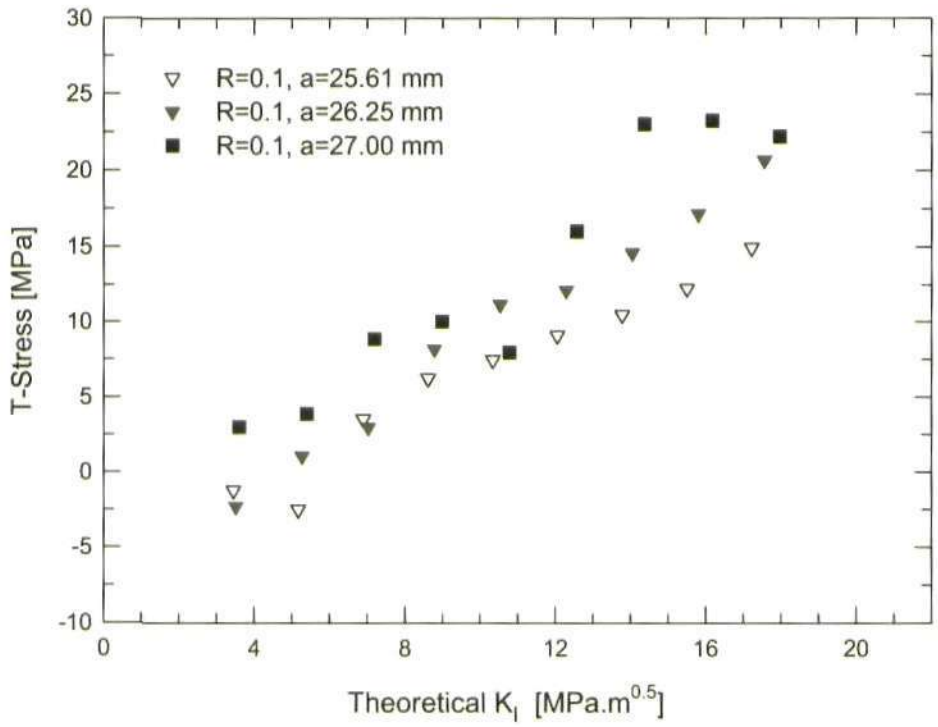

Figure 6.32 Plotting of the experimental results for T-stress through a half loading cycle for cracks of different lengths. ($P_{max} = 1200\ N,\ R = 0.1\ ,\ 10\ HZ$)

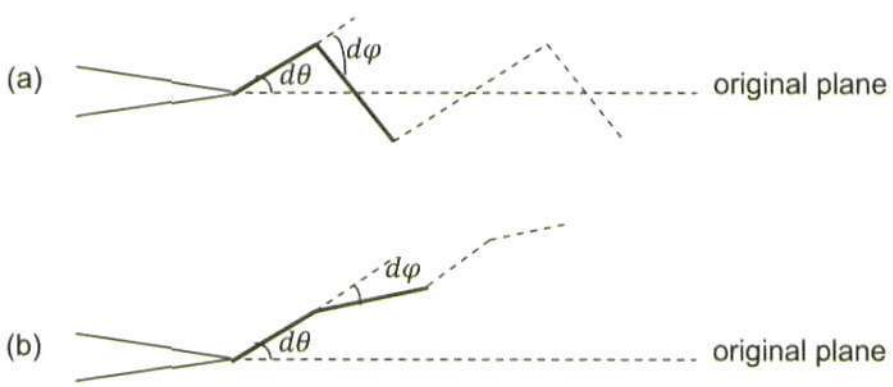

Figure 6.33 A schematic representation of the directional stability in crack growth: (a) $d\varphi > d\theta$ indicating stable crack growth; (b) $d\varphi < d\theta$ unstable crack growth.

Figure 6.34 plots the experiment results for K_F, K_R, K_S and T-stress as a function of crack length. The data is predicted from displacement data obtained at the maximum load for different crack lengths. The 95% confidence limits are also presented in the figure which indicates that the accuracy of the data is high. This figure again shows that the absolute values of K_F, K_R, K_S, and T-stress increase as the crack length increases as also seen in Figure 6.35, which plots the experiment results for all the cases with different crack lengths together for comparison. Figure 6.34 also shows that the difference between K_F and theoretical K_I is decreasing with increase in crack length. This does not mean that the effect of crack closure decreases as cracks grow longer. Due to the plastic zone growing larger at the same time, which ensures that the plastic bands along the crack flanks become wider, the effect of crack closure arising from the plastic deformation bands behind the crack tip also increases which is

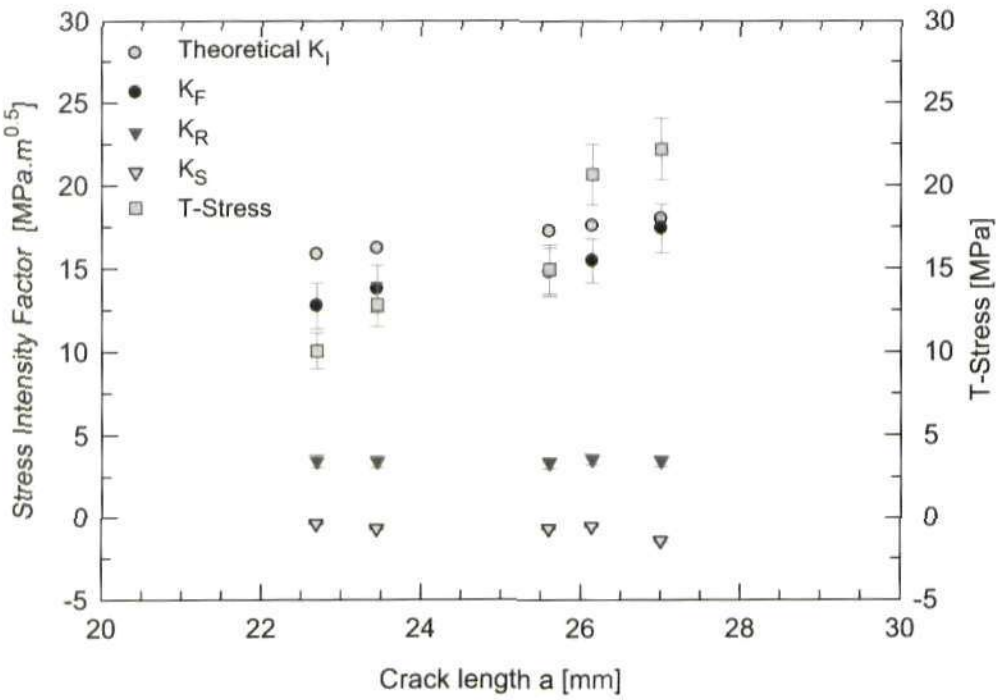

Figure 6.34 Plotting of the experimental results for K_F, K_R, K_S and T-stress predicted with the displacment data obtained at the maxinum load as a functin of crack length. ($P_{max} = 1200\ N,\ R = 0.1\ ,\ 10\ HZ$)

indicated by the increase in the value of the two parameters K_R and K_S. Therefore, the three parameters K_F, K_R and K_S should be employed together to account for the effect of crack closure on the crack growth.

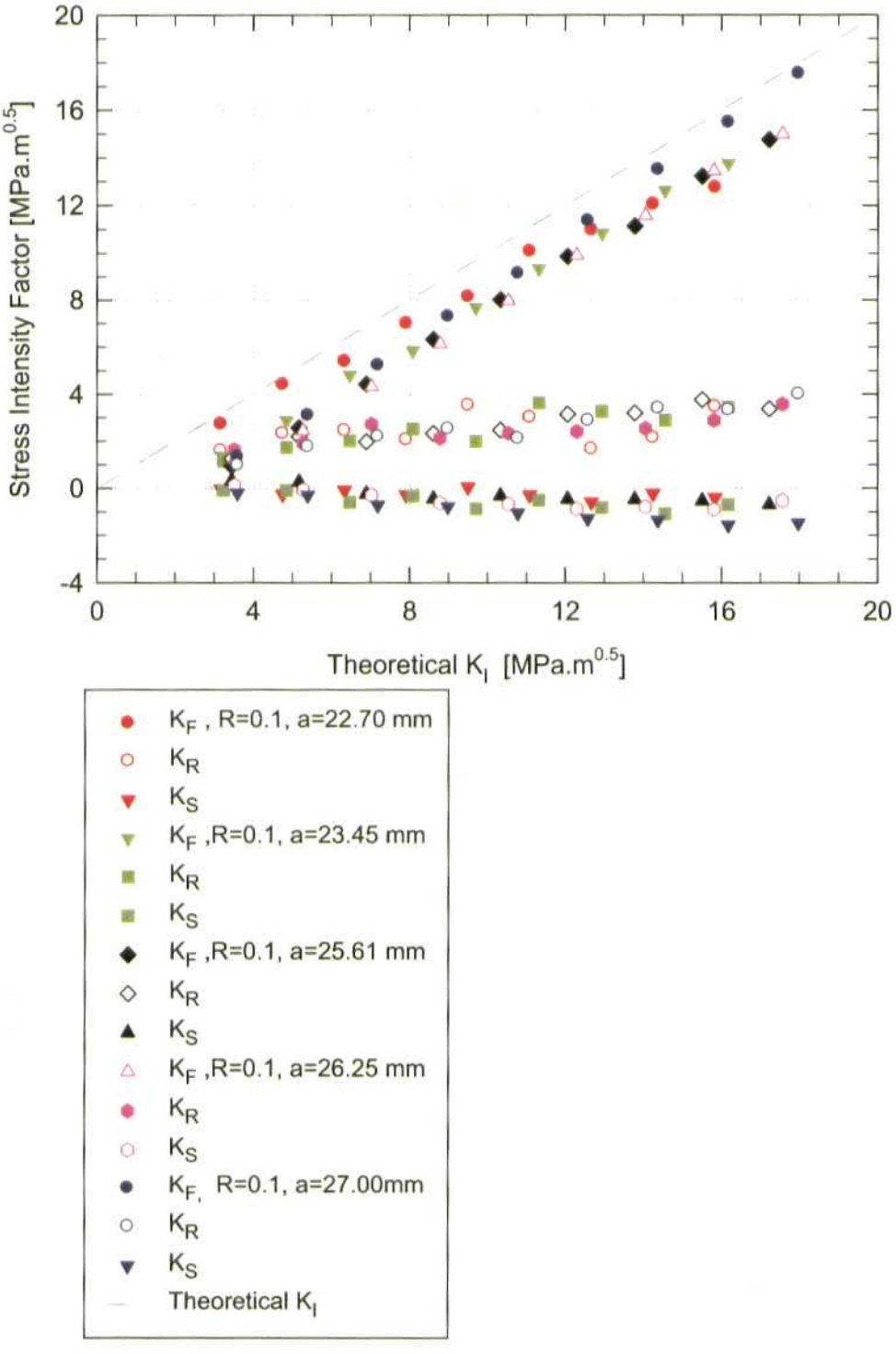

Figure 6.35 Plotting of the experimental results for K_F, K_R, K_S through a half loading cycle for cracks of different lengths. ($P_{max} = 1200\ N,\ R = 0.1\ ,\ 10\ HZ$)

6.7 Conclusions

The whole process for obtaining the full-field displacement data using the digital image correlation (DIC) technique on real fatigue cracks in aluminium compact tension (CT) specimens has been presented together with the solutions from fitting experimental displacement data to the extended four-parameter mathematical model.

Crack tip position and the measurement of crack length are done using the Sobel edge-detection method on the displacement fields which has been found to be efficient and robust, and yields satisfactory results. A sensitivity analysis of crack tip location was investigated, which showed that shifting the crack tip in the x direction introduces larger error in $K_F, K_R, K_S,$ and T compared with those arising from a shift of the same distance in the y direction. In general, shifting the coordinates in either x or y directions has a small effect on the values of K_F with errors less than 2.5% in all cases, whilst it has a significant effect on the values of $K_R, K_S,$ and T with relatively high error. In addition, incorrectly locating the crack tip especially in the x direction is the main source of error in the final solutions. It is believed that the accuracy of identifying the crack tip directly from the displacement maps would be improved if a high resolution camera was employed which would consequently increase the resolution of the displacement grid. Although a smaller facet size can be employed to increase the resolution of the displacement grid, a large computational effort is required which makes it impossible due to time constraints.

Detailed work on the selection of valid displacement data points was done. It is found that a rectangular shaped data collection zone can be used which is defined by three parameters, i.e. the inner limit, the width and the height to exclude any possible plastic deformation effect as well as boundary effects. To

obtain the best quality fit between the mathematical model and experiments, it is recommended that the inner limit is twice the Dugdale plastic zone size, the height of the rectangle is in the range from $0.7a_0$ to a_0 (actual crack extension), that data points are collected behind the crack tip no further than $0.7a_0$ as well as not too close to the crack tip, and that as many data points in front of the crack tip are collected as possible.

The results for the four parameters K_F, K_R, K_S and T were presented for aluminium CT specimens tested at $R = 0.1$, with cracks of different lengths. Reasonable trends were observed for the experimental inferred values of K_F, K_R, K_S, and T-stress for these cracks using both horizontal and vertical displacement data obtained from image correlation technique.

It was observed that the value of K_F is smaller than the corresponding theoretical K_I indicating the existence of crack tip shielding which is taken into account in the new mathematical model. In addition, the value of K_F increases with increase in the crack length as do the values of the other two stress intensity factors K_R, K_S and the constant term in the model T-stress. In most cases with a long crack length, the biggest difference between the inferred K_F from the model and the theoretical K_I occurs at small loads. High positive T-stress is obtained with longer cracks which facilitates the crack growth. Unstable crack growth is likely to occur when significant out-of-plane deformation exists possibly making the current model invalid for interpreting such cases. The value of K_R is positive in a range of $1 - 4MPa \cdot m^{0.5}$ and generally increases through a half loading cycle but with a 'drop' at about $K/K_{max} = 0.4$. The error analysis was also done for the fit between the model and experimental displacement data. The error bar plot for the four parameters

as a function of crack length (Figure 6.34) indicates that the fit is of good quality and that the accuracy of the solutions is high.

Chapter 7 Conclusions and Future work

7.1 Conclusions

The experimental investigations described in this thesis were carried out in order to validate a new four-parameter mathematical model characterising the elastic stress field around a crack contained within a plastic enclave, i.e. where the crack is essentially acting a blunt plastic inclusion in an elastic body. The model considers three stress intensity factors, i.e. a modified stress intensity factor perpendicular to the crack plane, called K_F, which drives crack growth in an analogous fashion to K_I, two additional stress intensity factors accounting for the shielding effect of the plastic enclave, i.e. an interfacial shear stress intensity factor, K_S, and a retarding stress intensity factor, K_R, and a constant non-singular term T-stress acting parallel to the crack propagation direction. According to the work done in this thesis, the following conclusions can be drawn:

1. The photoelastic stress analysis technique has successfully been used to assess the capability of the proposed four-parameter model for crack tip stresses. The work performed in this respect included:

    a) Exploring the repeatability of output data between duplicate tests on polycarbonate compact tension (CT) specimens tested under constant amplitude loading condition at different load ratios and several frequencies. The estimated values for the four stress

parameters demonstrate good data repeatability, and exhibit sensible trends as a function of crack length and load ratio. The trends are interpretable in terms of physically meaningful changes to the plastic enclave surrounding a fatigue crack.

b) The error of fit between full-field theoretical data and the experimental photoelastic data is better than that obtained using the traditional mode I stress intensity factor and the T-stress, and also better than that obtained from using the first four terms of the Williams stress equation.

2. This work has shown that correct identification of crack tip position and the definition of the region of experimental data collection are the two most important factors affecting the quality of fit, and hence accuracy of solution, in full-field experimental photoelastic modelling. A comprehensive investigation of the limits on data collection and on locating crack tip position has shown that the region of optimum data collection can be defined by an inner limit to exclude any plastic deformation effects and an outer limit in order exclude finite boundary effects. The value of this inner limit is recommended as two times the Dugdale plastic zone size, and a closed fringe loop of order > 3 is suggested to be taken as the outer limit. These limits yield reliable data, as shown in Section 5.5.3.

3. The model has been proven to be successful in characterising the stress field via comparison between the stress field predicted by the model and that found from the experimental data. In addition, it has been proven that the new four-parameter model can capture the subtleties of local

plastic perturbation of the global elastic stress field better than the Williams solution for crack tip stresses.

4. The four-parameter model characterising the elastic stress field around a crack has been extended to deal with displacement fields. Taking advantage of digital image correlation (DIC) techniques makes it possible to extend the investigations done using polycarbonate material to metallic specimens.

5. The resolution of displacement measurement and hence the accuracy of the DIC results rests on the resolution of the CCD camera employed in the digital image correlation system. The CCD in the cameras used in the DIC work had 1392×1040 pixels. Using the calibration procedure outlined in sections 4.3.3.7 and 4.3.4.4 gives a value for the magnification factor $k = 0.013\, mm/pixel$. The maximum corresponding image size around the crack tip is then about $17.6\, mm \times 13.2\, mm$. It has been shown that a recognizable feature to track requires an area of at least 3×3 pixels, which is termed a facet. These facets can be overlapped and hence the resolution of any feature, e.g. the crack tip position can be located to an accuracy of around $0.021\, mm$.

6. In a similar fashion to the photoelastic data, accurate location of the crack tip position and specific data collection zones are key parameters which control accuracy in a DIC study. The Sobel edge detection method uses a facet size of 3×3 pixels and was found to yield satisfactory predictions of the crack tip coordinates (i.e. equivalent to an error generally less than 1% in $K_F, K_R, K_S,$ and T when the crack tip is shifted by 1 pixel in the y direction and errors in K_F less than 2.5% when

the crack tip is shifted by 1 pixel in the x direction). There is already a standard routine in MATLAB for this purpose. A rectangular shaped data collection zone is employed in the current study. Due to the different trends exhibited by the stress field and displacement fields, displacement data with a high signal-to noise ratio from far behind and in front of the crack tip should be collected, while data inside the plastic enclave and at the image edges will be excluded.

7. Reasonable trends were again demonstrated by the experimental values of $K_F, K_R, K_S,$ and T-stress for cracks with different lengths, which were inferred by the new model characterising the displacement field around the crack tip using both horizontal and vertical displacement data obtained from image correlation technique.

7.2 Suggestions for future work

Previous experimental investigations using photoelastic and digital image correlation techniques have had reasonable success in assessing the ability of the new four-parameter mathematical model to characterise the stress and displacement fields ahead of the crack tip. However, there are still some issues that should be addressed as future work:

1. Though the utility of the new four-parameter model has been proven, in that it describes the real elastic field around the crack tip surrounded by a plastic enclave better than traditional one-parameter or two-parameter stress models, no work has yet been done on crack growth prediction using this model.

   Investigation on the relationship between the stress intensity factors K_F and K_R with the crack growth rate da/dN is an interesting research area.

It would seem quite feasible that some combination of the two intensity factors would be able to account for plasticity effects explicitly in making fatigue crack growth rate predictions. However, further work is required to verify this hypothesis. In addition, work might be also needed on identifying the crack opening load or closure load from the inferred stress intensity factors by the model by using one technique or a combination of different techniques which makes it possible to simultaneously measure both displacement data and the stress data, e.g. thermoelasticity and digital image correlation.

Future investigations should aim at improving the way in which the model captures effects of the plastic inclusion, and in exploring how to better define the stress intensity parameters and the effective range of stress intensity factors that provide the best predictive capability for characterising fatigue crack growth.

2. Experimental work will be required to apply the model to different specimen geometries, e.g. considering effects of the specimen thickness, and different loading conditions, e.g. overloads, varying amplitude loading conditions. The mathematical model could also be extended to mixed-mode cases. These could help to improve the ability and validity of the model in characterising the elastic stress and strain fields around the crack tip through an exploration of any limitations of the model.
3. A model with more terms might also be worthy of consideration. This investigation has been done on the Williams' and Muskhelishvili's stress solutions, and some work has indicated that using a 3-terms Williams' stress solution yields more satisfactory results [220] , whilst a 7-term model is recommended when using Muskhelishvili's stress solution [94].

4. In the current DIC experimental work, the network of random scratches obtained by polishing the bare metal surface was used for image correlation, instead of a speckle pattern painted on the surface of aluminium CT specimens; reflections could not be avoided in the current DIC study, and the uncertainties introduced by different methods for producing a speckle pattern need to be investigated in future.

   To be able to achieve a higher accuracy in locating the crack tip and hence of the final solution, the coordinates of the crack tip can be included into the system of equations as two unknowns and then using optimisation algorithms, e.g. a genetic algorithm and downhill simplex algorithm.

References

1. Singh, K.D., Parry, M.R. and Sinclair, I., *Some issues on finite element modelling of plasticity induced crack closure due to constant amplitude loading.* International Journal of Fatigue, 2008. **30**(10-11): p. 1898-1920.
2. Gonzalez-Herrera, A. and Zapatero, J., *Tri-dimensional numerical modelling of plasticity induced fatigue crack closure.* Engineering Fracture Mechanics, 2008. **75**(15): p. 4513-4528.
3. de Matos, P.F.P. and Nowell, D., *The influence of the Poisson's ratio and corner point singularities in three-dimensional plasticity-induced fatigue crack closure: A numerical study.* International Journal of Fatigue, 2008. **30**(10-11): p. 1930-1943.
4. de Matos, P.F.P. and Nowell, D., *Numerical simulation of plasticity-induced fatigue crack closure with emphasis on the crack growth scheme: 2D and 3D analyses.* Engineering Fracture Mechanics, 2008. **75**(8): p. 2087-2114.
5. Antunes, F.V. and Rodrigues, D.M., *Numerical simulation of plasticity induced crack closure: Identification and discussion of parameters.* Engineering Fracture Mechanics, 2008. **75**(10): p. 3101-3120.
6. Pokluda, J. and Pippan, R., *Analysis of roughness-induced crack closure based on asymmetric crack-wake plasticity and size ratio effect.* Materials Science and Engineering: A, 2007. **462**(1-2): p. 355-358.
7. de Matos, P.F.P. and Nowell, D., *On the accurate assessment of crack opening and closing stresses in plasticity-induced fatigue crack closure problems.* Engineering Fracture Mechanics, 2007. **74**(10): p. 1579-1601.
8. Singh, K.D., Khor, K.H. and Sinclair, I., *Roughness- and plasticity-induced fatigue crack closure under single overloads: Analytical modelling.* Acta Materialia, 2006. **54**(17): p. 4405-4414.
9. Singh, K.D., Khor, K.H. and Sinclair, I., *Roughness- and plasticity-induced fatigue crack closure under single overloads: Finite element modelling.* Acta Materialia, 2006. **54**(17): p. 4393-4403.
10. Jiang, Y.Y., Feng, M.L. and Ding, F., *A reexamination of plasticity-induced crack closure in fatigue crack propagation.* International Journal of Plasticity, 2005. **21**(9): p. 1720-1740.
11. Wei, L.W. and James, M.N., *Numerical modelling of plasticity-induced crack closure for interfacial cracks in bi-material specimens.* Engineering Fracture Mechanics, 2004. **71**(3): p. 309-327.
12. Solanki, K., Daniewicz, S.R. and Newman, J.C., *Finite element analysis of plasticity-induced fatigue crack closure: an overview.* Engineering Fracture Mechanics, 2004. **71**(2): p. 149-171.
13. Newman, J.A. and Piascik, R.S., *Interactions of plasticity and oxide crack closure mechanisms near the fatigue crack growth threshold.* International Journal of Fatigue, 2004. **26**(9): p. 923-927.
14. Solanki, K., Daniewicz, S.R. and Newman, J.C., *Finite element modeling of plasticity-induced crack closure with emphasis on geometry and mesh refinement effects.* Engineering Fracture Mechanics, 2003. **70**(12): p. 1475-1489.
15. McKellar, D.K., Nowell, D. and Hills, D.A., *The use of closure maps to characterise plasticity induced crack closure.* International Journal of Fatigue, 2003. **25**(3): p. 257-264.
16. James, M.N., Pacey, M.N., Wei, L.W. and Patterson, E.A., *Characterisation of plasticity-induced closure--crack flank contact force versus plastic enclave.* Engineering Fracture Mechanics, 2003. **70**(17): p. 2473-2487.

17. Zhang, X.P., Li, J.C., Wang, C.H., Ye, L. and Mai, Y.W., *Prediction of short fatigue crack propagation behaviour by characterization of both plasticity and roughness induced crack closures.* International Journal of Fatigue, 2002. **24**(5): p. 529-536.
18. Skinner, J.D. and Daniewicz, S.R., *Simulation of plasticity-induced fatigue crack closure in part-through cracked geometries using finite element analysis.* Engineering Fracture Mechanics, 2002. **69**(1): p. 1-11.
19. Rose, L.R.F. and Wang, C.H., *Self-similar analysis of plasticity-induced closure of small fatigue cracks.* Journal of the Mechanics and Physics of Solids, 2001. **49**(2): p. 401-429.
20. Kim, J.H. and Lee, S.B., *Behavior of plasticity-induced crack closure and roughness-induced crack closure in aluminum alloy.* International Journal of Fatigue, 2001. **23**(Supplement 1): p. 247-251.
21. Parry, M.R., Syngellakis, S. and Sinclair, I., *Numerical modelling of combined roughness and plasticity induced crack closure effects in fatigue.* Materials Science and Engineering A, 2000. **291**(1-2): p. 224-234.
22. Pippan, R. and Riemelmoser, F.O., *Visualization of the plasticity-induced crack closure under plane strain conditions.* Engineering Fracture Mechanics, 1998. **60**(3): p. 315-322.
23. Hou, C.Y. and Charng, J.J., *Estimation of plasticity-induced crack closure in a pre-existing plastic zone.* International Journal of Fatigue, 1996. **18**(7): p. 463-474.
24. Biner, S.B., Buck, O. and Spitzig, W.A., *Plasticity induced fatigue crack closure in single and dual phase materials.* Engineering Fracture Mechanics, 1994. **47**(1): p. 1-12.
25. Hermann, R., *Plasticity-induced crack closure study by the shadow optical method.* Scripta Metallurgica et Materialia, 1991. **25**(1): p. 207-212.
26. Llorca, J. and Sánchez Gálvez, V., *Modelling plasticity-induced fatigue crack closure.* Engineering Fracture Mechanics, 1990. **37**(1): p. 185-196.
27. Chermahini, R.G., Shivakumar, K.N., Newman Jr, J.C. and Blom, A.F., *Three-Dimensional aspects of plasticity-induced fatigue crack closure.* Engineering Fracture Mechanics, 1989. **34**(2): p. 393-401.
28. Shin, C.S. and Smith, R.A., *Fatigue crack growth at stress concentrations--the role of notch plasticity and crack closure.* Engineering Fracture Mechanics, 1988. **29**(3): p. 301-315.
29. James, M.N., *Some observations of the effect of microstructure, wake plasticity and fast cooling on fatigue crack closure.* International Journal of Fatigue, 1987. **9**(3): p. 179-183.
30. Fleck, N.A., *Finite element analysis of plasticity-induced crack closure under plane strain conditions.* Engineering Fracture Mechanics, 1986. **25**(4): p. 441-449.
31. Schijve, J., *Four lectures on fatigue crack growth: II. Fatigue cracks, plasticity effects and crack closure.* Engineering Fracture Mechanics, 1979. **11**(1): p. 182-196.
32. Rice, J.R., *Limitations to the small scale yielding approximation for crack tip plasticity.* Journal of the Mechanics and Physics of Solids, 1974. **22**: p. 17-26.
33. Rodrigues, D.M. and Antunes, F.V., *Finite element simulation of plasticity induced crack closure with different material constitutive models.* Engineering Fracture Mechanics, 2009. **76**(9): p. 1215-1230.
34. de Matos, P.F.P. and Nowell, D., *Experimental and numerical investigation of thickness effects in plasticity-induced fatigue crack closure.* International Journal of Fatigue, 2009. **31**(11-12): p. 1795-1804.
35. Fitzpatrick, M.E., Bhattacharjee, D., Cree, A.M. and Daykin, C.R.S., *Is fatigue surface roughness a sufficient condition for the generation of crack closure?* Scripta Materialia, 1996. **35**(11): p. 1335-1340.

36. Jung, H.Y. and Antolovich, S.D., *Experimental characterization of roughness-induced crack closure in Al-Li 2090 alloy.* Scripta Metallurgica et Materialia, 1995. **33**(2): p. 275-281.
37. Kamp, N., Gao, N., Starink, M.J., Parry, M.R. and Sinclair, I., *Analytical modelling of the influence of local mixed mode displacements on roughness induced crack closure.* International Journal of Fatigue, 2007. **29**(5): p. 897-908.
38. Kamp, N., Parry, M.R., Singh, K.D. and Sinclair, I., *Analytical and finite element modelling of roughness induced crack closure.* Acta Materialia, 2004. **52**(2): p. 343-353.
39. Li, S.X., Sun, L.Z., Zang, Q.S. and Wang, Z.G., *A geometric model for fatigue crack closure induced by fracture surface roughness under mode I displacements.* Materials Science and Engineering: A, 1992. **150**(2): p. 209-212.
40. Pippan, R., Strobl, G., Kreuzer, H. and Motz, C., *Asymmetric crack wake plasticity - a reason for roughness induced crack closure.* Acta Materialia, 2004. **52**(15): p. 4493-4502.
41. Sewell, G. and Marcus, H.L., *A model for fatigue crack closure based on surface roughness and residual strain.* Scripta Metallurgica, 1977. **11**(6): p. 521-524.
42. Wang, S.H. and Müller, C., *Fracture surface roughness and roughness-induced fatigue crack closure in Ti-2.5 wt% Cu.* Materials Science and Engineering A, 1998. **255**(1-2): p. 7-15.
43. Ma, L.Z., Chang, K.M. and Mannan, S.K., *Oxide-induced crack closure: an explanation for abnormal time-dependent fatigue crack propagation behavior in INCONEL alloy 783.* Scripta Materialia, 2003. **48**(5): p. 583-588.
44. Suresh, S. and Ritchie, R.O., *Some considerations on the modelling of oxide-induced fatigue crack closure using solutions for a rigid wedge inside a linear elastic crack.* Scripta Metallurgica, 1983. **17**(4): p. 575-580.
45. Liaw, P.K., Leax, T.R., Williams, R.S. and Peck, M.G., *Influence of oxide-induced crack closure on near-threshold fatigue crack growth behavior.* Acta Metallurgica, 1982. **30**(12): p. 2071-2078.
46. Tzou, J.L., Hsueh, C.H., Evans, A.G. and Ritchie, R.O., *Fatigue crack propagation in oil environments-- II. A model for crack closure induced by viscous fluids.* Acta Metallurgica, 1985. **33**(1): p. 117-127.
47. Du, B.P. and Li, N., *The influence of microstress on the effective fatigue threshold.* International Journal of Fatigue, 1989. **11**(1): p. 43-50.
48. Vasudeven, A.K., Sadananda, K. and Louat, N., *A review of crack closure, fatigue crack threshold and related phenomena.* Materials Science and Engineering: A, 1994. **188**(1-2): p. 1-22.
49. Uematsu, Y., Tokaji, K., Horie, T. and Nishigaki, K., *Fracture toughness and fatigue crack propagation in cast irons with spheroidal vanadium carbides dispersed within martensitic matrix microstructure.* Materials Science and Engineering: A, 2007. **471**(1-2): p. 15-21.
50. Kane, A. and Doquet, V., *Surface crack and cracks networks in biaxial fatigue.* Engineering Fracture Mechanics, 2006. **73**(2): p. 233-251.
51. Christopher, C.J., James, M.N., Patterson, E.A. and Tee, K.F., *Towards a new model of crack tip stress fields* International Journal of Fracture, 2007. **148**: p. 361-371.
52. Christopher, C.J., James, M.N., Patterson, E.A. and Tee, K.F., *A quantitative evaluation of fatigue crack shielding forces using photoelasticity.* Engineering Fracture Mechanics, 2008. **75**(14): p. 4190-4199.
53. Anderson, T.L., *Fracture mechanics: Fundamentals and Applications(2nd Edition).* 1994: p. 31-106.
54. Airy, G.B., Report of the British Association for the Advancement of Science, 1862.

55. Irwin, G.R., *Discussion of the paper: The dynamic stress distributuion surrounding a running crack-A photoelastic analysis.* Proc. SESA, 1958. **16**(1): p. 93–96.
56. Westergaard, H.M., *Bearing pressures and cracks.* Journal of Applied Mechanics, 1939. **6**: p. 49-53.
57. Wells, A.A. and Post, D., *The dynamic stress distribution surrounding a running crack: A photoelastic analysis.* Proceedings of SESA, 1958. **16**: p. 69-93.
58. Shi, G.C., *On the Westergaard method of crack analysis.* Internaltional Journal of Fracture Mechancis, 1966. **2**: p. 628-631.
59. Williams, M.L., *Stress singularities resulting from various boundary conditions in angular corners of plates in extension.* Journal of Applied Mechanics, 1952. **74**: p. 526-528.
60. Williams, M.L., *On the stress distribution at the base of a stationary crack.* Journal of Applied Mechanics, 1957. **24**: p. 109-114.
61. Muskhelishvili, N.I., *Some basic problems of the mathemtcial theory of elasticity.* Third edition, Noordhoff Ltd., Groningen, Holland, 1953.
62. Elber, W., *Fatigue crack closure under cyclic tension.* Engineering Fracture Mechanics, 1970. **2**(1): p. 37-44.
63. Suresh, S., *Fatigue of Materials* Second edition, Cambridge University Press, UK, 2001.
64. Louat, N., Sadananda, K., Duesbery, M. and Vasudevan, A.K., *A Theoretical Evaluation of Crack Closure. . Metallurgical Transactions*, 1993. **24A**: p. 2225-2232.
65. James, M.N., *Some unresolved issues with fatigue crack closure – measurement, mechanism and interpretation problems.* Proc. of the Ninth International Conference on Fracture, Sydney, Australia, Pergamon Press, 1997. **5**: p. 2403-2414.
66. Budiansky, B. and Hutchinson, J.W., *Analysis of closure in fatigue crack growth.* J. Applied Mechanics, Trans, ASME, 1978. **45**: p. 267-276.
67. Patterson, E.A. and Olden, E.J., *Optical analysis of crack tip stress fields: a comparative study.* Fatigue and Fracture of Engineering Materials and Structures, 2004. **27**(7): p. 623-635.
68. Nowell, D., Paynter, R.J.H. and de Matos, P.E.P., *Optical methods for measurement of fatige crack clousre: Moire, interferometry and digital iamge correlation.* Fatigue and Fracture of Engineering Materials and Structures, 2010: p. 1-13.
69. Asundi, A., *Recent advances in photoelastic applications.* Proceedings of SPIE 1997. **3211**: p. 463.
70. Aben, H., *Photoelasticity of Galss.* Berlin; New York: Springer-Verlag, 1993.
71. Coker, E.G. and Filon, L.N.G., *A treatise on photoelasticity.* New York, Cambridge University Press, 1931.
72. Oppel, G., *Polarisation optische.* Untersuchung raumlicher Spannungs und Dehungszustande, Forsch Geb Ingenieurw, 1936. **7**: p. 240-248.
73. Hetenyi, M., *The fundamentals of three dimensional photoelasticity.* Jounrnal of Applied mechanics, 1938. **5**(4): p. 149-155.
74. http://hyperphysics.phy-astr.gsu.edu/hbase/hframe.html.
75. http://www.wikimedia.org/.
76. http://www.ifsc.usp.br/~lavfis2/, *Experimental stress analysis.*
77. http://www.strainoptic.com/, *Fundamentals of Photoelasticity.*
78. Frocht, M.M., *Photoelasticity.* John Willey, New York, 1948.
79. http://www.doitpoms.ac.uk/tlplib/photoelasticity/intro.php.
80. http://mbarkey.eng.ua.edu/labs/photoelasticity/curved-bar/photoelasticity-lab.htm.
81. Sanford, R.J., *Application of the Least-squares Method to photoelastic analysis.* Experimental Mechanics, 1980. **20**: p. 192-197.
82. Bradley, W.B. and Kobayashi, A.S., *An investigation of Propagating cracks by dynamic photoelasticity.* Experimental Mechanics, 1970. **10**(3): p. 106-114.

83. Schroedl, M.A. and Smith, C.W., *Local stress near dead surface flaws under cylindrical bending fields.* ASTM STP 536, 1973: p. 45-63.
84. Theocaris, P.S. and Gdoutos, E.E., *A photoelastic determination of KI stress intensity factor.* Engineering Fracture Mechanics, 1975. **7**: p. 331-339.
85. Gdoutos, E.E. and Theocaris, P.S., *A photoelastic determination of mixed-mide stress-intensity factors.* Experimental Mechanics, 1978: p. 87-96.
86. Schroedl, M.A., McGowan, J.J. and Smith, C.W., *Determination of stress-intensity factors from photoelastic data with applications to surface-flaw problems.* Experimental Mechanics, 1974. **14**(10): p. 392-399.
87. Smith, C.W., *Use of three-dimensional photoelasticity in fracture mechanics.* Experimental Mechanics, 1973. **13**(12): p. 539-544.
88. Schroedl, M.A. and Smith, C.W., *A study of near and far field effects in photoelastic stress intensity determination.* Engineering Fracture Mechanics, 1975. **7**(2): p. 341-355.
89. Sanford, R.J. and Dally, J.W., *A general method for determining mixed mode stress intensity factors from isochromatic fringe patterns.* Engng Fracture Mech, 1979. **11**: p. 621-633.
90. Berghaus, D.G., *Overdetermined photoelastic solutions using least squares.* Experimental Mechanics, 1973: p. 97-104.
91. Smith, C.W. and Olaosebikan, O., *On the extraction of stress intensity factors from near-tip photoelastic data.* Experimental Mechanics, 1986. **26**(4): p. 313-318.
92. Nurse, A.D. and Patterson, E.A., *Determination of predominantly Mode II stress intensity factors from isochromatic data.* Fatigue and Fracture of Engineering Materials and Structures, 1993. **16**(12): p. 1339-1354.
93. Pacey, M.N., James, M.N. and Patterson, E.A., *A new photoelastic model for studying fatigue crack closure* Experimental Mechanics, 2005. **45**(1): p. 42-52.
94. Lopez-Crespo, P., *Fatigue crack characterization by image correlation* PhD. Thesis, University of Sheffield., 2007.
95. http://dankuchma.com/cee498/presentations/.
96. Quinta da Fonseca, J., Mummery, P.M. and Withers, P.J., *Full-field strain mapping by optical correlation of micrographs acquired during deformation.* Journal of Microscopy, 2005. **218, Pt 1**: p. 9-21.
97. Bruck, H.A., McNeill, S.R., Sutton, M.A. and Peters, W.H., *Digital image correlation using Newton-Raphson method of partial differential correction* Experimental Mechanics, 1989. **29**(3): p. 261-267.
98. Van Paepegem, W., Shulev, A.A., Roussev, I.R., De Pauw, S., Degrieck, J. and Sainov, V.C., *Study of the deformation characteristics of window security film by digital image correlation techniques.* Optics and Lasers in Engineering. **47**(3-4): p. 390-397.
99. Rae, P.J., Palmer, S.J.P., Goldrein, H.T., Lewis, A.L. and Field, J.E., *White-light digital image cross-correlation (DICC) analysis of the deformation of composite materials with random microstructure* Optics and Lasers in Engineering, 2004. **41**(4): p. 635-648.
100. LaVision GmbH, *PIV Software Mannual: DaVis.* Gottingem, Germany, 7.1 edition, 2005.
101. http://www.dantecdynamics.com/.
102. Dantec Q400 v2.3, *Software: Istra 4D Version 4.2.1 Mannual V1.8.* 2006.
103. Evans, W.T. and Luxmoore, A., *Measurement of in-plane displacements around crack tips by a laser speckle method* Engineering Fracture Mechanics, 1974. **6**(4): p. 735-743.
104. Chu, T.C., Ranson, W.F. and Sutton, M.A., *Applications of digital-image-correlation techniques to experimental mechanics* Experimental Mechanics, 1985. **25**(3): p. 232-244.
105. McNeill, S.R., Peter, W.H. and Sutton, M.A., *Estimation of stress intensity factor by digital image correlation.* Engineering Fracture Mechanics, 1987. **28**(1): p. 101-112.

106. Sutton, M.A., McNeill, S.R., Jang, J. and Babai, M., *Effects of subpixel image restoration on digital correlation error estimates.* Optical Engineering, 1988. **27**: p. 870-877.
107. Sutton, M.A., Turner, J.L., Chao, Y.J., Bruck, H.A. and Chae, T.L., *Experimental investigations of three-dimensional effects near a crack tip using computer vision* Internaltional Journal of Fracture Mechancis, 1992. **53**(3): p. 201-228.
108. Durig, B., Zhang, F., McNeill, S.R., Chao, Y.J. and Peters III, W.H., *A study of mixed mode fracture by photoelasticity and digital image analysis.* Optics and Lasers in Engineering, 1991. **14**(3): p. 203-215.
109. Gang, H., Sutton, M.A., Chao, Y.J. and Lyons, J.S., *A study of stable crack growth in thin SEC specimens of 304 stainless steel by computer vision.* Engineering Fracture Mechanics, 1995. **52**(3): p. 525-555.
110. Yoneyama, S., Morimoto, Y. and Takashi, M., *Automatic Evaluation of Mixed-mode Stress Intensity Factors Utilizing Digital Image Correlation.* Strain, 2006. **42**(1): p. 21-29.
111. Yoneyama, S., Ogawa, T. and Kobayashi, Y., *Evaluating mixed-mode stress intensity factors from full-field displacement fields obtained by optical methods* Engineering Fracture Mechanics, 2007. **74**(9): p. 1339-1412.
112. Kirugulige, M.S. and Tippur, H.V., *Measurement of Fracture Parameters for a Mixed-Mode Crack Driven by Stress Waves using Image Correlation Technique and High-Speed Digital Photography.* Strain, 2008. **45**(2): p. 108-122.
113. Dawicke, D.S. and Sutton, M.A., *CTOA and crack-tunneling measurements in thin sheet 2024-T3 aluminum alloy* Experimental Mechanics, 1994. **34**(4): p. 357-368.
114. McNeill, S.R., Sutton, M.A., Miao, Z. and Ma, J., *Measurement of surface profile using digital image correlation.* Experimental Mechanics, 1997. **37**(1): p. 13-20.
115. Mekky, W. and Nicholson, P.S., *The fracture toughness of Ni/Al2O3 laminates by digital image correlation I: Experimental crack opening displacement and R-curves.* Engineering Fracture Mechanics, 2006. **73**(5): p. 571-582.
116. Mekky, W. and Nicholson, P.S., *The fracture toughness of Ni/Al2O3 laminates by digital image correlation II: Bridging-stresses and R-curve models.* Engineering Fracture Mechanics, 2006. **73**(5): p. 583-592.
117. Lagattu, F., Brillaud, J. and Lafarie-Frenot, M.C., *High strain gradient measurements by using digital image correlation technique.* Materials Characterization, 2004. **53**(1): p. 17-28.
118. Pan, B., Asundi, A., Xie, H. and Gao, J., *Digital image correlation using iterative least squares and pointwise least squares for displacement field and strain field measurements.* Optics and Lasers in Engineering. **47**(7-8): p. 865-874.
119. Verhulp, E., Rietbergen, B.V. and Huiskes, R., *A three-dimensional digital image correlation technique for strain measurements in microstructures.* Journal of Biomechanics, 2004. **37**(9): p. 1313-1320.
120. Tao, G. and Xia, Z.H., *A non-contact real-time strain measurement and control system for multiaxial cyclic/fatigue tests of polymer materials by digital image correlation method.* Polymer Testing, 2005. **24**(7): p. 844-855.
121. Hwang, S.F., Horn, J.T. and Wang, H.J., *Strain measurement of SU-8 photoresist by a digital image correlation method with a hybrid genetic algorithm.* Optics and Lasers in Engineering, 2008. **46**(3): p. 281-289.
122. Vanlanduit, S., Vanherzeele, J., Longo, R. and Guillaume, P., *A digital image correlation method for fatigue test experiments.* Optics and Lasers in Engineering. **47**(3-4): p. 371-378.
123. Tung, S.H., Shih, M.H. and Sung, W.P., *Development of digital image correlation method to analyse crack variations of masonry wall* SADHANA, 2008. **33**(6): p. 767-779.
124. Goh, J.Y.L., Pitter, M.C., See, C.W., Somekh, M.G. and Vanderstraeten, D., *Sub-pixel image correlation: an alternative to SAM and dye penetrant for crack detection and mechanical stress localisation in semiconductor packages.* Microelectronics Reliability, 2004. **44**(2): p. 259-267.

125. Abanto-Bueno, J. and Lambros, J., *Investigation of crack growth in functionally graded materials using digital image correlation.* Engineering Fracture Mechanics, 2002. **69**(14-16): p. 1695-1711.
126. Li, M., Zhang, J., Xiong, C.Y., Fang, J., M Li, J. and Hao, Y., *Damage and fracture prediction of plastic-bonded explosive by digital image correlation processing.* Optics and Lasers in Engineering, 2005. **43**(8): p. 856-868.
127. Hutt, T. and Cawley, P., *Feasibility of digital image correlation for detection of cracks at fastener holes.* NDT & E International, 2009. **42**(2): p. 141-149.
128. Huang, Y.H., Liu, L., Yeung, T.W. and Hung, Y.Y., *Real-time monitoring of clamping force of a bolted joint by use of automatic digital image correlation.* Optics & Laser Technology, 2009. **41**(4): p. 408-414.
129. Tong, F.C. and Gary, T.G.F., *Fatigue crack closure study based on whole-field displacements.* 1996. **18**(8): p. 593-601.
130. de Matos, P.F.P. and Nowell, D., *Experimental and numerical investigation of thickness effects in plasticity-induced fatigue crack closure* Internaltional Journal of Fracture Mechancis, 2009. **31**(11-12): p. 1795-1804.
131. He, Z.H., Sutton, M.A., Ranson, W.F. and Peters, W.H., *Two-dimensional fluid-velocity measurements by use of digital-speckle correlation techniques* Experimental Mechanics, 1984. **24**(2): p. 117-121.
132. Dugdale, D.S., *Yielding of steel sheets containing slits.* Journal of the Mechanics and Physics of Solids, 1960. **8**(2): p. 100-104.
133. Dill, H.D. and Saff, C.R., *Analysis of crack growth following compressive high loads based on crack surface displacements and contact analysis.* MCAIR 76-006, McDonnell Aircraft Co., 1976.
134. Fuhring, H. and Seeger, T., *Dugdale crack closure analysis of fatigue cracks under constant amplitude loading.* Engineering Fracture Mechanics, 1979. **11**(1): p. 99-122.
135. Codrington, J. and Kotousov, A., *A crack closure model of fatigue crack growth in plates of finite thickness under small-scale yielding conditions.* Mechanics of Materials, 2009. **41**(2): p. 165-173.
136. Newman Jr, J.C., *A crack closure model for predicting fatigue crack growth under aircraft spectrum loading.* Methods and Models for Predicting Fatigue Crack Growth under Random Loading, ASTM STP 748, Chang,J.B. and Hudson, C.M., (eds), 1981: p. 53-84.
137. Mirzaei, M. and Provan, J.W., *A new method for the analysis and assessment of fatigue crack closure. I: modeling.* Theoretical and Applied Fracture Mechanics, 1992. **18**(1): p. 47-58.
138. Mirzaei, M. and Provan, J.W., *A new method for the analysis and assesment of fatigue crack closure. II: experimental study.* Theoretical and Applied Fracture Mechanics, 1992. **18**(1): p. 59-63.
139. Newman Jr, J.C., *A finite element analysis of fatigue crack closure.* Mechanicsl of Crack growth ASTM STP 590, 1976: p. 281-301.
140. McClung, R.C. and Sehitoglu, H., *On the finite element analysis of fatigue crack closure--1. Basic modeling issues.* Engineering Fracture Mechanics, 1989. **33**(2): p. 237-252.
141. Wei, L.W. and James, M.N., *Fatigue crack closure for inclined and kinked cracks* Internaltional Journal of Fracture, 2002. **116**(1): p. 25-50.
142. Hucker, S.A. and Farris, T.N., *Modified crack closure method using boundary elements.* Engineering Fracture Mechanics, 1993. **46**(5): p. 763-772.
143. Chao, R.M. and Chang, C.H., *Boundary element method for the frictionless arc-shaped crack closure problem.* Engineering Analysis with Boundary Elements, 1996. **17**(3): p. 245-252.
144. Schijve, J., *Fatigue crack closure: Observations and technical significance.* Mechanics of Fatigue Crack Closure, ASTM STP 982, 1988: p. 5-34.
145. Jones, J.W., Macha, D.E. and Corbly, D.M., *Observations on fatigue crack opening load determinations* Internaltional Journal of Fracture, 1978. **14**(1): p. R25-R30.

146. Bowman, R., Antolovich, S.D. and Brown, R.C., *A demonstration of problems associated with crack closure measurement techniques.* Engineering Fracture Mechanics, 1988. **31**(4): p. 703-712.
147. Hudak Jr, S.J. and Davidson, D.L., *The dependence of crack closure on fatiuge loading variables.* Mechanics of fatigue crack closure, ASTM STP 982. Ed by Newman, J. C., and Elber, W., 1988: p. 121-.
148. Minakawa, K. and McEvily, A.J., *On crack closure in the near-threshold region.* Scripta Metallurgica et Materalia, 1981. **15**: p. 633-636.
149. Evans, W.J. and Spence, S.H., *Characterization of crack tip and geometry induced closure.* International Journal of Fatigue, 1997. **19**(93): p. 205-210.
150. Huang, X.Y., Lang, M., Wu, X.R. and Doker, H., *Analysis of crack closure by different measurement methods.* Key Engineering Materials, 1998. **145-149**: p. 637-643.
151. Garz, R.E. and James, M.N., *Observations on evaluating fatigue crack closure from compliance traces.* International Journal of Fatigue, 1989. **11**(6): p. 437-440.
152. James, M.N. and Knott, J.F., *Critical aspects of the characterization of crack tip closure by compliance techniques.* Materials Science and Engineering, 1985. **72**(1): p. L1-L4.
153. Gan, D. and Weertman, J., *Crack closure and crack propagation rates in 7050 aluminum.* Engineering Fracture Mechanics, 1981. **15**(1-2): p. 87-93.
154. Pippan, R., *The sensitivity to measure crack closure with strain gauges near the crack tip.* Engineering Fracture Mechanics, 1988. **31**(5): p. 867-871.
155. Vecchio, R.S., *Anomalous aspects of crack closure* Internaltional Journal of Fracture, 1986. **31**(2): p. R29-R33.
156. Davidson, D.L., *Fatigue crack closure.* Engineering Fracture Mechanics, 1991. **38**(6): p. 393-402.
157. Sutton, M.A., Zhao, W., McNeill, S.R., Helm, J.D., Piascik, R.S. and Riddell, W.T., *Local crack closure measurements:development of a measurement system using computer vision and a far-field microscope.* ASTM STP1343, 1999: p. 145-156.
158. Diaz, F.A., Patterson, E.A., Tomlinson, R.A. and Yates, J.R., *Measuring stress intensity factors during fatigue crack growth using thermoelasticity.* Fatigue and Fracture of Engineering Materials and Structures, 2004. **27**(7): p. 571-584.
159. Yisheng, W. and Schijve, J., *Fatigue crack closure measurements on 2024-T3 sheet specimens.* Fatigue and Fracture of Engineering Materials and Structures, 1995. **18**(9): p. 917-921.
160. Roberson, L.J. and Kirk, M.T., *A statistical approach to crack closure determination.* Mechanics of fatigue crack closure, ASTM STP 982. Ed by Newman, J. C., and Elber, W., 1988: p. 230-246.
161. Allison, J.E., Ku, R.C. and Pompetzki, M.A., *A comparison of measurement of methods and numerical procedures for the experimental characterization of fatigue crack closure.* Mechanics of fatigue crack closure, ASTM STP 982. Ed by Newman, J. C., and Elber, W., 1988: p. 171-185.
162. McClung, R.C., *The influence of applied stress, crack length, and stress intensity factor on crack closure* Metallurgical and Materials Transactions A, 1991. **22**(7): p. 1559-1571.
163. Drury, W.J., Gokhale, A.M. and Antolovich, S.D., *Effect of crack surface geometry on fatigue crack closure* Metallurgical and Materials Transactions A, 1995. **26**(10): p. 2651-2663.
164. Chen, D.L., Weiss, B., Stickler, R. and Wang, Z.G., *Brief review and reconsideration of fatigue crack closure effect in materials.* J. Mater. Sci.Technol., 1997. **13**(1): p. 1-14.
165. Vasudevan, A.K., Sadananda, K. and Louat, N., *Two critical stress intensities for threshold fatigue crack propagation* Scripta Metallurgica et Materalia, 1993. **28**(11): p. 65-701.

166. Lal, D.N., *A detailed physical analysis of the R-effect on LEFM fatigue crack growth--I. On the combined roles of critical zones, LEFM parameters and stress ratio.* Engineering Fracture Mechanics, 1996. **55**(1): p. 115-132.
167. Ritchie, R.O. and Suresh, S., *Some considerations on fatigue crack closure at Near-threshold stress intensities due to fracture surface morphology.* Metallurgical Transactions A, 1982. **13A**: p. 937-940.
168. Suresh, S. and Ritchie, R.O., *A geometric medol for fatigue crack closure induced by fracture surface roughness.* Metallurgical Transactions A, 1982. **13A**: p. 1627-1631.
169. Kondo, Y., Sudo, T. and Kubota, M., *Critical crack size that causes retardation of short fatigue crack by single overload.* Fatigue and Fracture of Engineering Materials and Structures, 2009. **32**(10): p. 856-864.
170. Fleck, N.A. and Smith, R.A., *Crack closure - is it just a surface phenomenon?* International Journal of Fatigue, 1982. **4**(3): p. 157-160.
171. Sehitoglu, H., *Crack opening and closure in fatigue.* Engineering Fracture Mechanics, 1985. **21**(2): p. 329-339.
172. Shih, T.T. and Wei, R.P., *A study of crack closure in fatigue.* Engineering Fracture Mechanics, 1974. **6**(1): p. 19-32.
173. Andersson, M., Persson, C. and Melin, S., *Experimental and numerical investigation of crack closure measurements with electrical potential drop technique.* International Journal of Fatigue, 2006. **28**(9): p. 1059-1068.
174. Bachmann, V. and Munz, D., *Fatigue crack closure evaluation with the potential method.* Engineering Fracture Mechanics, 1979. **11**(1): p. 61-71.
175. Pippan, R., Haas, G. and Stuwe, H.P., *Comparison of two methods to measure crack closure in ultra-high vacuum.* Engineering Fracture Mechanics, 1989. **34**(5-6): p. 1075-1084.
176. Chen, D.L., Weiss, B. and Stickler, R., *A new evaluation procedure for crack closure.* International Journal of Fatigue, 1991. **13**(4): p. 327-331.
177. Betegón, C. and Hancock, J.W., *Two-parameter characterization of elastic-plastic crack-tip fields.* J. Appl. Mech, 1991. **58**(1): p. 104-110.
178. Du, Z.Z. and Hancock, J.W., *The effect of non-singular stresses on crack-tip constraint.* Journal of the Mechanics and Physics of Solids, 1991. **39**(4): p. 555-567.
179. Zhao, L.G., Tong, J. and Byrne, J., *Stress intensity factor K and the elastic T-stress for corner cracks* Internaltional Journal of Fracture, 2001. **109**(2): p. 209-225.
180. Larsson, S.G. and Carlsson, A.J., *Influence of non-singular stress terms and specimen geometry on small-scale yielding at crack tips in elastic-plastic materials.* Journal of the Mechanics and Physics of Solids, 1973. **21**(4): p. 263-277.
181. Tong, J., *T-stress and its implications for crack growth.* Engineering Fracture Mechanics, 2002. **69**(12): p. 1325-1337.
182. O'Dowd, N.P. and Shih, C.F., *Family of crack-tip fields characterized by a triaxiality parameter--I. Structure of fields.* Journal of the Mechanics and Physics of Solids, 1991. **39**(8): p. 989-1015.
183. Tong, J., Byrne, J., Hall, R. and Allabadi, M.H., *A comparison of corner notched and compact tension specimens for high temperature fatigue testing.* Beynon JH, Brown MW, Smith RA, Lindley TC, Tomkins B, editors. Engineering against fatigue,, 1999: p. 583-590.
184. Leevers, P.S. and Radon, J.C., *Inherent stress biaxiality in various fracture specimen geometries* 1983. **19**(4): p. 311-325.
185. Roychowdhury, S. and Dodds, R.H., *Effect of T-stress on fatigue crack closure in 3-D small-scale yielding.* International Journal of Solids and Structures, 2004. **41**(9-10): p. 2581-2606.
186. Kim, Y., Zhu, X.K. and Chao, Y.J., *Quantification of constraint on elastic-plastic 3D crack front by the J-A2 three-term solution.* Engineering Fracture Mechanics, 2001. **68**(7): p. 895-914.

187. Tvergaard, V. and Hutchinson, J.W., *Effect of T-stress on mode I crack growth resistance in a ductile solid.* International Journal of Solids and Structures, 1994. **31**(6): p. 823-833.
188. Cotterell, B., *Notes on the paths and stability of cracks* Internaltional Journal of Fracture, 1966. **2**(3): p. 526-533.
189. Cotterell, B. and Rice, J.R., *Slightly curved or kinked cracks* Internaltional Journal of Fracture, 1980. **16**(2): p. 155-169.
190. Meliani, M.H., Azari, Z., Pluvinage, G. and Matvienko, Y.G., *The effective T-stress estimation and crack paths emanating from U-notches.* Engineering Fracture Mechanics, 2010. **77**(11): p. 1682-1692.
191. James, M.N. and Knott, J.F., *An assessment of crack closure and the extent of the short crack regime in Q1N (HY80) steel.* Fatigue and Fracture of Engineering Materials and Structures, 1985. **8**(2): p. 177-191.
192. James, M.N. and Garz, R.E., *Relating closure development in long cracks to the short-crack regime.* International Journal of Fatigue, 1991. **13**(2): p. 169-173.
193. Wei, L.W. and James, M.N., *A study of fatigue crack closure in polycarbonate CT specimens.* Engineering Fracture Mechanics, 2000. **66**(3): p. 223-242.
194. Ewalds, H.L. and Wanhill, R.J.H., *Fracture mechanics.* Edward Arnold, New York,, 1984: p. 97.
195. Tada, H., Paris, P.C. and Irwin, G.R., *The stress analysis of cracks handbook.* ASME, New York, 2000: p. 62.
196. Srawley, J.E., *Wide-Range Stress Intensity Factor Expressions for ASTM E399 Standard Fracture Toughness Specimens.* Internaltional Journal of Fracture, 1976. **12**(3): p. 475-480.
197. Pappalettere, C., *Annealing polycarbonate sheets.* Strain, 1984. **20**(4).
198. Patterson, E.A. and Wang, Z.F., *Towards full-filed automated photoelastic analysis of complex components.* Strain, 1991. **27**: p. 49-56.
199. Patterson, E.A., *Digital photoelasticity: Principles, practice and potential.* Strain, 2002. **38**(27-39).
200. Siegmann, P., Díaz-Garrido, F. and Patterson, E.A., *Robust approach to regularize an isochromatic fringe map.* Applied Optics, 2009. **48**(2): p. E24-E34.
201. Siegmann, P., Backman, D. and Patterson, E.A., *A robust approach to demodulating and unwrapping phase-stepped photoelastic data.* Experimental Mechanics, 2005. **45**(3): p. 278-289.
202. http://www.opticalstrain.org/.
203. Sutton, M.A., Orteu, J.J. and Schreier, H., *Image Correlation for Shape, Motion and Deformation Measurements.* Basic Concepts,Theory and Applications. 2009: Springer Science.
204. Adam, G.A., Cross, A. and Haward, R.N., *The effect of the thermal pre-treatment on the mechanical properties of polycarbonate.* Journal of Materials Science, 1975. **10**: p. 1582-1590.
205. Siegmann, P. and Patterson, E.A., *Operating instructions for RICO(Regularized osochromatic phase map compution) programme Version 1.0.* 2008.
206. Schroedl, M.A., McGowan, J.J. and Smith, C.W., *An assessment of factors influencing data obtained by the photoelastic stress freezing technique for stress fields near crack tips.* Engineering Fracture Mechanics, 1972. **4**(4): p. 801-809.
207. Kambour, R.P., *Refractive indices and compositions of crazes in several glassy polymers.* Journal of Polymer Science Part A: General Papers, 1964. **2**(9): p. 4159-4163.
208. Hariharan, P., Optical Interferometry, 2nd Edition, Academic Press, New York, 2003: p. 119.
209. James, M.N., Lu, Y.W., Christopher, C.J. and Patterson, E.A., *A multiparameter frature mechanics approach to plasticity-induced crack tip shielding.* Workshop IGF, 2010.

210. Cotterell, B., *On fracture path stability in the compact tension test* International Journal of Fracture, 1970. **6**(2): p. 189-192.
211. Cheng, P., Sutton, M.A., Schreier, H.W. and McNeill, S.R., *Full-field speckle pattern image correlation with B-Spline deformation function* Experimental Mechanics, 2002. **42**(3): p. 344-352.
212. Goldberg, D.E., *Genetic Algorithms in Search, Optimization and Machine Learning* 1989: Addison Wesley; 1 edition
213. Nelder, J.A. and Mead, R., *A simplex method for function minimization.* The Computer Journal, 1965. **7**(4): p. 308-313.
214. Diaz, F.A., *Thermoelastic investigation of fatigue crack closure.* PhD. Thesis, University of Sheffield., 2004.
215. Ziou, D. and Tabbone, S., *Edge Detection Techniques - An Overview.* International Journal of Pattern Recognition and Image Analysis, 1998. **8**: p. 537--559.
216. Canny, J., *A computational approach to edge detection.* IEEE Trans. Pattern Analysis and Machine Intelligence, 1986. **8**: p. 679-714.
217. Sobel, I., *An isotropic 3×3 image gradient operator.* Machine. Vision for Three-Dimensional Scenes, ed. H. Freeman. 1990, NY: Academic. Press.
218. Prewitt, J., *Object Enhancemet And Extraction.* Picture Processing and Psychopictorics, ed. B.L.a.A. Rosenfeld. 1970, NY: Academic Press.
219. The Matheworks Inc., *Image processing toolbox user's guide.* 2009.
220. Zanganeh, M., *Experimental investigation of crack paths.* PhD. Thesis, University of Sheffield., 2008.